UNIVERSITY OF OKLAHOMA

GRADUATE COLLEGE

CONSTITUTIVE BEHAVIOR OF WELLBORE CEMENT

A DISSERTATION

SUBMITTED TO THE GRADUATE FACULTY

in partial fulfillment of the requirements for the

Degree of

DOCTOR OF PHILOSOPHY

By

ALEXANDRA CEDOLA
Norman, Oklahoma
2023

CONSTITUTIVE BEHAVIOR OF WELLBORE CEMENT

A DISSERTATION APPROVED FOR THE
MEWBOURNE SCHOOL OF PETROLEUM AND GEOLOGICAL ENGINEERING

BY THE COMMITTEE CONSISTING OF

Dr. Runar Nygaard, Chair

Dr. Ahmad Ghassemi

Dr. Catalin Teodoriu

Dr. Andrew Elwood Madden

Acknowledgements

To start, I would like to begin by thanking my advisor Dr. Runar Nygaard, for everything that he has helped me achieve and learn during my time as his student. In 2017, Dr. Nygaard was needing a student who was highly knowledgeable on all things wellbore cement…and then he got me. Under Dr. Nygaard's guidance, I have been able to grow significantly as both a researcher and a person. To say that Dr. Nygaard is the best advisor anyone could ever have would be an understatement, and I that think any of his current or previous students would wholeheartedly agree. Thanks for making me the cement nerd that I am.

I would like to thank my committee members Dr. Ahmad Ghassemi, Dr. Catalin Teodoriu, and Dr. Andrew Elwood Madden. I truly appreciate the time that they have taken to help me throughout my time as an OU Ph.D. student and their input and suggestions pertaining to my research. Each of their expertise has proven to impact the path of my research and gain a further understanding as to the importance of their respective research areas.

Shoutout and thanks to my parents and sister, Steve, Kathy, and Lizzy, for their love and support throughout my time as a Ph.D. student-I couldn't have done it without them and truly can not thank them enough for all that they have helped me through! I also love your updates on all things you've learned regarding cement (sometimes concrete)! I'd like to thank Mark Palmer, who has been there for me during all of the ups and downs of this process. Palmer's support, encouragement, optimism, and prime planning skills throughout this process have been so influential and have truly helped keep me sane-so thanks beebs! Also your ability to network and make things happen…truly unmatched. Just like your golf game.

Huge thank you to my research group, Na Yuan, Ashutosh Sharma, and Tunc Burrak for always being there to help out and encourage my research. Special thanks to one of the old group members and my office mate, Dr. Jarrett Wise-way to go buddy. You beat me to the degree.

I would like to thank Jeff McCaskill and Gary Stowe for their help with my research and equipment as well as Steve Dwyer, Yawei Li and John Zhou for their assistance running the hydrostatic compression and triaxial tests. I would like to thank Preston Larson for his help with running microscopy on my samples. I would also like to thank Sonya Grant, Francey Freeman, and Danika Hines-Barnett for all of their help and support throughout my time at OU. A big thank you to Katie Shapiro-you have been such a lifesaver and I can't tell you how much I appreciate all that you have done to help guide me, keep me on track, and keep me enrolled (and get me graduated). I really appreciate y'alls help!

Thank you to Dr. Geir Hareland for giving me my start in graduate studies. I would also like to thank ConocoPhillips, specifically Dale Doherty and Zach Litton, for their help with this research.

TABLE OF CONTENTS

List of Figures

List of Tables

Abstract

Cement is one of the most integral components of a wellbore, yet minimal experimental research has been done to understand the basic processes as to what ensures a cement sheaths' success. Globally, minimizing greenhouse gas emissions has become one of the most influential factors in material selection for both households and industries, and it is common knowledge that the manufacturing of cement is one of the largest contributors to greenhouse gas emissions, specifically, carbon dioxide. Industries that rely on cement for structural purposes, including the petroleum industry, have begun to investigate cement alternatives or cement replacement materials to minimize the emissions associated with cement manufacturing. Pozzolanic materials such as fly ash, slag, and metakaolin are common wellbore cement additives that have proven to be advantageous in achieving the required downhole mechanical properties but many of these materials have also become less prevalent as emissions are reduced due to their cost and availability. During the drilling process, there is an abundance of a pozzolanic material that has not been utilized as a cement additive or replacement material: shale. In this work, an investigation on the poroelastic constant for class H wellbore cement is conducted. The poroelastic constant is a common input parameter for wellbore modelling and is regularly assumed to be the same as unconsolidated material. The poroelastic constant is a key parameter for determining effective stress and has an impact on cement design in wellbores. Consolidated isotropic drained (CID) testing on class H cement is also performed at three confining stress to obtain a Mohr-Coulomb failure envelope. During CID testing, the samples are sheared and an understanding of shear behavior is evaluated. This information can be used to generate more detailed failure criteria for wellbore cements and be applied to cement system designs and modeling programs. From the results of this work, it can be concluded that cement is indeed a poroelastic material. An investigation on curing time, particle size, and additive quantity is also conducted to determine the feasibility of using shale cuttings as a cement additive or replacement material. It has been determined that the samples containing micron particle sized shale tended to have superior results for all quantities when compared to the millimeter and micron samples, possibly due to these particles being similar to the size of the cement. While this work is preliminary, future validation of the findings could be instrumental in decreasing the amount of waste and emissions produced both from cement manufacturing as well as from the recycling of drill cuttings.

Chapter 1: Introduction

In a world that is becoming increasingly cognizant of climate change and minimizing greenhouse gas emissions, both individuals and industries are attempting to reduce their carbon footprint. Hydrocarbon production has long been considered the highest producer of greenhouse gases (GHG), specifically carbon dioxide (CO_2), and a significant number of hydrocarbon producing companies are expanding their portfolios to renewable energy generation in an attempt to offset their GHG footprint. While renewable energy is becoming significantly more prevalent, the transition is slow and the need for petroleum and natural gas will remain for the foreseeable future. There are a number of areas within the petroleum industry that contribute to GHG emissions, but the largest has to do with one of the most common materials used downhole to successfully produce oil and natural gas: cement.

Wellbore cement is the primary barrier material in all wellbores, be it petroleum and natural gas wells, hydrogen storage wells, geothermal wells, or carbon capture and storage (CCS) wells. According to the USGS, 90 million tons of Portland cement was produced within the U.S. in 2021, with less than about three percent being used in the hydrocarbon sector (USGS, 2022). This amount may seem minimal, yet many operators and service companies have begun to investigate possible cement alternatives or replacement material to cut down on the amount of cement being used in the downhole environment. Natural, man-made, synthetic and recycled materials have all been investigated to determine their feasibility as supplementary cementitious material and have had optimistic results. However promising a number of these alternatives are, availability, cost, and long-term behavior are often overlooked. Pozzolanic material has been used as a cement additive or cement replacement for decades, but there is one such material that has not been investigated despite the fact that it is readily available and would be exceptionally

advantageous for operators: drill cuttings. Cuttings are a by-product of every hydrocarbon well and must be disposed of or recycled, further costing an operator. Shale is the most commonly drilled formation (Huang et al., 2011) and consists of a variety of clay or pozzolanic minerals such as kaolinite, smectite, and montmorillonite, begging the question of whether or not cuttings could be a feasible cement additive or cement replacement material (Laik, 2018). To better understand the practicality of using cuttings or any material within a slurry to be used downhole, it is imperative to understand current cement behavior, including but not limited to the mechanical and poroelastic properties.

Mechanical testing of cement provides insight into its short- and long-term behavior, both of which are important for establishing and maintaining wellbore integrity. While significant mechanical testing has been performed on cement, many researchers do not focus on testing samples after the early hydration period has been achieved, or after curing for 28 days. Prior to the early hydration period, cement will experience significant changes to its unconfined compressive strength (*UCS*) and chemical composition thus providing inaccurate test results. Such inaccuracies could be detrimental to long-term downhole cement systems in that they are unable to withstand the harsh environments and could ultimately fail, leading to hydrocarbon migration, inability to support the casing or formation, and a number of other significant issues. Inability of an alternative cementitious material to achieve the necessary strength and ductility requirements would prove disastrous either shortly after being placed downhole or in the long-term during completions, production, or abandonment process.

Compatibility between the cement and additives are often overlooked or understudied; the chemistry and bonding capabilities need to be taken into consideration when using additives or an alternative material as these parameters could affect the establishment of mechanical

properties and degradation. The compatibility of the cement system and drilling mud should also be regularly investigated to understand any severe adverse effects.

Another topic of importance when it comes to cement and its behavior downhole are the poroelastic properties, specifically the poroelastic constant or the Biot coefficient, which has been widely studied in soil and rock, but little has been investigated pertaining to its values within cement. The Biot coefficient is an important parameter in that it describes the effect of fluid within the pores with changes in bulk volume and is integral in effective stress determination. Having an accurate understanding of the downhole cement effective stress allows for a better knowledge of when and how failure will occur as well as allow for more accurate slurries to be designed for specific wellbore conditions, regardless of the type of additive used in the slurry.

The objective of this work is twofold: gain a better understanding of the poroelastic properties of class H cement for downhole use and to investigate the feasibility of using a readily available upcycled pozzolanic material, drill cuttings, as a cement additive. In chapter 4 of this work, an investigation on the poroelastic coefficient is performed on neat class H cement using cement from Central Plains Cement Company in Tulsa, Oklahoma. Once the poroelastic coefficient is obtained, triaxial testing is done at three varying confining stress so that a failure envelope can be created and used in conjunction with the poroelastic coefficients to establish a better understanding of constitutive *in-situ* cement behavior and this is described in chapter 5. Having determined the mechanical and poroelastic coefficient for neat class H cement, chapter 6 details an analysis on the mechanical properties of class H cement containing various amounts of an unconventional geologic additive, drill cuttings, is executed. In conjunction with varying the quantity of the cuttings within the cement, size of cuttings will also be examined to determine the

impact that this parameter has on cement mechanical properties. Microscopy is also utilized on tested samples to understand the macro- and microstructure of the cement as well as provide insight as to the chemical compositions and variations in compositions encountered throughout the samples.

Experiments conducted within this work, specifically regarding the utilization of cuttings within cement, are preliminary and further testing is required to validate results and ensure field applicability. Regardless, having a basic understanding of both the poroelastic constant and how the addition of cuttings to cement effects cement behavior are exceptionally beneficial to the petroleum industry. Such information could potentially lead to less cement being used downhole, minimizing cuttings disposal, and better wellbore integrity, all of which lead to a reduction in CO_2 emissions.

Chapter 2: Literature Review

Wellbore cement is a complex material that, while being highly studied, is not fully understood. This section will provide insight as to cement hydration processes, classification of wellbore cements, slurry design, reasons for degradation, key properties needed to design wellbore cement, and test methods to determine these properties.

2.1 Background

Wellbore cement is an integral part of a wells' success. The purpose of the cement is to provide zonal isolation, prevent hydrocarbon migration, and support the casing/formation. While cement is the most widely used barrier material within hydrocarbon wells, there is a substantial amount of information that remains to be learned about cement behavior downhole and long term. One area that exemplifies this is the utilization of additives and the effect that they have on cement

mechanical properties under downhole conditions. Oftentimes, the effect of additives on mechanical properties are investigated at surface conditions and for a short hydration period, frequently being tested prior to the completion of the early hydration portion of curing. There is a plethora of materials that have been utilized for investigating their potential as a cement additive, but more often than not, cost, availability, and environmental concerns associated with said materials are not considered. Another aspect of wellbore cement that has often been overlooked is the determination of the poroelastic properties. Poroelastic properties, specifically the Biot coefficient, are pertinent for downhole effective stress calculations which, in turn, dictate wellbore cement design. The primary reasons why testing to determine the poroelastic properties of a material are not commonly performed is due to the time required to obtain such parameters as well as the costs associated with running the tests.

It should be noted that while the findings obtained within this work are prolific, it is a preliminary study and further testing needs to be done to further verify and expand on the feasibility of the findings within. If proven feasible, the use of such information could impact not just cement design, but also aid in promoting more environmentally friendly materials within petroleum engineering. Using a recycled (or upcycled) material has the potential to minimize the amount of cement needed to provide an acceptable downhole barrier and ultimately could reduce emissions associated with cement production. Having a better understanding of how cement behaves downhole and the basic impact of the poroelastic constant on effective stress calculations may lead to a safer well design thus promoting safer, more stable wellbores with less environmental impact.

2.2 Cement Overview

Portland cement clinker, or the solid cementitious material, has a dynamic chemical composition, but there are four primary chemical compounds that are found in unhydrated Ordinary Portland cement (OPC): tricalcium silicate (alite; C_3S), dicalcium silicate (belite; C_2S), tricalcium aluminate (aluminate; C_3A), and tetracalcium aluminoferrite (ferrite; C_4AF). Alite is the most common constituent of the clinker and as such is the most commonly used chemical to describe the process of cement hydration. Typical OPC clinker compositions range from 55-65% C_3S, 15-25% C_2S, 8-12% C_3A, 8-12% C_4AF and small amounts of gypsum to the cement clinker when it is being ground to prevent particle temperature from increasing and causing the particles to stiffen (Michaux et al., 1990; Kurdowski, 2014). An image of a conventional cement clinker prior to hydration is shown in Fig. 2.1; while cement composition is widely described in literature, it is difficult to find microscopy of labeled clinker containing the four primary components (Locher, 2006; Sintef, 2007). It can be seen that alite, which is the shown to be the largest, most prevalent particle type is highly angular and is somewhat darker in color than the other clinker components. Belite, while also fairly large in size, is much more circular and lighter in color. The small, dark, oblong segments are the aluminate while the white rods are the ferrite.

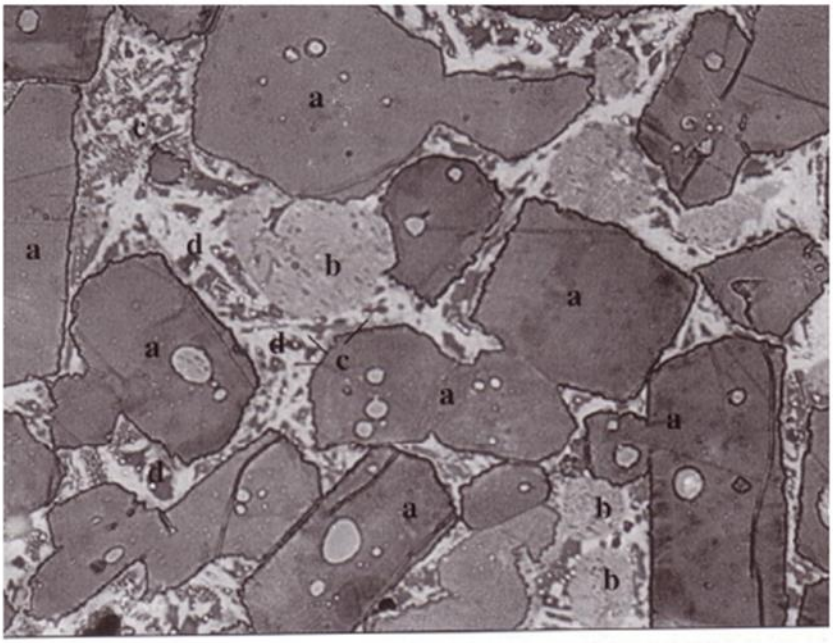

Figure 2.1. Optical microscopic image of cement clinker showing (a) alite, (b) belite, (c) aluminate, (d) ferrite (Locher, 2006; Sintef, 2007).

2.3 Cement Hydration Process

To begin the hydration process, water is added to the cement; the water-cement ratio can vary depending on cement requirements. Once the water has been added to the cement slurry, the primary silicate material within the cement (C_3S and C_2S) react with the water and undergo similar chemical reactions. Alite hydration is shown as (Eq. 2.1),

$$2C_3S + 7H = C_3S_2H_4 + 3CH \tag{2.1}$$

Where the calcium hydroxide (CH) is crystalline and the calcium silicate hydrate ($C_3S_2H_4$), better known as C-S-H gel, is not crystalline and does not have a fixed composition (Sintef, 2007). Belite hydration is a slower, but nearly identical to the hydration of alite (Eq. 2.2):

$$2C_2S + 5H = C_3S_2H_4 + CH \tag{2.2}$$

For the purpose of cement hydration studies, alite is typically the chemical that is used to describe the cement hydration process due to it being the main material within cement clinker. A schematic plot showing the five stages of alite (and belite) hydration is shown in Fig. 2.2.

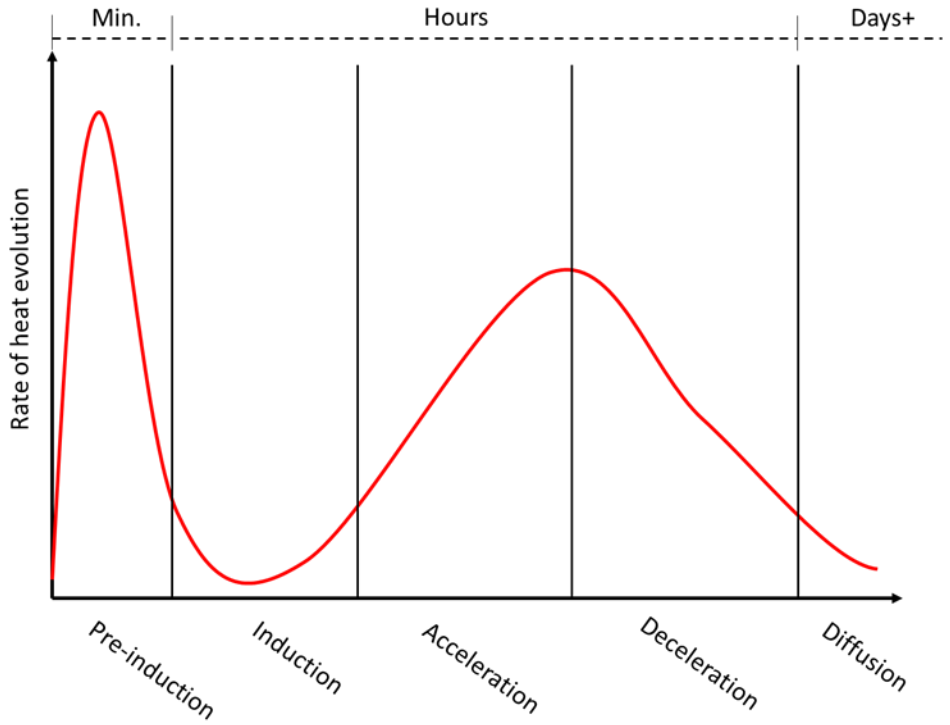

Figure 2.2. Schematic of alite hydration phases.

In regards to the alite hydration process, there is some disagreement between the number of stages that occur during hydration (Bullard et al., 2010; Meredith et al., 1995). Some researchers categorize the process as a three-phase process while others say four and some state more (Chandra & Flodin, 1987; Li et al., 2017; Meng et al., 2021; Qi et al., 2021; Dorn at al., 2022). It is the opinion of the author that, upon looking at Fig. 2.2, five stages are appropriate and seemingly details what is occurring in full in regards to the rate of heat evolution.

The first stage of the cement hardening process is the preinduction phase, which occurs when the cement slurry is being mixed and immediately after (Michaux et al., 1990). During this phase,

water is introduced to the cement clinker and the primary reactions that take place are between C_3A, gypsum and the water (Brandão et al., 2017). The preinduction phase is characterized by rapid dissolution and precipitation of chemicals thus modifying the chemical structures (Cadix et al., 2016).

Following the preinduction phase is the induction phase, and this phase lasts hours (Michaux et al., 1990). During the start of this phase, the cement is only slightly hydrated (Cadix et al., 2016). When hydration is in the induction phase, the chemical reactions wane and the consistency does not change (Meredith et al., 1995; Preece et al., 2000). The end of the induction phase and the point where the acceleration phase begins is debated within the chemistry community (Michaux et al., 1990).

At the start of the third phase, the acceleration phase, the initial setting of the cement begins to occur (Wang et al., 2019). During this phase, the cement releases a significant amount of heat due to the increase in C-S-H crystal formation (Li et al., 2021). The C-S-H gel forms on both the surface of the cement particles as well as within the pores (Liu et al., 2019). The acceleration phase is marked by a significant increase in the cement hydration rate, decrease in porosity, and development of compressive strength (Karakosta et al., 2015; Liu et al., 2019).

Once the peak exothermic reaction is reached, the deceleration phase begins to occur as seen in Fig. 2.2. In this phase, the C-S-H gel mitigates water and chemical movement and hydration rate decreases (Michaux et al., 1990). The final phase of cement hardening is the steady state, or diffusion phase. In this phase, any residual C_3S continues to be hydrated while other materials like C_2S, C_3A, and C_4AF will begin to be hydrated and form C-S-H gel over time (Meng et al., 2021).

The hydration of C_3A can vary depending upon the amount of calcium sulfate, which is typically added to cement in the form of gypsum; when calcium sulfate is not present, the C_3A reaction with water will form a gel on the surface of the C_3A particles and eventually lead to the formation of hexagonal crystals, which form a barrier and lessen hydration (Sintef, 2007). Further chemical reactions occur and form cubic katoite (C_3AH_6) (Sintef, 2007) (Eq. 2.3).

$$2C_3A + 27H = C_2AH_8 + C_4AH_{19} = 2C_3AH_6 + 15H \quad (2.3)$$

When calcium sulfate is present, C_3A hydration in the early stages of cement hydration occurs in three stages (Michaux et al., 1990). First, the gypsum dissolves in water and react with the C_3A by products to produce ettringite (AFt; $C_6AS_3H_{32}$) leading to an induction period where gypsum is continuing to be consumed and the ettringite is precipitating (Michaux et al., 1990; Quennoz & Scrivener, 2012). This induction period can last a number of hours to days depending upon the amount of gypsum in the system. Once the sulfate ions in the system are depleted, C_3A dissolution will occur and react with the ettringite and water to produce monosulfoaluminate (Quennoz & Scrivener, 2012). This process occurs rapidly and then experiences a steep decline in reaction rate (Bullard et al., 2010). Fig. 2.3 shows a schematic of the C_3A hydration process and phases. An example of how these reactions occur is shown in Fig. 2.4.

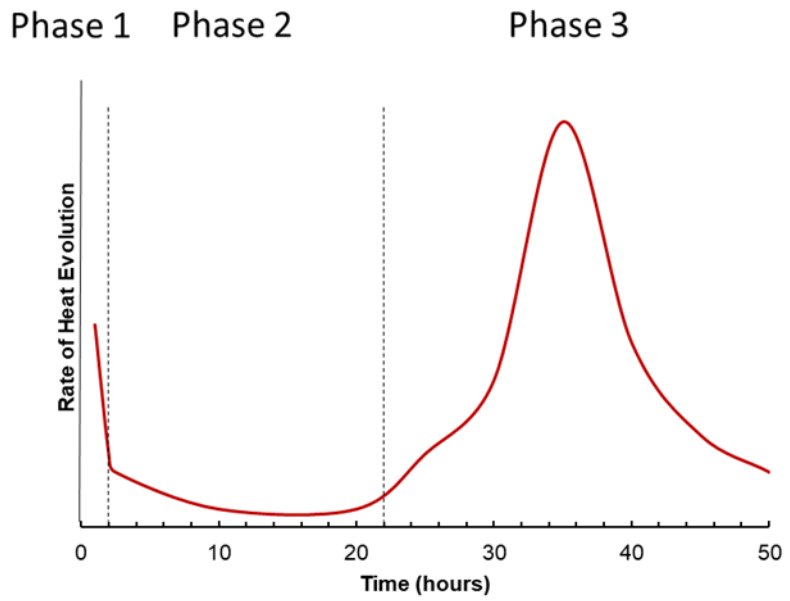

Figure 2.3. Schematic of aluminate hydration.

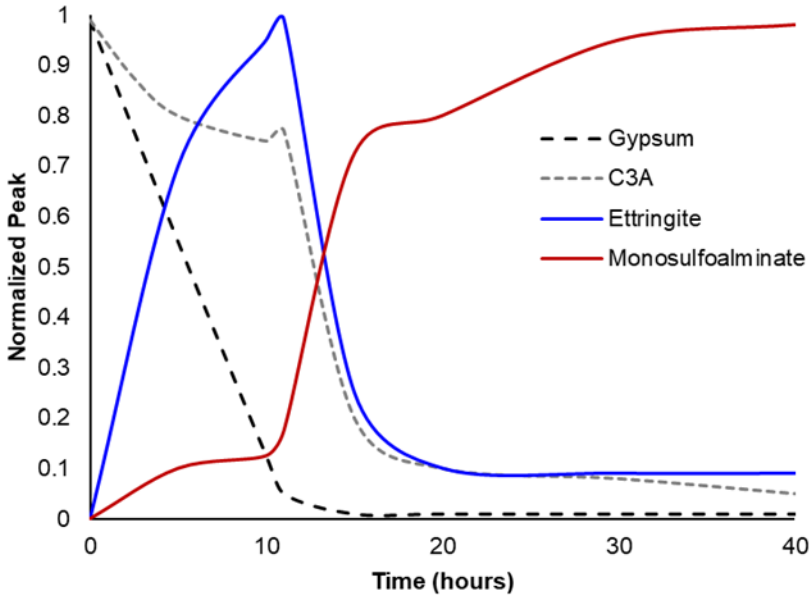

Figure 2.4. Aluminate reaction products with time (Modified from Quennoz & Scrivener, 2012).

While the hydration of neat OPC has been presented here, this rate of hydration and heat evolution can be altered when additives are included within the slurry. Fineness of cement can also increase the rate of hydration; smaller particles will hydrate faster (Quennoz & Scrivener, 2012). This is important because additives may have the ability to alter the reaction products or

quantity of a product and could impact the mechanical and thermal properties of cement, yet there has not been significant research on the mechanisms and reactions with additives. This could be due to continuous x-ray powder diffraction (XRD) or other expensive and time consuming techniques such as Raman spectroscopy are required for the entirety of the first four phases of hydration (Quennoz & Scrivener, 2012). Another aspect that should be taken into account for the purpose of understanding cement hydration is the composition of the water being used to hydrate the cement and how chemicals within the water could affect cement hydration products.

2.4 Types of Wellbore Cements

The most common cement in the petroleum industry is American Petroleum Institute (API) cement, in which there are eight classes. Each class has a specified depth, fineness, and composition and can be either ordinary, moderately sulfate-resistant, or highly sulfate-resistant. Table 2.1 shows typical chemical compositions of the various classes of wellbore cement, chemical types, common water/cement ratios and range of depths that the cement type can be used at (Smith, 1987; API, 2002; Khalifeh & Saasen, 2020).

Table 2.1. Chemical composition, types, and selection material of API wellbore cements.

API Class	C_3S	C_2S	C_3A	C_4AF	Available Types*	Water-Cement Ratio	Depths (ft)	Slurry Weight (ppg)	Fineness (cc/g)
A	53	24	8	8	O	0.46	0-6,000	15.6	1,500-1,900
B	47	32	5	12	MSR; HSR	0.46	0-6,000	15.6	1,500-1,900
C	58	16	8	8	O; MSR; HSR	0.56	0-6,000	14.8	2,000-2,800
D	26	54	2	12	MSR; HSR	0.38	6,000-10,000	16.4	1,200-1,600
E	26	54	2	12	MSR; HSR	0.38	10,000-14,000	16.4	1,200-1,600
F					MSR; HSR	0.38	10,000-16,000	16.2	

G	50	30	5	12	MSR; HSR	0.44	0-8,000	15.8	1,400-1,700
H	50	30	5	12	MSR; HSR	0.38	0-8,000	16.4	1,400-1,700

**O=Ordinary Type; MSR=Moderate Sulfate-Resistant Type; HSR=High Sulfate Resistant Type*

ASTM has also described their own Portland cement classification system as detailed in standard C150/150M-21, but it is not commonly used for wellbore cementing (ASTM, 2021). There are five types of ASTM cements with some having air-entrapment and moderate sulfate subsets (ASTM, 2021). Due to their lack of use in modern wellbores, ASTM cements will not be discussed in detail.

Class H and class G cement, which are nearly identical apart from fineness, are the most commonly used cements used within a wellbore. Classes A and B are Portland cement and are very similar to ASTM Type I and Type II cements, respectively. Class C cement is similar to ASTM Type III cement and should be used in conditions where high early strength is necessary; high early strength is achieved by increasing the alite within the cement clinker and finer grinding of the clinker (Smith, 1987). Class D, E, and F cement are retarded cements where elevated pressures and temperatures are experienced (Smith, 1987). Class D is meant for moderate HPHT conditions, class E for high HPHT, and class F for extreme HPHT conditions (Smith, 1987). It should be noted that there is not much literature discussing class F, possibly because classes D, E, and F are rarely used as wellbore cements (Khalifeh & Saasen, 2020).

Previous literature has listed various “specialty cements”, but in modern times, these cements are more widely used, studied, and commonly include a specific additive rather than a novel cement blend therefore considered cement with additives rather than a “specialty cement”. These include pozzolanic cements, resin cements, permafrost cements, diesel cements, calcium aluminate cements, expanding cements, and latex cements (Smith, 1987).

2.5 Cement Slurry Characterization and Design

Cement slurries are designed to provide zonal isolation, protect the casing from corrosive fluids, and mechanically support the casing under the given wellbore conditions. There are three initial parameters that need to be considered when designing a cement slurry: placement depth and configuration, downhole environment, and temperature/pressure information (Rae, 1990). Slurry design takes the following into consideration: rheology, hydrostatic pressure control, fluid loss control, static gel strength development, fluid/gas invasion resistivity, strength development, shrinkage and expansion properties, and long-term integrity (API, 2010). It is also important to design a cement so that the mechanical properties are able to withstand any pressure, temperature and stress variations that will be experienced over the life of a well once the cement has been placed (Thiercelin et al., 1998).

In order to actually pump cement into a wellbore, the cement must be designed to have a consistency lower than 70-100 Bearden consistency units (Bc) (Teodoriu & Asamba, 2015). Water-cement ratio (W/C) is an important parameter that is considered when designing a wellbore cement in that enough water needs to be present to optimally hydrate the clinker but low enough so as to not negate compressive strength buildup (Tan et al., 2012). W/C may need to be adjusted when utilizing additives in the cement and this may vary by weight or quantity. Pore and fracture pressure considerations must also be considered so as to not fracture the formation, prevent loss of circulation, mitigate the risk of a kick or blowout (Guo et al., 2019). Knowledge of fracture pressure gradient also allows for proper equivalent circulating density (ECD) to be designed to ensure that the ECD is lower than the fracture gradient (Gahlawat et al., 2016).

There is not one “right way” to characterize a wellbore cement/slurry. Potentially the easiest, least descriptive way to characterize a cement is by the type of casing or depth in which it is placed. An example of this is surface casing cement, or the cement that is used to ensure that the zone that spans the water table. One additional way that cement slurries can be classified is by the use of additives to achieve specific properties once downhole. Additives can be used to change the behavior of a cement slurry, therefore making a cement retarded, high early compressive strength, sulfate resistant, expandable, foamed, etc. Composition of the cement is another way in which cement and cement slurries can be classified; examples of this are cements containing high amounts of pozzolans or other unconventional material thus deeming it a “specialty cement”. Examples of these types of cements are discussed earlier in this work. Another way in which cement and cement slurries can be classified is by their density. While there is not necessarily a "set" limit to what constitutes a specific density range for slurry characterization, there is not a commonality on what density range a slurry can be characterized. Cement characterization ranges from ultra-lightweight to heavy weight cements depending upon the density of the cement slurry (Kalyanraman et al., 2021). Ultra-lightweight cements can have densities ranging from 7.3-11.0 ppg and typically utilize either stable foam or lightweight microspheres to obtain such low density slurries (Kulakofsky et al., 2006). Pernites et al. (2019) describe the creation of a lightweight cement slurry with density that ranges from 10.5-15.5 ppg. Neat, or conventional cements, are said to have densities ranging between 14.8-16.4 ppg depending upon the class of API cement used (Smith, 1987). High density (or heavy weighted) cement slurries have densities of 17.0 ppg or greater (Ahmed et al., 2020). Determining which slurry density is optimal for a well is dependent upon pressure, temperature, and other downhole conditions.

2.6 Laboratory Testing of Wellbore Cement

To ensure long-lasting wellbore integrity, various properties need to be considered from the initial design of the cement. There are various types of tests that need to be conducted to evaluate the feasibility of the cement design and determine how it will behave over time. It should be noted that test methods can vary on location and regulatory agency. In the U.S., there are three main regulatory bodies that describe test standards for conducting mechanical and slurry testing on wellbore cement: American Petroleum Institute (API), American Society for Testing and Materials (ASTM), and the International Organization for Standardization (ISO). The most commonly used standards for cementing wellbores are detailed in API RP 10B (Garnier et al., 2007). There are five parts to this document: Recommended Practice for Testing Well Cements, Testing of Well Cements Used in Deepwater Well Construction, Preparation and Testing of Foamed Cement Formulations at Atmospheric Pressure, Recommended Practice on Determination of Shrinkage and Expansion of Well Cement Formulations at Atmospheric Pressure, and Recommended Practice on Determining the Static Gel Strength of Cement Formulations. ISO standard ISO-10426-2:2003, Petroleum and Natural Gas Industries-Cements and Materials for Well Cement Testing-Part 2: Testing of Well cements is based on API RP 10B. ASTM standards are not as easy to define in that they do not specify that these methods are for wellbore cement and are not compiled into one easily accessible document.

Cement test methods can be divided into three primary categories: slurry testing, quasi-slurry testing and mechanical testing. Slurry testing refers to testing performed on a cement slurry while it is still in the liquid phase. Mechanical testing is typically conducted on cement that has been cured anywhere from a few hours to extended periods of time. Quasi-slurry testing refers to the testing that is performed on cement when it begins testing as a liquid but during the testing

process transitions to a hardened cement. Fig. 2.5 describes some of the various test types that can be performed on cement slurries, quasi-slurries, and hardened cement.

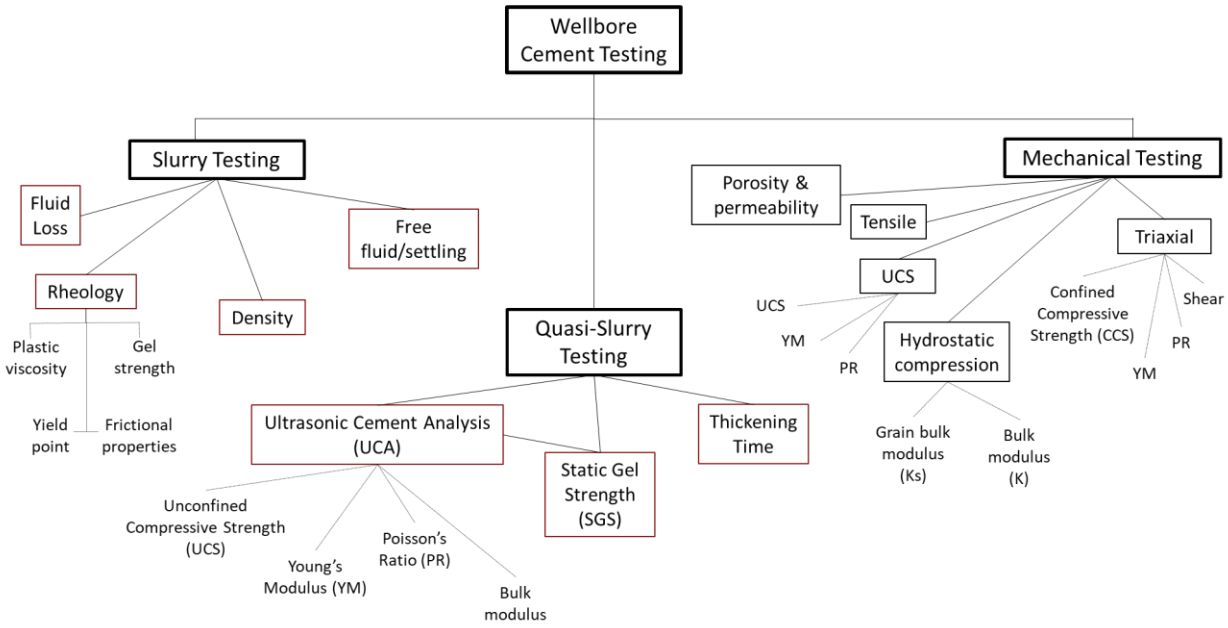

Figure 2.5. Various types of wellbore cement tests.

Mixability is important when preparing a slurry in that conditions and methods vary from the laboratory to the field and the method and conditions of mixing have shown to have some impact on cement slurry and mechanical properties (Saleh & Teodoriu, 2016). Slurry testing is important for determining the pumpability, placement, and strength development of the cement sheath (Saleh & Teodoriu, 2016). Once the slurries have been prepared, a number of laboratory tests can be performed to evaluate the potential for field performance. Slurry thickening time tests, which are performed to determine the length of time that a slurry will be pumpable under specific wellbore conditions, use a pressurized consistometer to heat and pressurize the slurry until it reaches a consistency of 100 Bearden units (Bell & Nelson, 1990). Another test method on cement slurries is fluid loss evaluation, where the slurry is placed into a filter press cell where it is subjected to downhole conditions and differential pressure is measured over a 30-minute

period at 1,000 psi, thus providing insight on slurry dehydration when placed in a wellbore (Bell & Nelson, 1990). Free-fluid and settling tests are performed simultaneously to understand water separation and migration as well as particle sedimentation characteristics of a slurry; this test lasts for a period of two hours (Sarmah et al., 2016). Rheological measurements are performed using a rotational viscometer and a variety of slurry properties can be obtained including the plastic viscosity, yield point, frictional properties and gel strength (Sarmah et al., 2016). Density of the slurry is found using a mud balance and should be pressurized to obtain accurate results (Romanowski et al., 2018). Ultrasonic cement analyzers (UCA) allow the slurry strength development under wellbore conditions to be measured over time (Bhaidasna & Leblanc, 2009). Compatibility testing is another important test to determine whether the various cement systems (spacer, tail, lead) are able to properly function when ran downhole. To determine compatibility, various quantities of spacer and tail as well as tail and lead are separately mixed and then combined for a specific period to determine whether any abnormalities are detected.

The main properties for well integrity evaluation are obtained from mechanical testing and include *UCS*, tensile strength, failure criteria obtained from the failure envelope and conventionally Mohr-Coulomb, Young's Modulus (*YM*), and Poisson's Ratio (*PR*) (Garnier et al., 2007). To obtain *UCS* values, uniaxial loading on either a cubic or cylindrical specimen is performed (Garnier et al., 2007). *UCS* is greater when using cubic samples due to the type of test machine used and the stress-strain rate in which the sample is being crushed, lack of planarity, and stress distribution (Garnier et al., 2007). *YM* and *PR* can also be found via *UCS* testing. Vertical strain and stress data is being recorded in order to obtain *UCS* values, and by taking the tangent at 50% of the stress-vertical strain curve, *YM* can be determined. *PR* can be found in a similar method by placing a radial strain gauge or radial extensometer on the sample, so that

radial strain and vertical stress data is being compiled in unison with axial strain data. By taking the tangent at 50% of the horizontal strain-stress curve, *PR* can be found.

Failure criteria of cement can be found via triaxial testing. One type of triaxial test that can be done to obtain a failure envelope is consolidated isotropic drained (CID) testing. At least three confining stress need to be used to create an accurate Mohr-Coulomb failure envelope and from this angle of friction and cohesion can be obtained. *YM* and *PR* can also be determined during triaxial testing by using linear variable differential transducers (LVDT's) and again taking the tangent at 50% of horizontal and vertical strain vs stress. *YM* and *PR*, which are indicative of a materials stiffness and the materials radial change and the ratio of lateral strain to longitudinal strain, respectively, need to be low to have a successful cement sheath that is able to adapt to thermal and mechanical loading; cement with high *YM* and *PR* is more likely to experience radial fracturing (Nygaard et al., 2011). It is optimal for a cement to have a lower *YM*, *PR*, and high compressive strength to prevent wellbore integrity failure (Nygaard et al., 2011).

Tensile strength determination is also important for wellbore integrity evaluation because cement will almost always fail in tension (Heinold et al., 2002). As of 2003, there are no API standards for tensile testing but two methods of determining the tensile strength of cement are the splitting tensile strength test and the direct uniaxial tensile strength test (Heinold et al., 2002).

Other types of mechanical testing such as porosity, permeability, and hydrostatic compression testing can be performed to further understand and characterize cement. It is common for porosity and permeability testing to be done simultaneously and these properties can be obtained at various pressures to see if there is any variation. This is important in wellbore cements because pressure increases with depth and knowing these parameters can help optimize cement design and achieving wellbore integrity. Hydrostatic compression testing is used to determine

both the bulk and solid bulk moduli which can then be used to calculate the poroelastic constant, better known as the Biot coefficient. Knowledge of the Biot coefficient can then be used to obtain more accurate effective stress calculations which in turn leads to more accurate slurry designs, placement, and potentially even optimized hydraulic fracturing (Fallahzadeh & Rasouli, 2012).

2.7 Overview of Cement Replacement Materials & Additives

Due to limitations associated with using ordinary Portland cement (OPC) as a well sealing material, specifically pertaining to ensuring well integrity, various materials have been used as a cement replacement in copious ways including but not limited to: sealing gaps between the formation and casing, mitigating water or gas production, and when a well is plugged and abandoned (P&A'ed). These materials have been dubbed sealing materials and are designed with the expectation that they are able to perform better than OPC when subjected to downhole conditions (Ziashahabi et al., 2019). While many sealing materials have shown promise when tested in the lab both at ambient and high pressure high temperature (HPHT) conditions, little is known about how these materials perform under downhole conditions or over time. Sealing materials show considerable promise when it comes to achieving and preserving well integrity, yet there is a considerable amount of research and real-well observation that needs to be done prior.

While sealing materials are considered to be cement alternatives or cement replacements, cement additives are materials that are added to the cement to aid in establishing/maintaining well integrity given the specific downhole conditions. To optimally attain the aforementioned sealing material qualifications, cement slurries are attempted to be designed with the desired mechanical properties to best suit an individual well over an extended length of time. In order to achieve the

necessary mechanical properties, the addition of additives or an alteration to the water-cement (w/c) ratio may be utilized. It is important to note that while additives or w/c ratio modifications may be beneficial to some extent, there is a "limit" in which such modifications could prove detrimental to cement integrity. Such factors could also impact cement pumpability and placement. If a slurry is too thick, it may be difficult to pump which could impact cost and equipment performance. Slurries with excess additives or a low w/c ratio may also be difficult to properly place and settling of additives could become an issue. In this day in age, the use of additives in cement is not a new concept. Additives are used for a variety of reasons such as accelerants, retardants, dispersants, viscosifiers, density-reducers, and fluid loss control (Thakkar et al., 2019). Novel testing of common and uncommon additives is crucial for understanding the impact said material has on the mechanical properties of cement, both short- and long-term. While there are innumerous additives that have been utilized in wellbore cements, a majority of these additives have been investigated solely at a lab scale and have not been observed in field applications. Some of the common types of additives used in wellbore cementing include nanoparticles, polymers, fibers/cellulose materials, and pozzolans.

Particle size is an important parameter that needs to be taken into consideration when selecting wellbore cement additives. The smaller the additive particle size, the greater the surface area thus more reactivity potential (Mangadlao et al., 2015). On the other hand, it should be noted that smaller average particle sizes also increase the viscosity of a slurry and could be problematic during pumping (Khalil et al., 2020). Smaller particle sizes are more likely to exhibit flow resistance as well (Ashraf et al., 2021). The distribution of particles within the cement should be homogenous to ensure well dispersed hydration and allow for uniform strength not concentrated in one area (Mangadlao et al., 2015).

2.7.1 Drill Cuttings

Drill cuttings, which are pieces of geologic material created as the drill bit penetrates downhole formations above the target reservoir, are produced in massive quantities and are required, by law, to be disposed of. The way in which cuttings are disposed is dictated by the type of drilling mud used, which can be either water-based mud (WBM), oil-based mud (OBM), or synthetic-based mud (SBM), the latter two types often called non-aqueous drilling muds (Lyon et al., 2019). Use of OBM and SBM is becoming more prevalent due to the increase in shale reservoirs, which tend to swell in the presence of water (Scott & Candler, 2010). While WBM requires little to no cleaning in order to be disposed of, non-aqueous muds must be treated and cleaned to ensure any residual aromatics are removed to minimize harm to the environment (Lyon et al., 2019).

There are a number of techniques used to dispose of or recycle drill cuttings. Offshore, cuttings can be cleaned using thermal processing techniques, a dryer, or chemical extraction (Wu et al., 2021). Once cleaned to regulatory standards, the cuttings can be discharged to the sea; oftentimes WBM cuttings do not require cleaning and can be immediately discharged (Innes et al., 2021). Skip-and-ship and bulk transfer of cuttings are offshore cuttings disposal techniques in which the cuttings are offloaded to a ship and brought to an onshore facility to be recycled. Onshore disposal techniques also require the cuttings to be cleaned and meet regulatory specifications; once the cuttings are cleaned, they can be used, if permitted, for landfarming or biological treatment, landspreading, stabilization or solidification, burial, landfill, or reuse (Clements et al., 2010). Another method for cuttings disposal both onshore and offshore is reinjecting the cuttings downhole. Cuttings injection can be done for all mud types and has a number of advantages

including that it is environmentally friendly, minimal to no treatment, reduced transportation and storage costs, and control of injection rate to support drilling operations (Benelkadi et al., 2019).

Cuttings disposal can prove problematic in that it can be costly, require a large amount of space, and contribute to greenhouse gas emissions (Sun et al., 2022). The skip and ship as well as the bulk transfer of cuttings offshore requires cuttings to be shipped from the wellsite to an onshore facility and produces almost 120 times more greenhouse gas emissions than onsite treatment and disposal techniques (Innes & Morris, 2020). Onshore disposal or recycling offshore cuttings onshore requires the cuttings to be relocated thus generating additional emissions. Cuttings reinjection may require additional equipment which could increase costs and space on location as well as negatively impact drilling (Sun et al., 2022). An additional issue is that offshore discharge can negatively effect the marine environment (Zhang et al., 2016).

More recently, utilization of cuttings in drilling and completion techniques has been investigated. Carrascal-Delgado et al. (2022) described the potential for using Eagle Ford cuttings as proppant material. An additional study detailed the potential conversion of shale cuttings to high-strength proppant material (Hellmann et al., 2014). Drill cuttings have also been utilized in drilling mud for lost circulation control (Salmina et al., 2019). Foroutan et al. (2017) described using drill cuttings in concrete applications; it was seen that in quantities up to 20%, the drill cuttings were able to achieve compressive strength similar to that of concrete without cuttings. An investigation to understand the feasibility of using drill cuttings in asphalt for road pavement has also been done (Khodadadi et al., 2020). It was found that washed cuttings are a suitable material for asphalt mixtures and showed similar results to the samples containing no cuttings. In 1993, approximately 75% of all formations that were drilled were shale; in modern times, the number of shale reservoirs has increased thus implying that this number is significantly higher (Huang et

al., 2011; Taghiyev et al., 2015; Dzialowski et al., 1993). In South Texas alone, over 10.8 million cubic feet of cuttings are present and in modern times, when a well is drilled it will typically produce between 35,315.0 and 176,573.0 cubic feet of cuttings (Khodadadi et al., 2020; Hınıslıoğlu & Ağar, 2004; Foroutan et al., 2017). For every foot of well drilled, approximately 1.21 barrels of cuttings are generated (Khodadadi et al., 2020; Sellassie, 2011).

2.8. Cement Microscopy

Knowledge of cement microstructure is imperative for understanding their use in a variety of applications (Franus et al., 2015). The use of microscopy can shed light on a materials chemical composition, macrostructure, microstructure, and surface abnormalities. The use of optical microscopy can also provide information on surface and pore structure of a material at lower magnifications. While there are a variety of microscopy techniques, scanning electron microscopy (SEM) is the most widely used to observe the surface structure of cement at lower magnification and higher resolution. SEM works by emitting an electron beam through a series of electromagnetic fields and magnetic lenses (Jaidka et al., 2022). When the electron beam hits the sample surface, elastic and inelastic collisions between the electrons within the inner and outer shells of the atoms will occur and this electron excitation can be read and used to produce backscatter and secondary electron images (Egerton & Zhu, 2022). Energy-dispersive X-ray spectroscopy (EDS) can be used in conjunction with SEM to obtain insight as to the chemical composition of surface locations. EDS works when the electron beam hits atoms on a material's surface and penetrates the inner shell of the atoms. This will cause an electron in the inner valances to be knocked out and an electron from the next outer valance to fill this void; this movement emits an X-Ray that is specific to an element (Gibson, 2005). Cement microscopy can be utilized to verify additive reactivity, arrangement of hydration products, and crystalline size

variations with the addition of cement replacement materials (Majhi & Nayak, 2019; Forni et al., 2015; Li et al., 2022). Microscopy has also been utilized to understand how microstructure varies with the addition of varying amounts of supplementary cementitious material (Dadsetan & Bai, 2017).

It is interesting to note that while testing on wellbore cements is thoroughly detailed in API, ISO, NORSOK and CEN standards and guidelines, there is seemingly no set standard for performing elemental/chemical composition and microstructure and crystalline structure of cement via microscopy. These are two techniques that can be utilized to determine the chemical composition and products that were formed during cement hydration as well as understand the microstructure (and to some degree macrostructure) of the cement. Investigating such topics could allow researchers to better understand how additives can alter the mechanical properties, aid in cement optimization, and potentially provide a better outcome in regards to long-term wellbore integrity.

Chapter 3: Dissertation Objectives

The focus of this dissertation is sub-divided into five chapters. The following is a brief description of what research was conducted and key parameters in question for the research are listed below.

- Chapter 4 of this work focuses on the determination of the poroelastic constant of a class H cement blend. Hydrostatic compression testing, which is a combination of two non-destructive tests, is performed on three class H cement samples to determine the solid and bulk ratio of the material. Utilizing this data, a correlation can be used to determine the Biot coefficient and is further described in chapter four of this work. SEM-EDS analysis was also carried out to determine the chemical composition of the sample and to

understand the microstructure of the samples using a FEI Quanta microscope and Bruker XFlash 6130 Energy Dispersive X-Ray Spectrometer.

- In chapter 5, consolidated isotropic drained (CID) tests were performed on class H cement at three varying confining stress to better understand downhole behavior and obtain a Mohr-Coulomb failure envelope. Samples were sheared and failure angles were also analyzed to determine real-world failure behavior. SEM images were obtained to understand the microstructure at the fracture surface and determine any significant differences when compared to the intact surrounding matrix.
- In chapter 6 of this work, an investigation on the addition of various sizes, quantities, and curing time of cement with shale cuttings and Eagle Ford cuttings addition has been investigated. Microscopic analysis was done on the samples to obtain both a microstructural and chemical analysis and determine whether there is a difference when adding this novel material to class H cement.

Chapter 4: Poroelastic Properties of Wellbore Cement

In well construction for geothermal, CO_2, and oil and gas wells wellbore cement is imperative for ensuring wellbore integrity, zonal isolation, and mitigating migration of fluids. To establish the necessary barriers for well construction, cement is placed downhole at elevated pressures and temperatures. In this study, mechanical and poroelastic properties of class H wellbore cement are experimentally determined to develop a better understanding regarding the constitutive behavior of the cement at realistic downhole conditions. Previous testing on wellbore cement has centered around short-term mechanical testing and neglected to understand the effect of poroelasticity and its impact on effective stress calculations. Poroelastic properties are obtained through hydrostatic compression testing and further corroborated with porosity and permeability determination. The

hardened cement structure is investigated with optical and scanning electron microscopes. The poroelastic behavior of oil well cement acts linearly over a wide range of confining stresses. The experimentally obtained Biot coefficient, α, solid bulk modulus, K_s, and the drained bulk modulus, K, of the Class H cement range from 0.80-0.82, 51.6-52.8 GPa, and from 9.7-10.3 GPa, respectively. This study shows that oil well cement behaves as a poroelastic material and is within the porosity, permeability, and poromechanical properties range of a shale. Hence poroelastic models developed for shale can be used to analyze oil well cement systems. Determining the poroelastic properties of an oil well cement system can allow for well constructions to be better designed for specific downhole effective stress conditions and shear failure potential.

4.1 Introduction

Wellbore cement is imperative for ensuring wellbore integrity, zonal isolation, and mitigating hydrocarbon migration. If wellbore cement is improperly placed or incorrectly designed, risk of failure is plausible. Hydrocarbon, geothermal, hydrogen, and carbon capture and storage wellbores are designed in a way such that there are a number of mechanical barriers present to prevent failure. This includes steel casing, cement, and a number of additional mechanical components such as packers and centralizers. In theory, if one barrier fails there should always be another barrier to mitigate any hazards that could occur. For instance, improper cementing of the annulus in the production liner could equate to excess load on the casing string causing it to burst, which could lead to hydrocarbon leakage to the surface or infiltration of the water table, but the cement should be the next viable barrier. While there are a number of barrier elements within a wellbore at any given time, the most significant and oftentimes the most utilized is wellbore cement. Regardless of the well type, the cement sheath is considered the primary barrier

and is often subjected to a number of temperature, pressure, and geologic fluctuations making it highly susceptible to damage or leakage over time.

Estimates regarding wellbore leakage have identified sustained casing pressure (SCP) or Bradenhead pressure, surface casing vent flow (SCVF), and/or gas migration are the primary reasons for wellbore leakage (Nelson & Guillot, 2006; Wolterbek et al., 2021; Wise et al., 2022). A study by Watson & Bachu (2009) found that of the 316,439 wells drilled in Alberta, Canada, 4.6% experienced gas migration, SCVF, or a combination of the two thus indicating the probability of leakage. Of 250,000 drilled wells in Ohio and Texas, it was found that 396 had leakage of fluids into the aquifer (Kell, 2011; Wise, 2021). As of 2017 in British Columbia, Canada, of the 25,119 drilled wells, 2,329 wells were shown to have leakage (Wisen et al., 2019). In a study conducted by Lackey et al. (2021) pertaining to hydrocarbon wellbores in Pennsylvania, New Mexico, and Colorado, it was found that 15,130 of 105,031 wellbores, approximately 14.4%, had experienced leakage at some point in their life. Determining leakage of onshore wells is markedly easier than offshore wells, yet due to the conditions associated with offshore wells, it is sufficient to say that the amount of wells leaking is probably higher. Wellbores in earthquake prone regions such as California, British Columbia, and Oklahoma may also be more susceptible to leakage due to geologic wellbore integrity related issues (Kang et al., 2019). Leakage rates even in properly cemented wellbores have been determined to be 967,980 L/year of natural gas (Lavrov & Torsæter, 2018; Wise, 2021). Best practices to mitigate such leakage relies primarily on the wellbore cement sheath.

Cementing of a wellbore begins by mixing and pumping the cement, water, and whatever additives are needed downhole as a slurry before the slurry hardens through a hydration process and solidifies to become a hardened cement sheath (Lavrov & Torsæter, 2018). The hardened

cement is a granular material consisting of unhydrated cement, partially hydrated cement, cement hydration products, and pores.

The failure of the cement sheath can be divided into primary and secondary failure mechanisms (Weideman & Nygaard, 2014). The primary leakage paths are caused by improper cement placement during well operations and is outside the scope of this work. Secondary leakage paths can be due to cement debonding at the casing-cement and cement-formation boundaries, fractures or channels within the cement or formation, chemical alterations of the cement sheath, and wear or chemical alterations of the casing (Weideman & Nygaard, 2014).

To analyze these secondary sources of the cement sheath failure, analysis of the cement sheath has been investigated based on debonding between cement and casing or cement and formation, tensile fractures in the cement, or compressional shear failure of the cement (Ford et al., 2018) either based on analytical equations (Bois et al., 2011, 2017) or finite element simulations (Bosma et al., 1999; Fleckenstein et al., 2001; Ravi et al., 2002; Gray et al., 2009; Zielonka et al., 2014; Wise, 2021). A parametric failure analysis study using finite element simulation on the cement sheath has shown that the pore pressure and in-situ stresses in the cement has the largest impact on stress development and failure analysis in wellbore cement sheaths.

In the U.S., there are three main regulatory bodies that describe test standards for conducting mechanical and slurry testing on cement: American Petroleum Institute (API), American Society for Testing and Materials (ASTM), and the International Organization for Standardization (ISO). The most commonly used standards for cementing wellbores are detailed in API RP 10B (Garnier et al., 2007). There are five parts to this document: Recommended Practice for Testing Well Cements, Testing of Well Cements Used in Deepwater Well Construction, Preparation and Testing of Foamed Cement Formulations at Atmospheric Pressure, Recommended Practice on

Determination of Shrinkage and Expansion of Well Cement Formulations at Atmospheric Pressure, and Recommended Practice on Determining the Static Gel Strength of Cement Formulations. The ISO is an internationally recognized organization in which 167 nations are members of and as of February 2023, has over 24,668 international standards (ISO, 2023). The ISO standards relating to wellbore cementing include: ISO standard ISO-10426-2:2003, Petroleum and Natural Gas Industries-Cements and Materials for Well Cement Testing-Part 2: Testing of Well cements is based on API RP 10B. ASTM standards are not as easy to define in that they do not specify that these methods are for wellbore cements and are not compiled into one easily accessible document. ASTM standards are not based on API or ISO standards and often have relevance to the construction-based cements and concretes.

The main properties for well integrity evaluation are obtained from mechanical testing and include *UCS*, tensile strength, failure criteria obtained from a failure envelope which is conventionally Mohr-Coulomb, *YM*, and *PR* (Garnier et al., 2007). To obtain *UCS* values, uniaxial loading on either a cubic or cylindrical specimen is performed (Garnier et al., 2007). *UCS* values are greater when using cubic samples due to the type of test machine used and the stress-strain rate in which the sample is being crushed, lack of planarity, and stress distribution (Garnier et al., 2007). *YM* and *PR* can also be found via *UCS* testing. Vertical strain and stress data is recorded in order to obtain *UCS* values, and by taking the tangent at 50% of the stress-vertical strain curve, *YM* can be determined. *PR* can be found in a similar method by placing a radial strain gauge or radial extensometer on the sample, so that radial strain and vertical stress data is being compiled in unison with axial strain data. By taking the tangent at 50% of the horizontal strain-stress curve, *PR* can be found.

Failure criteria of cement can be found via triaxial testing. One type of triaxial test that can be done to obtain a failure envelope is consolidated isotropic drained (CID) testing. At least three confining stress need to be used to create an accurate Mohr-Coulomb failure envelope and from this angle of friction and cohesion can be obtained. *YM* and *PR* can also be determined during triaxial testing by using linear variable differential transducers (LVDT's) and again taking the tangent at 50% of horizontal and vertical strain vs stress. *YM* and *PR*, which are indicative of a materials stiffness and the materials radial change and the ratio of lateral strain to longitudinal strain, respectively, need to be low to have a successful cement sheath that is able to adapt to thermal and mechanical loading; cement with high *YM* and *PR* is more likely to experience radial fracturing (Nygaard et al., 2011). It is optimal for a cement to have a lower *YM, PR*, and high compressive strength to prevent wellbore integrity failure (Nygaard et al., 2011).

Tensile strength determination is also important for wellbore integrity evaluation because cement will almost always fail in tension (Heinold et al., 2002). As of 2003, there are no API standards for tensile testing but two methods of determining the tensile strength of cement are the splitting tensile strength test and the direct uniaxial tensile strength test (Heinold et al., 2002).

The above testing methods assume that the cement behaves as a linear elastic material under compression or tensile stresses until brittle failure at peak conditions. Assuming linear elastic material until brittle failure might be good assumption for cement used in concrete mixtures; however, at *in-situ* conditions in a wellbore with elevated pressures, temperatures and pore fluid present makes this assumption more questionable. Sedimentary rocks in the subsurface are better described as a poroelastic material where part of the subsurface compressive stresses are carried by the pore fluids, as first described by Terzaghi (1923). Since cement resembles the structure of sedimentary rocks, wellbore cement may also be seen as a poroelastic material.

In this paper, an investigation of the poroelastic properties is done on class H cement to determine the impact on in situ stress. Poroelastic properties of a material under realistic downhole conditions are also necessary for accurate failure criteria determination. While such parameters are widely included in wellbore stability models, there is very little experimental data regarding wellbore cement poroelastic properties due to the extensive time required to obtain such parameters. To ensure the success of a cement sheath both long-and short-term, knowledge of mechanical and poroelastic properties need to be understood. Poroelastic calculations are needed to accurately calculate effective stress which influences fracture design, plug and abandonment, and long-term wellbore integrity.

4.1.1. Poroelasticity of Sedimentary Rocks

Terzaghi (1923, 1925) established the initial theory of poroelasticity to describe the one-dimensional effect of in-situ pore fluids on consolidated soils. In this theory, the pore fluid and the solid grains are taken to be incompressible, as the medium of study was unconsolidated soils. The theory determined that volume change of the unconsolidated media are due to rearrangements of the solid particulate and thus alterations to the pores. In saturated soil media, fluid volume changes are due to changing pore and solid volume.

Assuming that the solid matrix is incompressible is viable for soils because the pore space within the system is significantly more compressible than the solid components but is not completely valid in consolidated materials. Terzaghi's effective stress law, which is formulated using the aforementioned assumptions, states that (1) the mechanical response of soils is controlled by effective stresses, and (2) effective stresses are the differences between the total stresses plus the addition of pore pressure (Eq. 4.1).

$$\sigma' = \sigma - PP \tag{4.1}$$

where σ' is total stress tensor, PP is the pore pressure and σ is the total stress.

Biot furthered the theory of poroelasticity to model consolidated solid material containing pore fluid (Biot, 1957). Biot's theory outlines bulk volume change of a consolidated material due to pore pressure variations at constant stress under drained conditions. This theory, which is commonly referred to as the theory of poroelasticity for poroelastic fluid saturated media, was furthered to account for drained conditions for both jacketed and unjacketed specimen (Biot, 1957). It was also further extended from a one-dimensional to three-dimensional theory. Assumptions of the theory are that there is linearity between the stress, strain, and ductility of the consolidated material. The addition of the Biot coefficient to the law of effective stress is representative of the ratio of fluid in the pores of a solid material to the total volume of the material (Bear, 1972; Dassanayake & Fujii, 2014; Biot, 1957). The inclusion of Biot's poroelastic constant to the effective stress law is shown using the following equation (Eq. 4.2):

$$\sigma' = \sigma - \alpha PP \tag{4.2}$$

Where σ' represents effective stress, σ is total stress, α is the Biot coefficient or poroelastic constant, and PP is pore pressure.

Skempton established a pore pressure coefficient, B, to be applied for specimens under undrained conditions to describe the ratio of increased pore pressure with variations in confining stress (Skempton, 1960). Combining the Biot coefficient and the Skempton coefficient yields the poroelastic coupling of a solid material (He et al., 2014). Utilization of the Biot and Skempton coefficients for effective stress determination within hydrocarbon and geologic wellbores often overlooked but could prove to significantly affect calculations.

Biot's theory of linear poroelasticity has been further altered for use in specific scenarios. Verruijt (1969) established a form of the Biot theory for application in soil mechanics, specifically aquifers. Rice & Cleary (1976) redefined Biot's theory to understand ways that pore

fluids can impact shear fault motion. There have been further advancements of the Biot theory to nonlinear constitutive equations (Zienkiewicz, 1987; Prevost, 1980; Prevost, 1982; Coussy, 1989). Gutierrez & Lewis (2002) described a method to use coupled Biot equations to address situations of fluid injection or extraction.

There are a number of experimental techniques that have been employed to determine poroelastic properties, specifically, the Biot coefficient, but many of these methods have only been used on rock. Geertsma (1957) detailed a method of extending the Gassmann and Biot theories and using elastic and viscous constants to describe variations in both pore and rock bulk volumes with porosity. This extension of Biot's theory was shown to work for a variety of conventional reservoir rock types. Franquet & Abass (1999) described a method to find the Biot coefficient using changes in bulk and pore volume. He et al. (2016) described a technique that determined the Biot coefficient of Bakken shale from changes in pore pressure and confining stress. Skempton (1961) detailed a method to find the Biot coefficient from elastic moduli. Elastic moduli, also known as the bulk modulus (K) and grain bulk modulus (K_s), are indicative of a materials compressibility. Determination of the Biot coefficient is not commonly investigated in low permeable material due to the amount of time and equipment needed to perform the necessary tests (Selvadurai, 2019).

4.1.2. Previous Investigation on Cement Poroelasticity

The Biot coefficient can drastically impact effective stress calculations and is commonly taken to be 1, assuming that the stresses acting on a material are only applied to the granulitic framework, not the pore fluid (Bodaghabadi & Moosavi, 2008). The Biot coefficient also impacts the potential for shear failure within the cement sheath (Kim et al., 2016). Ghabezloo et al. (2008) performed drained and undrained compression tests as well as drained and unjacketed

compression tests to determine the Biot coefficient of a class G oilwell cement and found that both methods showed similar values at varying stress; the Biot coefficient ranges from 0.58-0.7. Meng et al. (2020) tested class G cement cured for 3, 10 and 28 days showed that the Biot coefficient of the cement ranges from 0.6 to 0.8, meaning that using a Biot coefficient of 1 leads to inaccurate effective stress calculations. While there is minimal literature regarding the Biot coefficient of cement, there is even less research using microscopy techniques to further understand how the microstructure impacts this coefficient. Microscopy techniques provide critical insight regarding surface topography, pore structures, microstructures, and chemical analysis all of which impact the mechanical and poroelasticity of cement (Franus et al., 2015).

4.2 Methodology

To determine the poroelastic properties of class H wellbore cement, this section outlines the procedures for creation of the slurry, hydrostatic compression testing, and porosity and permeability determination.

4.2.1 Specimen Preparation

25.4 mm (1.0 inch) diameter cement samples are made using a deionized water to Central Plains class H cement (w/c) ratio of 0.38 according to ASTM C192/C192M-14 standard practices, and 0.2% defoaming additive to reduce air bubbles within the sample (provided by Halliburton, 2020) (ASTM, 2015). The samples are mixed and placed in 25.4 mm by 101.6 mm (1.0 inch by 4.0 inch) stainless steel molds for 24 hours following ASTM standard practice C192/C192M-14 (ASTM, 2015). The samples are removed from the molds and placed in a 0.4% sodium hydroxide (NaOH) brine water bath at 65.6°C (150°F) oven. After curing for more than 90 days, the cement samples are removed from the oven and were cut 50.0 to 75.0 mm length (2.0-2.5 L/D). The ends of the samples are grinded and parallel ends are verified by taking three caliper

measurements of the sample length at 120º different orientation. The samples are then weighed to obtain wet weight measurements and placed in a 65.6°C (150°F) vacuum oven for 48 hours to remove any excess fluid trapped within the samples. Post-vacuuming, the samples are re-weighed to obtain fluid content. The cement sample sizes, weight and density are given in Table 4.1.

Table 4.1. Specimen descriptions.

Test Number	Test Type*	Average Length (mm)	Wet Weight (g)	Dry Weight (g)	Water Weight (g)	Bulk Density (g/ cm^3)	Particle Density (g/ cm^3)	Porosity (%)	Pore Volume (cm^3)
1	H	61.2	63.1	52.7	10.4	11.0	13.1	16.5	10.4
2	H	62.0	64.3	53.9	10.4	11.0	13.2	16.2	10.5
3	H	61.2	61.1	53.0	8.1	11.0	12.7	13.2	8.1
11	P&P	63.0	64.4	57.9	6.5	11.7	13.0	10.1	6.5
12	P&P	60.2	60.3	51.8	8.4	11.0	12.8	14.0	8.4

**H=hydrostatic compression test; P&P=porosity and permeability test*

4.2.2 Hydrostatic Compression Testing

Three samples underwent nondestructive hydraulic compression testing to obtain the bulk modulus, K, and grain bulk modulus, K_s. Once both elastic moduli are determined, the Biot coefficient is calculated for each confining stress using Eq. 4.3.

$$\alpha = 1 - {}^{K}/_{K_s} \tag{4.3}$$

Four linear variable differential transformers (LVDT's), two axial and two radial, are mounted on the sample and connected to a data acquisition system. Following LVDT placement, the sample is placed between two solid steel cylinders and jacketed to prevent fluid penetration during testing. It is then placed into the base of a GCTS HTRX-H70 triaxial cell (rated to 70 MPa maximum confining stress) and closed. A Teledyne-Isco 260D syringe pump filled with mineral oil is used to apply cell confining stress. Two Teledyne-Isco 100DX syringe pumps are connected to an argon gas cylinder and are used to apply pore pressure to the cell.

The first part of the hydrostatic compression test is to determine the K_s by applying both pore pressure and confining stress to the cell simultaneously. The confining stress is 1.4 MPa (200.0 psi) higher than the pore pressure. After each step the pressures are allowed to reach equilibrium. LVDT readings are recorded and both the pore and stress increased by 100.0 psi. To calculate the volumetric strain, the average from the two axial sensors are taken as are the average of the two radial sensors (values shown at the bottom of the computer screen in the MTS software). A plot is created in which stress is on the y-axis and volumetric strain is on the x-axis. After confining stress reaches 2,700.0 psi (pore pressure is 2,500.0 psi), the confining stress is gradually decreased to the initial confining stress (1.4 MPa, 200.0 psi). To determine the grain bulk modulus, linear regression is performed on the data. The slope of this line is grain bulk modulus. Once the unloading process is completed, the next portion of the hydrostatic compression test began: determining the K of cement samples. K is representative of the change in stress due to a materials change in volume (Bakjorji & Schmitt, 2010). This is done by holding pore pressure and confining stress equal and increasing both as such to 18.6 MPa (2,700.0 psi). The pressures are allowed to reach equilibrium at each pressure interval and the LVDT readings are recorded. To calculate the volumetric strain, the average from the two axial sensors and the average of the two radial sensors are taken. A plot is created in which stress is on the y-axis and volumetric strain is on the x-axis and a linear trendline is placed over the data. The slope of this line is taken to be the bulk modulus.

4.2.3 Porosity & Permeability Testing

Porosity and permeability of two samples are measured using a CoreTest AP-608 Automated Permeameter Porosimeter. This apparatus performs pressure decay using helium for porosity and permeability determination. In both hard and soft rock, changes in stress will have an impact on

the porosity and permeability (Sigal, 2002). For each sample, porosity and permeability are determined at three confining stress: 7.0 MPa (1,015.3 psi), 15 MPa (2,175.6 psi), and 30.0 MPa (4,351.1 psi). The AP-608 is unable to test at pressures below 7 MPa (1,000.0 psi), so porosity and permeability at 5.0 MPa (725.0 psi) are not obtained.

4.2.4 Microscopy

To understand the macrostructure of the cement surface, two samples are analyzed using a National Zoom Stereo Microscope optical microscopy under 10, 20, 30, and 40x magnification. Scanning electron microscopy (SEM) and energy-dispersive X-ray spectroscopy (EDS) are performed using a FEI Quanta microscope and Bruker XFlash 6130 Energy Dispersive X-Ray Spectrometer to gain an understanding of the microstructure and chemical composition of the samples. Prior to placing the sample within the microscope's chamber, the sample was sputter coated in palladium and gold using a Denton Vacuum Desk V to prevent charging effects. Two types of SEM images are obtained at various locations on the sample surface at varying magnifications; secondary electron detection is used to provide microstructural characteristics while backscatter electron detection yielded the topographic behavior. Energy dispersive X-ray spectroscopy (EDS) is also done at different locations on the sample surface using a low magnification to understand chemical composition and composition variations within the sample.

4.3 Results

The results obtained from hydrostatic compression, porosity and permeability testing as well as optical and SEM microscopy are presented within this section.

4.3.1 Hydrostatic Compression Testing

The first portion of hydrostatic compression testing involves determining K_s of the samples. K_s for sample 1, 2, and 3 are 51.6, 52.1, and 52.8 GPa (7,484.0, 7,556.0, and 7,658.0 psi),

respectively and are shown in Fig. 4.1. Values for K_s were similar and have a standard deviation of 0.5 GPa with an average of 52.2 GPa between the three samples. All samples show a linear trend between the confining stress and volumetric strain.

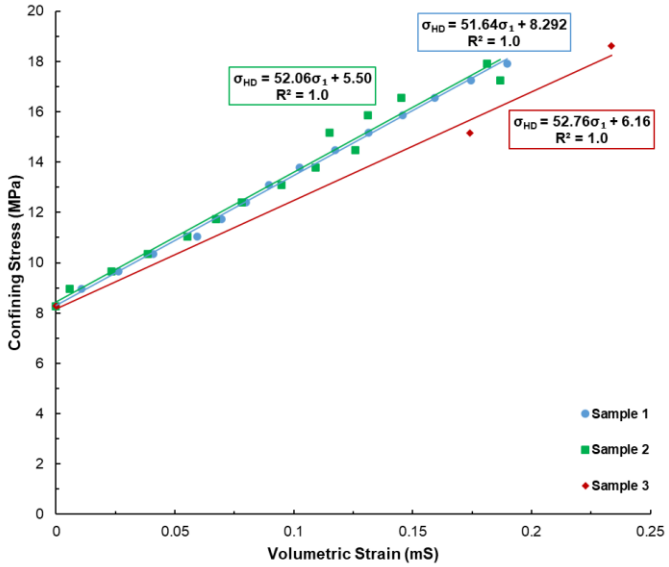

Figure 4.1. K_s for the three cement samples.

The second part of the hydrostatic compression testing is determining the K of the samples. K for sample 1, 2, and 3 is 9.9, 10.3, and 9.7 GPa (1,436.0, 1,494.0, and 1,407.0 psi), respectively and are shown in Fig. 4.2. The samples also exhibited comparable K behavior with the average being 10.0 GPa and standard deviation of only 0.3 GPa.

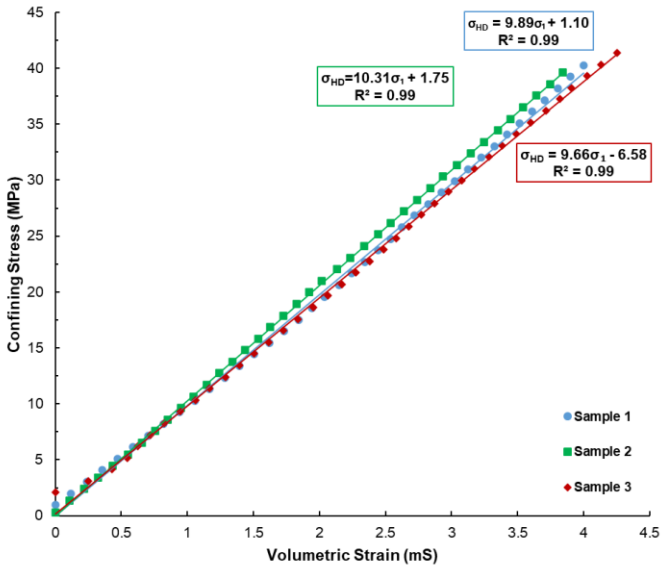

Figure 4.2. K for the three cement samples.

Once K_s and K are determined for the three cement samples, the Biot coefficient is able to be obtained at each measurement throughout the tests using Eq. 4.3. Fig. 4.3 shows Biot coefficient variations for the three samples during hydrostatic compression testing. As seen in Fig. 4.3, the Biot coefficient for all three samples are in agreement with average values being 0.81±, 0.80±, and 0.82± for samples 1, 2, and 3, respectively.

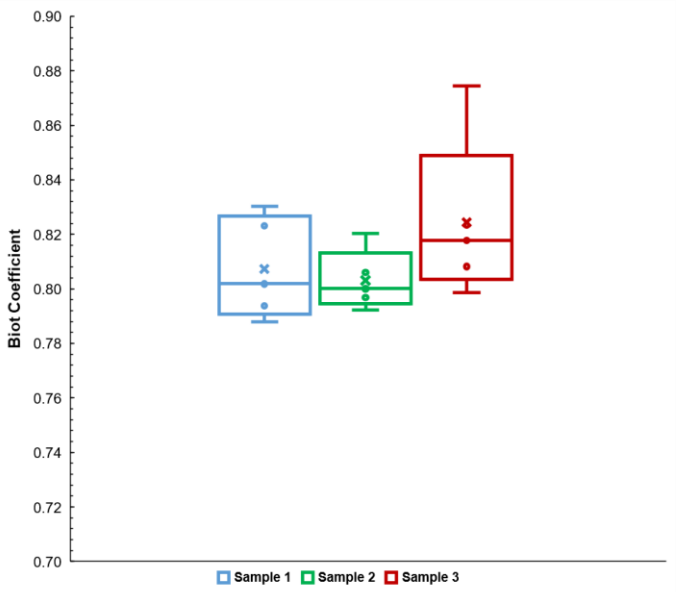

Figure 4.3. Biot coefficient comparison at varying stress.

4.3.2 Porosity & Permeability Testing

Porosity and permeability testing at three stresses for cement samples are shown in Fig. 4.4.

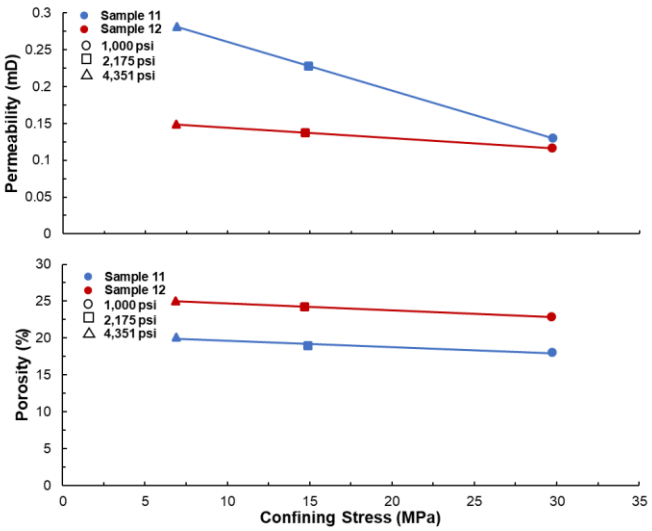

Figure 4.4. Porosity and permeability data at various confining stress.

Average porosity for sample 12 is 24.0% while average porosity for sample 11 is 19.0%. Both sample porosities had a 1.0% standard deviation. Sample 12 has an average permeability of 0.1 mD and sample 11 average permeability is 0.2 mD. Standard deviation for sample 11 permeability is 0.08 mD, which is slightly higher than that of sample 12, or 0.02 mD.

4.3.3 Microscopy

After samples 11 and 12 underwent porosity and permeability testing, they are fractured and observed under an optical microscope to visualize the macrostructure of the sample. Fig. 4.5 shows two different magnification results from optical microscopy observed in sample 11 while Fig. 4.6 shows the optical microscopy from two magnifications on sample 12.

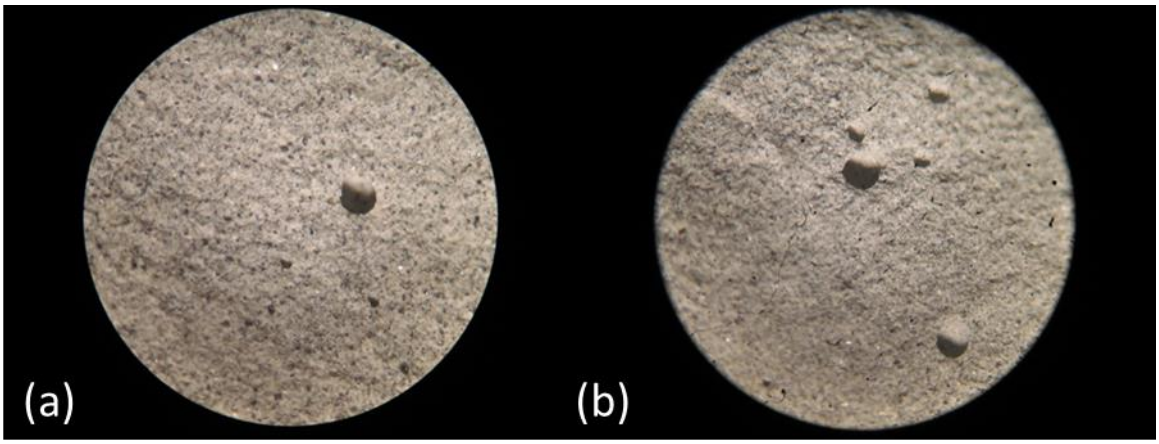

Figure 4.5. Sample 11 optical microscopy: a) 30x magnification; b) 20x magnification.

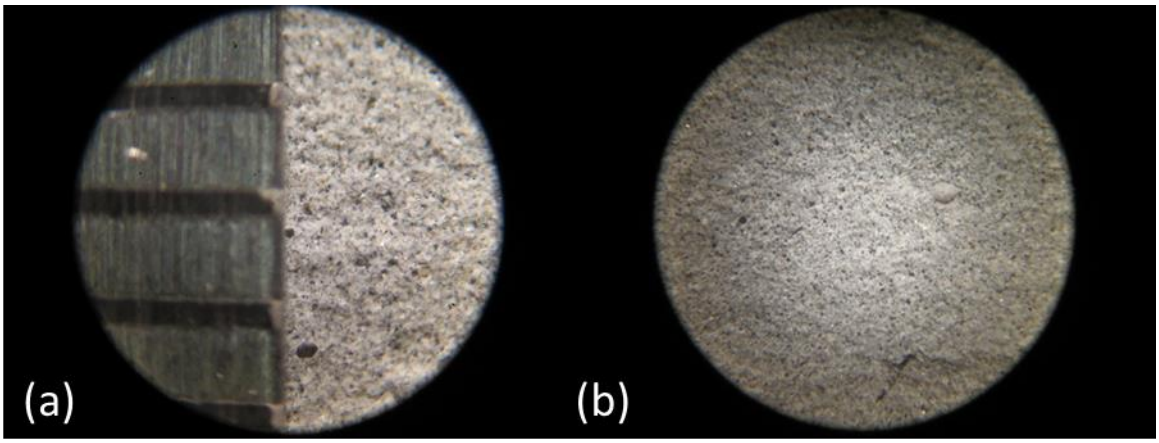

Figure 4.6. Sample 12 optical microscopy: a) 40x magnification; b) 20x magnification.

In Fig. 4.6 (a), a ruler is used to show the size of the field of view in millimeters at 40x magnification, which is approximately 4 mm.

SEM and EDS analysis is performed on a small piece of cement once triaxial testing has been performed. To understand the microstructure of the samples, backscatter electron and secondary electron images of the sample are taken at varying magnifications and locations and shown in Fig. 4.7. It should be noted that the backscatter images are more indicative of particle composition while secondary electron images represent the topography.

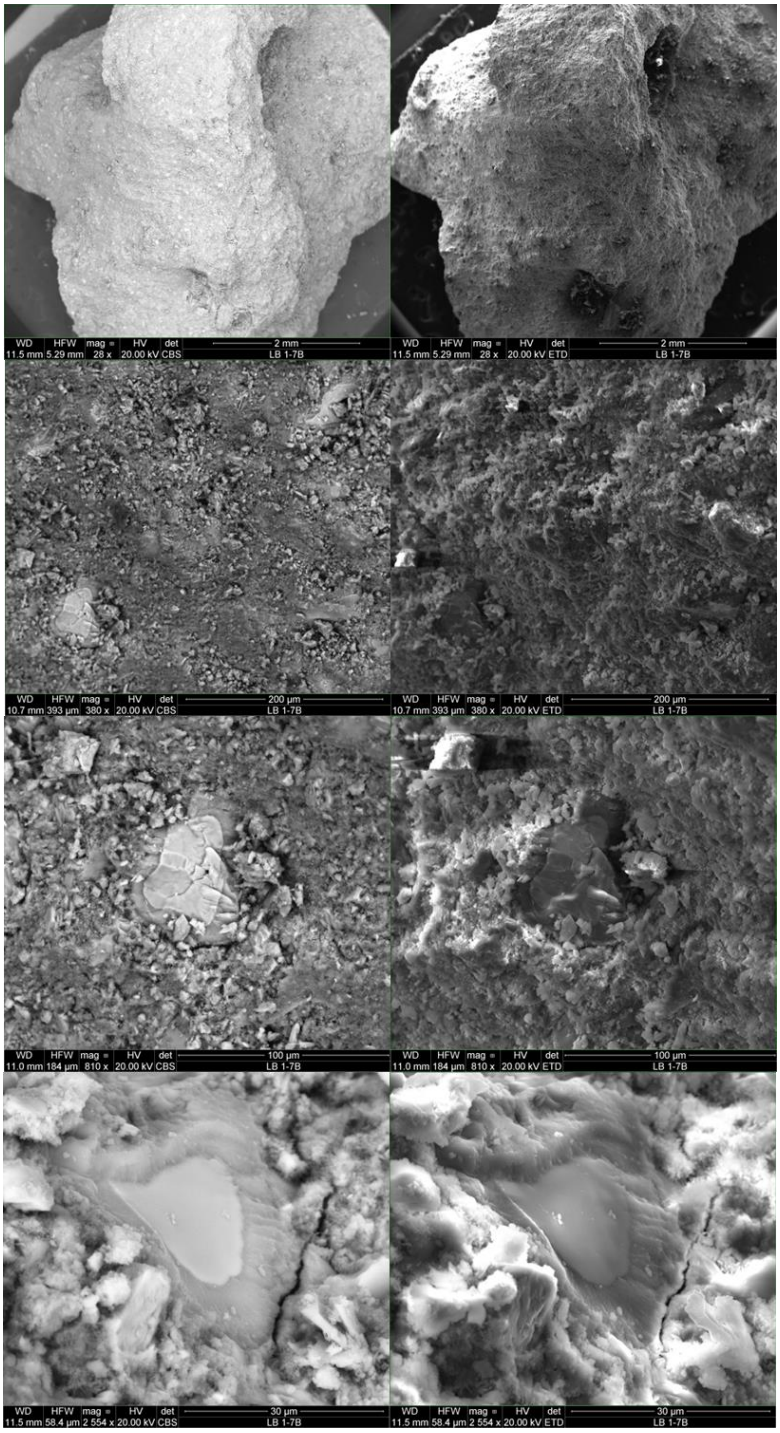

Figure 4.7. Sample 8 backscatter electron and secondary electron images obtained via SEM.

EDS is performed using a low-resolution backscatter electron image and selecting three surface locations as shown in Fig. 4.8.

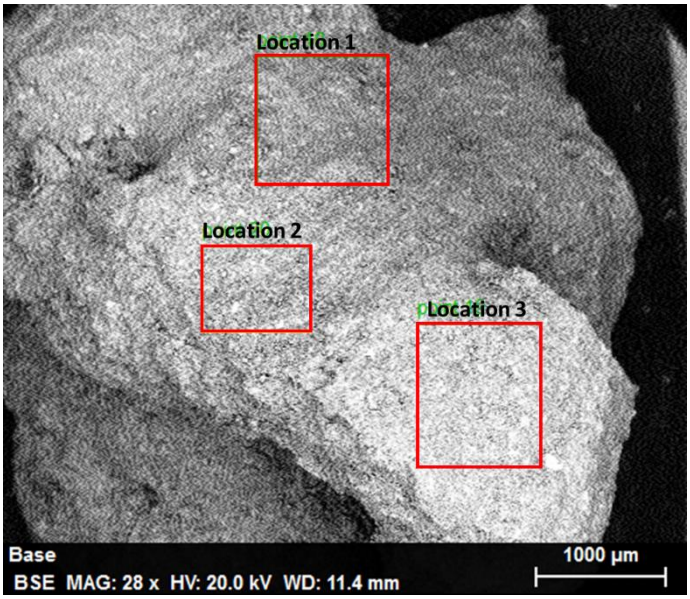

Figure 4.8. Sample 8 EDS sample locations.

Table 4.2. shows the most common elements within the sample at various surface locations.

Table 4.2. EDS elemental analysis for the three surface locations.

Element	Location 1 Normalized Wt. (%)	Location 2 Normalized Wt. (%)	Location 3 Normalized Wt. (%)
C	21.4	22.1	24.1
O	46.1	43.1	44.8
Na	2.0	1.5	1.7
Mg	1.1	0.6	0.8
Al	2.4	1.5	1.5
Si	3.3	3.8	3.8
S	0.2	0.2	0.2
K	5.9	4.8	4.0
Ca	14.5	20.0	17.5
Fe	0.5	0.9	0.7
Pd	2.0	0.2	0.2
Au	0.7	1.4	0.8

4.4 Discussion

Analysis of the results from hydrostatic compression testing, porosity and permeability investigation, and microscopy evaluation are further discussed within this section.

4.4.1 Hydrostatic Compression Testing

Values for both K_s and K are uniform, which is to be expected for materials of the same composition. It is known that the bulk modulus has an inverse relation to compressibility, meaning the greater the bulk moduli, the less compressible the material. From the results in Fig.s' 4.1 and 4.2, it can be seen that the bulk material exhibits markedly higher compressibility than the cement grains alone. K_s results of class H cement are greater than that of granites (45.0 GPa), shales (40.4-49.3 GPa) and sandstones (26.1-35.6 GPa) but are near or lower than previously reported values of carbonates, which can range from 52.6-74.4 GPa (Rice & Cleary, 1976; Mesri et al., 1976; Hart et al., 1995; Fabre & Gustkiewicz, 1997; Wawrzyniak-Guz, 2019; Kim & Makhnenko, 2020; Kasani & Selvadurai, 2022).

Our results imply that cement does not, in fact, behave as an unconsolidated material. Therefore taking the Biot coefficient to be one when determining the effective stress of cement will result in inaccurate failure calculations as discussed by Welch et al., 2019. A Biot coefficient of 1.0 indicates that the matrix of the material is significantly more compressible than the solid component (Ma & Gutierrez, 2021). Biot coefficient results on various rock types show that reported cement Biot coefficient values are the same as black shale (Zhou et al., 2017) and are higher than other types of rock, specifically granites, claystones, limestones, and sandstones (Fabre & Gustkiewicz, 1997; Detournay & Cheng, 1993; Cosenza et al., 2002; Orlander et al., 2018). There is limited literature regarding the Biot coefficient of wellbore cements, but the results shown in Fig. 4.3 are in good agreement with data published by Meng et al. (2020), in which the Biot coefficient was found to range between 0.70-0.81 for class G wellbore cement. Knowing that the Biot coefficient is less than 1 can also allow for more accurate *in situ* effective stress calculations to be determined which can also allow for improved understanding of the

stress at which cement will experience shear failure (Regel et al., 2017). The Biot coefficient can also have an influence on fracture initiation pressure; material with a high Biot coefficient will have a lower fracture initiation pressure (Chen et al., 2021). Biot coefficient also has the potential to be indicative of a materials permeability. Geologic and cementitious materials that exhibit high permeability will have high Biot coefficients (Meng et al., 2020).

4.4.2 Porosity & Permeability Tests

Porosity for both samples decrease slightly at increased confining stress while Klinkenberg permeability showed a more pronounced decrease at higher confining stresss as evident in Fig. 4.4. Neat OPC with a w/c ratio of 0.4 has porosity of 29.6% (Soroka, 1979). A study on the mechanical properties of neat class H cement conducted by Cvetic et al. (2020) showed that of the five samples, the lowest porosity was 21.3%, highest porosity of 23.5% and an average porosity of 22.4% while other literature reports cement permeability ranges from 1.0 nD to 1.0 mD (Roy et al., 1993; Bachu & Bennion, 2009). These values are in agreement with the porosity testing performed within this work.

4.4.3 Microscopy

Sample 12 has a more homogeneous macrostructure than that of sample 11. From Fig.s' 4.6 (a) and 4.6 (b), voids within the selected area on sample 12 are less than than a quarter of a millimeter in size whereas the voids within the selected area of sample 11 were larger and of varying in sizes as seen in Fig.s' 4.5 (a) and 4.5 (b). Voids within the cement are likely due to the presence of air bubbles during the setting period thus impacting the porosity, permeability, and fracture potential of the sample (Lavrov et al., 2016).

SEM analysis shows the presence of voids throughout the sample surface as indicated by the dark spots, which helps corroborate the porosity and permeability results for the cement samples.

Microcracks can also be seen on the surface of the sample. Partially hydrated cement grains are also seen as indicated by particles with lighter centers and darker coloration around the bright center in a backscatter electron image; this darker rim is indicative of the hydration shell. From the EDS analysis, it can be seen that the three sampled locations all had similar elemental compositions. Oxygen, carbon, and calcium were the most prevalent elements within the cement, which is in accordance with the chemical analysis provided by Central Plains Cement for the batch used in this study. The presence of magnesium, iron, silicon, potassium, and sulfur are in quantities that are also expected. It should be noted that the gold and palladium present within the sample are due to the sputter coating of the sample and are not naturally found within cement.

4.4.4. Wellbore Cement as a Poroelastic Material

Biot coefficients and porosity data have been collected from literature for various types of rocks and compared to the results from this work (Detournay & Cheng, 1993; Orlander et al., 2018; Salemi et al., 2018; Andreassen, 2017; Alam et al., 2009; Ling et al., 2016; He & Ling, 2014). The maximum, minimum, and average values were determined and standard deviation calculated. A plot comparing the reported ranges of Biot coefficient and porosity of various rock types, including various types of sandstones, limestones, chalks, granites, Bakken shales, and Tennessee marble, to the class H cement is shown in Fig. 4.9.

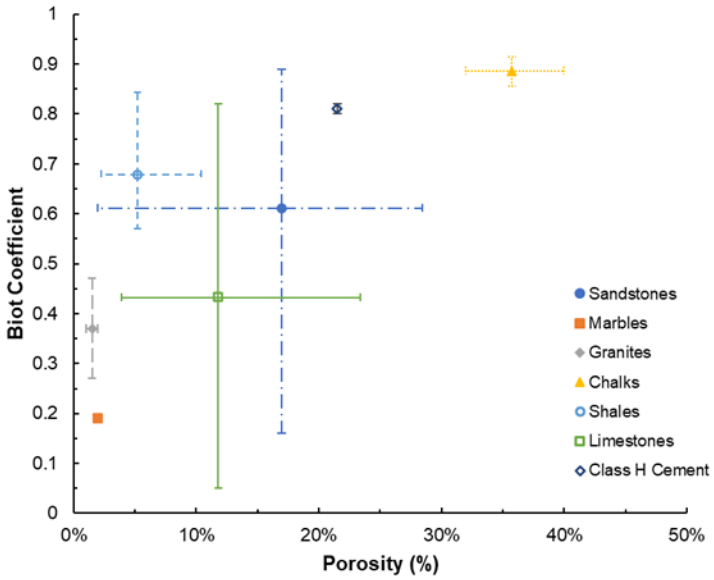

Figure 4.9. Biot-porosity range comparison for various rocks and class H cement.

Previous work shows a significant spread in Biot coefficients for the various rock types, specifically sandstones and limestones. Fig. 4.9 shows the overall trend of reducing Biot coefficient with reducing porosity. Class H cement has similar Biot coefficient values to Bakken shale (Ling et al., 2016; He & Ling, 2014). It should also be noted that the class H cement falls into previously reported ranges of limestones and sandstones as well. From this information, it can be deduced that cement is a poroelastic material and can be modeled using poroelastic theories developed for rocks.

4.5 Conclusions Regarding Poroelastic Testing of Wellbore Cement

This chapter investigated the poroelastic properties of class H wellbore cement. by performing hydrostatic compression experiments, porosity and permeability testing, and microscopic evaluation to get a better understanding on the poroelastic properties of wellbore cement to improve cement design to withstand hydraulic fracturing, evaluate P&A, and secure long-term wellbore integrity. From the results it can be seen that:

1. Class H wellbore cement has K_s of 52.2 GPa, K of 10.0 GPa and Biot coefficient of 0.81 ±0.01 and show linear behavior over the stress interval tested. This behavior is similar to porous sedimentary rocks and cement should be analyzed as a poroelastic material.
2. Porosity and permeability obtained within this work were within previously reported values for wellbore cement. Optical microscopy verified that porosity is evenly distributed in the sample.
3. SEM analysis supports the porosity and permeability results in that voids are seen throughout the surface of the sample. Unhydrated and partially hydrated cement grains, while observed, were not extensively present on the surface of the cement.
4. The elemental composition of the cement is homogeneous throughout the sample. The main constituents of the cement are oxygen, carbon, and calcium which are in agreement with previously reported data on class H cement.

Chapter 5: Shear Behavior of Wellbore Cement

This chapter investigates the compressive shear behavior of class H wellbore cement under confining stress. Consolidated isotropic drained (CID) testing is performed to observe the mechanical behavior and fracture characteristics of *in-situ* behavior of well cements. Analysis of the sheared cement samples in conjunction with the failure envelope can determine the cohesion and angle of friction the cement is experiencing under wellbore conditions. Using this information can optimize cement slurry designs to be made for specific wellbore conditions.

5.1 Introduction

Understanding the mechanical behavior of wellbore cement is crucial for establishing and maintaining wellbore integrity. Knowledge of the mechanical properties and failure criteria of cement can aid in more accurate cement design for all stress variations that will be experienced

in hydrocarbon, geothermal, and carbon capture and storage (CCS) wellbores. During hydraulic fracturing, the cement sheath will undergo two primary pressure and temperature variations: when fracturing and subsequently pumping the frac fluid into the wellbore; during these times the casing will expand and contract thus altering the radial stress on the cement (Liu et al., 2018). To ensure minimal failure within the cement sheath, knowledge of the mechanical properties of the cement should be used to design a sheath that is able to withstand such alterations. Another significant issue that can arise with improper cement design is sustained casing pressure (SCP), which is an issue in gas wells where failure of the cement sheath primarily due to debonding and shrinkage resulting in gas migration (Zhao et al., 2019).

There are numerous types of testing available to provide insight regarding cement mechanical properties, with crushing strength being the most widely performed type of testing. While it is the most common, few researchers take into consideration realistic downhole conditions when curing the samples used in testing. One common type of test in which the sample undergo destructive testing is the consolidated isotropic drained (CID) triaxial testing, which allows for a number of mechanical properties to be determined throughout the test including confined compressive strength (*CCS*), Young's modulus (*YM*), Poisson's ratio (*PR*), and angle of failure, which is found once the samples have been sheared. Another parameter that can be found is the plasticity modulus, which shows the brittle-ductile behavior of a material. While this type of testing is commonly performed on rock and unconsolidated sands, there is little experimental triaxial test data on class H wellbore cement and, more specifically, samples cured past the early hydration period. Liteanu et al. (2009) tested class A cement samples with a water/cement (w/c) ratio of 0.5 that were tested at confining stress ranging from 1.5 MPa (217.6 psi) to 30.0 MPa (4351.1 psi) for investigating applications to CO_2 storage. Takla et al. (2011) tested class G

cement samples cured for one month in lime water to observe the effects of carbonation at four confining stress. Other studies focus primarily on triaxial testing of wellbore cement containing additives and the implications the additives have on mechanical properties. Yang & Deng (2018) performed triaxial testing on class G cement containing a number of various additives and cured for a 7-day period and observe the effect of the additives on the flexure and strength of the cement.

Once a sample has been sheared, observations on the shear plane can yield information related failure behavior (Schwartz, 1964). Shearing the sample also allows for the plasticity modulus to be determined, which can determine the brittle-ductile behavior of the material indicating when irreversible deformation will occur.

5.2 Methodology for CID Testing

To obtain the mechanical properties and shear behavior of class H wellbore cement, consolidated isotropic drained triaxial tests are performed at varying confining stress. This section describes the process for sample preparation and testing procedures to obtain a number of mechanical and shear properties.

5.2.1 Specimen Preparation for CID Testing

25.4 mm (1.0 inch) diameter cement samples are made using a deionized water to Central Plains class H cement (w/c) ratio of 0.38 according to ASTM D7012-14 standards, and 0.2% defoaming additive to reduce air bubbles within the sample (provided by Halliburton, 2020). The samples are mixed and placed in 25.4 mm by 101.6 mm (1.0 inch by 4.0 inch) stainless steel molds for 24 hours. The samples are removed from the molds and placed in a 0.4% sodium hydroxide (NaOH) brine water bath at 65.6°C (150°F) oven. After curing for more than 90 days, the cement samples are removed from the oven and cut 50.0 to 75.0 mm length (2.0-2.5 L/D). The ends of the

samples are grinded and parallel ends are verified by taking three caliper measurements of the sample length at 120.0º different orientation. The samples are then weighed to obtain wet weight measurements and placed in a 65.6°C (150°F) vacuum oven for 48 hours to remove any excess fluid trapped within the samples. Post-vacuuming, the samples are re-weighed to obtain dry weight. A summary of the prepared samples is shown in Table 5.1.

Table 5.1. Sample description for samples undergoing CID testing.

Test Number	Test Type*	Average Length (mm)	Wet Weight (g)	Dry Weight (g)	Water Weight (g)	Bulk Density (g/ cm^3)	Particle Density (g/ cm^3)	Porosity (%)	Pore Volume (cm^3)
1	H,CID	61.2	63.1	52.7	10.4	11.0	13.1	16.5	10.4
2	H,CID	62.0	64.3	53.9	10.4	11.1	13.2	16.2	10.5
3	H,CID	61.2	61.1	53.0	8.1	11.0	12.7	13.2	8.1
4	CID	61.2	62.6	52.0	10.6	10.8	13.0	16.9	10.6
5	CID	59.7	61.3	51.2	10.1	10.9	13.1	16.4	10.1
6	CID	58.7	58.7	51.4	7.3	11.2	12.7	12.4	7.3
7	CID	61.7	65.2	56.2	9.1	11.6	13.5	13.9	9.1
8	CID	59.4	60.2	50.2	10.0	10.8	12.9	16.6	10.0
9	CID	62.0	65.2	55.1	10.1	11.3	13.4	15.5	10.1
10	CID	59.2	58.8	51.1	7.7	11.0	12.7	13.1	7.7
11	P&P	63.0	64.4	57.9	6.5	11.7	13.0	10.1	6.5
12	P&P	60.2	60.3	51.8	8.4	11.0	12.8	14.0	8.4

**H=hydrostatic compression test; CID=consolidated isotropic drained test; P&P=porosity and permeability test*

5.2.2 CID Testing

Consolidated isotropic drained triaxial testing is performed at three different confining stress: 5.0 MPa (725.2 psi), 15.0 MPa (2175.6 psi), and 30.0 MPa (4351.1 psi). For each confining stress, three samples are tested to ensure repeatability. Cement samples were placed between two solid steel cylinders and jacketed to ensure no fluid penetration during testing. A radial LVDT is placed around the middle of the sample while two steel O-rings are placed at the top and the bottom of the sample to hold two axial LVDT's for measuring axial deformation during testing. The jacketed sample is then placed into the GCTS HTRX-H70 triaxial cell, and the LVDT's connected to the corresponding sensor. Axial LVDT's are calibrated to read approximately -1.0

MPa (-145.0 psi) while the radial LVDT is calibrated to around 1.0 MPa (145.0 psi). Once calibration is achieved, the cap of the triaxial cell is placed onto the sample and the inner cavity filled with mineral oil. A piston is inserted to remove any excess fluid and seal the cell. A check of the tubing connection to a Teledyne-Isco 100DX syringe pump filled with mineral oil which provided confining stress. The triaxial cell is then placed onto the center of the bottom platen of a MTS 318 250kN load frame. Steel cylinders are placed on the top of the triaxial cell piston to ensure complete contact with the upper piston of the MTS 318 load frame. A schematic of the consolidated isotropic drained triaxial test setup is shown in Fig. 5.1.

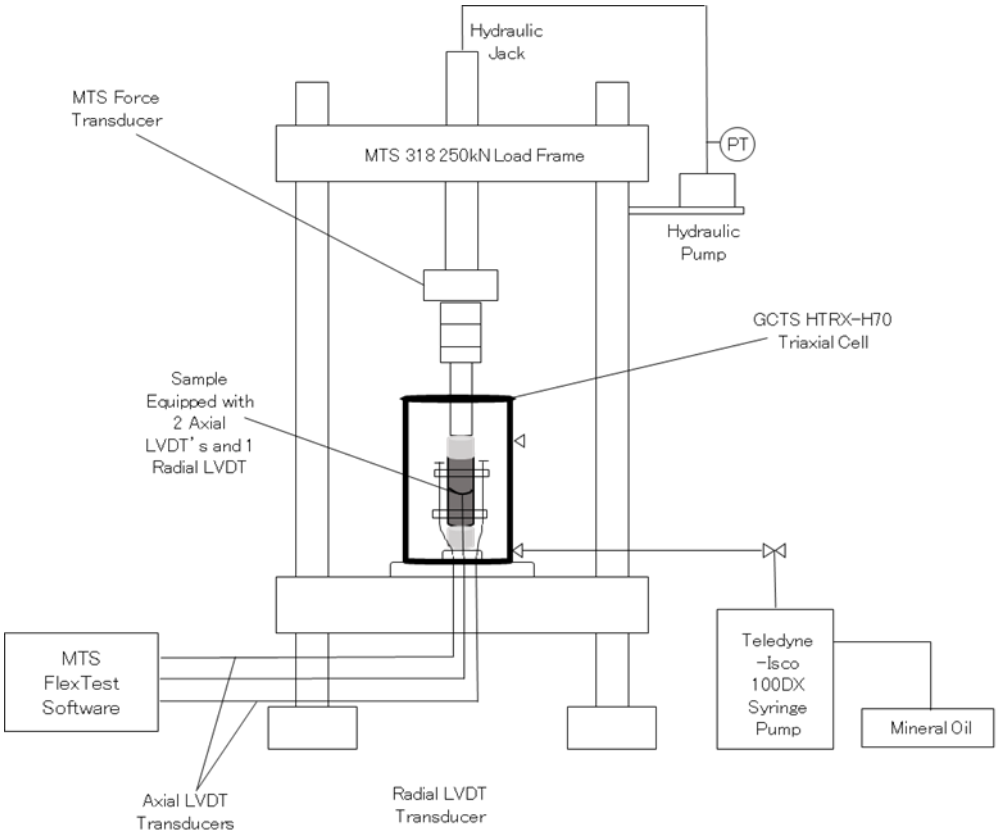

Figure 5.1. Single-stage consolidated isotropic drained test setup.

The lower the upper load frame platen is slowly lowered until the piston is touching the sample. The test is initiated and plots of the axial, radial and volumetric strain are obtained in real-time. Once the sample reaches peak yield and the residual shear stress stabilizes, the test is concluded.

5.2.3 Scanning Electron Microscopy (SEM)

Scanning electron microscopy (SEM) back scatter electron (BSE) images are taken for two of the samples post CID testing at the fracture surface and in the post-test *in-situ* material to determine any significant microstructural differences. For the fractured and *in-situ* material, 5 locations are sampled at various magnifications of 200x, 1,000x, and 2,000x.

5.3 Results

5.3.1 CID Tests

Once CID testing is completed, stress-strain curves are created and analyzed to determine *CCS*, *YM*, and *PR*. *CCS* is taken to be the highest stress exhibited by the sample. *PR* and *YM* are found using stress-strain measurements preceding the occurrence of failure. *YM* is found by taking the tangent at 50% of the *CCS*-axial strain curve. *PR* is determined by finding the slope of the tangent at 50% of the *CCS* for the *UCS*-radial strain curve and dividing this by *YM*. The stress-strain curves for the samples tested at 5.0 MPa, 15.0 MPa, and 30.0 MPa are shown in Fig.'s 5.2, 5.3, and 5.4 respectively.

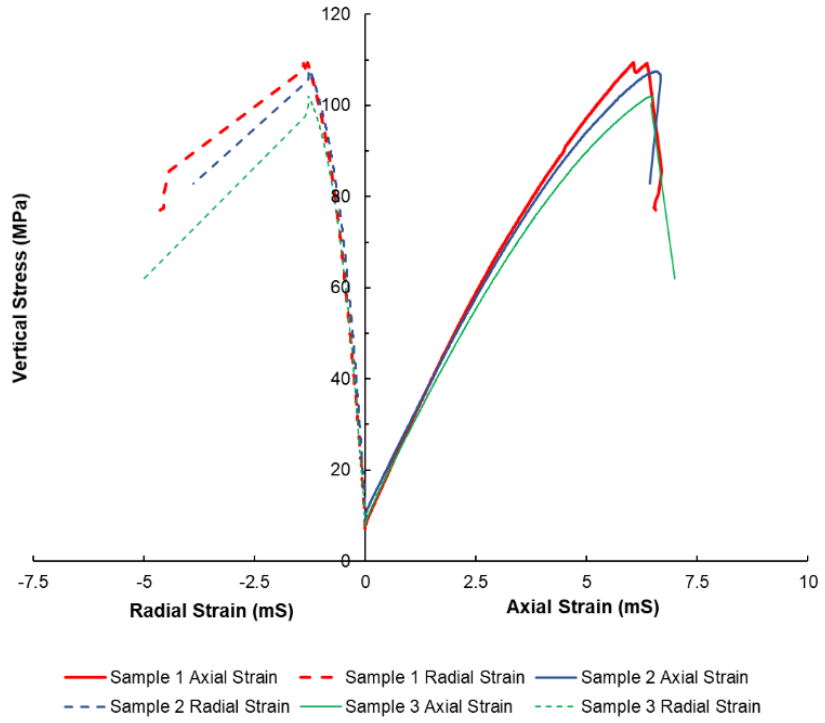

Figure 5.2. Single-stage consolidated isotropic drained stress-strain curves at 5 MPa confining stress.

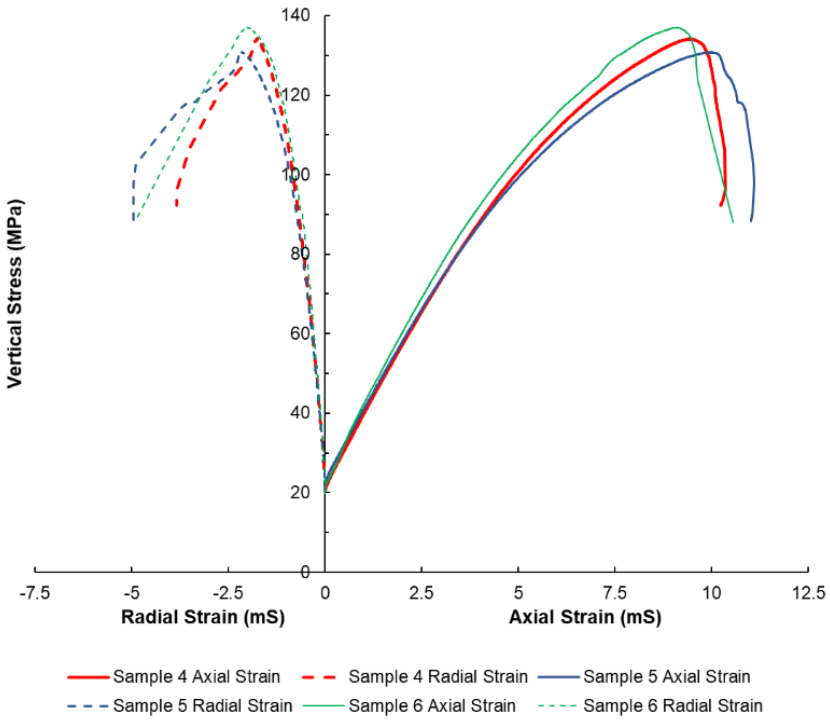

Figure 5.3. Single-stage consolidated isotropic drained stress-strain curves at 15 MPa confining stress.

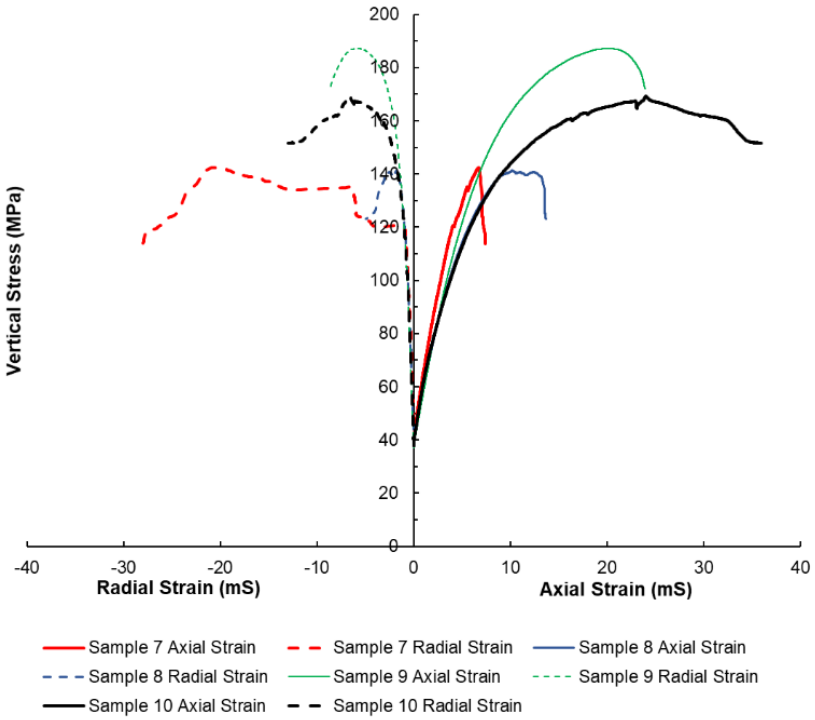

Figure 5.4. Consolidated isotropic drained stress-strain curves at 30 MPa confining stress.

Using the stress and strain data obtained from CID tests, a Mohr-Coulomb failure envelope is created to determine when class H wellbore cement will experience shear failure, or the amount of stress that can be applied to the wellbore cement before it will fail (Saint-Marc et al., 2008). It should be noted that during the CID testing, all samples are sheared at the respective confining stresss; here, shearing refers to the stress required to initiate a fracture.

A plot showing yield stress versus confining stress and *YM* versus confining stress for the samples tested at 5.0 MPa, 15.0 MPa, and 30 MPa are shown in Fig.s' 5.5 And 5.6, respectively.

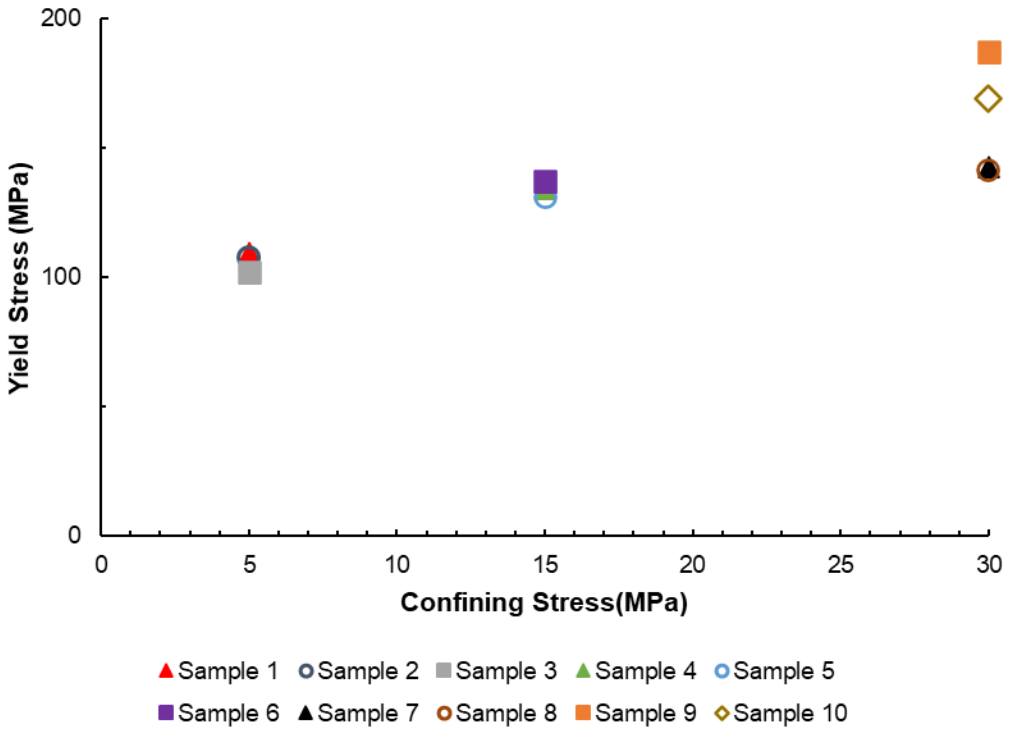

Figure 5.5.Yield stress versus confining stress for the samples tested at 5 MPa, 15 MPa, and 30 MPa..

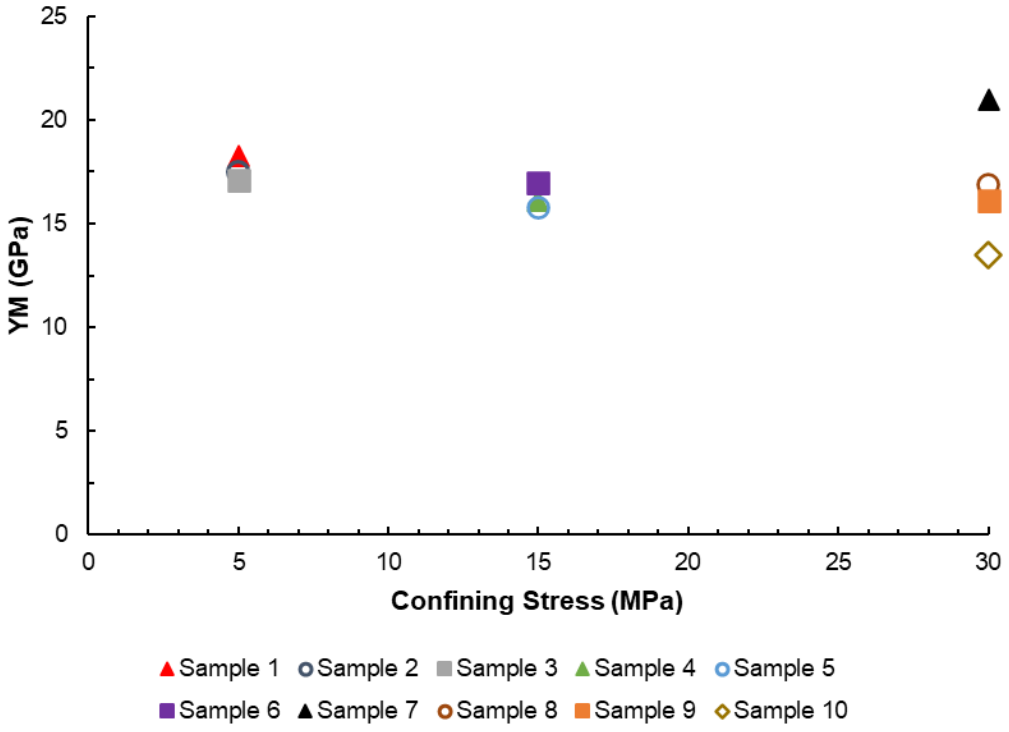

Figure 5.6. YM versus confining stress for the samples tested at 5 MPa, 15 MPa, and 30 MPa.

5.3.2 Shear Failure

After the samples are tested and sheared, the samples are unjacketed and photographed to determine the plane of failure. Fracture angles for each sample are determined by dividing the sample in a 12 by 20 grid and determining the angle of fracture within each grid box. Fracture angle results are shown in Fig. 5.7 and described in Table 5.2. It should be noted that fracture angles are determined using the primary fractures, which are shown in blue. Other fractures that are present have been mapped and shown in red, but not included in fracture angle analysis.

Table 5.2. Fracture angle analysis.

Confining Stress (MPa)	Test Number	Average	Std. Dev.
5	1	59.5˚	30.9˚
	2	72.5˚	21.2˚
	3	116.4˚	29.0˚
15	4	70.6˚	15.6˚
	5	57.0˚	16.6˚
	6	112.5˚	23.7˚
30	7	69.8˚	7.5˚
	8	57.8˚	31.5˚
	9	57.4˚	16.5˚
	10	60.2˚	35.8˚

Figure 5.7. Fracture angle determination for a) Sample 1; b) Sample 2; c) Sample 3; d) Sample 4; e) Sample 5; f) Sample 6; g) Sample 7; h) Sample 8; i) Sample 9; j) Sample 10.

5.3.3 Microscopy

To understand the effect that CID testing has on the microstructure of a sheared sample, SEM back scatter microscopy is performed on the fracture surface and the surrounding material (i.e. intact material outside of the fractured area). Fig.s' 5.8, 5.9, and 5.10 shows three separate SEM BSE images at 1,000x magnification on the fracture surface of sample 1, which underwent CID testing at a confining stress of 5 MPa.

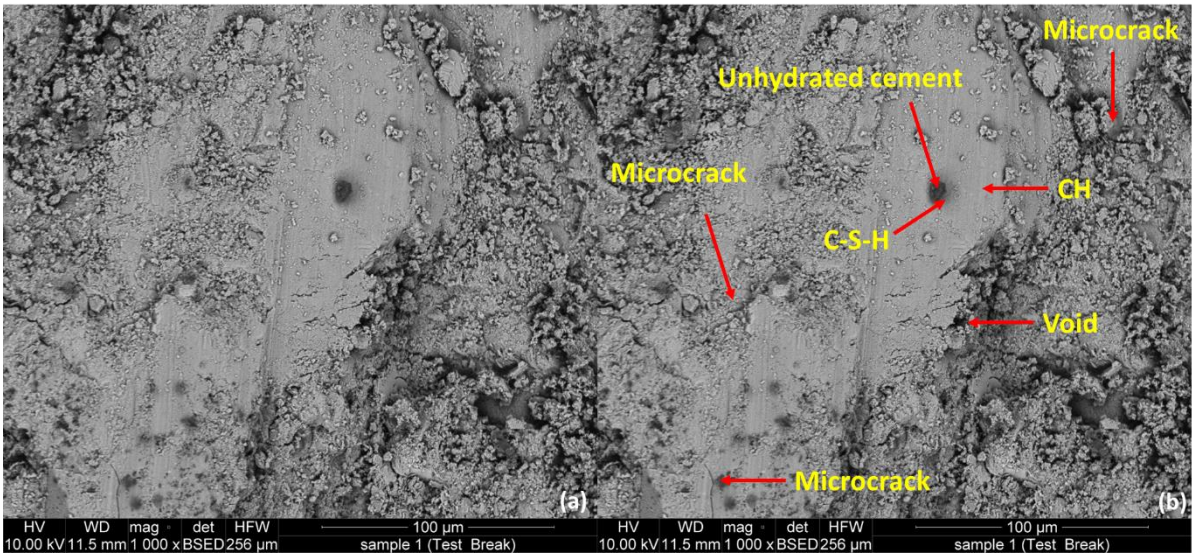

Figure 5.8 SEM BSE image at 1,000x magnification for a point on sample 1 fractured surface: (a) BSE image; (b) BSE image with notable microstructures labeled.

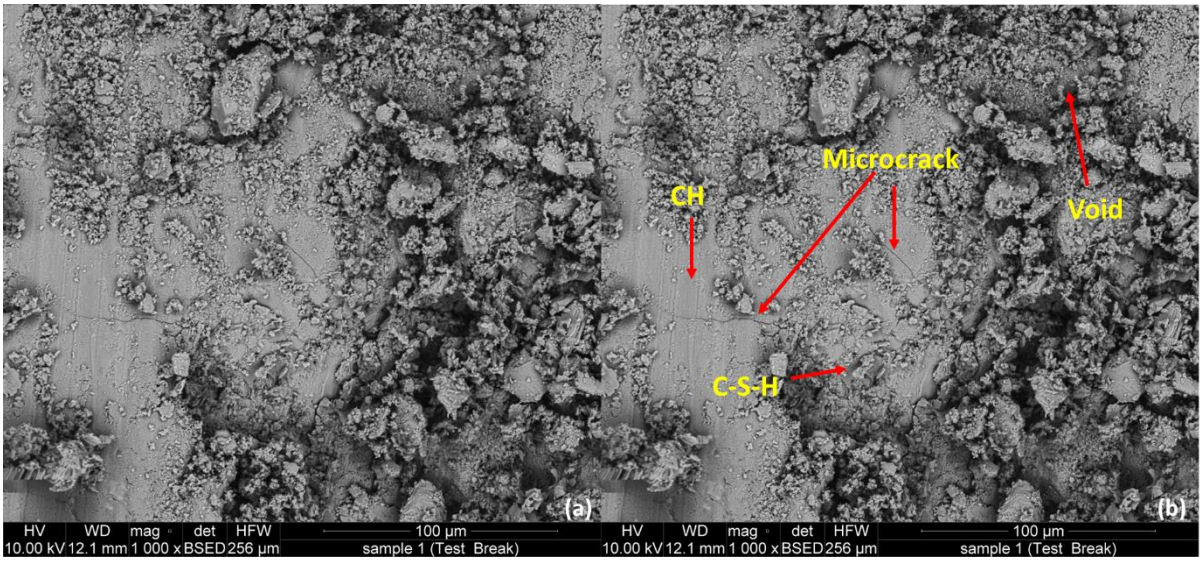

Figure 5.9. SEM BSE image at 1,000x magnification for a second point on sample 1 fractured surface: (a) BSE image; (b) BSE image with notable microstructures labeled.

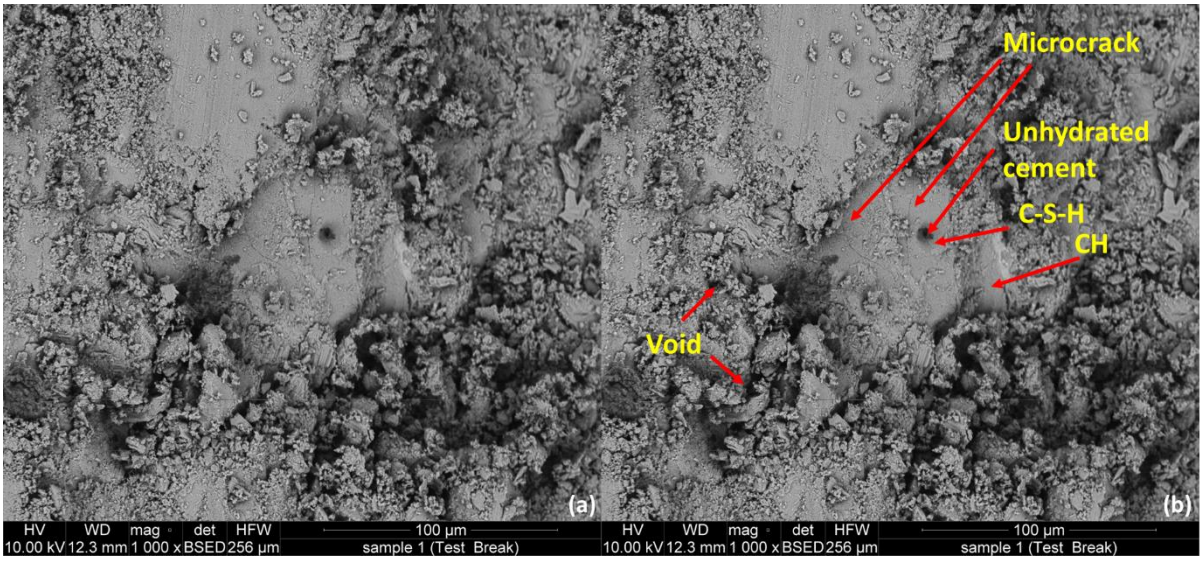

Figure 5.10. SEM BSE image at 1,000x magnification for a third point on sample 1 fractured surface: (a) BSE image; (b) BSE image with notable microstructures labeled.

Fig.s' 5.11, 5.12, and 5.13 shows three separate SEM BSE images at 1,000x magnification on the fracture surface of sample 9, which underwent CID testing at a confining stress of 30 MPa.

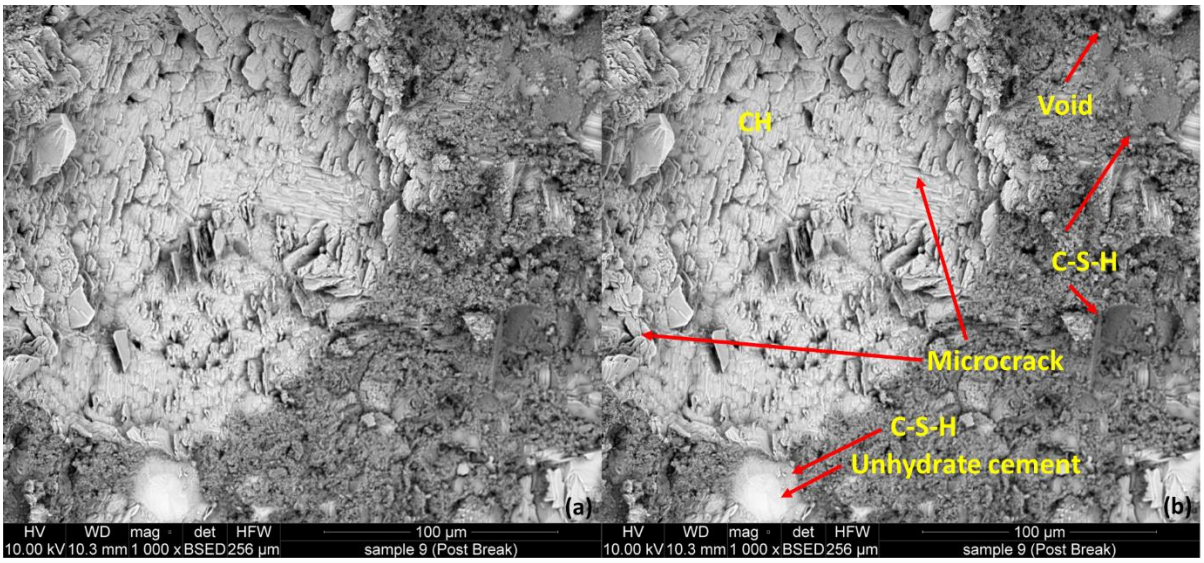

Figure 5.11. SEM BSE image at 1,000x magnification for a point on sample 9 fractured surface: (a) BSE image; (b) BSE image with notable microstructures labeled.

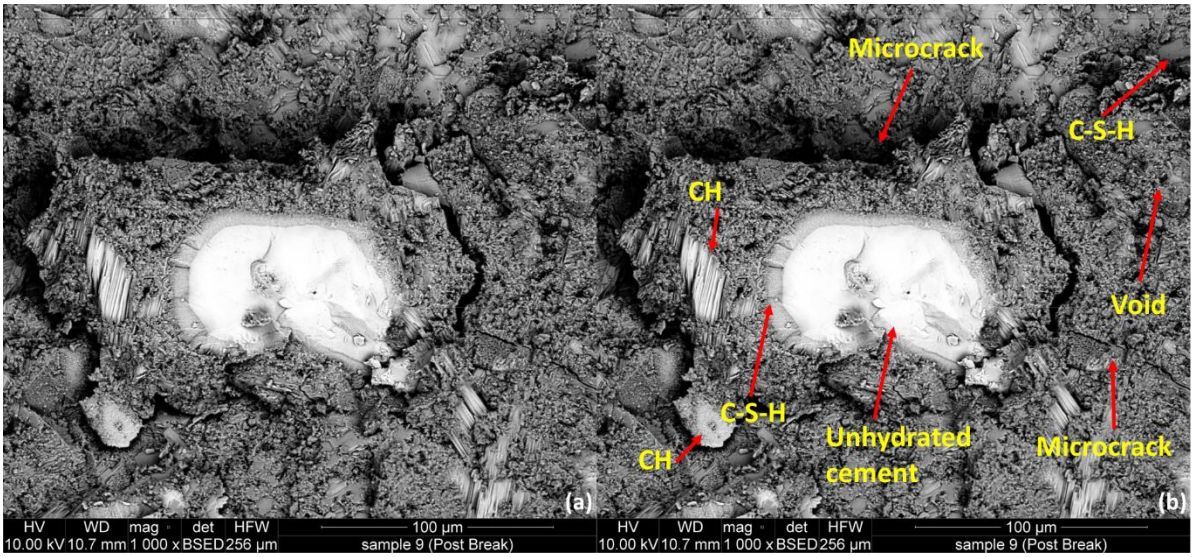

Figure 5.12. SEM BSE image at 1,000x magnification for a second point on sample 9 fractured surface: (a) BSE image; (b) BSE image with notable microstructures labeled.

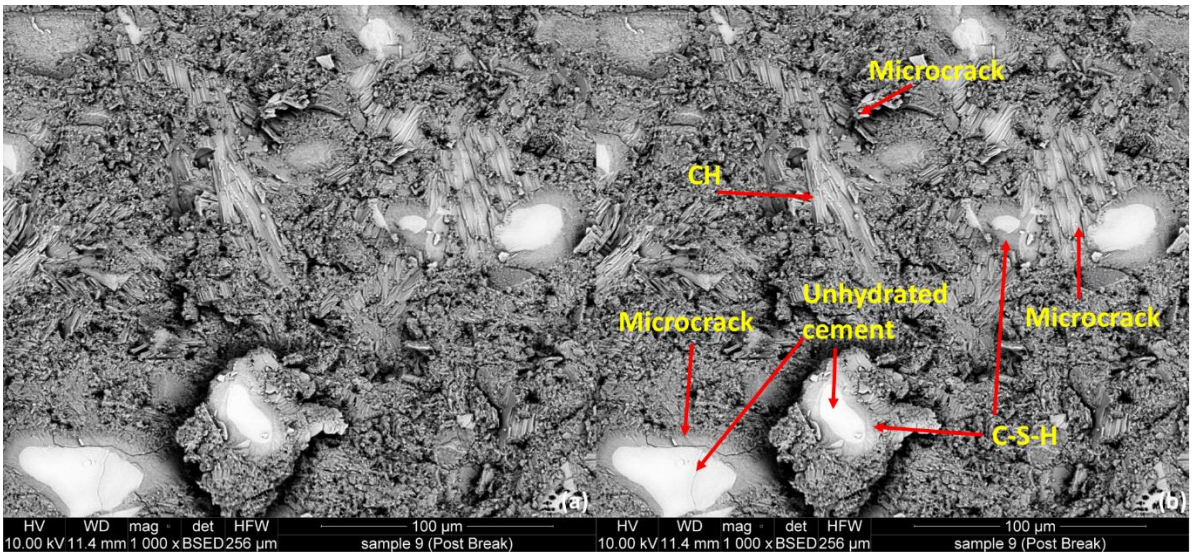

Figure 5.13. SEM BSE image at 1,000x magnification for a third point on sample 9 fractured surface: (a) BSE image; (b) BSE image with notable microstructures labeled.

Fig.s' 5.14, 5.15, and 5.16 show three separate SEM BSE images at 1,000x magnification of the intact material for sample 1, which underwent CID testing at a stress of 5.0 MPa.

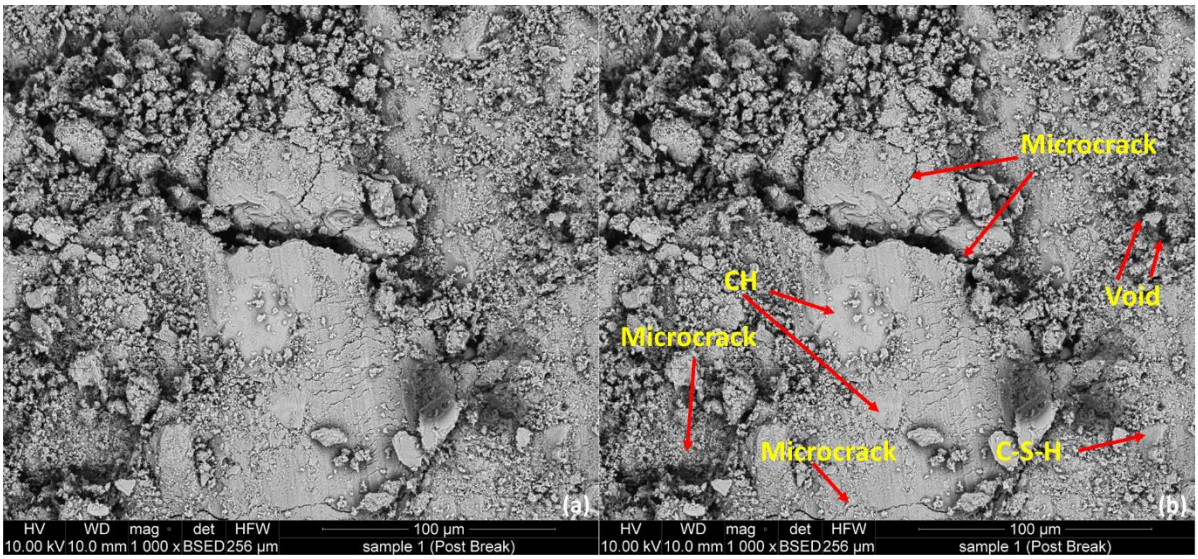

Figure 5.14. SEM BSE image at 1,000x magnification for a point on sample 1 intact material: (a) BSE image; (b) BSE image with notable microstructures labeled.

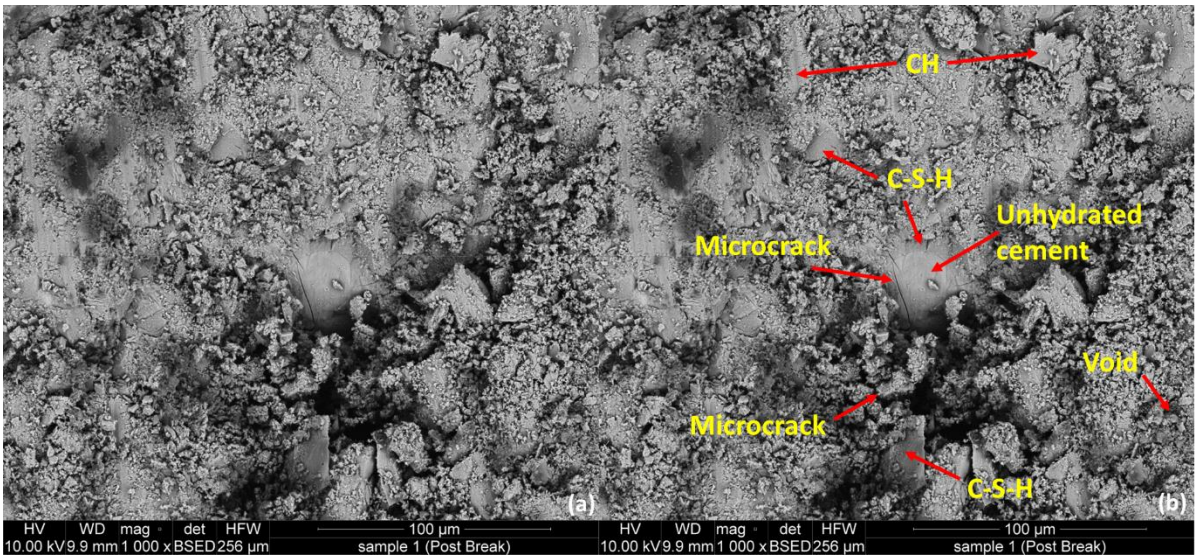

Figure 5.15. SEM BSE image at 1,000x magnification for a second point on sample 1 intact material: (a) BSE image; (b) BSE image with notable microstructures labeled.

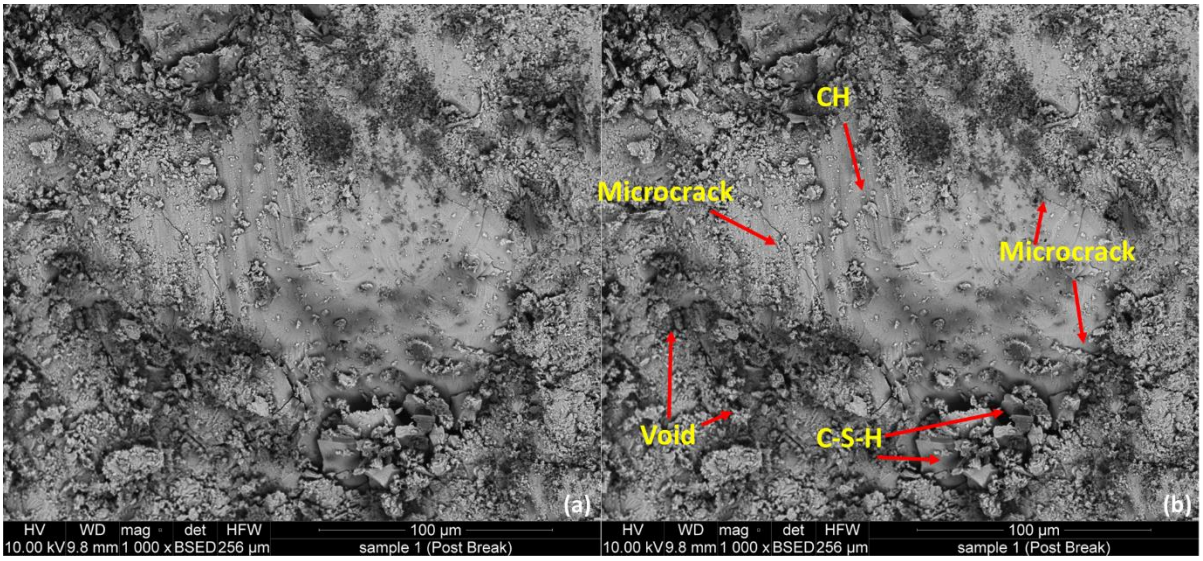

Figure 5.16. SEM BSE image at 1,000x magnification for a third point on sample 1 intact material: (a) BSE image; (b) BSE image with notable microstructures labeled.

Fig.s' 5.17, 5.18, and 5.19 show three separate SEM BSE images at 1,000x magnification of the intact material for sample 9, which underwent CID testing at a stress of 30.0 MPa.

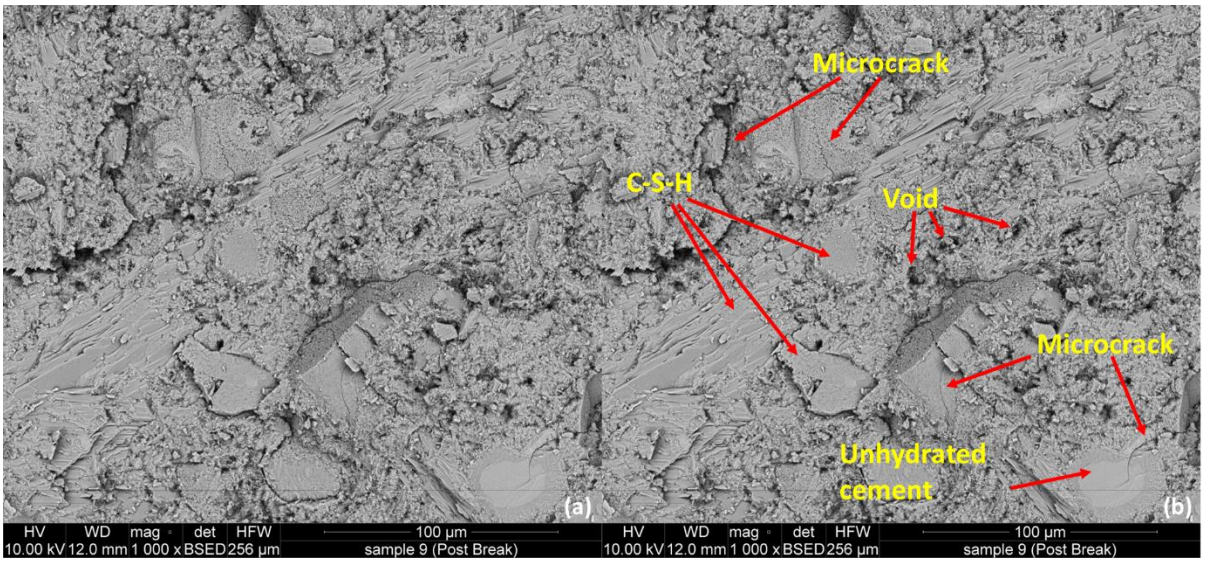

Figure 5.17. SEM BSE image at 1,000x magnification for a point on sample 9 intact material: (a) BSE image; (b) BSE image with notable microstructures labeled.

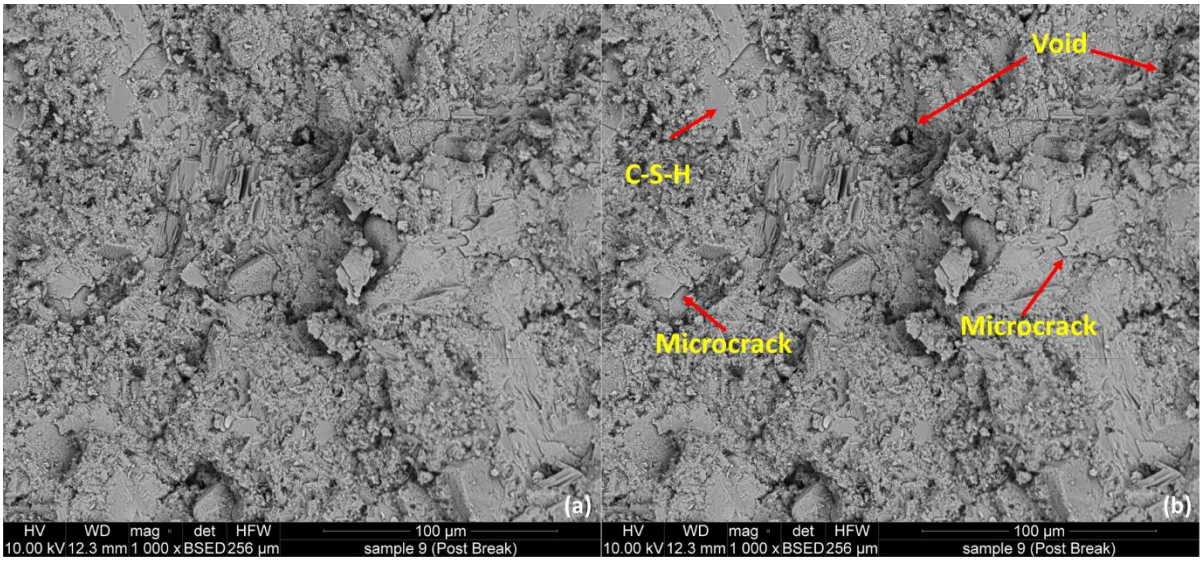

Figure 5.18. SEM BSE image at 1,000x magnification for a second point on sample 9 intact material: (a) BSE image; (b) BSE image with notable microstructures labeled.

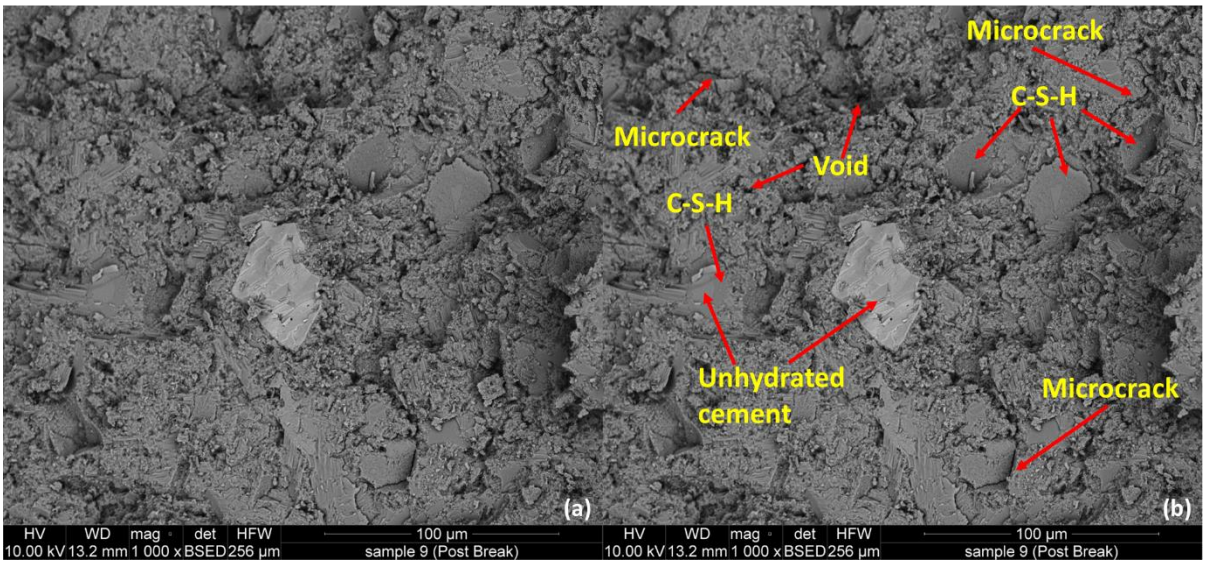

Figure 5.19. SEM BSE image at 1,000x magnification for a third point on sample 9 intact material: (a) BSE image; (b) BSE image with notable microstructures labeled.

EDS results taken at 28x magnification at three locations on the sample is shown in Fig. 5.20. EDS is performed over a larger portion of the fractured surface area rather than a point to have a better representation of the entire surface composition.

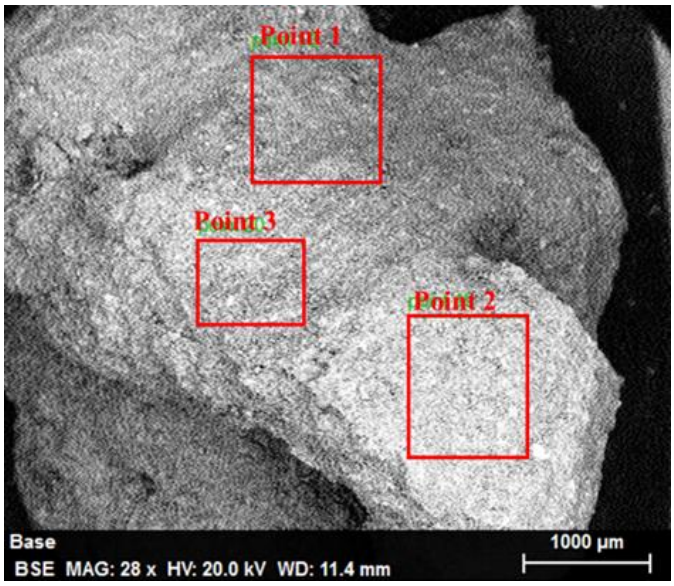

Figure 5.20. Three selected EDS locations on the cement sample.

5.4 Discussion

5.4.1 CID Tests

An analysis of the stress-strain curves is performed to understand the effect that stress has on the mechanical and shear properties of class H cement. This includes determining strain behavior, *CCS*, *YM*, *PR*, and plasticity of the samples tested at 5.0, 15.0, and 30.0 MPa. From Fig. 5.2, the stress-strain curves for all three samples tested at 5.0 MPa stress until the yield point. *CCS* for the samples confined and sheared at 5.0 MPa is 106.3 MPa with a standard deviation of 3.8 MPa. *YM* is 17.6 GPa with standard deviation being 0.6 GPa and *PR* of 0.2 ±0.01.

The samples confined and sheared at 15.0 MPa also show the same trends and have *CCS* of 134.0 MPa ±3.1 MPa as seen in Fig. 5.3. The *YM* is 16.3 GPa ±0.6 GPa and *PR* of 0.2 ±0.01. Axial strain for all samples is approximately double the value of the radial strain when sheared. For the four samples confined and sheared at 30 MPa shown in Fig. 5.4, the stress-strain curves has a larger spread in the results; samples 7 and 8 have a yield point around 140 MPa and the yield points for samples 9 and 10 are over 20 MPa greater. The yield point is less evident for

samples 8 and 9 while the point of failure is somewhat identifiable for sample 10. Sample 7 is the only sample tested at 30.0 MPa confining stress that shows a clear yield point at which the cement failed. *CCS* at 30.0 MPa confining stress proved to be highly variable with lowest being 141.4 MPa and the highest being 187.2 MPa. Average *CCS* is 160.1 MPa for the four samples tested at 30.0 MPa confining stress with standard deviation being 22.2 MPa. *YM* also varies greatly with an average of 16.9 GPa and the standard deviation is high at 3.1 GPa; *PR* is comparable to the values obtained from the samples tested at lower confining stress with an average of 0.2 and standard deviation is 0.03. Sample 7 had the highest *YM* and *PR* of the samples tested at 30.0 MPa confining stress, which is the reason for the sharp drop in vertical stress and axial strain following failure yet radial strain increases after the sample has been sheared. Samples 9 and 10 have the lowest *YM* which may be why the samples do not necessarily exhibit a definitive point of failure.

CCS, which is the maximum stress prior to shearing, increases with confining stress due to an increase in material strength at higher pressures. It is also seen that as confining stress increases, strain measurements increase as well, which is due to the strain hardening effect. Post-peak slope becomes less steep with increased confining stress. Both *YM* and *PR* stay relatively constant with confining stress variation.

Results from class H and G cement data compiled and previously reported found that *YM* values for these cement types range from 0.004-26.2 GPa while *PR* values range from 0.02-0.3 (Appendix E). In this work, both the lowest and highest *YM* is observed at 30.0 MPa confining stress, the highest being sample 7 with *YM* of 21.0 GPa and the lowest of 13.5 GPa exhibited by sample 9. A minimum *PR* value of 0.2 was observed in samples 2, 6, 8, and 9 while a max *PR* of 0.2 is observed from samples 7 and 10, both of which are tested at 30.0 MPa confining stress. All

tested samples have *YM* and *PR* values that agree with previous literature. In cement, low *YM* is important for ductility but cement with low *YM* also allows for shear failures to propagate faster within the wellbore (Kim et al., 2016; Petty et al., 2003).

From Fig. 5. It can be seen that the *CCS* increases linearly for the samples confined at 5 MPa, 10 MPa, and two of the samples tested at 30 MPa, or samples 9 and 10. *CCS* values for samples 7 and 8 were similar to those tested at 15 MPa. This could be due to infiltration of the sample during testing or due to the properties within the sample, such as microstructure, porosity, or permeability. Fig. 5. Shows that from 5 MPa to 10 MPa and for one of the samples tested at 30 MPa (sample 10) stress, the *YM* decreases. Samples 8 and 9 have *YM* values that were similar to those seen in the samples tested at 15 MPa. Sample 7 had the highest *YM* of all the samples and this could be due to sample infiltration during testing. From these results, *CCS* of cement will increase with confining stress while *YM* will decrease or remain constant at higher confining stress.

Plastic deformation of cement is used to help classify the brittle-ductile behavior of the samples. When a materials elastic response during loading has reached a pinnacle, plastic deformation will the take place (Pariseau, 1988). Plasticity modulus, which describes how material shape will be plastically altered during deformation, is also found using the stress-strain curves obtained during consolidated isotropic drained tests to observe the linear-elastic behavior of cement. Higher plasticity suggests that a material will undergo higher stress relaxation when under confinement; material with low plasticity exhibit a sudden increase in strain during the loading portion of the tests (Milman et al., 1993). Basically, determining what the strain of the material if it were completely elastic at the point of shear and finding how great the difference between the strain at shear and if the material is completely elastic. The greater the difference in strain, the

more plastic (i.e. less elastic) a material is. Table 5.3 shows the modulus of elasticity for the class H samples.

Table 5.3. Determination of material plasticity.

Confining Stress (MPa)	Test Number	Axial Strain at Shear (mS)	Axial Strain Elastic (mS)	Difference	% Difference
5	1	6.1	5.3	0.8	-13.2%
	2	6.6	5.4	1.2	-18.6%
	3	6.5	5.2	1.3	-19.5%
15	4	9.4	6.8	2.7	-28.3%
	5	10.0	6.6	3.4	-34.2%
	6	9.1	6.5	2.6	-28.7%
30	7	6.7	4.7	2.0	-30.4%
	8	10.2	5.8	4.3	-42.6%
	9	20.2	8.8	11.4	-56.3%
	10	24.0	8.8	15.2	-63.5%

Axial strain at shear indicates length deformation at shear while elastic axial strain is indicative of the strain if the material were to be fully elastic (unable to be sheared). To determine this, a linear line is extrapolated from the elastic region of the axial portion of the stress-strain curve. From this, Eq. 5.1 is used to find the elastic axial strain of the samples.

$$\varepsilon_{elastic} = (CCS - b)/m \tag{5.1}$$

Where b is the y-intercept of the linear line and m is the slope of the linear line. The greater the difference between the axial strain at shear and elastic axial strain, the less elastic and more plastic a material is. Plasticity modulus is greater at higher confining stress, which is to be expected due to the dilatancy the material experiences under higher pressure.

It can be seen that plasticity of the cement increases with confining stress, meaning that the material tends to have increased deformation at increased pressures. During consolidated isotropic drained triaxial testing, cement undergoes three stages: an elastic stage, a hardening

stage, and a softening stage (Vermeer, 1998). The elastic portion of the test begins once the test is initiated and the material is solely experiencing elastic deformation. Once the material begins to deviate from elastic to inelastic, the hardening stage occurs and the cement continues to become more inelastic as confining stress increases. Once the sample is sheared, it has been fractured and deformation is irreversible and at this point strain-softening begins to occur. At high confining stress, the hardening stage occurs for a longer duration thus increasing the materials plasticity. Plots showing plasticity are shown in Appendix B.

5.4.2 Failure Criteria

For each consolidated isotropic drained test, the major and minor principal stresses are plotted versus strain to develop a Mohr-Coulomb diagram shown in Fig. 5.21.

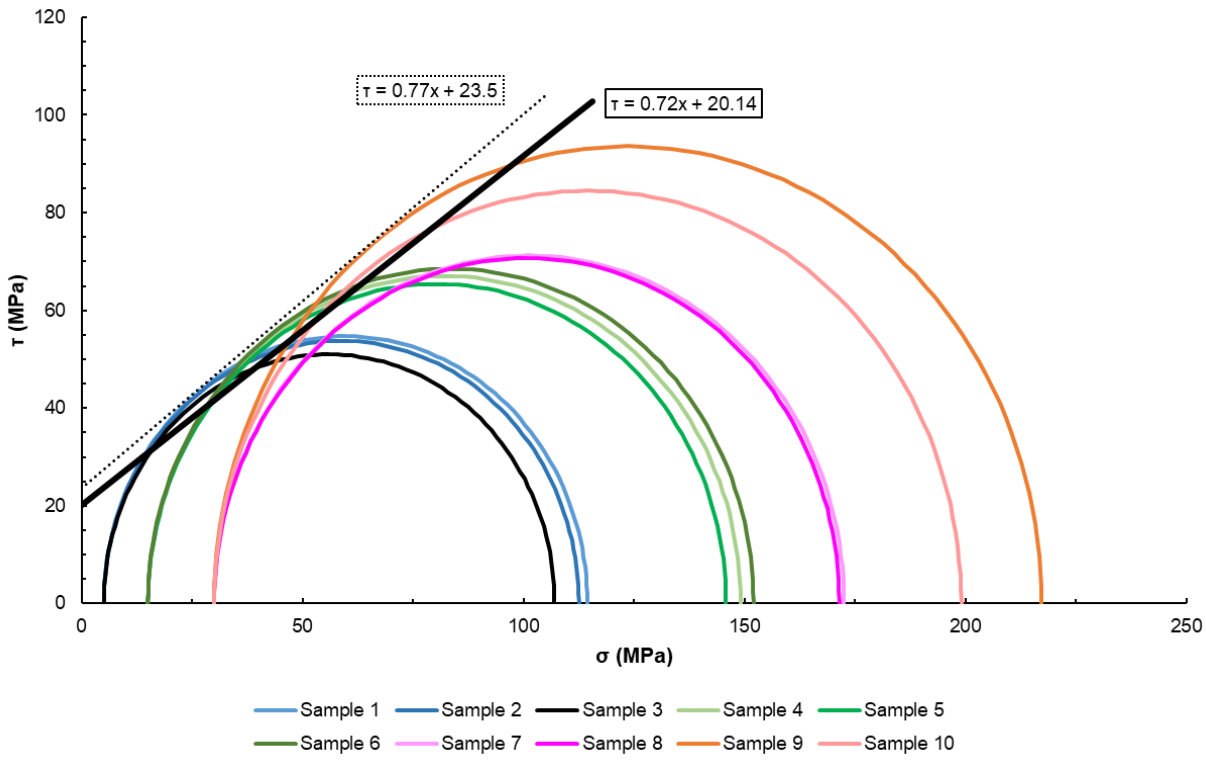

Figure 5.21. Mohr-Coulomb failure envelope for class H cement.

The black line is established based on correlations of the yield points of all samples that underwent CID testing. The dotted black line is the outer Mohr-Coulomb failure envelope. It should be noted that the minor principal stresses are equal to the confining stress during testing. Using this diagram, shear strength parameters, or cohesion and friction angle, are able to be determined for the consolidated isotropic drained tests on class H cement. The angle of internal friction describes the effect of confining stress on material strength; higher angle of internal friction denotes a larger effect of confining stress on strength (Chang et al., 2006). Cohesion is indicative of the shear strength of the cement when the normal stress acting on it is zero (Perez et al., 2015). A Mohr-Coulomb failure envelope is created using the consolidated isotropic drained triaxial test results for class H cement at the three confining stress to determine the shear strength parameters using Eq. 5.2.

$$\tau = c + \sigma_n' tan\phi \tag{5.2}$$

Where c is cohesion, ϕ is friction angle, and σ_n' is effective normal stress. Material is said to fail in shear if shear stress is greater than shear strength (Welch et al., 2019). It is determined that for the outer Mohr-Coulomb envelope, cohesion is 23.5 MPa (3,408.4 psi) and friction angle is 44.1˚ for class H cement. For the correlated envelope, cohesion is 20.1 MPa (2,921.1 psi) and friction angle is 41.3˚. Friction angle is indicative of surface morphology of the fractured material (Wyllie & Norrish, 1996). Materials with greater surface roughness have a greater resistance to shear and will result in higher friction angles (Wang et al., 2022). Angular particles can increase shear strength due to their ability to interlock with one another (Uesugi & Kishida, 1986; Wang et al., 2022). Cohesion is influenced by cementation and bonding of a material (Sullivan et al., 2011). The high cohesion and friction angle obtained within this work indicate that the cement has coarse and more angular grains on the fracture surface. The outer failure envelope is linear

for the maximum *CCS* of cement at 5.0, 15.0, and 30.0 MPa confining stress. Samples sheared at 5.0 MPa and 15.0 MPa all have a similar peak shear while the samples sheared at 30.0 MPa are somewhat less uniform. For the correlated failure envelope, it shows that all of the samples will experience shear failure except for samples 7 and 8, which are tested at 30.0 MPa confining stress.

5.4.3 Shear Failure

Of the samples sheared at 5.0 MPa confining stress, samples 1 and 3 very clearly exhibit shear fracturing as seen by the angle of fracture in Fig. 5.7, meaning that the maximum stress during shear is in the vertical direction. Sample 1 had an average fracture angle of 59.5˚ while sample 3 proved to have an average fracture angle of 116.4˚; these samples indicate that at higher angle of fracture, fractures are more uniform and exhibit fewer secondary fractures which is similar to the results obtained on testing of marble and sandstone (Gong et al., 2020). Sample 2, however, has a different type of failure mode, extensional fracturing, as evidenced by the fracture angle seemingly being nearly horizontal as well as the sharp negative decline post-peak on the stress-strain curve.

Samples tested at 15.0 MPa confining stress, shown in Fig. 5.7 (d), (e), and (f), all experienced shear fractures. Samples 5 and 6 have linear fracture planes while sample 4 experienced wing cracks around the shear fracture, as seen in Fig. 5.7 (d). Wing cracks occur at the ends of pre-existing microcracks within the material and propagate in the direction of the major principal stress, which in this case, is vertical stress (Zhang & Li, 2019).

Test results for those samples sheared at 30.0 MPa confining stress to be somewhat irregular as can be seen in Fig. 5.7. (g), (h), (i) and (j). Samples 8, 9, and 10 experienced shear fracturing while sample 7 exhibits extension fracturing. From Fig. 5.4, the stress-strain curve for sample 7

is significantly steeper and fluctuation of strain measurements pre-shear can be observed, which could be the cause of the extension fracture.

5.4.4 Poroelastic Constant Determination

As discussed in chapter 4 of this work, the poroelastic constant, or Biot coefficient, is an important parameter for wellbore modeling and is frequently taken to be 1. The parameters used to calculate the Biot coefficient can be either calculated or determined experimentally. Experimental determination of the Biot coefficient was discussed in chapter 4 of this work and was done using hydrostatic compression testing results, where the Biot coefficient can be calculated using the bulk and solid bulk modulus of a material. Solid bulk modulus is a relatively constant material parameter and this can be seen in the previous chapter (Dung et al., 2017). Bulk modulus, *K*, is related to *YM* and *PR* and can be calculated using the following Eq. 5.3:

$$K = \frac{E}{(3 - 6\upsilon)} \tag{5.3}$$

Utilizing the *YM* and *PR* values obtained via CID testing, *K* is calculated for all tested cement samples and used to calculate the Biot coefficient in conjunction with the solid bulk moduli found in chapter 4. Average solid bulk modulus is 52.2 GPa, and the calculated bulk modulus and Biot coefficient for the class H cement samples that underwent CID testing is shown in Table 5.4.

Table 5.4. Calculated K and Biot coefficient for all tested samples.

Sample	YM (GPa)	PR	K (GPa; Calculated)	Biot (Calculated)
1	18.2	0.2	9.5	0.8
2	17.4	0.2	8.5	0.8
3	17.1	0.2	8.6	0.8
4	16.2	0.2	8.4	0.8
5	15.7	0.2	8.4	0.8
6	17.1	0.2	8.4	0.8

7	21.0	0.2	11.8	0.8
8	17.0	0.2	8.3	0.8
9	16.1	0.2	8.9	0.8
10	13.5	0.2	6.6	0.9

As shown in chapter 4, hydrostatic compression testing on the three class H cement samples is found to range between 0.80-0.82. Most of the calculated bulk modulus and Biot coefficients proved similar to those obtained via hydrostatic compression testing with the exception being samples 7 and 10, both of which were tested at 30.0 MPa confining stress. While there is some deviation, the samples all exhibited a poroelastic constant less than one and were similar to results obtained for class G cement.

5.4.5 Microscopy

From Fig.s' 5.8, 5.9, and 5.10, it can be seen that there are a number of microfractures that occur at the point where the sample was sheared. There are also a number of unhydrated cement grains, which implies that the bonds around these grains are less than fully hydrated cement and could have some affect as to why the sample sheared at the location and manner it did. From Fig. 5.8 (a) and (b), there are a number of microcracks present; voids are also present within the sample and the voids are between 5.0-25.0 microns in diameter. Partially hydrated cement is also seen with the center of these grains containing unhydrated cement surrounded by C-S-H. A majority of the sample is smooth CH. In Fig. 5.9, long, thin microcracks were visible at multiple points in the sample. CH is the most prevalent structure at this point and there were voids present in areas without CH. Small amounts of C-S-H were also visible as smooth particles that are slightly darker than the CH. A description of the microstructure seen at this sample location is shown in Fig. 5.9 (b). In Fig. 5.10 (a) and (b), a BSE image of a third location on the fracture surface is shown along with a description of the microstructure. CH is the most common component in

most of the sample, in both high and low concentrations. Microcracks are present in areas with high CH concentration. C-S-H and unhydrated cement can also be seen and there are a high amounts of voids at this location.

From Fig. 5.11 (a) and (b), it can be seen that the sample location has a composition made up primarily of CH. Microcracks are visible and are primarily within the CH. There are multiple partially hydrated cement particles, which the unhydrated and C-S-H are labeled in Fig. 5.11 (b). There are a small amount of voids at the sample location, and a majority of the voids have a diameter below 25 microns. Fig. 5.12 (a) show a second location on the sample 9 fracture surface and Fig. 5.12 (b) describes the microstructure of the image. A large partially hydrated cement particle, which has unhydrated cement that is approximately 100.0 microns in diameter, can be seen as well as a thin layer of C-S-H surrounding the unhydrated grain. Platy CH is also dispersed within the sample location. A microcrack can be seen and follows the shape of the partially hydrated cement particle. Voids are not highly present as most of the dark areas are part or a continuation of the centralized microcrack. Fig. 5.13 (a) and (b) show a third sample location and a description of the microstructure on sample 9's fracture surface. There are numerous partially hydrated cement particles at this location as well as platy CH. Microcracks are found to be around the C-S-H layer of the partially hydrated cement. There are small voids, less than 10 microns, scattered throughout the location.

From Fig. 14 (a) and (b), it can be seen that CH is the largest component of this location with small amounts of C-S-H also present. A large and wide microcrack, approximately 300.0 microns and length and up to 25 microns wide at some points, can be seen within this point of study. Thinner microcracks can be seen branching off the large microcrack. Small voids are also seen. Fig. 15 (a) and (b) shows the presence of CH, C-S-H, and partially hydrated cement. The

CH is well dispersed. Microcracks are present but are primarily short and thin. The BSE image shown in Fig. 5.16 (a) and (b) shows a large concentration of CH with some C-S-H dispersed throughout the surface. Microcracks are visible, but are short and thin; they are predominantly within the CH.

BSE image 5.17 (a) and (b) show a highly consistent composition within the surface location. There are a number of partially hydrated cement particles, but the unhydrated portion is small and the outer C-S-H layer constitutes for most of these structures. There are small voids within the sample and most are below 10 microns in diameter. Microcracks are present with a majority being thin and short; a larger microcrack can be seen on the left side of the sample that is approximately 200 microns in length and is wide in some areas and thin in others. Fig. 5.18 (a) and (b) shows a highly consistent composition with littler variation in bright- or darkness. C-S-H is the main constituent in this location and minimal microcracks are present. While voids are seen, they are small in diameter; most are less than 10.0 microns in diameter. Partially hydrated or unhydrated cement particles are not seen indicating a high degree of hydration. From Fig. 5.19 (a) and (b), an unhydrated cement grain can be seen and is indicated by its bright appearance. Voids, most of which are below 10 microns in diameter, are seen throughout the sample. Partially hydrated cement particles are also seen throughout the sample, with the unhydrated portion being much smaller than the C-S-H shell. There are some microcracks, and they are short in thin, most being less than 50.0 microns in length.

It can be determined that the microstructure at the fracture surface does have some differences when compared to the intact material post CID testing. Sample 1 fracture surfaces shown in Fig.s' 5.8, 5.9, and 5.10 show large areas of CH with longer, more connected microfractures. BSE images of sample 1 intact material show that CH is still present, but may not be as

concentrated (Fig.s' 5.14, 5.15, 5.16). Surface composition for the intact material is much more heterogeneous than that of the fractured surface.

From the fracture surface of sample 9, it can be seen that there are high amounts of CH, partially hydrated cement, and wide microcracks (Fig.s' 5.11, 5.12, 5.13). The unhydrated center of the partially hydrated cement constitutes a majority of the particle with the C-S-H outer layer being much smaller. Microcracks are prevalent around or near the partially hydrated particles due to the lack of hydration structures that have formed. The amount of partially hydrated and unhydrated cement can lead to weaker zones more prevalent to fracturing. BSE images for the intact material of sample 9 show a much more homogenous composition. There is less CH within this material and C-S-H is more prevalent. While partially hydrated grains are present to a certain degree, there are not many partially hydrated or unhydrated particles. This indicates that the material is able to achieve a higher degree of hydration and is less susceptible to failure due to the microstructures that were formed. Less microcracking was visible within the intact material meaning that the shear fracture may not have greatly affected the mechanical properties throughout the sample.

EDS results obtained from three fractured surface locations are in agreement, indicating that the chemical composition is homogenous at the sample surface locations as shown in Fig. 5.20. From the cement mill test report provided by Central Plains Cement for the batch used to create the samples, calcium oxide, silicon dioxide, ferric oxide, aluminum oxide, sulfur trioxide, and magnesium oxide are the predominant compounds within the cement clinker. There are also minimal amounts of free lime and insoluble residue within the clinker. EDS analysis is in agreement with the information provided within the mill report, with high amounts of oxygen at each location as well as lesser amounts of calcium, iron, aluminum, sulfur, magnesium, and

silicon. Sodium is also present in smaller quantities, likely from the free lime content. The one element that is not in agreement with the listed compounds on the mill report is potassium, indicating that it could be considered insoluble residue. Gold and palladium are also detected in the EDS analysis due to the sample being sputter coated in these elements and are not considered as part of the chemical composition of the cement.

5.5 Conclusions Found from CID and Shear Analysis

The results for this portion of the work done details CID testing on class H wellbore cement to obtain a variety of mechanical properties and fracture mechanisms. From the results, it can be seen that class H cement yielded fairly similar *CCS* values at varying confining stress. It can also be seen that average *YM* and *PR* were analogous for all tested samples. The high cohesion and friction angle seen from testing indicate that the cement has coarse and more angular grains on the fracture surface, which is corroborated by microscopy analysis. The results obtained in this chapter are in good agreement with various rock types thus supporting the theory that cement can be treated as a poroelastic material. The plasticity moduli determined for the samples increased with increasing confining stress thus indicating that the transition from ductile to brittle behavior occurs much faster at higher pressures. Using the *YM* and *PR* values found from CID testing, the bulk modulus can be calculated and using the solid bulk modulus found previously, the Biot coefficient can be calculated. The calculated results are in good agreement with those values determined experimentally. SEM BSE images for the fractured surfaces and intact material show that both the fractured and intact material have CH, but the intact material has less concentrated and more widespread CH and has less microcracking. The fractured surfaces also have more partially hydrated cement with high amounts of unhydrated cement. It should be noted that the less linear the stress-strain relationship of the samples, the more likely that microcracking is

occurring within the sample during CID testing (Mechtcherine & Müller, 2001). Further SEM analysis should be done to verify this phenomena. EDS results are in agreement with the mill report provided by Central Plains Cement Company for the batch used to make the samples, indicating the carbonation or outside contamination have not likely occurred. Results from this work are important in that they can be used for designing a cement slurry for specific downhole conditions and understanding how the cement will behave with variations in pressure. Due to the cement being cured past the early hydration period, the results are more applicable to real-world scenarios and can provide insight into long-term cement behavior as well.

Chapter 6: Cuttings Effect on Cement Mechanical Properties

To understand the mechanical properties of wellbore cement with shale and eventually, drill cuttings, various studies are conducted to understand how these properties change with the addition of shale in the short-term and after the early hydration period takes place.

6.1. Cuttings Disposal in Cement: Investigation of the Effect on Mechanical Properties

Offshore, drill cuttings may be discharged, cleaned and discharged, or transported onshore to be recycled. Such options are governed by the type of drilling fluid used and can prove to be considerably costly. Additives have been used in cement for enhancing mechanical properties thus ensuring/maintaining wellbore integrity. Pozzolanic materials such as fly ash and metakaolin have been seen to react with calcium hydroxide ($Ca(OH)_2$) resulting in additional calcium silicate hydrate formation thus enhancing the mechanical properties of wellbore cement, which begs the question: why not cuttings? The use of drill cuttings as a cement additive may prove beneficial in more ways than one in that cuttings would be environmentally friendly, reduce the cost for removal, and potentially eliminate the need for other additives while maintaining the mechanical integrity of the cement. In this study, various sizes and quantities of

Woodford shale fragments in sizes from 100.0 mm down to 100.0 nm are added to class H cement and mechanical stability was determined through unconfined compressive strength (*UCS*) testing. The results of this study show that the addition of shale is able be used as an additive in cement without significantly altering the mechanical properties. This work is the first step in evaluating disposal of cuttings and cutting derived products in cement.

6.1. Introduction

Drill cuttings are an inevitable byproduct associated with drilling a well. Cuttings are a combination of different sized geological material and drilling fluid, which can be either water based (WBM), oil based (OBM), or synthetic (SBM) (Henry et al., 2017). Two of the biggest issues regarding drill cuttings is cleaning and disposal. Cleaning and disposing of cuttings is a costly operation and alternative methods for the use of drill cuttings have become widely investigated. Depending on the drilling fluid used, cuttings are required to undergo cleaning in order to remove any remaining mud prior to disposal. Methods for cleaning drill cuttings include but are not limited stabilization/solidification (s/s) treatment (Leonard & Stegemann, 2010), thermal desorption (Huang et al., 2018), microemulsions (de Castro Dantas et al., 2019), microwave treatment (Petri et al., 2019), bioremediation (Somee et al., 2018), and mechanical equipment (Wu et al., 2019).Various methods used for cuttings disposal include the use of cuttings in spud mud (Taghiyev et al., 2015), offshore disposal, ship-to-shore/onshore disposal (Stanciu et al., 2016), and reinjection into the subsurface (Reddoch, 2000).

Cementing a well is crucial for establishing wellbore integrity and it is necessary that the cement be able to withstand downhole conditions. To ensure this, cement additives are used to fine-tune cement mechanical properties. In the past, cements with a high *UCS* were thought to be ideal for achieving and maintaining zonal isolation and well integrity (Li et al., 2015). While this cement

design may have been used in conventional wells, it is used less in unconventional wellbores. In many unconventional wells, conventional cement systems are not favorable due to higher temperatures and pressures. To account for these conditions, ductile cement is favorable as opposed to high strength. Ductile cement is able to undergo numerous loading cycles and is less likely to permanently deform under severe downhole conditions (Tabatabaei et al., 2019). This is important in unconventional wells where not only are pressure and temperature fluctuations occurring, but also human factors such as recompletions. One way to address this issue is to design a cement that is able to achieve high UCS, and a low Young's Modulus (*YM*) (Deshpande et al., 2019). Lower *YM* is important for low cement ductility (Petty et al., 2003). Low Poisson's ratio (PR) is optimal for a cement system, with conventional cements having a *PR* of approximately 0.2 (Verba et al., 2017). To engineer this balance, cement additives have been widely studied to better understand the effect that they have on a cements mechanical properties (Jafariesfad et al., 2020; Li et al., 2015).

Pozzolanic materials, which are highly siliceous and aluminous materials, are one type of cement additive that have an effect on cement mechanical properties (Salehi et al., 2016). Examples of pozzolanic material include metakaolin, fly ash, and slag. These materials work to fill void space within the cement and expedite cement hydration (Xiaoyu, et al., 2018). The size and texture of the pozzolanic material plays a significant role in hydration and nucleation but requires that the material is uniformly dispersed (Lapeyre et al., 2019). In concrete, metakaolin impacts the strength in three ways: the filler effect, expedited hydration, and pozzolanic reactions with calcium hydroxide (Wild et al., 1996). Ramezanianpour & Jovein (2012) found that adding metakaolin to concrete, long-term compressive strength proved to be higher than concrete without metakaolin. Pozzolanic materials high in silica, aluminum oxide, and iron oxide react

much more quickly than conventional cement additives to calcium hydroxide thus establish a higher *UCS* in less time (Pernites et al., 2018).

The objective of this work is to evaluate how the size and quantities of shale cuttings added to cement affects *UCS, YM*, and *PR*. The shale cuttings investigated are Woodford shale, a source rock and an unconventional reservoir found in the Anadarko Basin in Oklahoma (Johnson & Cardott, 1992). Woodford shale has a similar composition to other pozzolanic materials in that it is silica-rich (Cardott, 2012). Having the ability to integrate cuttings into a cement system could reduce the cost for cuttings disposal while still allowing well integrity to be achieved and maintained throughout the life of a well. The use of cuttings as a cement additive also has environmental benefits in that drilled geomaterial is being returned to the subsurface rather than having to be transported or discharged to the seafloor.

6.1.2. Methodology

Class H oilwell cement provided by Central Plains Cement Company is used to make the samples. Woodford shale is collected from an outcrop in Murray County, Oklahoma. Dry shale is ground to achieve millimeter, micron, and submicron particles with the submicron particle sized being achieved with an EMAX nanogrinder. The term submicron refers to particle sizes less than one micrometer. For the three different sizes, shale is added in 5%, 10%, and 15% increments by weight of cement (BWOC). The samples are prepared according to ASTM standard D7012-14 and deionized (DI) water is used for all sample sets. Halliburton D-AIR 5000 is used to reduce air within the cement. For each case, three replicate samples are made. Table 6.1 shows the cement composition used in this study. Water-solids (w/s) ratio is kept constant at 0.38 and the various sizes of shale are added at 5%, 10%, and 15% intervals. The samples are

named based on the percentage of shale and size of the shale particles (i.e. 5% mm means cement sample with 5% millimeter sized shale particle added).

Table 6.1. Cement slurry composition.

	Mass in Solution (%)	Mass BWOC (%)
DI Water	175.8	-
Class H Cement	462.5	-
Shale	Varies	Varies
D-Air 5000	0.7	0.2
Slurry Density (g/cc)	2.0	
Slurry Weight (ppg)	16.5	

After the cement is mixed it is placed into cylindrical molds with 4.0-inch height and 2.0-inch diameter and cured at ambient conditions for 24 hours. The samples are removed from the molds and placed into a sodium hydroxide brine water bath prior to being placed into a 150˚F oven for 7 days. The samples are then removed from the water bath, cut, and both ends of the cement cylinder are polished to ensure a flat surface for testing. The samples are compressed along the vertical axis of the cylinder using an Instron 600DX compression only load frame with internal vertical strain measurements and equipped with an Epsilon diametral extensometer to measure horizontal strain. A strain rate of 0.04 mm/min is used during the testing process. The samples are visually inspected after failure to determine the orientation of the failure plane and type of failure. From the testing, it is seen that all samples exhibit tensile failure.

6.1.3. Results and Discussion

Fig. 6.1 shows a typical stress-strain curve obtained via *UCS* testing. The right portion of the x-axis is representative of vertical strain while left of the x-axis axis is horizontal strain. For all

plots, *UCS* is selected at the point where compressive strength is the greatest. *YM* is found for all samples by taking the tangent at 50% of the *UCS* vertical strain curve. *PR* is determined by taking the slope of the tangent of *UCS* and horizontal strain at 50% of the *UCS*, then dividing this by *YM*.

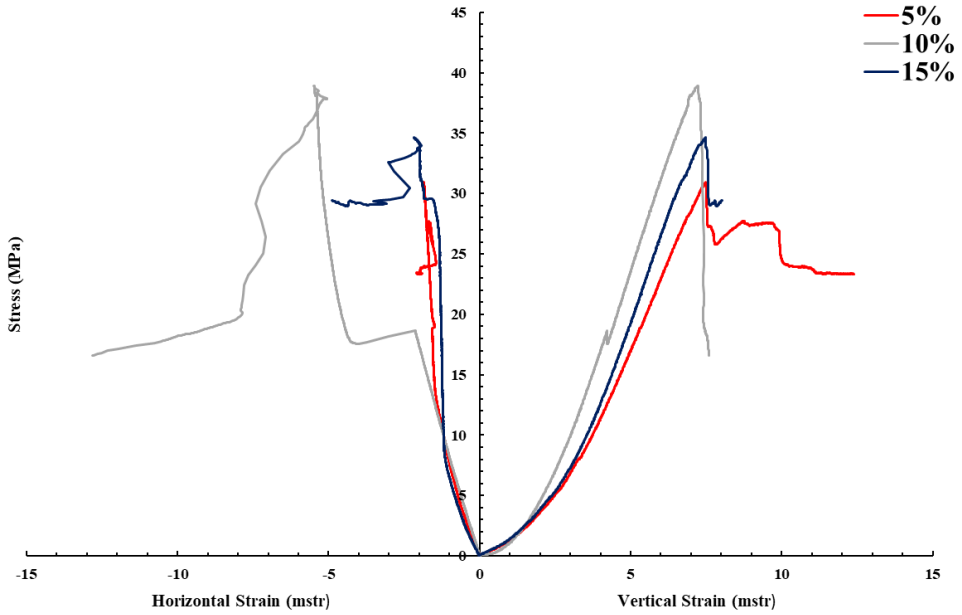

Figure 6.1. Stress-strain curves obtained from UCS testing for the 5%, 10%, and 15% millimeter samples. The highest UCS shown is for the sample with 10% shale.

Some of the tests results had an unexpected sudden increase of horizontal strain prior to reaching the peak vertical stress determined to be *UCS*, as is seen in Fig. 6.2.

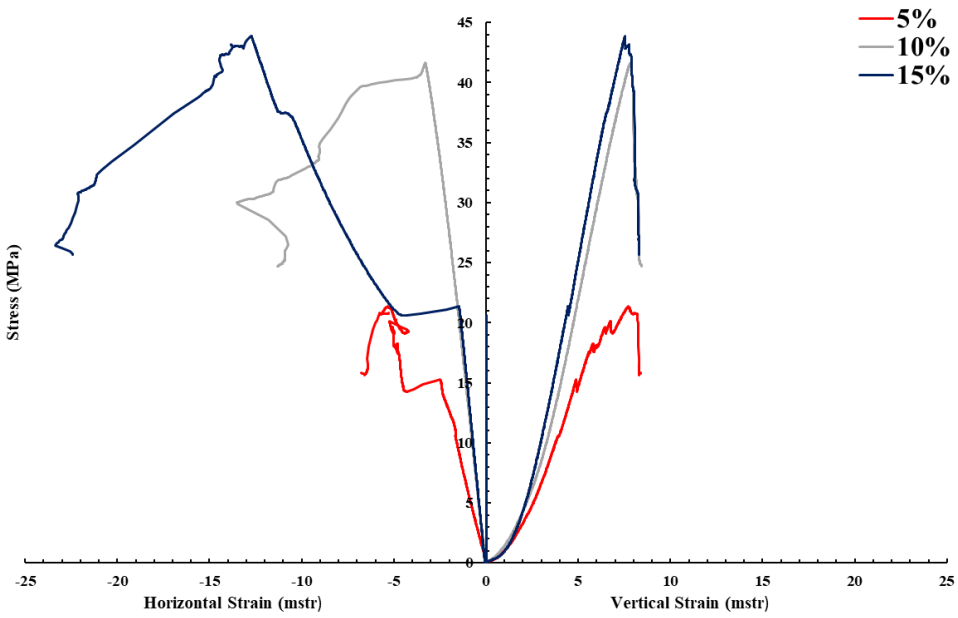

Figure 6.2. Stress-strain curves obtained from UCS testing for the 5%, 10%, and 15% samples with the highest UCS for micron samples. The highest UCS shown is for the sample with 15% shale.

To compensate for this, *YM* and *PR* are found using stress-strain readings before this decrease occurred.

Fig. 6.3 (a) shows a 5% submicron cement sample after *UCS* testing. Fig. 6.3 (b) shows a 10% millimeter shale sample after being tested. From Fig. 6.3 (a) and (b), there is evenly distributed shale within the sample. It has been known that particle size distribution is of the utmost importance when conducting mechanical testing of cement additives. From Fig. 6.3 it is seen that the samples exhibit tensile fracturing rather than shear fracturing.

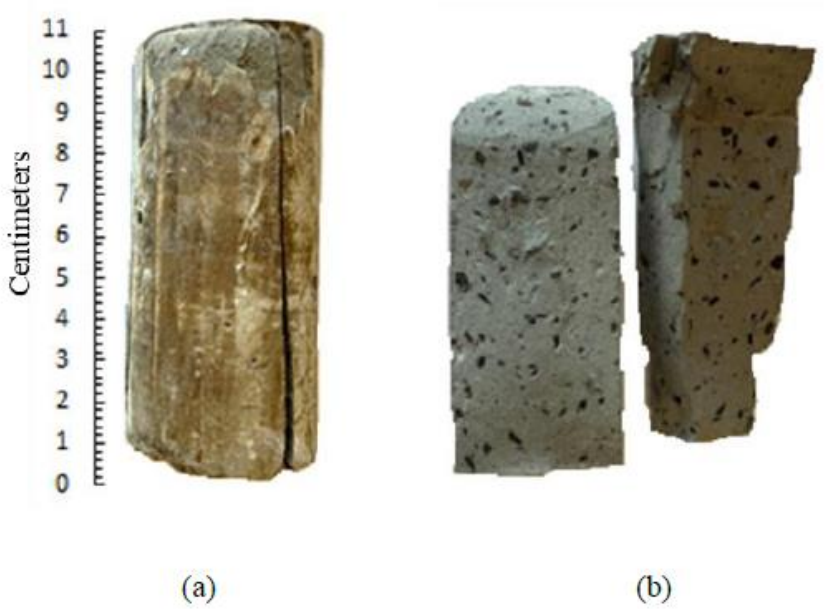

Figure 6.3. (a) A 5% submicron cement sample after UCS testing. (b) A 10% millimeter sample after UCS testing.

UCS, YM, and *PR* test results are shown in Table 6.2 as well as fracture orientation and fracture type. The highest *UCS* observed, 42.7 MPa, is seen in a 10% micron sample while the lowest *UCS* exhibited is 6.1 MPa associated with a 5% micron sample. For the millimeter and micron sample sets, the addition of 15% shale yielded, on average, the highest *UCS*, while the 5% shale samples obtained the maximum *UCS* values for submicron shale addition. On average, the 5% micron samples produced the lowest *YM* while the 5% millimeter samples yielded the highest. *PR* is highest in a 5% submicron sample and lowest in a 5% micron, 5% millimeter and 15% millimeter samples. There is significant scatter for *UCS, YM,* and *PR* results as shown from standard deviation.

Table 6.2. UCS test results for base case, millimeter, micron, and submicron samples.

	Sample #	% Shale	Length (in)	Dia. (in)	UCS (MPa)	Ave.	Std. Dev.	YM (GPa)	Ave.	Std. Dev.	PR	Ave.	Std. Dev.
Base	1	0	3.4	1.5	35.2	29.9	3.8	7.5	6.0	1.6	0.1	0.3	0.2
	2	0	3.5	1.5	27.9			6.7			0.6		
	3	0	3.3	1.5	26.6			3.7			0.3		
Millimeter	1	5	3.4	1.5	30.9	21.3	10.1	5.8	4.4	1.6	0.1	0.1	0.0
	2	5	3.3	1.5	25.7			5.3			0.1		
	3	5	3.4	1.5	7.4			2.2			0.0		

	1	10	3.3	1.5	11.0			2.8			0.2		
	2	10	3.4	1.5	24.1	17.9	5.4	5.6	4.8	1.4	0.2	0.4	0.2
	3	10	3.4	1.5	18.6			6.0			0.7		
	1	15	3.4	1.5	34.6			6.8			0.1		
	2	15	3.5	1.5	11.8	23.4	9.3	2.9	4.3	1.8	0.3	0.2	0.1
	3	15	3.5	1.5	23.9			3.2			0.2		
	1	5	3.5	1.5	14.3			3.5			0.5		
	2	5	3.5	1.5	21.3	13.9	6.2	3.8	3.2	0.7	0.4	0.3	0.2
	3	5	3.4	1.5	6.1			2.2			0.1		
	1	10	3.2	1.5	41.6			7.6			0.5		
Micron	2	10	3.4	1.5	20.0	27.7	9.8	7.6	6.7	1.3	0.6	0.5	0.1
	3	10	3.4	1.5	21.6			4.9			0.3		
	1	15	3.3	1.5	24.1			7.0			0.5		
	2	15	3.5	1.5	42.7	31.5	8.7	7.7	6.9	0.7	0.4	0.4	0.0
	3	15	3.4	1.5	30.4			6.0			0.4		
	1	5	3.3	1.5	32.1			6.5			0.5		
	2	5	3.3	1.5	27.9	34.0	5.9	3.9	5.9	1.4	0.9	0.7	0.2
	3	5	3.4	1.5	41.9			7.3			0.6		
	1	10	3.3	1.5	9.8			2.9			0.2		
Submicron	2	10	3.2	1.5	17.8	16.5	5.0	3.4	4.1	1.3	0.3	0.3	0.1
	3	10	3.4	1.5	21.8			5.9			0.4		
	1	15	3.8	1.5	39.1			6.2			0.6		
	2	15	3.6	1.5	37.3	31.2	10.0	6.6	5.4	1.4	0.3	0.4	0.2
	3	15	3.8	1.5	17.1			3.4			0.2		

Single-factor ANOVA tests were performed to better understand the significance of shale size and quantity to cement and the results are shown in Table 6.3.

Table 6.3. Single-factor ANOVA results for the class H cement samples containing various sizes and quantities of shale cured for 7 days.

Shale Size		Assumption	Groups	Count	Sum	Average	Variance	P-Value
Millimeter		Amount of millimeter shale has no impact on mechanical properties.	0	3	89.7	29.9	21.5	0.5
			5	3	64.0	21.3	152.4	
			10	3	53.7	17.9	43.3	
			15	3	70.3	23.4	130.1	
		Concentration does not matter for millimeter samples.	5	3	64.0	21.3	152.4	0.8
			10	3	53.7	17.9	43.3	
			15	3	70.3	23.4	130.1	
Micron		Amount of micron shale has no impact on mechanical properties.	0	3	89.7	29.9	21.5	0.2
			5	3	41.7	13.9	57.9	
			10	3	83.2	27.7	144.9	
			15	3	94.5	31.5	114.3	
		Concentration of shale does not matter for micron samples.	5	3	41.7	13.9	57.9	0.2
			10	3	83.2	27.7	144.9	
			15	3	94.5	31.5	114.3	
Submicron			0	3	89.7	29.9	21.5	0.1

		Amount of submicronshale has no impact on mechanical properties.	5	3	101.9	34.0	51.6	
			10	3	49.4	16.5	37.3	
			15	3	93.5	31.2	149.2	
		Concentration of shale does not matter for submicron samples.	5	3	101.9	34.0	51.6	0.1
			10	3	49.4	16.5	37.3	
			15	3	93.5	31.2	149.2	

Mechanical properties of class H and G cements are previously reported (Wise et al., 2020). Class G cement is included since the only differences between the two are water specification requirements and texture (Bensted, 2002). An example comparison between *UCS* values for various shale size/quantity to *UCS* found from previously reported literature is shown in Fig. 6.4. Standard deviation error bars have been included to show the range of the data.

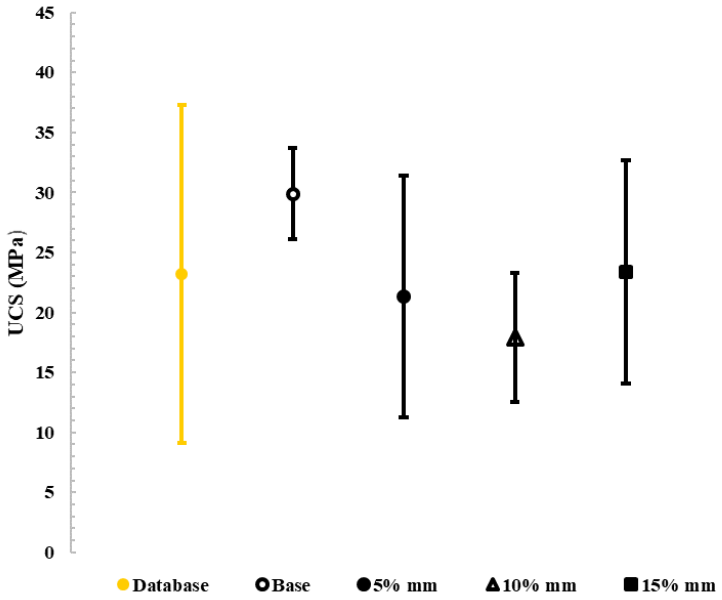

Figure 6.4. Experimentally determined UCS results for all millimeter samples. The yellow sample represents average UCS and standard deviation data obtained from previous literature.

A comparison of previously reported *UCS* data to the base case, millimeter, micron, and submicron sample sets is shown in Fig. 6.5.

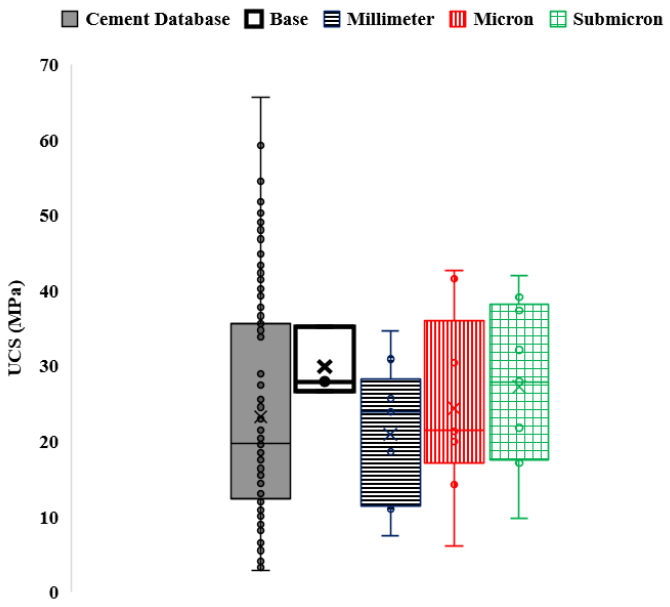

Figure 6.5. Comparison of cement UCS obtained from previous literature to the UCS of cement with varying shale particle size addition; x is the mean of the datasets.

Average *UCS* for the millimeter samples is slightly below the average of previously published values (Wise et al., 2020). It is interesting to note that the base case achieved a higher average *UCS* than all of the millimeter samples and two of the micron sample sets. This could imply that the addition of these sizes of shale may have an adverse effect on strength. For the millimeter, micron, and submicron sample sets, the addition of shale at 15% BWOC was higher the average *UCS* from previously reported. When looking at the effect of shale size on *UCS*, the addition of shale, at any size, did not alter *UCS* when compared to previous studies. All sample sizes exhibited, on average, higher *UCS* than those previously reported as indicated by the upper and lower bounds in Fig. 6.5. While the plots appear to show that UCS values for the samples do not have a large effect on *UCS*, the p-value obtained indicates the opposite. For the millimeter, micron, and submicron samples, the p-values are above 0.05, and the amount of shale and concentration does have an effect on UCS. This is contradictory to what is seen in Fig.s' 6.4 and 6.5 where it appears that the addition of shale to cement has little effect on *UCS.*

An example comparison between *YM* obtained from varying shale size/quantity to *YM* obtained from previously reported literature is shown in Fig. 6.6. Standard deviation error bars have been included to show the range of the data.

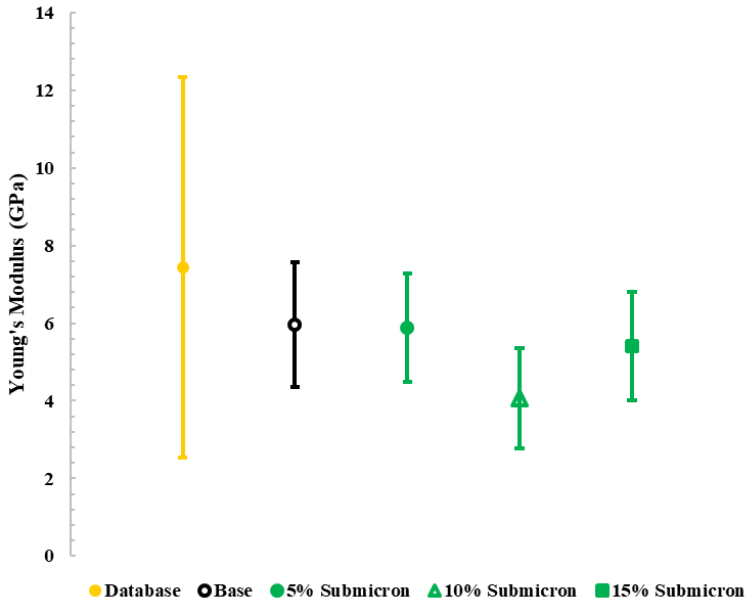

Figure 6.6. Experimentally determined YM results for submicron shale addition varying from 0-15%. The yellow sample represents average YM and standard deviation data obtained from previous literature.

A comparison of previously reported *YM* data (Wise et al., 2020) to the base case, millimeter, micron, and submicron sample sets is shown in Fig. 6.7.

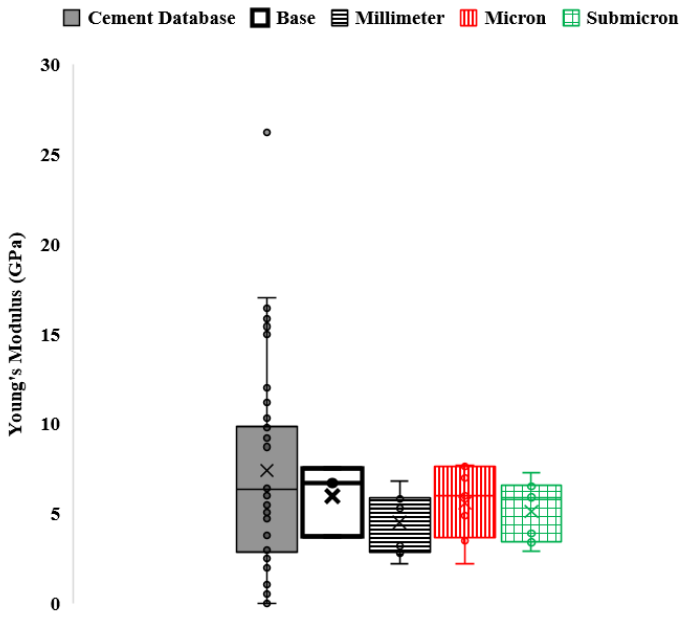

Figure 6.7. Comparison of cement YM obtained from previous literature to the YM of cement with varying shale particle size addition; x is the mean of the datasets.

Average *YM* for all the samples containing shale is lower than the average database *YM*. A lower *YM* is desirable when designing wellbore cement and after a seven day curing time, shale addition at any size or quantity could allow for a lower *YM* to be achieved. The addition of 5% micron sized shale particles produced the lowest average *YM* results while the millimeter samples produce the lowest *YM* in comparison to the other particle sizes. From Fig. 6.7, *YM* for all shale size addition yielded comparable results to previously reported data. All sample sizes aside from the base case yielded lower *YM* values than those previously reported as indicated by the upper and lower bounds of the box-and-whisker plots in Fig. 6.7. While the plots do not show the effect that shale amount and concentration have on the *YM*, the ANOVA tests validate that they do have an effect on the *YM*.

A comparison between *PR* obtained from varying shale size/quantity to *PR* obtained from previously reported literature (Wise et al., 2020) is shown in Fig. 6.8. Standard deviation error bars have been included to show the range of the data.

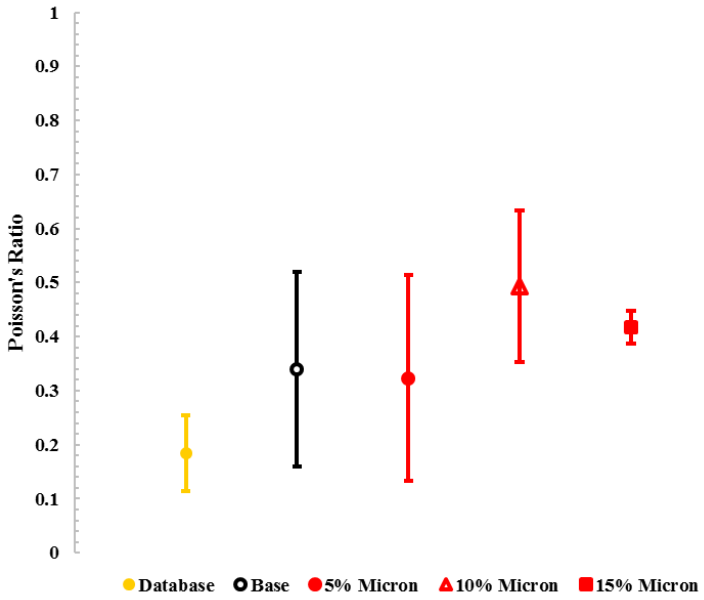

Figure 6.8. Experimentally determined PR results for micron shale addition varying from 0-15%. The yellow sample represents average PR and standard deviation data obtained from previous literature.

A comparison of previously reported *PR* data to the base case, millimeter shale, micron shale, and submicron shale sample sets is shown in Fig. 6.9.

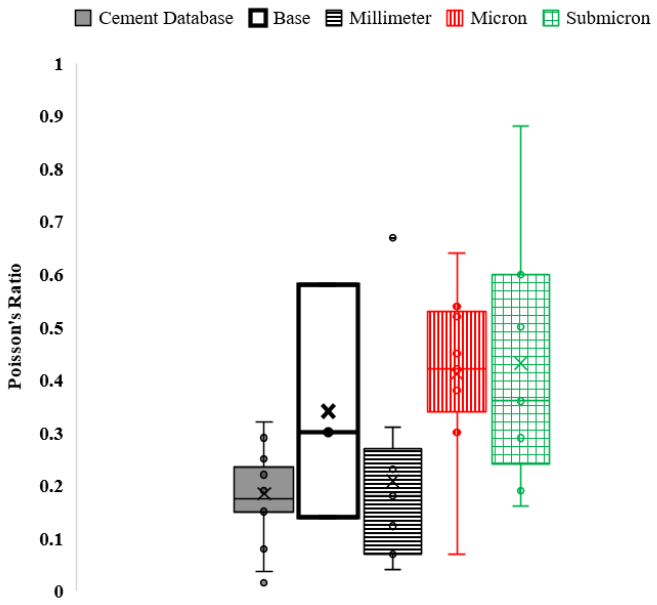

Figure 6.9. Comparison of cement PR obtained from previous literature to the PR of cement with varying shale particle size addition; x is the mean of the datasets.

Average *PR* for all samples containing shale as well as the base case samples is higher than the *PR* for conventional wellbore cement. A cement with a high *PR* has the potential to reduce the stresses a cement experiences and could help to establish and maintain the integrity of the cement (James & Boukhelifa, 2006). From the results, the addition of shale allow for higher *PR* to be obtained thus potentially having a positive impact on wellbore integrity. The addition of micron and submicron size shale has the largest impact on *PR*. 5% submicron shale yielded the most desirable average *PR*. The submicron sample set showed a high *PR* range and could be attributed to human or equipment error. From Fig. 6.9, all sample sets containing shale exhibited, on average, a higher *PR* than previously reported cement data and this is in agreement with the ANOVA tests that indicate that the amount and concentration of shale added to cement will have an effect on the *PR*. The submicron sample set showed a significantly high *PR* range and could be attributed to human or equipment error.

All of the tested samples exhibited *UCS* values comparable to those determined from previous literature. *YM* values are also within the range of previously reported values, including the upper and lower bounds. Increased *PR* is seen with the addition of shale, regardless of particle size and quantity. Statistical analysis shows that for all size of shale added to the cement, the amount and concentration will effect the mechanical properties, implying that the trends seen on the plots are misleading and do not accurately represent what is occurring.

From these results, addition of shale could impact the mechanical properties and allow for a more desirable wellbore cement. While further research is needed to conclusively determine how shale and/or cuttings effect the mechanical properties of cement, this research shows promising results in that the parameters most often considered when designing cement are elevated with the addition of shale. It should be noted that these values could be attributed to the curing time and

early cement hydration not having been achieved. Longer curing time is shown to lead to an evolution of mechanical properties (Shadravan et al., 2015). Early cement hydration is known to conclude after twenty-eight days, which could be a reason why the high spread of data since small change in level of hydration affect the development of mechanical properties and give larger data spread. The other potential cause of the variation in the data is that the cutting materials is causing clustering of weak spots in the shale causing it to prematurely break. From visual inspection of the samples the cutting fragments are evenly distributed, but this needs to be further evaluated.

6.1.4. Conclusions

This study evaluated the use of integrating cuttings into oil well cements to reduce costs and improve environment of cuttings disposal. Based on the *UCS* testing results of adding of shale at 5, 10 and 15 weight % concentrations and with 7 days curing period the following conclusions can be drawn:

- The addition of shale to cement does not significantly alter the *UCS* but does lower *YM* and increase the *PR* of the cement. It can be concluded that shale particle size could, in fact, affect the mechanical properties of cement though further testing is critical to accurately understand to what extent.
- The amount of shale added to cement is also significant when investigating how shale/cuttings affect cement mechanical properties.

The results show that there are no negative impacts on the cement mechanical properties and using shale/cuttings as a cement additive could have the potential for being a cost effective and environmental beneficial method to dispose cuttings. Further testing is needed to validate the results. The samples within this work were cured for seven days and should be repeated to

further validate the results. The shale that was used was dry and an investigation into how oil-wet samples affect cement mechanical properties will be conducted.

6.2. Cuttings Addition to Wellbore Cement and Their Effect on Mechanical Properties Over the Early Hydration Period

Mitigation of greenhouse gas emissions is becoming a significant factor in all industries. Cement manufacturing is one of the industries responsible for greenhouse gas emissions, specifically carbon dioxide emission. To combat the emissions produced from cement manufacturing, many areas that utilize cement have begun investigating ways to minimize the amount of cement used for substitute or cement replacement material. Pozzolanic materials have long been used as cement additives or cement replacement material due to the pozzolanic reaction that occurs when hydrated and forms a cementitious material similar to that of cement. Shale is a pozzolanic material that is found globally both on the surface of the Earth and below it; with an increase in the number of target reservoirs being shale, drill cuttings have become increasingly composed of shale. To determine the feasibility of utilizing drill cuttings as a wellbore cement additive, this work investigates the effect of shale addition to class H cement in various quantities and sizes. Unconfined compressive strength of the cement containing shale was compared to cement without shale to observe the effect that both quantity and particle size effected this property. SEM-EDS microscopy was also performed to understand any notable variations in the cement microstructure or chemical composition when shale is used as an additive. While the investigation of shale as a cement additive was investigated within this work, it provides a preliminary understanding as to how drill cuttings may behave when added to a cement system. Utilizing cuttings as a cement additive in the future could prove beneficial for a number of reasons including that it would reduce the greenhouse gas emissions associated with cement

manufacturing, decrease additive expenses, and minimize costs and emissions related to the recycling of drill cuttings.

6.2.1. Introduction

Wellbore cement is the most commonly used barrier material in hydrocarbon, carbon capture and storage, geothermal, and hydrocarbon wellbores, primarily due to the ability to manipulate cement properties to adhere to the conditions at hand. In order for cement to mitigate hydrocarbon leakage, provide zonal isolation, and support the casing, the cement sheath must be able to withstand the overburden stress, remain intact during any subsequent wellbore operations, have the ability to securely bond to both the casing and formation, and be resistant to hydrocarbon migration. The cement must also be designed so that when it is in the liquid phase and being pumped downhole, it will be properly placed, remove any residual drilling mud, exhibit optimal rheological properties, and set in the appropriate period of time (Kimanzi et al., 2020). Cementitious materials, as a whole, are inflexible and susceptible to failures like cracking and shrinking (Jafariesfad et al., 2020). To enhance the mechanical properties of cement and prevent short- and long-term well integrity issues, additives are mixed with the cement slurry to procure the desired properties.

Additives can be divided into seven primary categories pertaining to the effect that they have on cement: densifiers, accelerators, retarders, viscosifiers, density reducers, friction reducers, and fluid loss prevention. Oftentimes, an additive will fall into more than one of these categories which makes finding a combination of additives to achieve each desired property difficult. Additive selection must take into consideration the pressure, temperature, chemical composition of the formation, mud type, and the presence of formation water, oil, and gas as well as the compatibility with other additives (Boul et al., 2016). While the list of additive material that has

been used to modify cement mechanical properties is ever-growing, some of the most common types of additives are nanoparticles, cellulose material, polymers, and pozzolanic material.

Nanoparticles are often used to enhance the mechanical properties of cement because they have large surface areas and are thus able to be more reactive with surrounding cementitious material (Lau et al., 2016; Deshpande & Patil, 2017). Common nanoparticles used in wellbore cements include but are not limited to silica nanoparticles, magnesium oxide nanoparticles, alumina nanoparticles, iron nanoparticles, carbon nanotubes, and magnetic nanoparticles (Alkhamis & Imqam, 2018). While nanoparticles have significant promise for enhancing cement mechanical properties, they are often expensive and significantly increase the cost for cementing (Tabatabaei et al., 2022).

Cellulose materials are often used in cement slurries to prevent fluid loss but have proved to be unreliable in both high- and low-temperatures as well as in areas with a high salt concentration (Dao & Vijn, 2002). Examples of cellulose materials commonly used in wellbore cement include hydroxyethyl cellulose (HEC), methyl hydroxyethyl cellulose (MHEC), and carboxymethyl hydroxyethyl cellulose (CMHEC), which when hydrated, immediately increase slurry viscosity (Doan et al., 2015). Cellulose materials can prove problematic in that this increased viscosity and lead to issues pumping the slurry.

Polymers are often added to cement to enhance elastic properties (Patel et al., 2021). Encapsulation of polymers has also been investigated and it was found that such additives beneficially impact cement mechanical properties and bonding, but due to the complex technique required to formulate such additives may prove costly (Contreras et al., 2021). The use of SMP, which is a type of polymer that is composed of low-molecular weight pre-polymers and crosslinking agents that has the ability to alter its shape when stimulated (Behl & Landlein, 2007;

Li et al., 2018; Ziashahabi et al., 2019). The addition of SMP will allow for a less brittle and more ductile cement which could prove beneficial for maintaining wellbore integrity for various aspects within the life of a well (Taleghani et al., 2017). One of the drawbacks of utilizing SMP's as sealing material is that they can be significantly impacted by temperature fluctuations (Mansour et al., 2017). Another downside to this additive material is that little testing has been done to determine how SMP's actually behave under downhole conditions (Flores et al., 2019). Polymers, while improving elasticity short-term, could negatively impact long-term well integrity in that the bond between cement and polymers is often weak and polymers could degrade under the elevated temperatures and pressures experienced within wellbores (Patel et al., 2021).

There are a wide variety of pozzalanic materials that have been utilized as wellbore cement additives. Pozzolanic material work when the amorphous silica within the pozzolans react with calcium hydroxide that is formed during cement hydration (Hossain, 2004). This reaction leads to an increase in compressive strength and durability by filling effective pore space thus reducing permeability, enhanced C-S-H phases associated with the pozzolanic reaction, higher amounts of inert pozzolanic minerals, and increased nucleation sites for C-S-H formation (Barry et al., 2022; Brandl et al., 2010). Common pozzolanic materials used as wellbore cement additives are fly ash, metakaolin, blast furnace slag, and glass microspheres. Fly ash, metakaolin, and blast furnace slag are biproducts of industrial manufacturing processes and tend to be readily available. Fly ash is created from the combustion of coal and is readily available; the addition of fly ash to cement is shown to increase compressive strength (Ahdaya et al., 2019). Metakaolin is made from calcined kaolin clay and when added to cement, decreases porosity and permeability, minimizes shrinkage, and minimizes chemical degradation (Foster et al., 2012). Blast furnace

slag is formed from the manufacturing of iron and has been shown to aid in preventing gas migration, setting time, and bonding (Sweatman et al., 1995; Tare et al., 1998). Glass microspheres are a type of pozzalanic material that is used to lower the density of cement but have many drawbacks such as their cost, separation tendencies, and the tendency to be crushed under pressure (Pang et al., 2018, Pernites et al., 2018, Anya, 2018).

While the use of pozzolanic materials has proven beneficial for a variety of reasons, one of the key aspects that make them so desirable is the potential to minimize the amount of cement needed. Cement manufacturing is one of the largest producers of greenhouse gases, specifically, carbon dioxide (CO_2). Using pozzolanic material either as a cement additive would reduce the amount of cement used in the petroleum industry which could lead to a significant decrease in CO_2 emissions.

While the aforementioned pozzolanic materials have been and continue to be investigated as cement additives, there is one type of pozzolanic material that is readily available in the petroleum industry yet has not been investigated: drill cuttings. Drill cuttings are pieces of formation coated in drilling mud that are brought to the surface during wellbore drilling operations. Cuttings disposal is dictated by the type of drilling fluid used and disposal methods can vary by geographic location.

The purpose of this research is to investigate the feasibility of using cuttings as a cement additive and to understand the effect on cement mechanical properties. Various particle sizes and quantities of shale are added to class H cement to understand how compressive strength is altered with the novel geologic additive. While the list of additives used to alter the mechanical properties of wellbore cement are ever-growing, many have solely been investigated in a laboratory and field feasibility is often overlooked (Virgilio et al., 2015). Woodford shale has a

highly similar chemical composition to other pozzolanic additives, specifically class F fly ash and metakaolin, and its similarities can be seen in Fig. 6.10 (Aïtcin, 2016; Mainali et al., 2016). Class F fly ash and metakaolin have both been added to slurries that are pumped in the field, indicating the promise of shale additive potential.

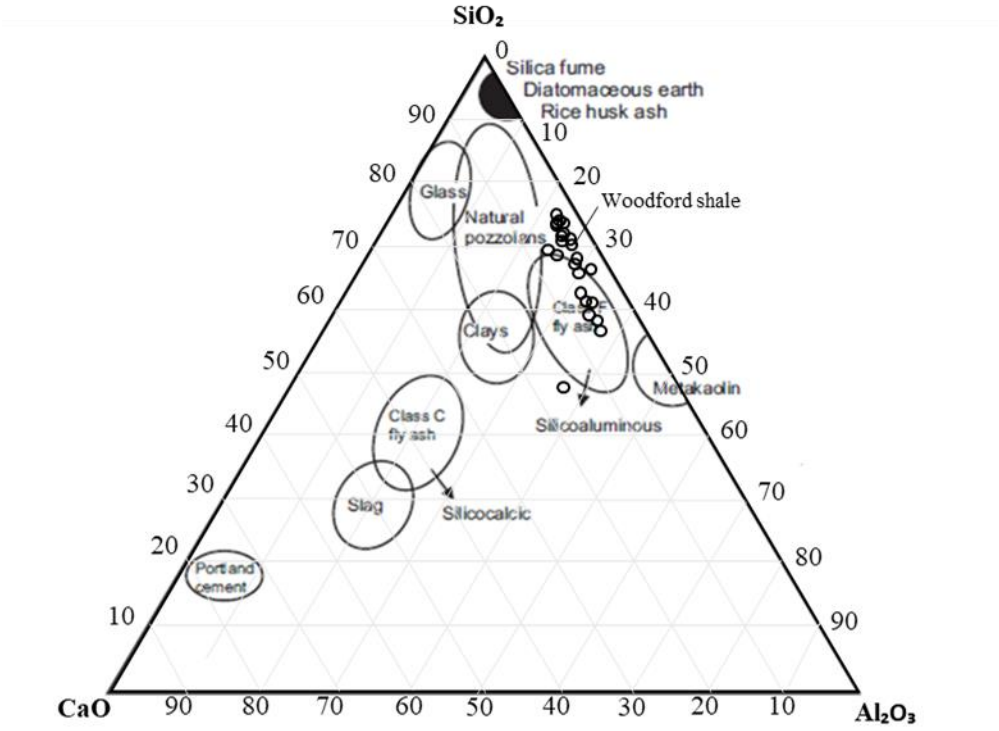

Figure 6.10. Ternary diagram showing various pozzolanic material chemical composition in comparison to Woodford shale (Aïtcin, 2016; Mainali et al., 2016).

While the purpose of this study is solely for feasibility purposes, it could prove to have significant beneficial effects if the work is furthered and various other properties of such slurries are tested and better understood. According to a 2007 study conducted by the International Energy Agency (IEA), cement manufacturing yielded 2 billion tons of CO_2 emissions (Barcelo & Kline, 2012). Unconventional wells can produce anywhere from 300-1,200 tons of drill cuttings depending upon the depth and lateral length (Hellmann et al., 2014). Utilization of cuttings within cement could lead to a reduction in the amount of cement used in wellbores, thus reducing

the amount of CO_2 emissions as well as lessen the cost needed to recycle drill cuttings and any associated emissions.

6.2.2. Methodology

To understand the feasibility of using cuttings as a cement additive, various sizes and quantities of shale are added to Central Plains class H wellbore cement. Woodford shale obtained from an outcrop in Murray County, Oklahoma is collected and ground so that there are equal amounts of millimeter (4.7-2 mm), micron (74-210 μm), and submicron (<1 μm) particles. While millimeter and micron size shale are able to be obtained using conventional grinding techniques, submicron samples are obtained using a Retsch EMAX high energy ball mill and particle size was verified using SEM techniques.

To make the samples, shale is added in 5%, 10%, 15%, 25%, 50% and 75% quantities to a slurry composed of Central Plains class H cement, a defoamer (Halliburton), and DI water. To ensure mixability, the density of each slurry is calculated to be 16.49 ppg and is obtained by changing the water content depending upon the amount of shale added to the system. To mix the slurry, a Chandler 3260 Constant Speed Mixer is used and mixing followed API 10RB specifications. The slurry is then poured into a greased 1.5" by 4.0" stainless steel molds and allowed to set for 24-hours. After this time, the samples are demolded and placed into a NaOH-DI brine in a 150˚F oven for 28 days. Samples are regularly checked to ensure that they are covered in the brine solution. After 28 days, the samples are removed from the oven, weighed, and placed in a 150˚F vacuum oven for 24 hours, then removed and cut/ground to ensure both ends of the sample are smooth and free of any abnormalities. Uniformity is confirmed using a caliper and rotating in at three locations with 90˚ spacing and the values are all within one-hundredth millimeter.

UCS testing is performed using a New England Research Autolab-500 load frame with a strain rate of 0.04 mm/min. A stainless steel top plate is placed between the top of the cement sample and the load frame top platen to further mitigate any potential surface abnormalities from affecting the test results. The upper piston is slowly lowered until it made contact with the upper surface of the top plate, and this is verified by the force reading on the computer. Once testing is initiated, samples are tested until axial force rapidly decreased to the initial axial force value indicating that the sample failed and *UCS* is reached indicating the test is concluded.

After the samples are tested, scanning electron microscopy (SEM) and energy dispersive X-ray spectroscopy (EDS) is performed on the millimeter and submicron sample sets that had the highest and lowest *UCS* values using a FEI Quanta 250 and Bruker XFlash 6130. Small pieces of the samples are sputter coated with gold and palladium using a Denton Vacuum Desk V Thin Film Deposition Solution so that the samples would not charge when using the electron beam. Once the samples are coated, they are placed onto the stage and inserted into the microscope where both SEM and EDS are performed on various locations on the sample surface.

6.2.3. Results

After each sample is tested, observations regarding particle distributions were made. Stress data obtained from *UCS* testing on the cement samples are plotted and analyzed to determine and compare *UCS* for the 57 samples. Results for the base, millimeter, micron, and submicron sample sets are shown in Fig.s' 6.11, 6.12, 6.13, and 6.14, respectively. A summary of all *UCS* tests is shown in Table 6.4. For the millimeter and micron sample sets, all samples are able to be tested regardless of the amount of shale while for the submicron sample set, the 50% and 75% samples broke during the curing process and are unable to be tested.

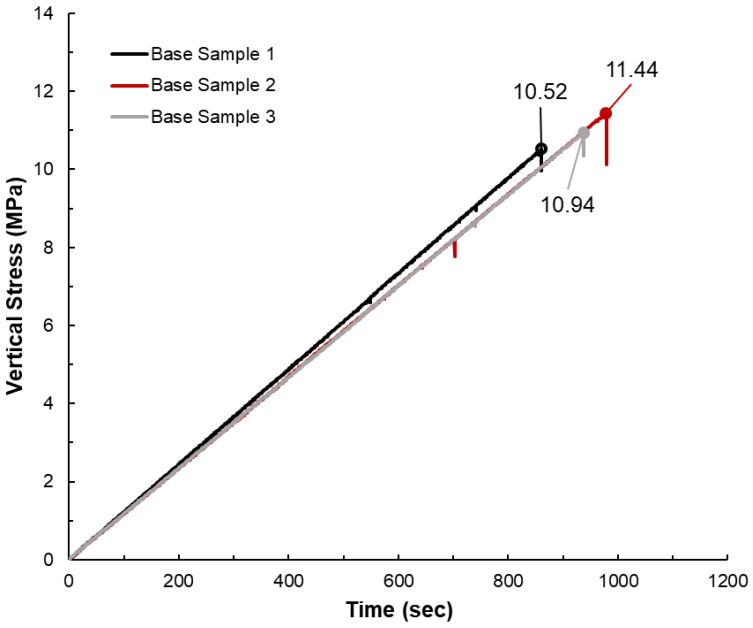

Figure 6.11. Base sample UCS results.

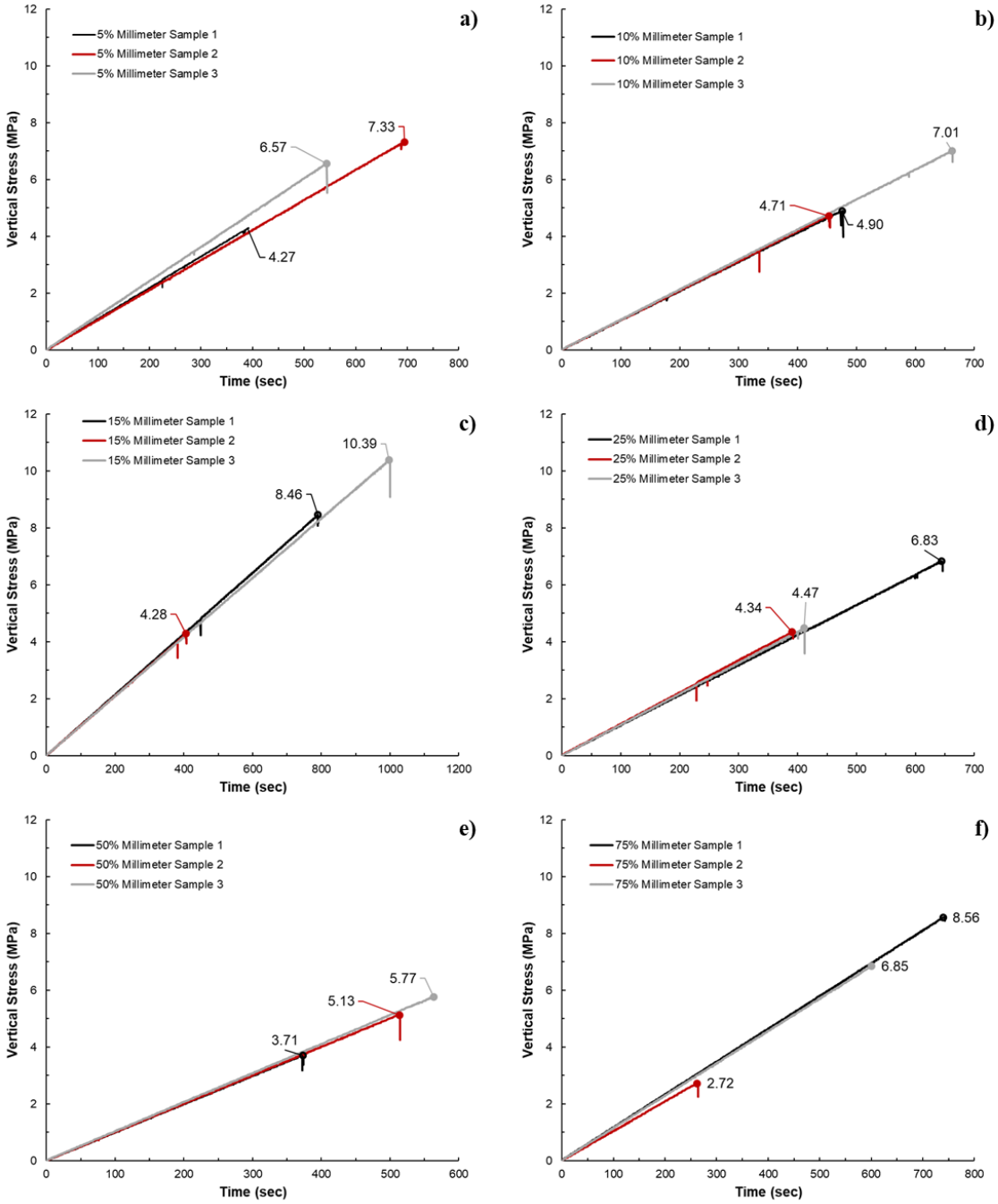

Figure 6.12. Millimeter shale UCS results for the: a) 5% millimeter samples; b) 10% millimeter samples; c) 15% millimeter samples; d) 25% millimeter samples; e) 50% millimeter samples; f) 75% millimeter samples.

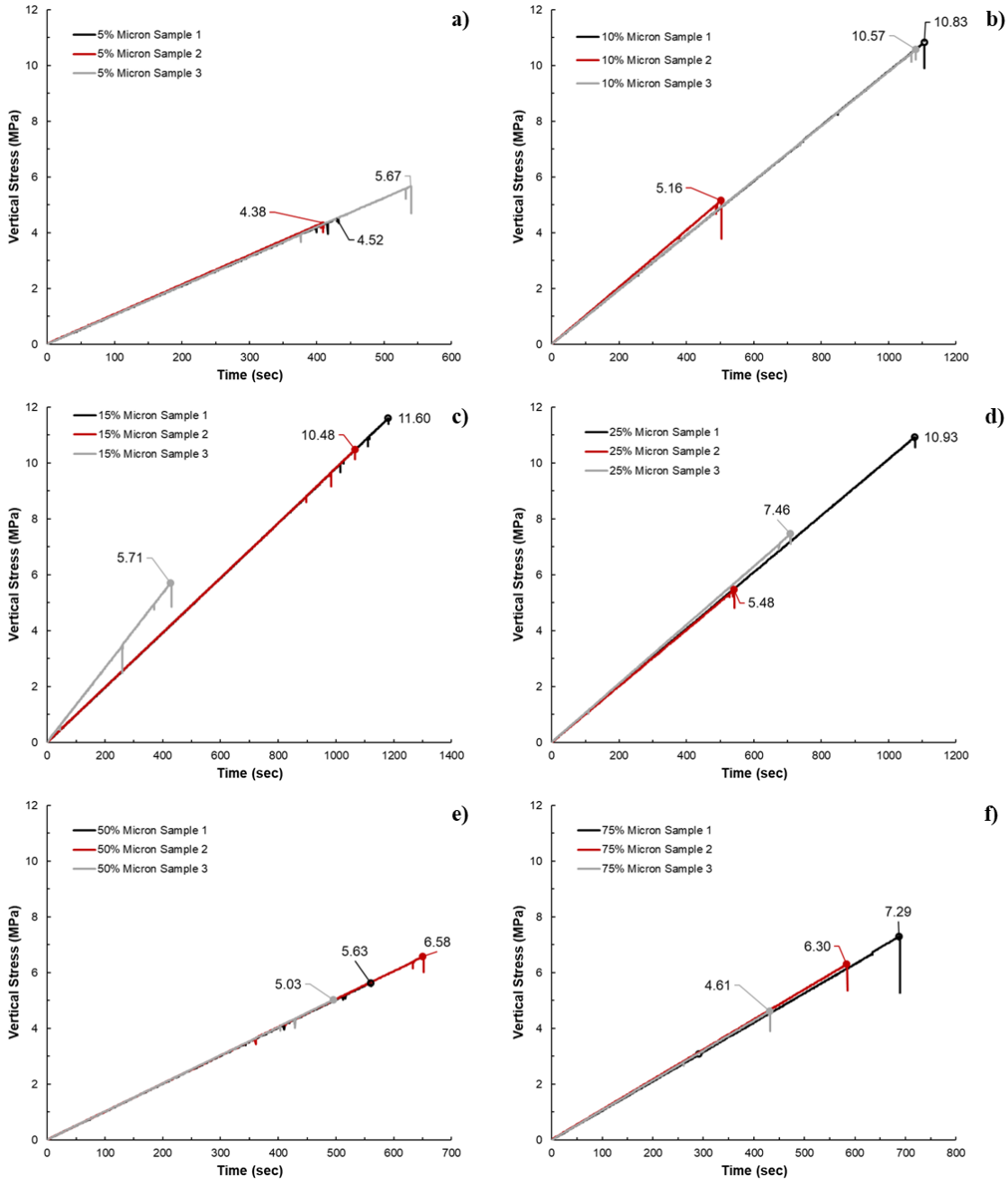

Figure 6.13. Micron shale UCS results for the: a) 5% micron samples; b) 10% micron samples; c) 15% micron samples; d) 25% micron samples; e) 50% micron samples; f) 75% micron samples.

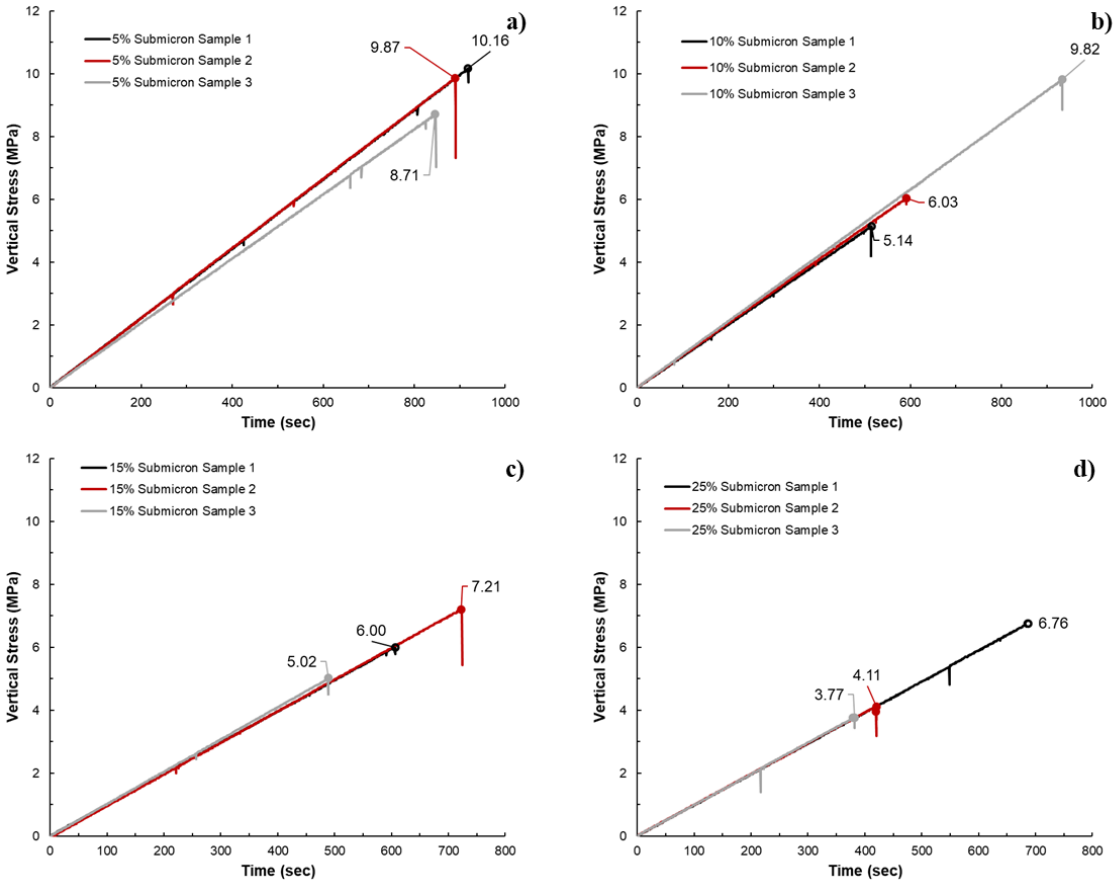

Figure 6.14. Submicron shale UCS results for the: a) 5% submicron samples; b) 10% submicron samples; c) 15% submicron samples; d) 25% submicron samples.

Table 6.4. UCS test results for the samples cured over 28 days.

Shale Size	% Shale	Sample Number	UCS (MPa)	Avg. UCS (MPa)	Std. Dev. (MPa)
Base	0%	1	10.52	10.97	0.38
		2	11.44		
		3	10.94		
Millimeter	5%	4	4.29	6.06	1.29
		5	7.33		
		6	6.57		
	10%	7	4.90	5.54	1.04
		8	4.71		
		9	7.01		
	15%	10	8.46	7.71	2.55
		11	4.28		
		12	10.39		
	25%	13	6.83	5.21	1.14
		14	4.34		
		15	4.47		
	50%	16	3.71	4.87	0.86
		17	5.13		
		18	5.77		
	75%	19	8.56	6.04	2.45
		20	2.72		
		21	6.85		

Micron	5%	22	12.06	9.79	2.02
		23	10.17		
		24	7.15		
	10%	25	10.83	8.85	2.61
		26	5.16		
		27	10.57		
	15%	28	11.60	9.26	2.55
		29	10.48		
		30	5.71		
	25%	31	10.93	7.96	2.25
		32	5.48		
		33	7.46		
	50%	34	5.63	5.75	0.64
		35	6.58		
		36	5.03		
	75%	37	7.29	6.07	1.11
		38	6.30		
		39	4.61		
Sub-Micron	5%	40	10.16	9.58	0.63
		41	9.87		
		42	8.71		
	10%	43	5.14	7.00	2.03
		44	6.03		
		45	9.82		
	15%	46	6.00	6.08	0.90
		47	7.21		
		48	5.02		
	25%	49	6.76	4.88	1.34
		50	4.11		
		51	3.77		
	50%	52	Not Tested.		
		53			
		54			
	75%	55	Not Tested.		
		56			
		57			

To understand the effect of shale size and quantity on *UCS*, single-factor ANOVA testing is performed on the 28-day samples and the results are shown in Table 6.5.

Table 6.5. Single-factor ANOVA results for the class H cement samples containing various sizes and quantities of shale cured for 28 days.

Shale Size	Assumption	Groups	Count	Sum	Average	Variance	P-Value
Millimeter	Addition of millimeter shale has no	0	3.0	32.8	10.9	0.2	0.02
		5	3.0	18.2	6.1	2.5	
		10	3.0	16.6	5.5	1.6	
		15	3.0	23.2	7.7	9.7	

	effect on UCS.	25	3.0	15.6	5.2	1.9	
		50	3.0	14.6	4.9	1.1	
		75	3.0	18.2	6.1	9.2	
	Concentration does not matter for millimeter samples.	5	3.0	18.2	6.1	2.5	0.6
		10	3.0	16.6	5.5	1.6	
		15	3.0	23.2	7.7	9.7	
		25	3.0	15.6	5.2	1.9	
		50	3.0	14.6	4.9	1.1	
		75	3.0	18.2	6.1	9.2	
Micron	Addition of millimeter shale has no effect on UCS.	0	3.0	32.8	10.9	0.2	0.1
		5	3.0	29.5	9.8	6.1	
		10	3.0	26.6	8.9	10.1	
		15	3.0	27.8	9.3	9.8	
		25	3.0	23.9	8.0	7.5	
		50	3.0	17.2	5.7	0.7	
		75	3.0	18.2	6.1	1.9	
	Concentration does not matter for micron samples.	5	3.0	29.5	9.8	6.1	0.3
		10	3.0	26.6	8.9	10.1	
		15	3.0	27.8	9.3	9.8	
		25	3.0	23.9	8.0	7.5	
		50	3.0	17.2	5.7	0.7	

		75	3.0	18.2	6.1	1.9	
Submicron	Addition of millimeter shale has no effect on UCS.	0	3.0	32.8	10.9	0.2	0.008
		5	3.0	28.8	9.6	0.6	
		10	3.0	20.9	7.0	6.2	
		15	3.0	17.6	5.9	5.4	
		25	3.0	14.7	4.9	2.7	
	Concentration does not matter for micron samples.	5	3.0	28.8	9.6	0.6	0.08
		10	3.0	20.9	7.0	6.2	
		15	3.0	17.6	5.9	5.4	
		25	3.0	14.7	4.9	2.7	

SEM and EDS is performed on all samples at low and high resolutions to understand variations in both the chemical composition within the samples as well as the surface microstructure. Two types of SEM images are able to be produced: secondary electron and backscatter electron (BSE). Secondary electron images are indicative of a samples topography while BSE produces variations in chemical composition in addition to topography. While the samples are sputter coated to reduce the charging effect, concave areas on the surface typically are not able to be fully coated and still appear dark. These dark areas are not wholly representative of pores or voids at the surface of the sample. EDS is done using a BSE image and can be performed using either a designated spot or a broader specified area on the surface of the sample. This type of chemical analysis can be done at any magnification but obtaining EDS information at various magnifications can provide information about the sample at both a small scale and a macroscale. Taking EDS at a low magnification is done to obtain an understanding of how the surface composition varies between locations. By investigating multiple locations at low magnification,

an understanding of how the quantity of shale could impact the overall chemical composition of the cement can be performed. Locations that visually looked as though they could contain shale particles are also selected for EDS analysis to understand compositional variations between the geologic material and cement. These locations are also ideal to understand any variations at the cement-shale interface to observe whether any atypical reactions may have occurred. SEM and EDS is performed on all of the 5% and 10% submicron samples as well as the 15% and 50% millimeter samples to investigate whether any differences in microstructure, hydration, porosity, or chemical composition amongst samples containing the same amounts of shale as well as the same particle sizes.

EDS analysis for samples 10, 11, and 12, which contain 15% millimeter shale, are shown in Figs' 6.15., 6.16., and 6.17., respectively.

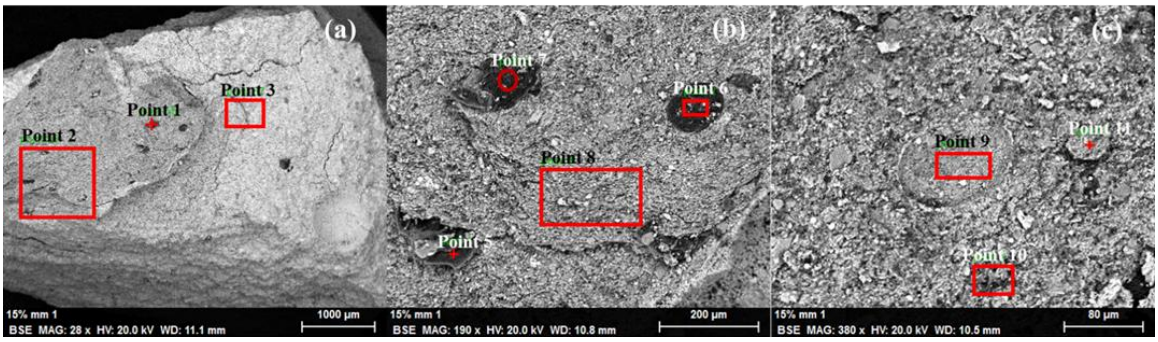

Figure 6.15. 15% millimeter sample 10 EDS results at a) 28x magnification; b) 190x magnification; c) 380x magnification.

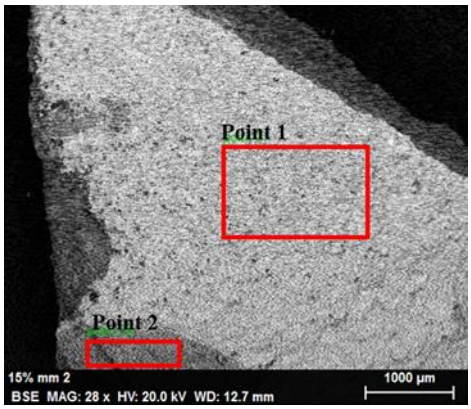

Figure 6.16. 15% millimeter sample 11 EDS results at 28x magnification.

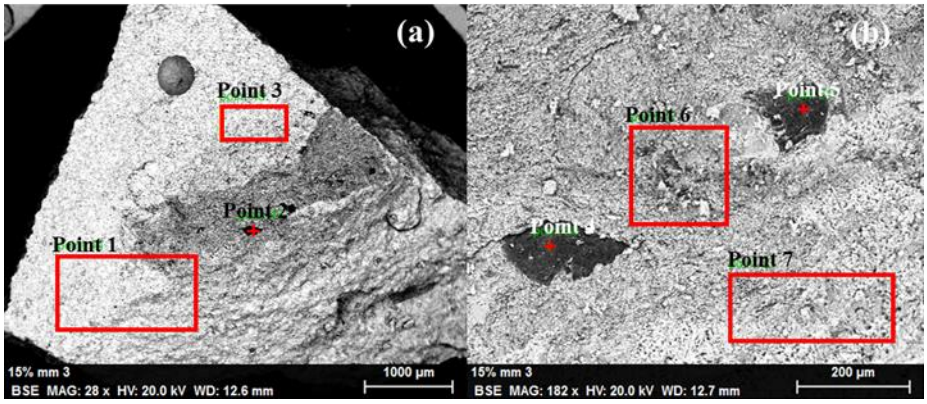

Figure 6.17. 15% millimeter sample 12 EDS results at a) 28x magnification; b) 182x magnification.

SEM analysis of the 15% millimeter samples are shown in Fig.'s 6.18., 6.19., and 6.20.

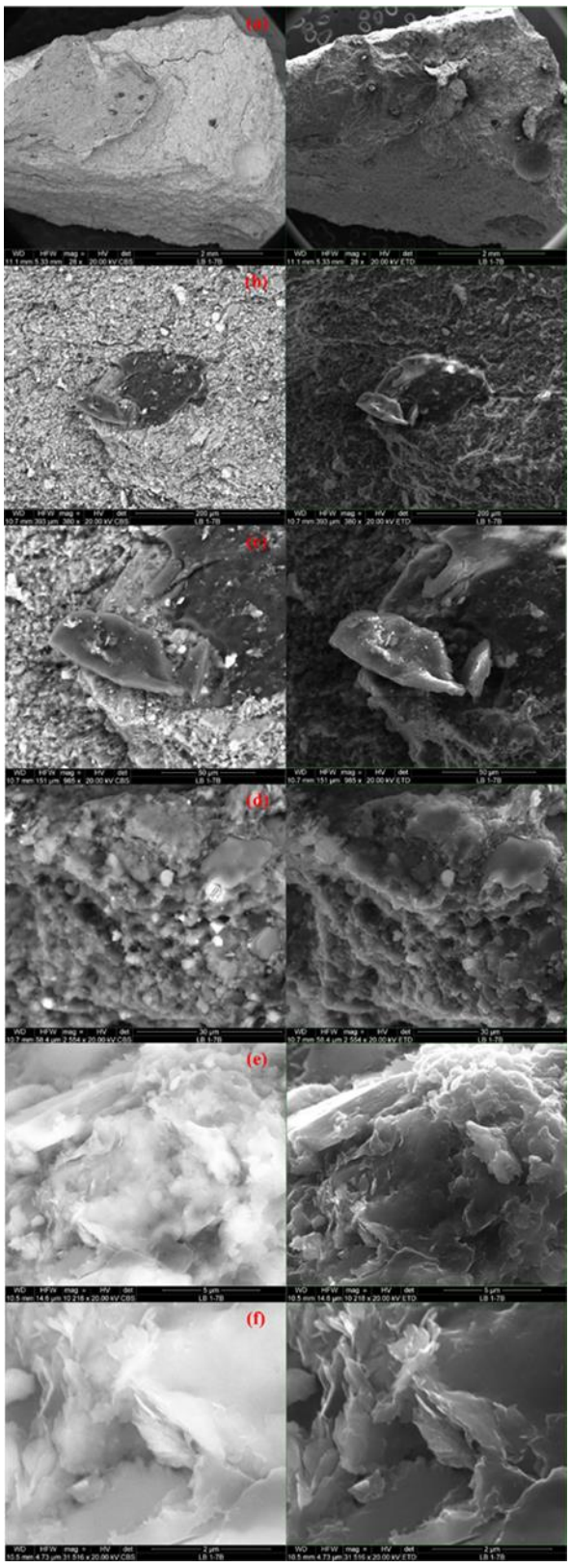

Figure 6.18. 15% millimeter sample 10 at (a) 28x magnification; (b) 380x magnification; (c) 985x magnification; (d) 2,554x magnification; (e) 10,218x magnification; (f) 31,516x magnification where the left images are the backscatter electron image and the right images are the secondary electron images.

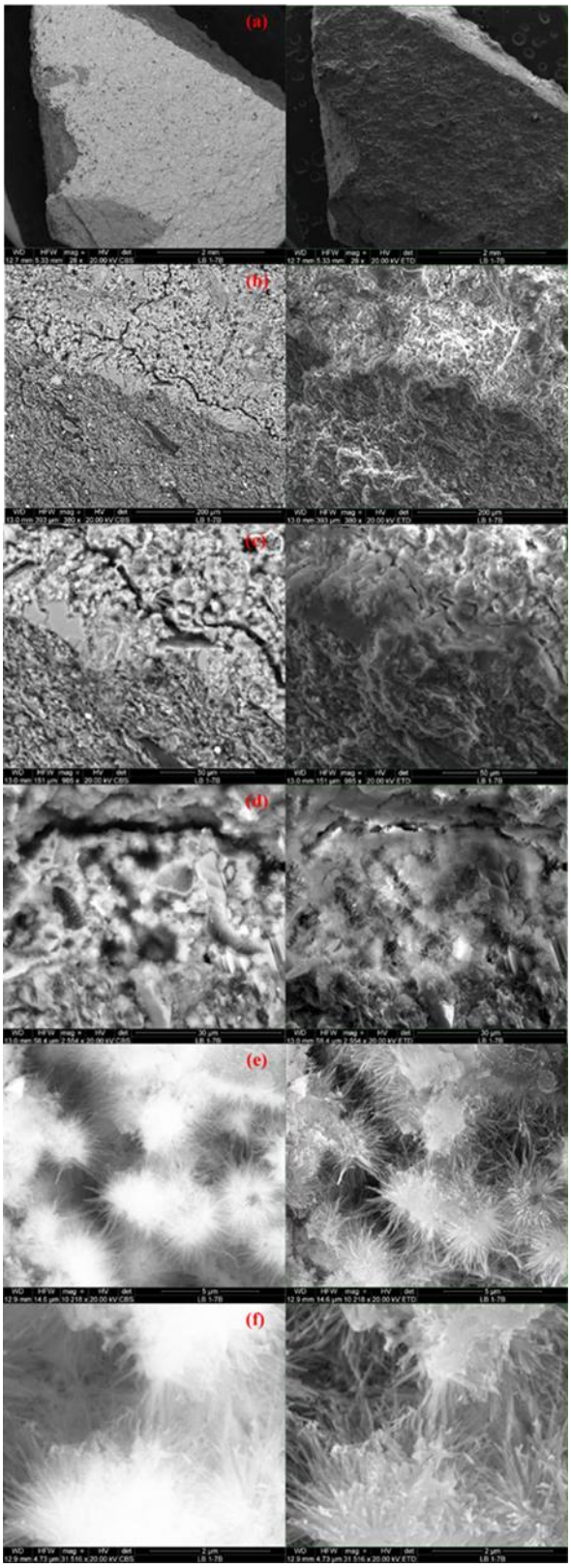

Figure 6.19. 15% millimeter sample 11 at (a) 28x magnification; (b) 380x magnification; (c) 985x magnification; (d) 2,554x magnification; (e) 10,218x magnification; (f) 31,516x magnification where the left images are the backscatter electron image and the right images are the secondary electron images.

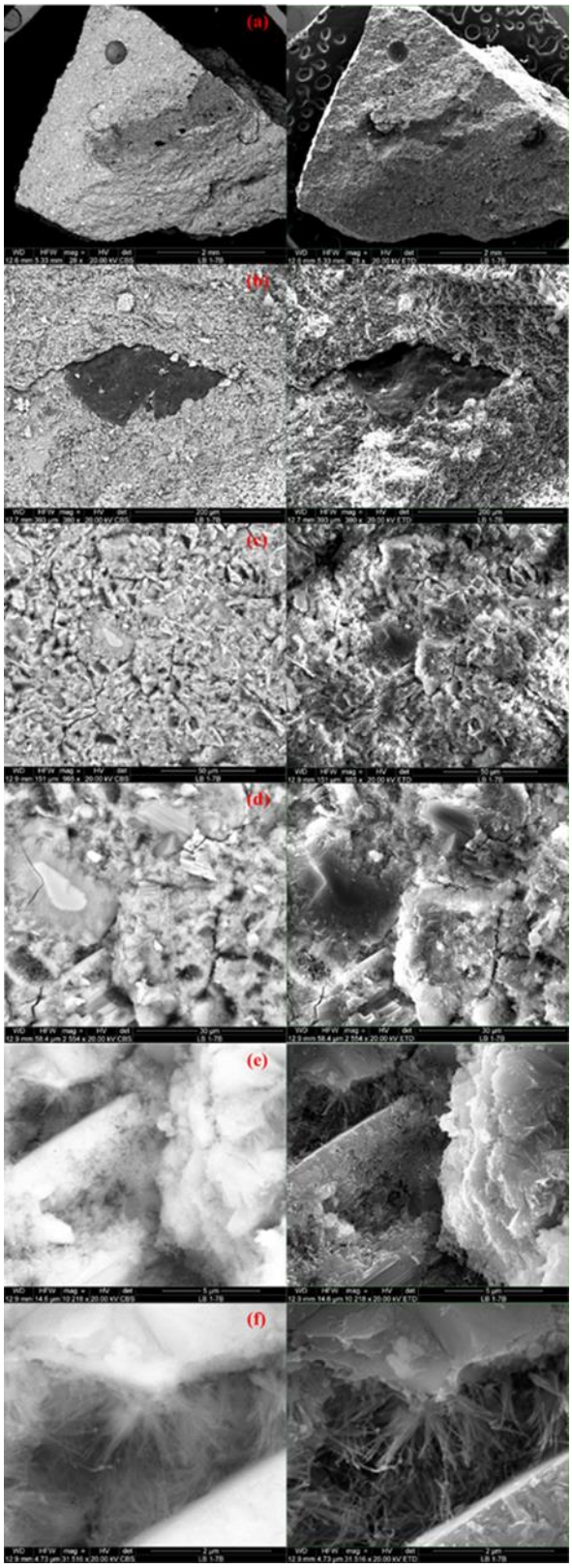

Figure 6.20. 15% millimeter sample 12 at (a) 28x magnification; (b) 380x magnification; (c) 985x magnification; (d) 2,554x magnification; (e) 10,218x magnification; (f) 31,516x magnification where the left images are the backscatter electron image and the right images are the secondary electron images.

EDS analysis for the 50% millimeter samples, or samples 16, 17, and 18, are shown in Figs' 6.21., 6.22., and 6.23., respectively.

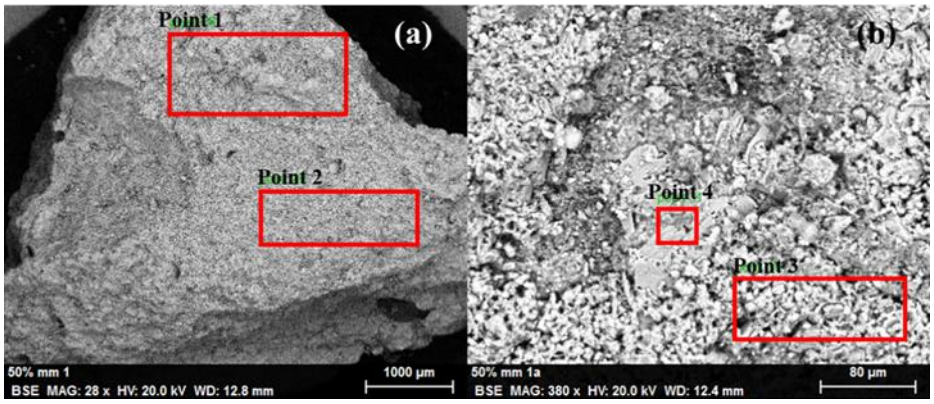

Figure 6.21. 50% millimeter sample 16 EDS results at a) 28x magnification; b) 380x magnification.

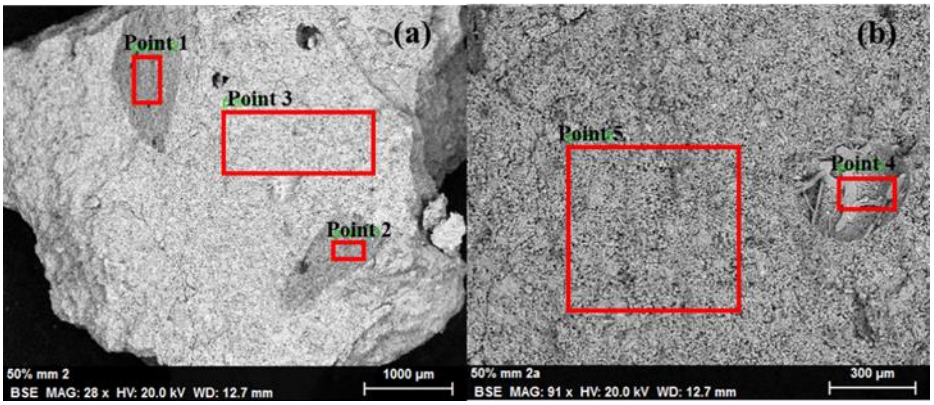

Figure 6.22. 50% millimeter sample 17 EDS results at a) 28x magnification; b) 91x magnification.

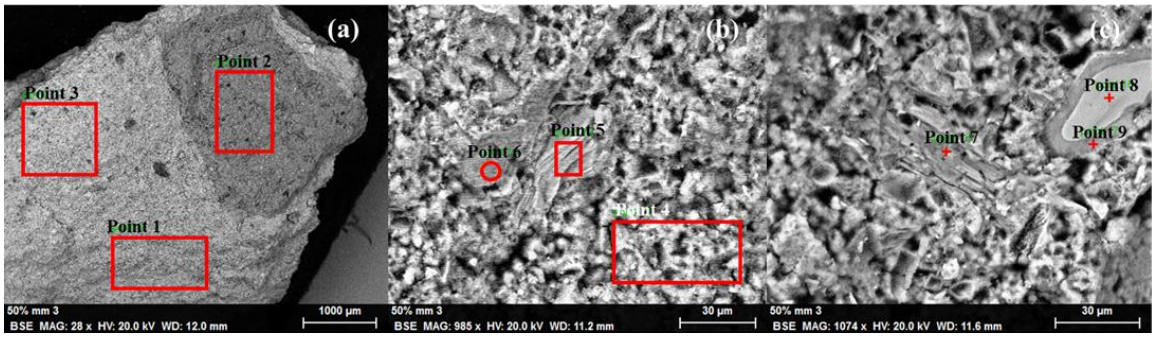

Figure 6.23. 50% millimeter sample 18 EDS results at a) 28x magnification; b) 985x magnification; c) 1,074x magnification.

SEM analysis of the 50% millimeter samples are shown in Fig.'s 6.24., 6.25., and 6.26.

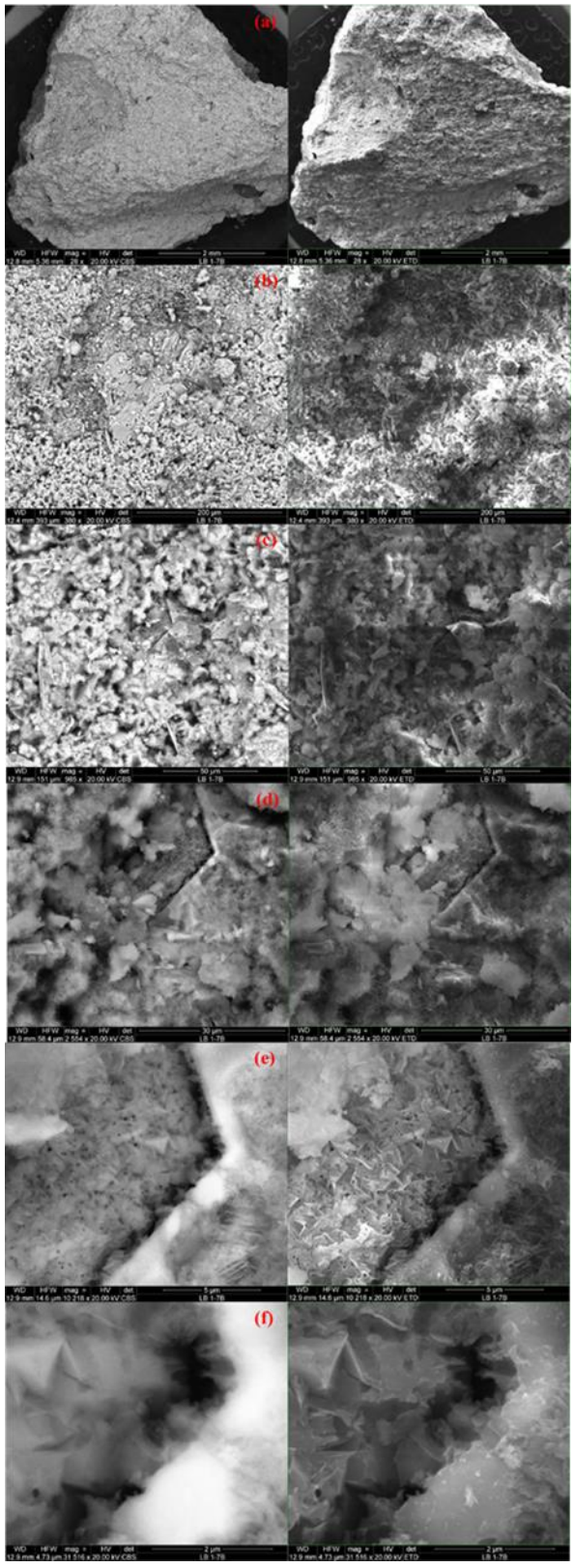

Figure 6.24. 50% millimeter sample 16 at (a) 28x magnification; (b) 380x magnification; (c) 985x magnification; (d) 2,554x magnification; (e) 10,218x magnification; (f) 31,516x magnification where the left images are the backscatter electron image and the right images are the secondary electron images.

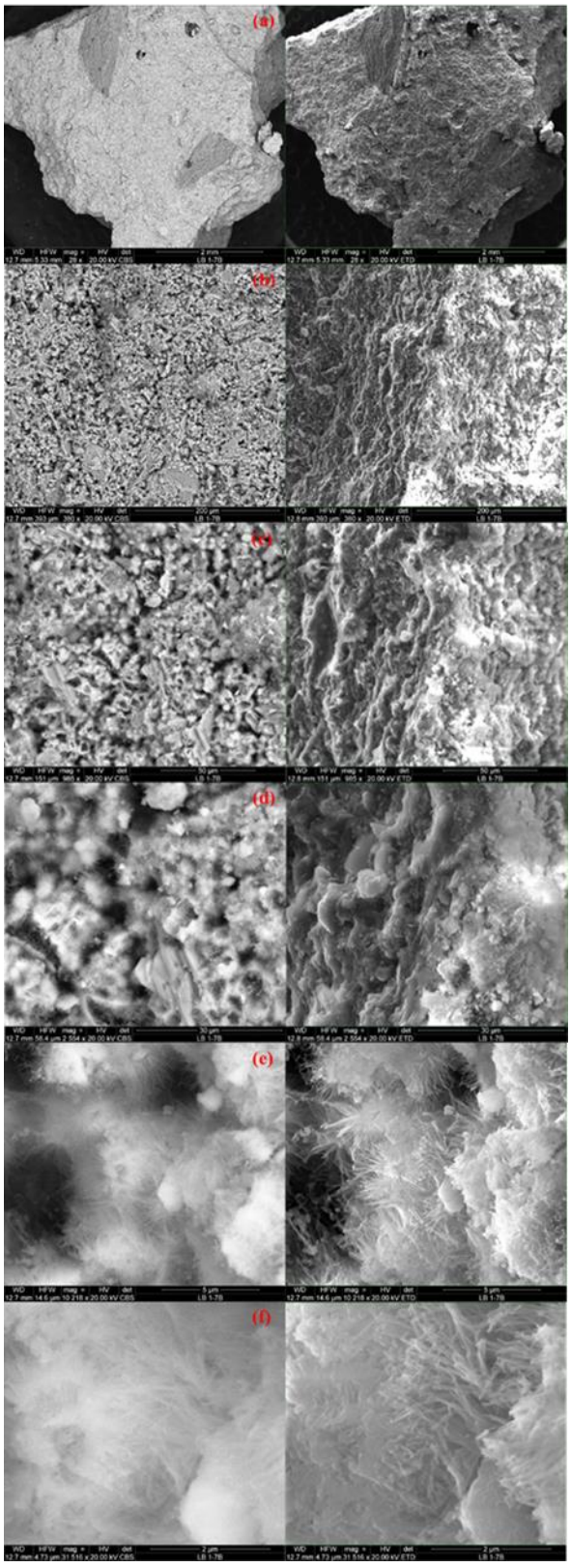

Figure 6.25. 50% millimeter sample 17 at (a) 28x magnification; (b) 380x magnification; (c) 985x magnification; (d) 2,554x magnification; (e) 10,218x magnification; (f) 31,516x magnification where the left images are the backscatter electron image and the right images are the secondary electron images.

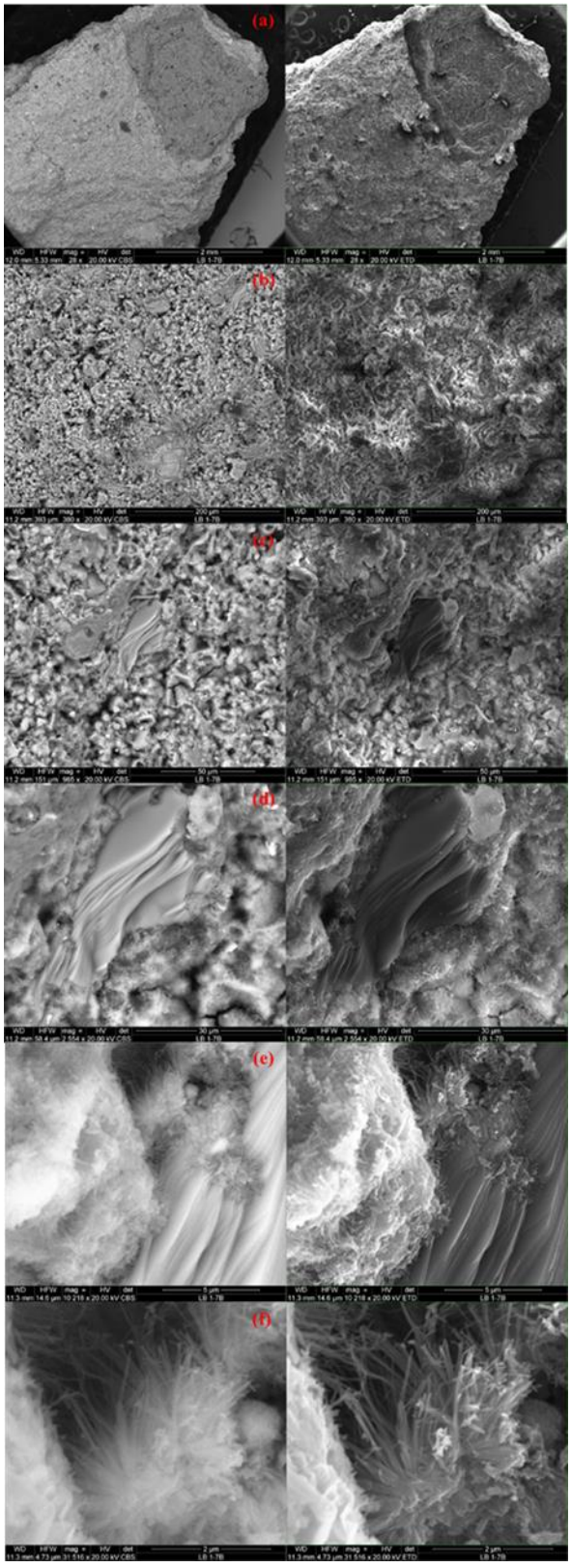

Figure 6.26. 50% millimeter sample 18 at (a) 28x magnification; (b) 380x magnification; (c) 985x magnification; (d) 2,554x magnification; (e) 10,218x magnification; (f) 31,516x magnification where the left images are the backscatter electron image and the right images are the secondary electron images.

EDS analysis for the 5% submicron samples, or samples 40, 41, and 42, are shown in Figs' 6.27., 6.28., and 6.29., respectively.

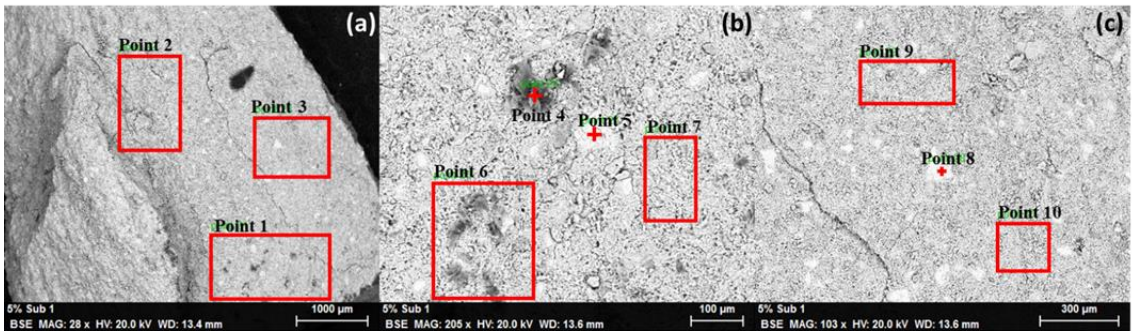

Figure 6.27. 5% submicron sample 40 EDS results at a) 28x magnification; b) 209x magnification; c) 103x magnification.

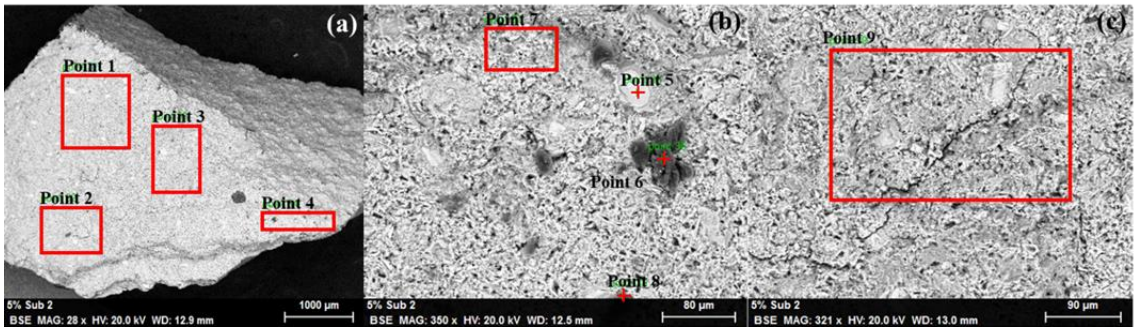

Figure 6.28. 5% submicron sample 41 EDS results at a) 28x magnification; b) 350x magnification; c) 321x magnification.

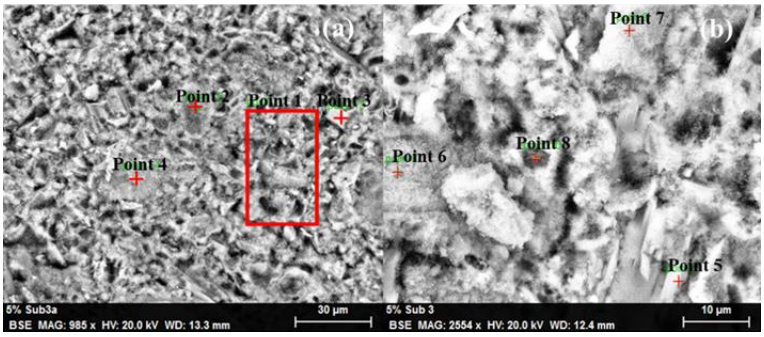

Figure 6.29. 5% submicron sample 42 EDS results at a) 985x magnification; b) 2,554x magnification.

SEM analysis of samples 40, 41, and 42, which contain 5% submicron shale, are shown in Fig.s' 6.30., 6.31., and 6.32.

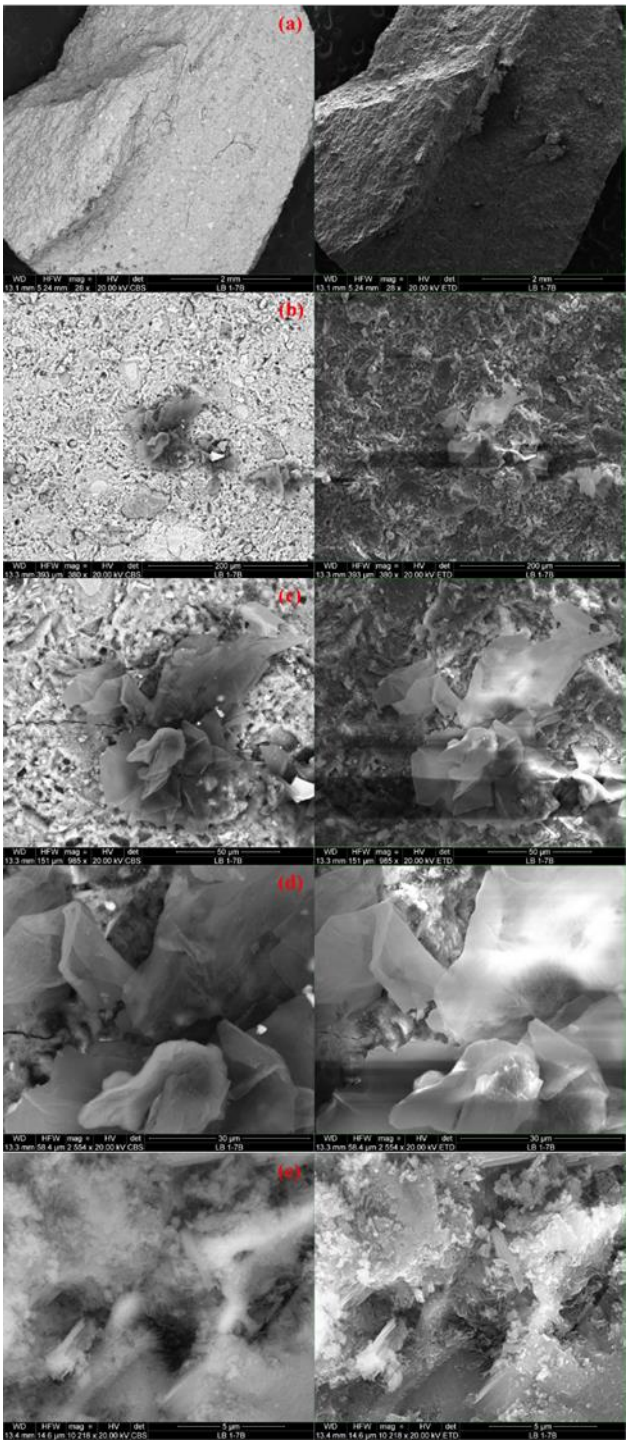

Figure 6.30. 5% submicron sample 40 at (a) 28x magnification; (b) 380x magnification; (c) 985x magnification; (d) 2,554x magnification; (e) 10,218x magnification where the left images are the backscatter electron images and the right images are the secondary electron images.

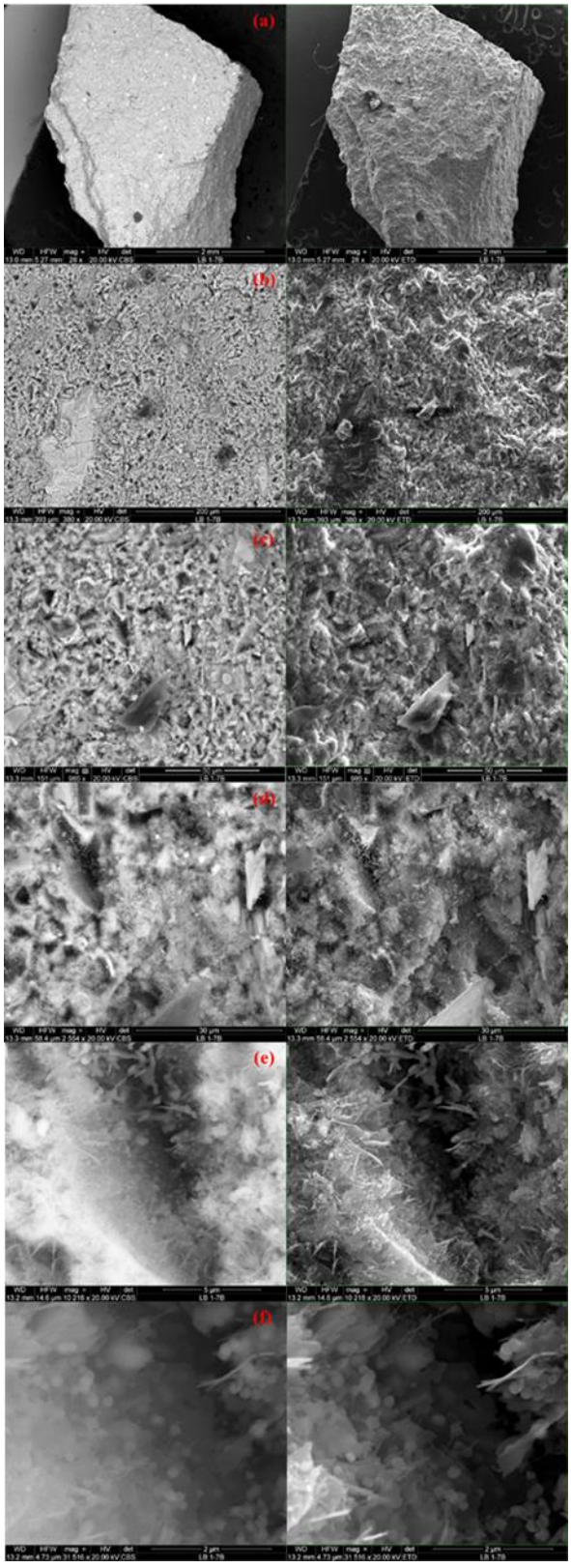

Figure 6.31. 5% submicron sample 41 at (a) 28x magnification; (b) 380x magnification; (c) 985x magnification; (d) 2,554x magnification; (e) 10,218x magnification; (f) 31,516x magnification where the left images are the backscatter electron images and the right images are the secondary electron images.

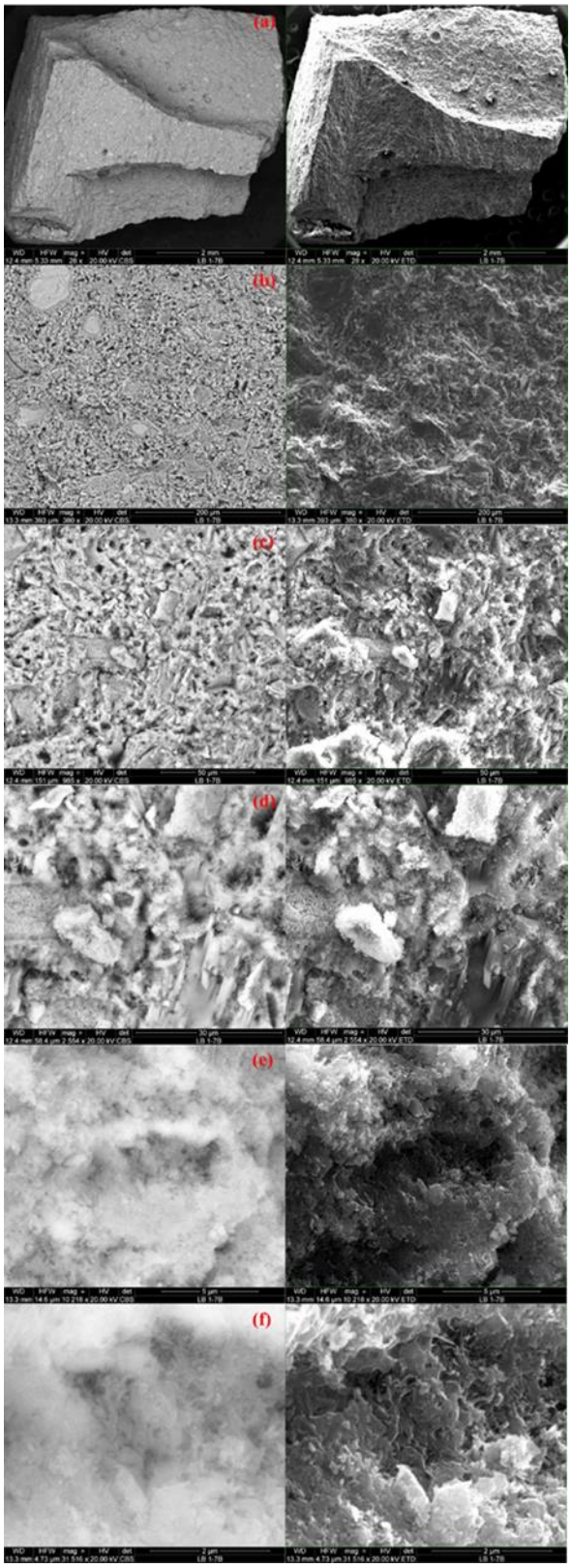

Figure 6.32. 5% submicron sample 42 at (a) 28x magnification; (b) 380x magnification; (c) 985x magnification; (d) 2,554x magnification; (e) 10,218x magnification; (f) 31,516x magnification where the left images are the backscatter electron images and the right images are the secondary electron images.

EDS analysis for the 10% submicron samples, or samples 43, 44, and 45, are shown in Figs' 6.33., 6.34., and 6.35., respectively.

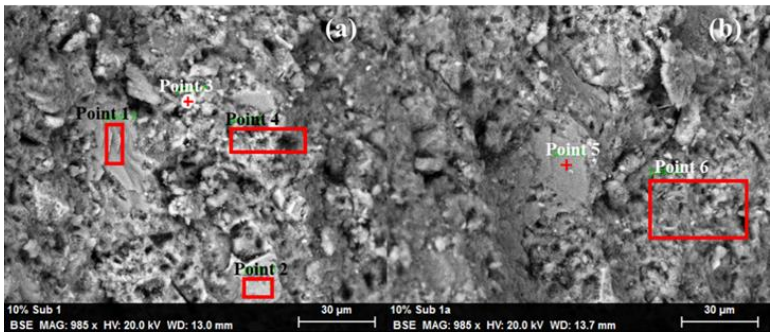

Figure 6.33. 10% submicron sample 43 EDS results at a) 985x magnification; b) and a separate location at 985x magnification.

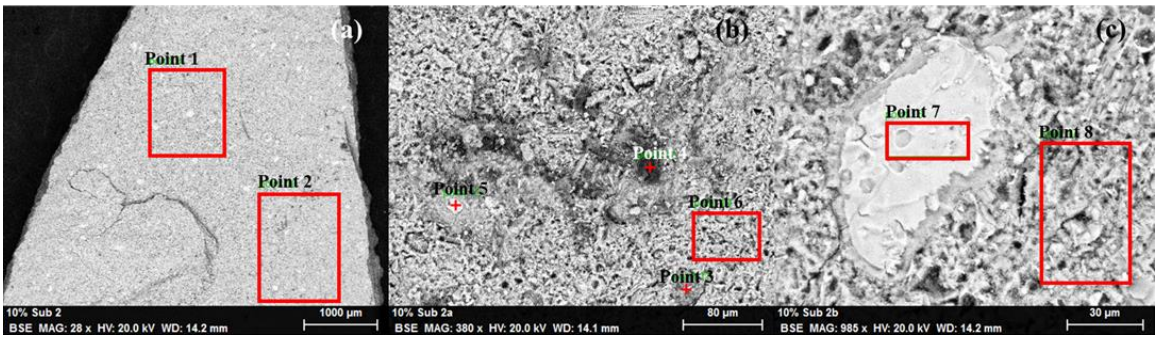

Figure 6.34. 10% submicron sample 44 EDS results at a) 28x magnification; b) 380x magnification; c) 985x magnification.

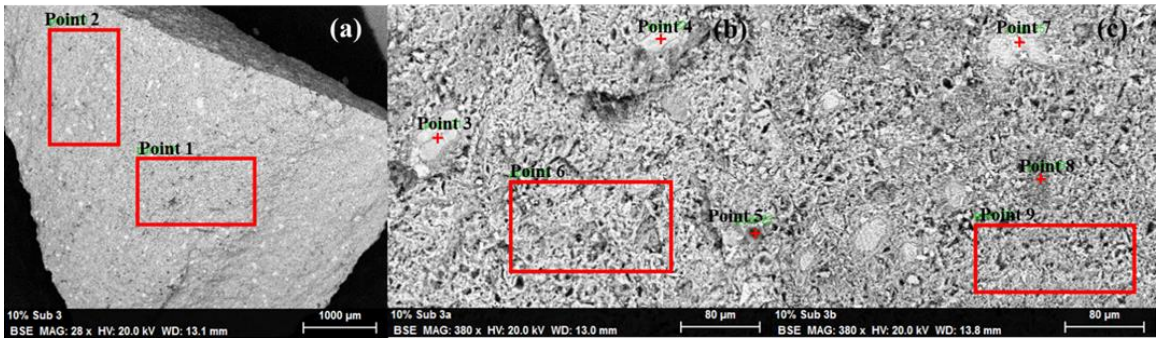

Figure 6.35. 10% submicron sample 45 EDS results at a) 28x magnification; b) 380x magnification; c) a separate location at 380x magnification.

SEM analysis of samples 43, 44, and 45, which contain 10% submicron shale, are shown in Fig.s' 6.36., 6.37., and 6.38.

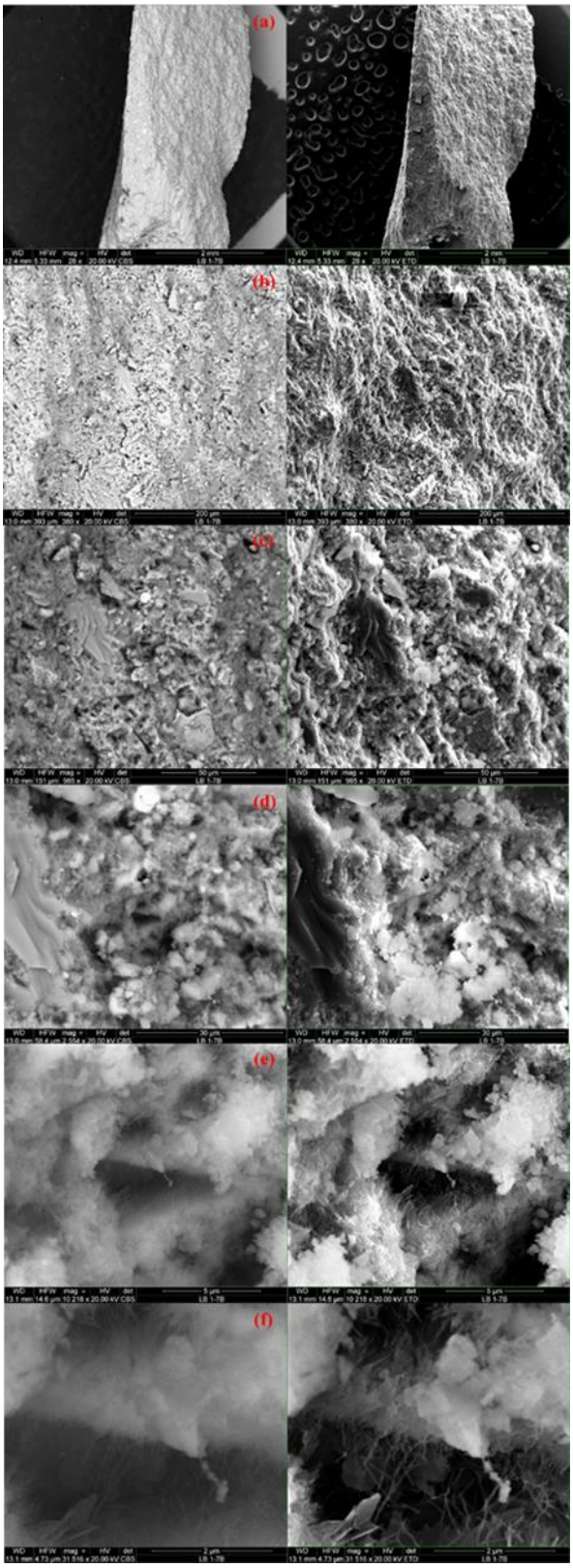

Figure 6.36. 10% submicron sample 43 at (a) 28x magnification; (b) 380x magnification; (c) 985x magnification; (d) 2,554x magnification; (e) 10,218x magnification; (f) 31,516x magnification where the left images are the backscatter electron images and the right images are the secondary electron images.

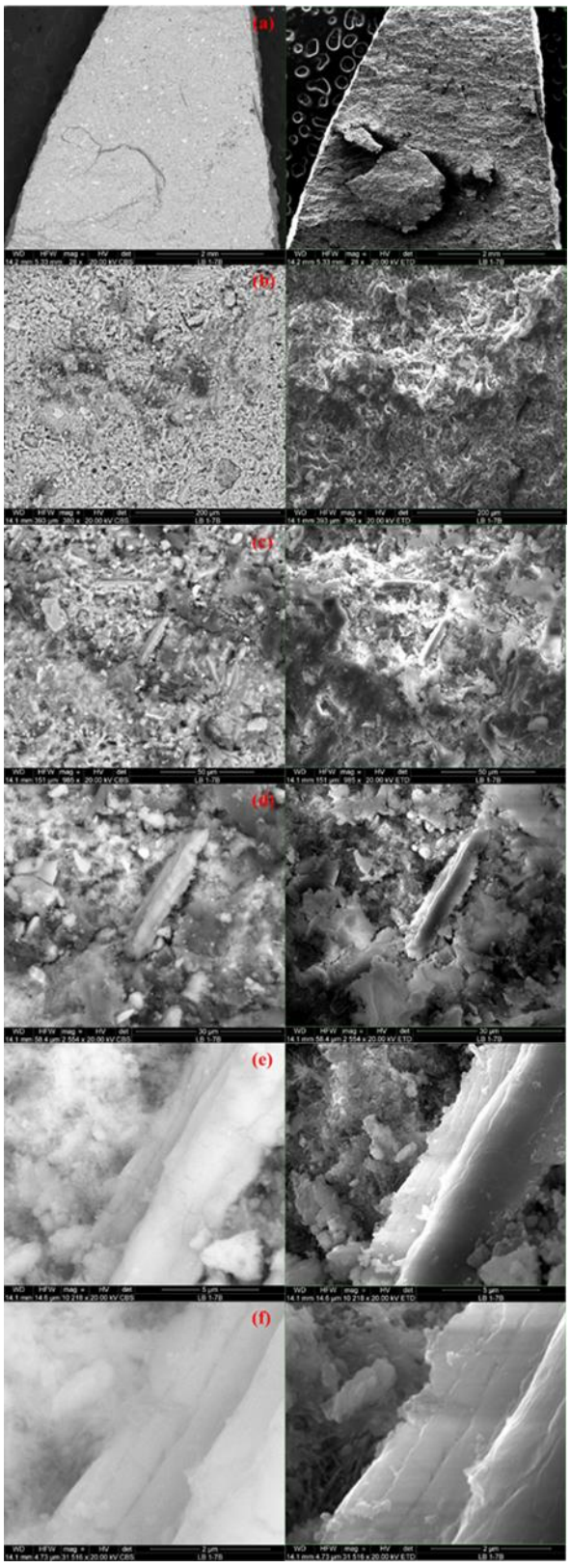

Figure 6.37. 10% submicron sample 44 at (a) 28x magnification; (b) 380x magnification; (c) 985x magnification; (d) 2,554x magnification; (e) 10,218x magnification; (f) 31,516x magnification where the left images are the backscatter electron images and the right images are the secondary electron images.

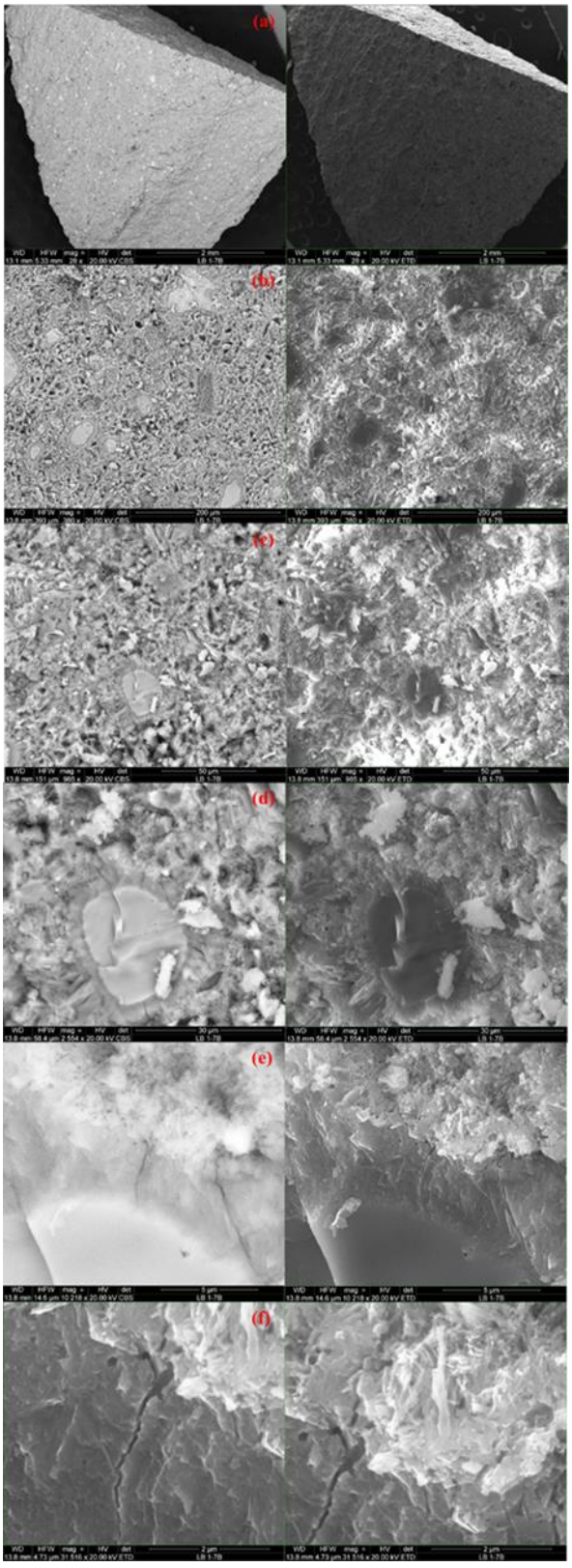

Figure 6.38. 10% submicron sample 45 at (a) 28x magnification; (b) 380x magnification; (c) 985x magnification; (d) 2,554x magnification; (e) 10,218x magnification; (f) 31,516x magnification where the left images are the backscatter electron images and the right images are the secondary electron images.

6.2.4. Discussion

After the samples are crushed, a visual check was performed to determine whether the shale particles are evenly distributed within the samples. Visual inspection was not able to be done in the micron and submicron samples due to the particles being too small to see with the naked eye. For all millimeter samples, particle distribution are fairly homogenous; the shale did not settle to the bottom or float to the top and did not agglomerate within the sample.

UCS test results proved to fluctuate considerably. From the *UCS* results, it can be seen that the base case samples achieved the highest average *UCS* and lowest standard deviation for all of the sample sets. The millimeter sample sets had significantly lower *UCS* values in comparison to the base case samples. For the millimeter sample sets, the 15% samples yielded the highest *UCS* while the 50% millimeter shale samples had the lowest average *UCS*. From the 15% millimeter sample set, sample 12 had the greatest *UCS* of 10.4 MPa, which is comparable to the base case results. The standard deviation for the 15% millimeter samples is the highest of all the millimeter sample sets with the difference between the highest and lowest samples being 6.1 MPa. Sample 11 achieved a *UCS* that was less than half of sample 12. The 50% millimeter sample set had the lowest average *UCS* values but had the lowest standard deviation, indicating that the results for this sample set are fairly consistent. While the 75% millimeter sample set have an average *UCS* of 6.0 MPa, it also contains the sample with the lowest *UCS* for all millimeter samples, sample 20, which has a *UCS* of 2.7 MPa. For all millimeter sample sets, it appears that two samples are fairly similar and one has a significantly higher or lower compressive strength. This could indicate that shale distribution amongst the samples are inconsistent and led to bonding issues.

The samples containing micron sized shale appear to achieve the highest strengths of all the samples containing shale. Of the micron sample set, the 5%, 10%, and 15% samples achieve the

highest average *UCS* but also have high standard deviations. Sample 31, which contained 25% micron shale, has a high UCS that was comparable to samples containing lesser amounts of micron shale. The highest and lowest average *UCS* sample sets with micron shale addition were 5% and 50%, respectively. The 5% micron sample set has an average *UCS* of 9.8 MPa with a standard deviation of 2.0. Sample 22 has the highest *UCS* of all the micron samples, 12.1 MPa, which is actually higher than any of the base case *UCS* values. Sample 28, which contained 15% micron shale, has a *UCS* of 11.6 MPa, which is also higher than any of the base cases. The 50% micron samples has both the lowest *UCS* and standard deviations indicating that the samples all exhibit similar behavior and *UCS* values show little variation.

Of the submicron samples, the 5% samples have the highest average *UCS* of 9.6 MPa with a standard deviation of 0.6 MPa while the 25% samples have the lowest average *UCS* of 4.9 MPa with a standard deviation of 1.3 MPa. The 10% submicron samples have a high standard deviation primarily due to sample 45 having a significantly higher *UCS* than samples 43 and 44. It appears that as the amount of submicron shale added to the cement, the *UCS* decreases fairly linearly. The 50% and 75% submicron samples were able to set after 24-hours and were removed intact and heated in a brine bath. During the early hydration period, the 50% and 75% submicron samples had all broken into smaller pieces and were unable to be tested. This occurrence could be due to thermal degradation or poor bonding between the submicron particles and the cement. There are very few studies that have investigated the effect of such high concentrations of pozzolanic material addition to cement, specifically past early stages of hydration.

From the *UCS* test results, it can be seen that the samples containing micron sized shale exhibited the most promising compressive strength properties. The 5% and 10% submicron sample sets prove to have higher *UCS* values than those containing the same amounts of

millimeter shale, yet the opposite was seen in the 15% and 25% sample sets with the same particle sizes. Fig. 6.39 shows a comparison of *UCS* values for the base case, millimeter, micron, and submicron samples to previously reported *UCS* values for class G and H cement (Wise et al., 2020).

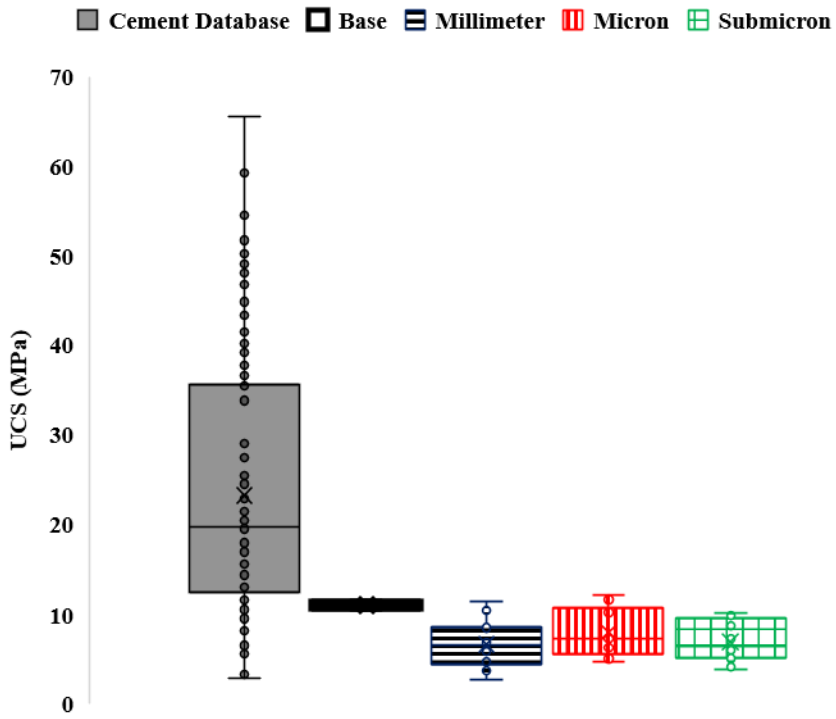

Figure 6.39. Comparison between various shale sizes on cement UCS.

The base case results obtained in this chapter are lower than 25% of the previously reported *UCS* values. The millimeter, micron, and submicron sample sets are also below the reported lower quartile and the micron samples had the highest average *UCS* of all samples containing shale. The millimeter shale has the largest variation of *UCS* while the submicron samples have the lowest. This is due to the 50% and 75% submicron samples not being tested and not included in this analysis.

A comparison between the quantity of millimeter shale on *UCS* to previously reported values for class G and H cement is shown in Fig. 6.40 (Wise et al., 2020).

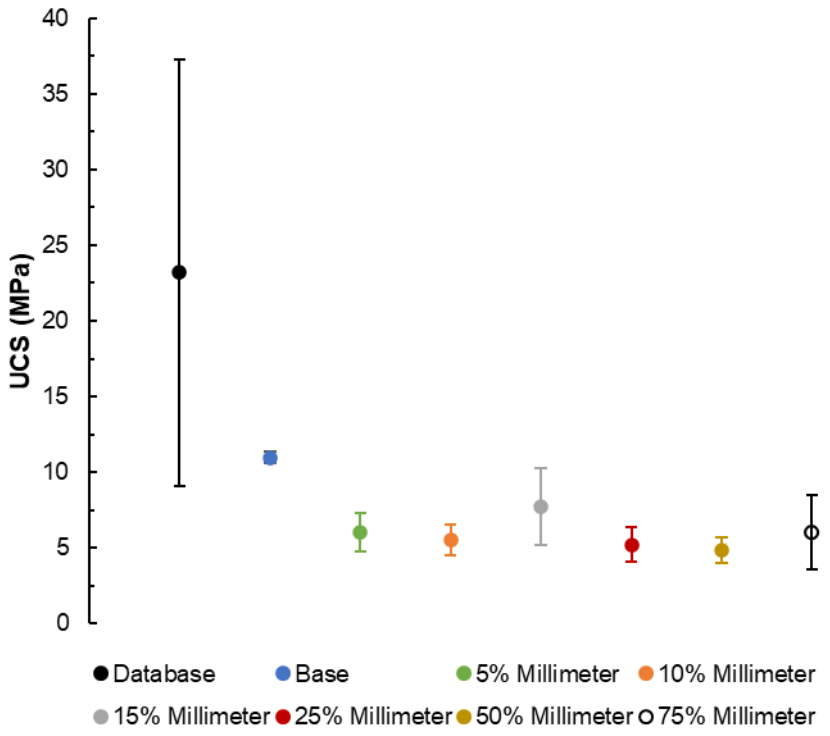

Figure 6.40 Addition of millimeter shale to cement UCS comparison.

From Fig. 6.40, the samples containing micron shale are all lower than previously reported *UCS* values for class G and H cement. The 15% and 75% samples have large *UCS* variation between the samples while the other quantities have more consistent *UCS.* None of the millimeter samples have *UCS* values equal to or above the base case indicating that the addition of millimeter shale to cement has a negative impact on *UCS* over the early hydration period.

A plot showing the effect that the quantity of micron shale has on *UCS* compared to previously reported values for class G and H cement is shown in Fig. 6.41 (Wise et al., 2020).

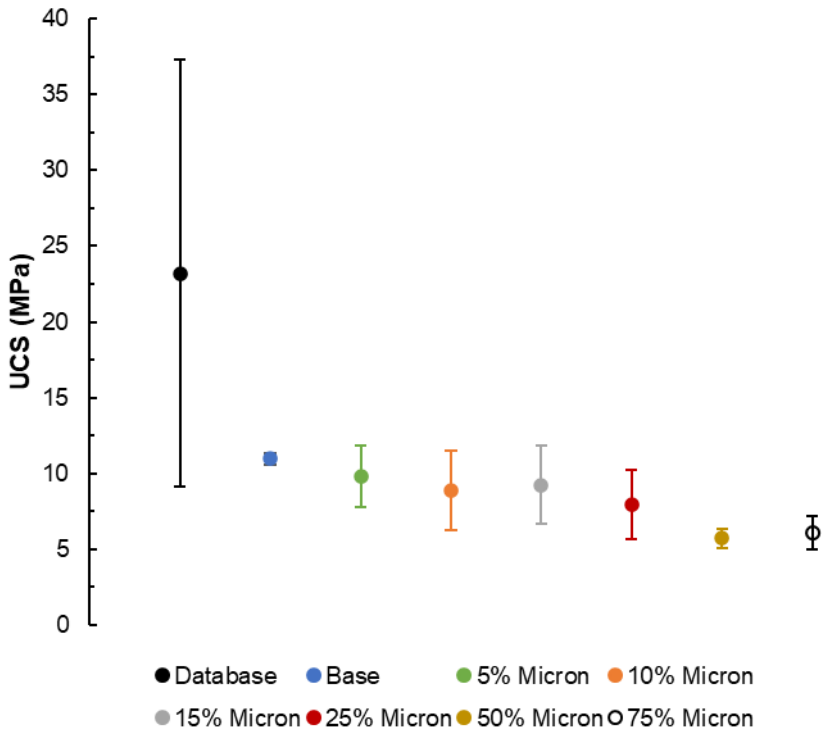

Figure 6.41. Addition of micron shale to cement UCS comparison.

It is seen that *UCS* decreases as the amount of micron shale addition to the cement is increased. An interesting increase in *UCS* between 10% and 15% micron shale can be seen as well as between 50% and 75% micron shale addition. Smaller differences in *UCS* within the 50% and 75% micron samples are also seen.

A comparison between the quantity of submicron shale on *UCS* to previously reported values for class G and H cement is shown in Fig. 6.42 (Wise et al., 2020).

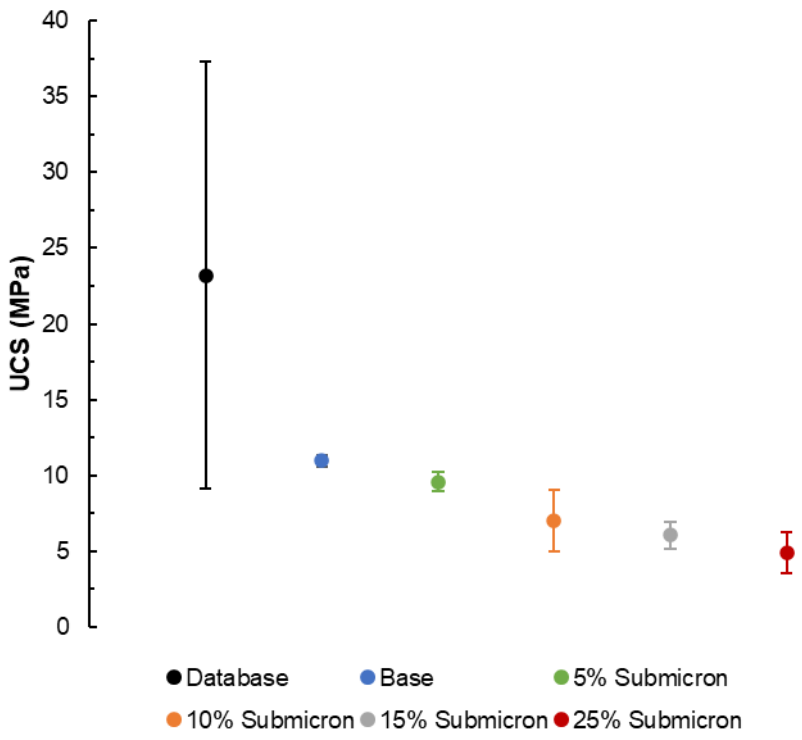

Figure 6.42. Addition of submicron sample to cement UCS comparison.

The *UCS* for cement containing submicron shale decreases linearly with the addition of shale. This is interesting because smaller particles have a higher surface area which in theory, allows for increased nucleation points and increased hydration.

From the single-factor ANOVA results shown in Table 6.5, it can be seen that the percentage of millimeter and submicron shale does not have an effect on the mechanical properties of cement therefore validating the null hypothesis; this is validated by the P-values for these samples being less than the alpha value, or 0.05. The percentage of micron shale added to cement, however, does have an effect on the mechanical properties as the P-values is greater than 0.05. For all shale sizes, it can be seen that the concentration of shale has an effect on the mechanical properties thus proving the null hypotheses invalid. This is shown by the P-values being greater than 0.05.

UCS results from a previous study by Cedola et al. (2020), which described the effect of 5%, 10%, and 15% millimeter, micron, and submicron cuttings addition on the mechanical properties of cement after 7-days curing, were compared to the results found in this study. It can be seen that for both short-term and long-term curing times, average base case results proved to achieve higher strengths than those with shale. In both cases, it was seen that the millimeter samples have inferior strengths in comparison to the micron samples. For the long-term study, the average *UCS* for the 5% submicron samples was closest to that of the base case.

SEM images of the 15% shale sample 10 clearly shows the variation in both composition and structure between the shale and cement. The cement is clearly smoother and darker than the surrounding cement material and the area between the two is platy and angular. It is apparent from secondary electron images that the shale is elevated in comparison to the surrounding matrix. BSE images of sample 10 clearly show that a shale particle appearing darker than the surrounding material. Fig. 6.18.(d) also shows lighter spherical C-S-H particles. SEM for sample 11 containing 15% millimeter shale shows that ettringite, thin, needle-like structures, are dense even at a magnification of 985x. At higher magnifications, it is apparent that the ettringite crystals form at various nucleation sites and start to connect with needles initiating from other sites. A microcrack can also be seen and it is evident that there may be compositional variations occurring on either side of it as evidenced by the lower portion of the image being darker. The topography within the sample is consistent. The BSE images show that the composition is fairly homogenous; in Fig. 6.19.(c), a smooth, angular shale particle is slightly darker than the surrounding matrix indicating a difference in chemical composition. Sample 11 had the lowest *UCS* of the 15% millimeter sample set and could be due to the lack of CH and C-S-H that was formed during hydration. For the 15% millimeter shale sample 12, a large void and a number of

large shale particles are apparent at low magnification. At higher magnification, predominant microstructures present include ettringite needles and CH. Secondary electron images show that there are regions of the surface that are slightly elevated. BSE images show that there does is some charging occurring in sample 12, but from Fig. 6.20.(d), it can be seen that the partially hydrated cement is darker in color than the surrounding structures. This is also true of the linear rod-like structures, which is likely CH. Sample 12 had the highest *UCS* of the three 15% millimeter samples and show that the shale was able to bond with the cement indicating that the addition of shale to cement could positively impact compressive strength. Sample 11 had the lowest *UCS* of the sample set and while dense areas of ettringite were present, long microcracks were evident implying and could have led to a decrease in strength.

For the 50% millimeter samples, SEM images are fairly similar. Sample 16 shows thin, linear structures within the matrix and at high magnifications, triangular structures, likely tobermorite, were present near a microcrack. BSE images show that the matrix of sample 16 is predominantly homogenous; small clusters of C-S-H did are brighter than the surrounding material. The tobermorite also varies in brightness, which makes sense due to varying chemical structure than other particles. Secondary electron images show that there is a concave portion on the surface and the C-S-H and tobermorite particles are raised, C-S-H more so. Ettringite needles were present within sample 17 but are less prevalent than was seen in the 15% millimeter shale samples where ettringite was occurring. Smoother, more rounded C-S-H particles were also seen near areas with ettringite. It can be seen that the BSE images show a uniform composition but at higher magnifications the occurrence of charging can be seen. From SEM images of sample 18, an understanding of the interaction between cement and shale is shown. Shale, which is the smooth, bedded structure, has begun to bond with the cement as shown in the high magnification

secondary electron images. Ettringite and C-S-H are shown to be nucleating on the shale, thus indicating that a reaction has occurred. Ettringite also seems to be surrounding a majority of the shale particle and at 2,554x magnification, the cement particles may actually be bonded to a portion of the shale. It is apparent that the shale is nearly the same brightness/color contrast as the surrounding matrix, meaning that the shale is of similar composition to the cement. Of the 50% millimeter samples, sample 16 had the lowest *UCS* and could be due to the occurrence of microcracking or tobermorite rather than other hydration products such as C-S-H and CH. While samples 17 and 18 had a similar *UCS*, sample 18 achieved a slightly higher *UCS*; this could be indicative of the success of shale bonding to the cement as evidenced by the BSE and secondary electron images.

5% submicron shale SEM images have more spherical particles than either the 15% and 50% millimeter shale samples. Sample 40 shows a submicron shale particle that has a thin, smooth, platy structure that is elevated within the cement. There is little to no presence of ettringite implying that the shale did not reliably bond to the cement. A number of unhydrated and partially hydrated cement particles can also be seen in the same area of the shale particle. This could imply that there was a lack of water to appropriately hydrate the particles. From secondary electron images, it can be seen that the shale particle is raised within the cement with areas of the shale being higher than others. Fig. 6.30. (e) shows areas of dense spherical C-S-H on the edge of the smooth shale. Sample 41 showed some presence of ettringite, but it is not present in large quantities. CH and C-S-H, the two most critical cement hydration products, occur in higher concentrations. BSE images of sample 42 show a fairly homogenous composition aside from the partially hydrated cement particles where the unhydrated center is significantly lighter than the matrix. Secondary electron images in Fig. 6.32.(c) and (d) show that there are spherical and

rectangular particles within the predominantly rodlike matrix. Fig. 6.32. (e) and (f) show more spherical and platy particles. From *UCS* testing for the 5% submicron shale addition to cement, sample 40 had the highest *UCS* and from SEM it can be seen that there are large amounts of CH and C-S-H, two of the primary cement hydration products within the sample, even around shale particles. Secondary electron images show that there are some shale particles that are raised above the matrix while others are within the cement. Sample 42 had the lowest *UCS* of the sample set and from SEM images there is less CH and C-S-H present but more C-S-H gel. For the three 5% submicron samples, there is not a significant amount of ettringite.

For the 10% submicron samples, similar structures to those seen in both the millimeter and 5% submicron samples are observed. For sample 43, Fig. 6.33. (b) shows that there are streaks that are darker than the surrounding matrix implying that there may be variation in hydration products, possibly due to the addition of the submicron shale. Fig. 6.36.(d) shows that a smooth, platy shale particle is slightly lighter than the surrounding material. Secondary electron images show that there is little variation in topography occurring at low magnifications of sample 43. At higher magnifications, dense, spherical particles of conglomerated C-S-H can be seen with some of the agglomerated particles having thin ettringite needles protruding from the C-S-H. Secondary electron images of sample 44 show that the surface topography seems to vary slightly; at high magnifications it can be seen that the rod CH particle is raised within the matrix. Fig. 6.37.(f) shows the angularity and platy-like structure of the CH in comparison to the bulbous C-S-H particles. Sample 45 secondary electron images show that the topography of the surface is fairly smooth; at high magnifications, there is a slightly raised area where the cement is bonding to the partially hydrated grain, but this elevation is minimal. The edges of the partially hydrated cement particle are more angular and there is an evident distinction between the smooth,

unhydrated portion and the partially hydrated portion. C-S-H and ettringite are also present at the interface. At low magnification, BSE images show a number of partially hydrated cement particles and a number of pores. The center of the partially hydrated cement is the cement that has not been hydrated and is much lighter than the surrounding material; while the outer area of these particles is somewhat darker than the unhydrated cement, it is not homogeneous to the matrix.

EDS is performed at a low resolution as well as at higher resolutions to observe whether chemical compositions varied significantly both at a large scale as well as over a smaller scale. Areas and points are used in the EDS analyses; points were specifically selected when it appeared that the minerology differed. From the Central Plains Cement mill sheet, the presence of calcium, oxygen, and silica were expected to be the primary constituents of the matrix with smaller quantities of aluminum, iron, magnesium, and sulfur as well as various elements attributed to the insoluble residue and is shown in Table 6.6.

Table 6.6. Central Plains class H cement chemical composition.

Compound	Amount in Cement (%)
SiO_2	21.4
Al_2O_3	3.2
Fe_2O_3	5.3
CaO	63.4
MgO	1.7
SO_3	2.4
Loss on Ignition	0.9
Na Eq.	0.40
Insoluble Residue	0.28
Free Lime	0.6

EDS results for the 15% mm, 50% mm, 5% submicron, and 10% submicron samples are shown in Table 6.7.

Table 6.7. EDS results for the 15% mm, 50% mm, 5% submicron, and 10% submicron cement samples.

Description	Sample #	Point	Element										
			C	O	Na	Mg	Al	Si	S	K	Ca	Fe	Trace Elements
15% mm	10	1	71.0	8.3	0.6	0.5	1.3	1.8	1.1	0.1	0.1	0.1	15.2
		2	21.9	41.1	1.8	1.6	8.4	16.8	0.7	1.7	1.7	0.9	3.4
		3	0.0	47.7	1.2	1.5	3.9	5.0	0.2	8.7	24.3	1.2	6.3
		4	0.0	38.1	9.6	7.5	8.7	10.5	11.5	1.7	1.4	0.3	10.8
		5	75.7	17.9	1.0	0.7	0.9	1.2	0.9	04	0.5	0.1	0.8
		6	76.1	10.4	0.8	0.9	1.7	1.9	0.6	0.1	0.0	0.0	7.4
		7	0.0	33.7	1.5	7.6	21.3	26.1	0.0	2.8	1.2	1.9	3.9
		8	0.0	44.5	1.8	4.8	18.0	25.7	0.3	1.8	0.1	0.3	2.7
		9	0.0	42.3	3.1	4.0	16.1	25.9	2.3	1.9	0.8	0.5	3.1
		10	0.0	41.8	3.5	2.4	14.2	28.9	2.8	2.1	0.1	1.4	2.9
	11	1	0.0	46.9	1.3	0.0	3.4	5.1	0.0	9.4	28.0	1.5	4.5
		2	17.1	38.0	0.8	0.8	7.6	13.5	0.0	1.1	0.6	1.0	19.6
	12	1	0.0	47.4	0.0	0.9	3.3	5.4	0.0	9.5	29.6	1.6	2.5
		2	0.0	27.7	6.5	5.9	14.0	23.7	8.9	3.4	3.7	0.0	6.3
		3	0.0	49.8	1.0	1.2	3.8	6.2	0.0	7.9	26.1	1.2	2.9
		4	0.0	38.2	5.5	4.1	8.2	13.1	15.1	1.8	1.7	0.0	12.4
		5	0.0	32.5	5.3	4.3	9.1	16.9	16.8	1.9	2.5	0.0	10.8
		6	21.3	42.7	1.3	0.6	7.2	14.6	0.4	2.5	5.1	1.3	3.0
		7	6.4	44.4	0.7	0.7	5.3	8.7	0.4	7.1	20.7	1.2	4.3
50% mm	16	1	3.3	41.9	0.0	0.0	1.6	4.6	0.4	5.6	22.9	1.4	18.3
		2	6.3	45.0	0.3	0.5	1.8	5.9	0.5	5.8	29.0	1.8	2.9
		3	0.9	31.4	0.0	0.0	1.4	3.5	0.0	11.1	35.1	2.7	13.9
		4	1.1	30.0	0.0	0.0	2.9	3.6	0.0	8.9	34.4	1.8	17.3
	17	1	17.2	36.2	0.3	0.0	8.8	12.6	0.0	1.7	1.1	1.5	20.5
		2	19.0	39.7	0.7	0.2	6.1	17.0	0.6	0.8	0.2	0.0	15.7
		3	0.0	50.0	0.0	1.0	3.4	5.8	0.0	9.1	26.9	1.4	2.5
		4	0.0	41.7	0.0	0.0	0.7	1.7	0.0	11.3	38.5	0.0	6.1
		5	0.0	48.8	0.0	0.0	3.5	5.8	0.0	9.2	28.7	1.5	2.6
	18	1	0.0	44.9	0.4	0.8	3.7	5.0	0.3	10.3	27.1	1.4	6.1
		2	0.0	41.6	1.9	4.7	18.2	23.8	1.2	2.7	1.4	1.5	3.0
		3	0.0	44.9	0.9	1.5	4.7	5.4	0.3	10.8	23.4	1.0	7.2
		4	0.0	51.7	0.8	1.0	3.9	7.5	0.7	6.9	25.0	0.8	1.7
		5	0.6	34.7	0.0	0.0	0.0	0.2	0.1	11.6	47.3	0.2	5.3
		6	2.0	51.4	0.9	1.5	3.3	8.9	0.9	5.7	22.8	0.5	2.1
		7	1.6	33.9	0.0	1.5	1.0	8.7	1.0	2.1	38.1	1.7	10.6
		8	2.3	30.2	0.1	0.4	0.9	7.5	0.0	4.9	41.9	0.3	11.6
		9	1.9	34.8	0.0	0.7	1.4	9.8	0.6	5.0	33.5	0.7	11.8
5% submicron	40	1	4.5	49.6	1.1	1.0	3.2	5.4	0.3	8.0	24.2	1.3	1.4
		2	0.0	56.2	0.9	1.0	1.4	7.1	0.8	1.3	29.0	1.5	0.9
		3	4.8	45.3	0.7	0.7	1.5	4.6	0.4	4.2	21.7	1.2	15.0
		4	0.0	0.0	16.0	6.9	5.9	7.3	8.4	38	23.2	0.4	28.1
		5	0.0	38.2	0.3	0.2	1.4	11.0	0.3	2.5	43.7	1.3	1.2
		6	16.7	44.2	0.8	0.7	1.7	5.3	0.5	4.8	23.3	1.2	0.9
		7	0.0	50.5	0.3	0.3	0.7	6.5	0.7	0.0	37.8	1.9	1.3
		8	0.0	30.9	0.0	0.2	0.0	9.0	0.0	0.2	57.5	0.5	1.8
		9	0.0	51.5	0.7	0.8	1.3	6.7	0.7	1.6	33.3	1.9	1.6
		10	5.0	46.9	0.8	0.7	0.0	5.1	0.5	2.9	23.5	1.3	13.4
	41	1	3.0	48.5	0.5	0.7	2.4	6.1	0.4	7.6	29.1	1.6	0.1
		2	3.7	47.1	0.6	0.7	1.8	5.9	0.5	5.6	30.2	1.9	2.0
		3	4.5	51.2	0.8	0.9	1.8	6.1	0.5	4.6	27.3	1.6	0.7
		4	7.7	49.1	1.0	1.0	2.4	5.9	0.5	6.2	24.2	1.3	0.9
		5	11.5	41.9	1.2	1.1	2.4	6.6	0.0	7.4	26.6	0.1	1.3
		6	61.5	29.0	2.2	0.4	0.3	0.3	0.8	0.9	0.7	0.1	5.3
		7	4.1	44.2	0.5	1.0	1.9	4.3	0.4	3.6	23.4	2.6	26.8

		8	47.6	27.5	1.5	0.5	0.7	1.4	0.7	4.0	14.4	0.2	2.8
		9	1.9	53.2	1.3	1.3	3.3	5.9	0.5	6.0	23.2	1.3	1.6
	42	1	0.0	45.4	1.3	1.7	4.3	5.2	0.3	10.0	23.5	1.0	7.5
		2	4.7	49.9	1.3	0.9	2.8	5.5	0.4	7.4	23.8	1.5	2.0
		3	4.1	52.7	1.7	1.2	3.6	5.5	0.4	7.9	20.4	1.3	1.5
10% submicron	43	1	0.0	40.2	1.3	1.0	0.0	0.0	0.0	0.0	38.7	1.0	0.0
		2	0.0	43.9	0.0	5.2	5.4	2.4	0.0	0.0	20.4	8.0	0.0
		3	6.8	21.5	1.5	0.0	1.8	2.9	11.1	0.0	4.1	14.7	7.2
		4	2.5	52.9	1.8	1.8	4.1	6.3	0.0	0.0	26.0	0.7	4.0
		5	0.0	42.7	0.0	0.0	0.0	0.0	0.0	0.00	46.0	0.0	11.3
		6	0.0	56.3	2.2	0.0	5.2	7.6	0.0	0.0	24.6	0.0	4.1
	44	1	0.0	50.3	1.8	0.0	5.5	7.3	0.0	0.00	27.7	1.6	6.0
		2	4.0	44.1	0.7	0.5	2.1	5.2	0.0	5.6	20.8	1.2	15.8
		3	4.8	34.2	0.4	0.0	9.3	15.5	0.0	8.5	20.6	5.1	1.9
		4	51.4	29.4	0.0	0.0	2.2	2.6	2.6	3.1	6.6	0.0	2.1
		5	0.0	31.3	0.0	0.0	4.7	6.7	0.0	15.4	35.0	0.0	6.9
		6	0.0	47.8	1.7	0.0	4.9	8.0	0.5	8.6	24.7	0.9	3.0
		7	0.0	32.3	0.0	1.9	4.3	7.6	0.0	0.0	41.5	0.0	12.4
		8	0.0	46.6	0.0	1.5	4.5	7.1	0.0	0.0	30.1	1.4	8.8
	45	1	0.0	0.0	0.0	0.0	3.5	5.7	0.0	9.3	30.0	1.8	49.8
		2	0.0	39.2	0.0	0.0	4.9	6.4	0.0	0.0	31.9	1.6	16.1
		3	0.0	26.7	0.0	0.0	4.1	6.7	0.0	0.0	46.9	0.0	15.5
		4	0.0	23.5	0.0	0.0	3.7	7.3	0.0	13.1	45.4	0.0	7.1
		5	10.0	22.7	0.0	0.0	3.4	9.5	0.0	0.0	40.5	0.0	13.9
		6	0.0	44.2	0.0	0.0	4.1	6.1	0.0	9.6	29.5	1.8	4.7
		7	0.0	47.1	0.0	7.5	7.2	1.2	0.0	0.0	24.0	10.5	2.5
		8	7.0	37.1	1.3	0.0	10.2	16.5	1.2	0.0	17.2	5.5	4.1
		9	0.0	46.1	0.0	0.0	3.6	6.7	0.5	9.0	30.8	1.5	1.9

In this table, the major elemental constituents of the sample locations as well as the trace elements, or the elements that are not common in all samples, are shown. Evidence of Woodford shale particles are evident by the presence of carbon. Areas containing both cement and shale contain carbon, but in lower amounts than the areas of pure shale. EDS analysis for the 15% millimeter samples are highly similar. For sample 10, four of the sample locations had the presence of carbon. Locations 1, 5, and 6 had approximately 75% carbon content while location 2 had nearly 22% carbon content. The three locations with the highest amount of carbon also have the lowest amounts of oxygen which implies the presence of shale and little to no cement. In the locations without carbon, silicon, aluminum, calcium, sodium, potassium and magnesium are present with higher amounts of oxygen. Of the two areas where EDS is performed on sample 11, point 1 is highly cementitious while point 2 has the presence of shale as evidenced by the

presence of carbon. Point 1 has an oxygen content of nearly 47% with smaller concentrations of calcium, potassium, silicon, sodium, aluminum, potassium and iron. Point 2 also has a fairly high amount of oxygen, 38%, and less amounts of silicon, aluminum, potassium, iron, calcium, and carbon. Because the EDS is performed over an area rather than a specific point, it can be said that there is a presence of both shale and cement within point 2. Fig. 6.8 shows the 7 locations where EDS is performed on sample 12. Points 2, 4, and 5 are darker than the other locations and are assumed to be shale, but from the elemental analysis only points 6 and 7 show the presence of carbon indicating that shale is present within the location areas. All sampled locations show that oxygen is the most prevalent element followed by calcium, silicon, sodium, aluminum, and potassium.

The 50% millimeter EDS results are consistent with one another, and the presence of shale is more prevalent in these three samples. For sample 16, all four of the points where EDS is performed had a presence of carbon. Point 1 has approximately 3% carbon, point 2 has roughly 6% carbon, point 3 has less than 1% carbon, and point 4 has about 2% carbon. This implies that there is most likely a varying degree of shale within the sample locations. Aside from the presence of carbon, EDS results show that there were high amounts of oxygen and calcium present at all points meaning that there is also a significant amount of cement. Lower amounts of aluminum, silicon, potassium and iron are also observed. EDS on sample 17 show that points 1 and 2 have the presence of carbon while the other 3 points do not. Points 3, 4, and 5 have higher amounts of oxygen and calcium than the points with carbon indicating a higher amount of cement. Sample 18 has the presence of carbon in 5 of the 9 EDS locations but the carbon was present in small amounts ranging from 0.5% to 2.3%. Oxygen content is higher in the samples without carbon. All points also had high amounts of calcium except for point 2, which has a

higher silicon and aluminum content than the other sample locations. This could also be somewhat indicative of the presence of shale.

For the 5% submicron samples, shale is detected in two of the three samples as evidenced by the presence of carbon. EDS weight percent results for the 5% submicron shale samples are all in good agreement with one another; calcium and oxygen are the two most prevalent elements with trace amounts of potassium, silicon, sulfur, iron, and sodium. Sample 40 shows that shale is present within the selected areas. For sample 41, there are two locations that have a significantly higher carbon and sodium content, points 6 and 8, indicating the presence of shale; all other elements are significantly lower than the cement. This is in agreement with the BSE images that show that these areas are darker than the surrounding matrix. Locations where EDS was performed on sample 42 are all in good agreement with one another and there was no location that showed elevated carbon content indicating that there was no evidence of shale present in this location. The cement material is primarily composed of oxygen and calcium, which is in agreement with the Central Plains Cement mill report.

For the 10% submicron samples, oxygen and calcium are the most present elements at all samples locations. For sample 43, locations 3 and 4 have the presence of carbon thus implying that there could be the presence of shale. Location 3 also has very low calcium content but higher iron and sulfur content. Of the 8 locations where EDS was performed on sample 44, 3 locations, 2, 3, and 4, show the presence of carbon. Location 4 is shown to be composed of over 50% carbon and a low amount of calcium, indicating that there is most likely a high amount of shale. For sample 45, only two of the nine locations where EDS was performed have any trace of shale, locations 5 and 8. Along with having the presence of carbon, these two locations also have

higher silicon content than the other locations. These locations are darker than the surrounding areas on the sample surface.

6.2.5. Conclusions

Understanding the effect of cuttings on wellbore cement mechanical properties allows for an understanding as to the feasibility of an environmentally friendly, readily available, upcycled material. Utilization of cuttings as a cement additive or replacement material is not just beneficial in that it minimizes the need for cuttings removal and recycling, but also that it reduces the amount of greenhouse gas emissions, specifically CO_2 associated with cement manufacturing. While this research is only the first step to the potential of utilizing cuttings as a wellbore cement additive, a number of insights were gained that may be beneficial for future applications.

1. While the submicron samples containing 50% and 75% shale split during the curing process, the samples that were tested have a fairly linear decrease in *UCS* with increased shale content.
2. For the millimeter and micron sample sets, the 75% average *UCS* values were similar and, in both cases, were greater than the samples containing 50% shale but the 75% sample sets had larger standard deviations. The 75% shale sample sets for both the millimeter and micron shale have the lowest *UCS* of all sample sets with the same particle size, meaning that the 50% sample sets all have fairly similar *UCS* values and may be more accurate.
3. While the base case samples, or samples containing zero shale, achieved the highest average *UCS*, micron samples with 5%, 10%, 15% and 25% shale addition had at least one sample that had a comparable *UCS*. The micron samples prove to have the highest

average *UCS* for all sample sets. The micron sample sets have the best results of all samples containing shale. This could be due to the fact that the micron shale particles were the most similar in size to that of the class H cement provided by Central Plains Cement Company. Having additives with larger or smaller particle size in comparison to the cement can have an effect on the hydration and permeability of the system. Ideally, cement particles should be between 7-200 microns (Zhang, 2011).

4. Future work should be conducted to further understand the effect of shale on cement mechanical properties. Determination of the Blaine fineness of the millimeter, micron, and submicron shale should be performed to understand the particle size of these additives in comparison to the cement, research on the rheology of cement with calcined clay showed that smaller particle size may lead to an increased yield point (Murtaza et al., 2020). Another aspect that needs to be considered is the rheology, consistency and thickening time of cement containing shale and how various sizes could impact pumpability (Mohamed et al., 2022). An understanding of the ideal w/c ratio needed to properly hydrate the slurries with this novel pozzolanic additive. It has been noted that pozzolanic materials such as fly ash require an increase in the amount of water needed for hydration, so using the conventional API water-cement ratio may not be ideal for shale or cuttings cements (Smith, 1987).

6.3. Utilizing Drill Cuttings as a Wellbore Cement Additive and the Effect on Unconfined Compressive Strength

OU, in collaboration with ConocoPhillips, has performed testing on a ConocoPhillips Eagle Ford cement blend to investigate and understand the effect of Eagle Ford cuttings on the mechanical properties of wellbore cement. The Eagle Ford is located in South Texas and wells are required

to meet the Texas Railroad Commissions' standards for cementing a wellbore, one of which is that wellbore cement must achieve a 250 psi compressive strength within 24-hours of placement in a wellbore. In this study, experiments in which dried water based drill cuttings from La Salle County, Texas (~2,000' TVD) and dried oil based drill cuttings from a Cheyenne Irvin 15H lateral well (~10,998' TVD) provided by Fluid Pro LLC were used as an additive within a ConocoPhillips cement blend to investigate the effect of drill cuttings on the mechanical properties of cement.

6.3.1. Introduction

The Eagle Ford shale play has become one of the largest gas shale plays in the world since its discovery in 2008 (Speight, 2017). The Eagle Ford shale encompasses a 20,000 square mile area in South Texas and is divided up into the Upper Shale Unit and the Lower Shale Unit (Kuuskraa, 2019).

6.3.2. Methodology

In order to create more uniform particles, water and oil based cuttings are separately ground using a Retsch EMAX grinder at 1,000 RPM's for 30 minutes. Particle size was initially performed using a Beckman Coulter LS 13 320 SW Laser Diffraction Particle Size Analyzer but clumping of the particles was observed and yielded inaccurate readings. To obtain more accurate results, a Zeiss Neon 40 microscope and an INCA Energy 250 Energy Dispersive X-ray Microanalysis system located in the Samuel Roberts Noble Microscopy lab on the OU-Norman campus are used to determine particle size and chemical composition of the cuttings. Prior to being placed in the SEM, the particles are sputter-coated with a small layer of iridium to ensure that the samples will be conductive.

Moisture content is also performed on the water and oil based cuttings by taking the weight of the cuttings, placing them in a 150˚F oven for 7 days, and then re-weighed to determine how much moisture is lost.

9 Energy provided a "Pilot Blend" slurry sheet from a Pleasonton, Texas lab location that was used to create the novel cement blends. The base blend (i.e. the slurry provided by 9 Energy), as well as the newly created sample compositions with 15%, 25%, 32% and 40% cuttings addition are shown in Table 6.8.

Table 6.8. Cement composition with cuttings.

Item	**Base**	**15%**	**25%**	**32%**	**40%**
Type I/II Pozz. Mix (g)	368.5	313.2	276.4	250.6	221.1
Cuttings (g)	-	55.3	92.1	117.9	147.4
KCl (g)	14.2	14.2	14.2	14.2	14.2
CPT-45 (g)	3.7	3.7	3.7	3.7	3.7
CPT-503P (g)	1.5	1.5	1.5	1.5	1.5
CPT-20A (g)	0.7	0.7	0.7	0.7	0.7
Citric Acid (g)	0.7	0.7	0.7	0.7	0.7
Water (g)	474.1	474.1	474.1	474.1	474.1

All additives are included in equal quantities as the initial "base blend" with only the cement and cuttings content varying; the amount of cuttings added is subtracted from the total amount of cement thus keeping the by-weight-of-solid (BWOS) content constant. It should be noted that DI water was used to create all slurries to minimize contamination. Oil based cuttings were used in the amount of 32% to observe the effects of oil based cuttings to water based cuttings. No changes to the slurry were done for the oil based sample preparation.

The slurries are mixed according to ASTM-C109/C109M-21 standards using a Chandler-Ametek blender and an Ofite 8-specimen brass cement mold is used to cast the samples. To determine whether the samples with cuttings meet this requirement, 2” by 2” cubic samples have been

made according to API 10RB and cured at ambient pressure and temperature for 24 hours before being tested using an AutoLab-500 system. Curing is done at atmospheric conditions. Each slurry produced four specimen. To prevent leakage, Super Lube Synthetic Grease is applied on all sides of the bottom portion of each mold. After 24-hours, the samples are removed from the mold. Prior to testing, length and height measurements are taken for all samples and averages have been calculated. Weight is also taken to determine whether there is a significant difference between samples and slurries. Table 6.9 shows a summary of the 24-hour sample measurements. Due to the fragility of the samples, polishing was not performed. To ensure accurate results, any samples that has considerable abnormalities (i.e. highly uneven surfaces or large pieces that broke off when de-molding) are not tested. Samples were tested on a New England Research Autolab-500 test system (Fig. 6.43 a). Within the test chamber, samples are placed on a four-inch diameter base plate and a two-inch diameter top plate is placed on the upper portion of the sample to assure that the force is evenly distributed (Fig. 6.43 b).

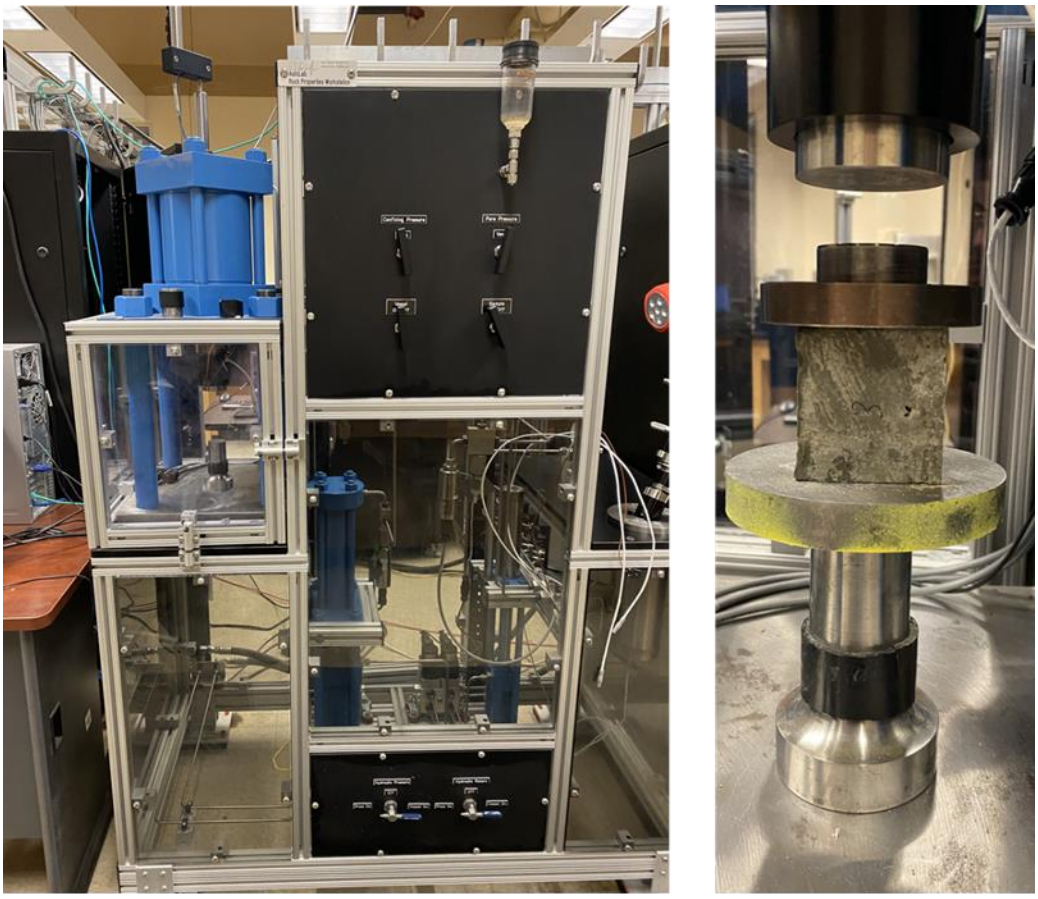

(a) (b)

Figure 6.43. a) New England Research Autolab-500 test system; b) Test setup.

Table 6.9. 24-hour sample measurements.

Slurry	Sample Number	Date Made	Date Tested	Avg. Length (in)	Avg. Height (in)	Weight (g)	Density (ppg)
Base	1	2/17/2022	2/18/2022	2.0	1.6	154.5	11.9
	2	2/17/2022	2/18/2022	2.0	1.7	159.6	11.8
	3	2/17/2022	2/18/2022	2.0	2.0	179.4	11.4
	4	2/17/2022	2/18/2022	2.0	1.7	150.1	11.6
15%	1	2/22/2022	2/23/2022	2.0	1.9	167.7	10.7
	2	2/22/2022	2/23/2022	2.0	2.0	176.5	11.5
	3	2/22/2022	2/23/2022	2.0	2.0	179.6	11.7
	4	2/22/2022	2/23/2022	2.0	1.8	166.7	11.7
25%	1	2/22/2022	2/23/2022	2.0	1.6	147.6	12.0
	2	2/22/2022	2/23/2022	2.0	1.6	147.8	12.0
32% Water	1	3/1/2022	3/2/2022	2.0	1.8	161.8	11.7
	2	3/1/2022	3/2/2022	2.0	1.7	156.5	11.6
	3	3/1/2022	3/2/2022	2.0	1.7	161.2	12.0
32% Oil	1	3/1/2022	3/2/2022	2.0	1.6	147.3	11.5
	2	3/1/2022	3/2/2022	2.0	1.6	147.8	12.2
	3	3/1/2022	3/2/2022	2.0	1.6	151.5	12.0
40%	1	2/28/2022	3/1/2022	2.0	1.6	146.3	12.1

	2	2/28/2022	3/1/2022	2.0	1.6	141.7	11.9
	3	2/28/2022	3/1/2022	2.0	1.6	144.2	11.9
	4	2/28/2022	3/1/2022	2.0	1.6	143.3	11.5

6.3.3. Results

Particle size analysis on the dried water based cuttings show average particle size to be 505.8 micron with a 388.8 micron standard deviation. The dried oil based cuttings are sieved and particles are found to be larger than 0.02 inches. Average particle size for the dried water based cuttings is determined by SEM analysis and was found to be 33.5 microns, significantly lower than the particle sizes obtained using laser particle size analysis. Particle size analysis on the dried water based particles at ten locations is shown in Fig. 6.44 and the results summarized in Table 6.10. From the SEM images, there may be some agglomeration occurring after grinding has been performed. EDS is also performed on the dried water based cuttings to determine the chemical composition and observe whether any abnormal elements are present. Figure 6.45 shows the locations of the 5 areas where EDS is performed. It should be noted that spectrum 1 is performed on the total area within the figure. Table 6.11 shows the chemical compositions for EDS performed on the 5 selected locations.

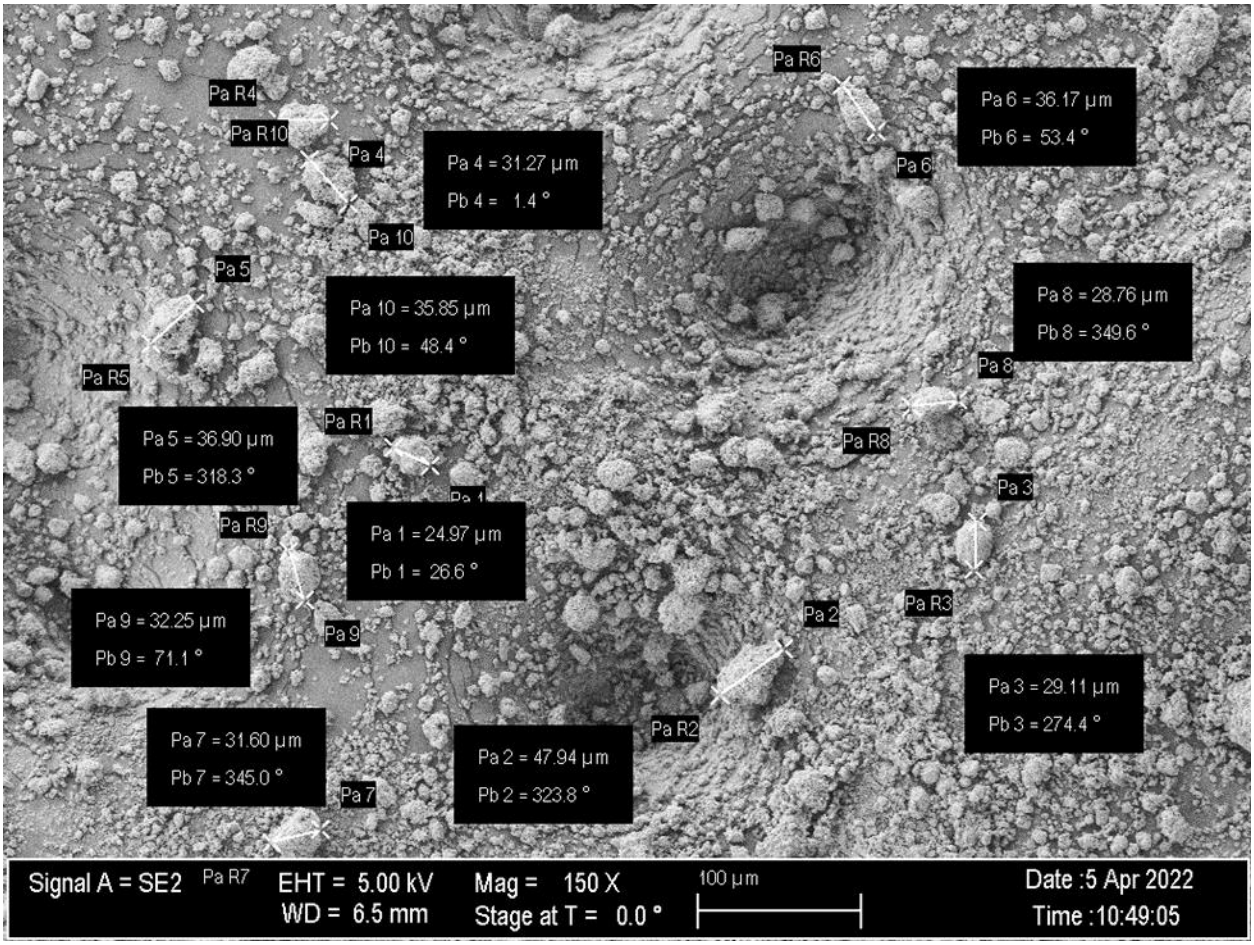

Figure.6.44. Particle size analysis on water based cuttings.

Table 6.10. Results of particle size analysis on water based cuttings.

Particle Number	Particle Size (µm)
1	25.0
2	47.9
3	29.1
4	31.3
5	36.9
6	36.2
7	31.6
8	28.8
9	32.3
10	35.9
Average:	**33.5**

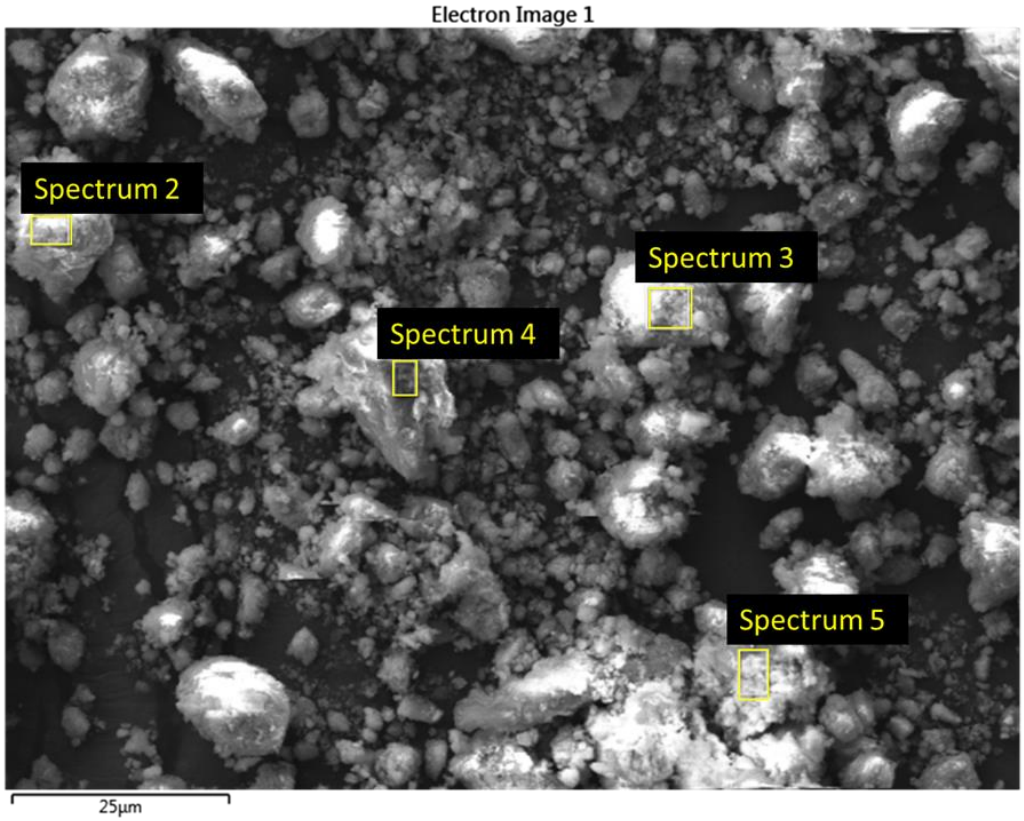

Figure 6.45. EDS sample locations for water based cuttings.

Table 6.11. EDS results for the selected locations on a water based cutting sample.

Element	Spectrum 1 (Wt. %)	Spectrum 2 (Wt. %)	Spectrum 3 (Wt. %)	Spectrum 4 (Wt. %)	Spectrum 5 (Wt. %)
Oxygen	41.0	55.3	49.1	47.7	52.2
Carbon	38.3	13.9	10.6	10.5	15.0
Silicon	10.3	15.7	22.3	21.1	13.2
Aluminum	3.1	4.8	5.0	5.9	6.2
Calcium	2.5	3.8	3.5	6.9	4.9
Iron	2.0	2.9	5.3	3.6	3.2
Potassium	0.9	1.2	1.3	1.6	1.6
Magnesium	0.6	0.8	0.8	0.9	1.7
Sodium	0.5	0.6	0.6	0.5	0.7
Chlorine	0.3	0.3	0.5	0.7	0.6
Sulfur	0.3	0.4	0.9	0.5	0.3
Titanium	0.2	0.2	0.2	-	0.2

Phosphorous	-	0.1	-	0.1	0.1

Moisture content analysis over 7 days shows that the dried water based cuttings have a moisture content of 3.9% while dried oil based cuttings have a moisture content of 8.5%.

UCS results for the four base case samples are shown in Fig. 6.46.

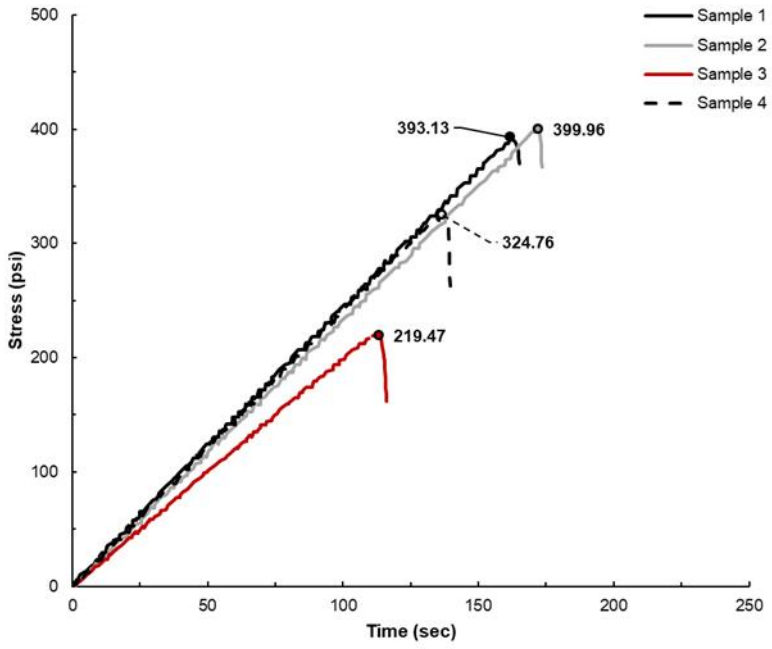

Figure 6.46. 24-hour base case UCS test results.

Test results for the samples made with 15% cuttings addition are shown in Figure 6.47.

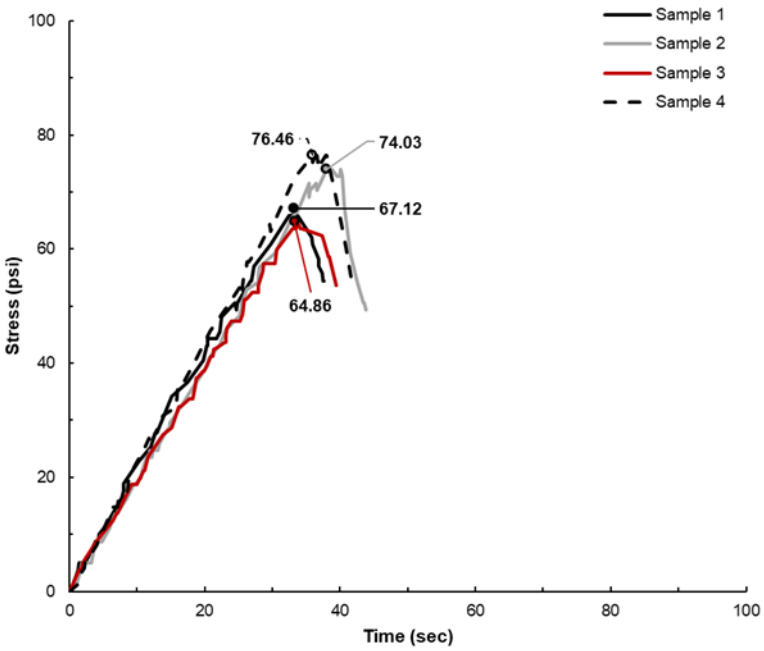

Figure 6.47. 24-hour samples with 15% cuttings addition UCS test results.

UCS test results for the 24-hour samples with 25% dried water based cuttings are shown in Figure 6.48.

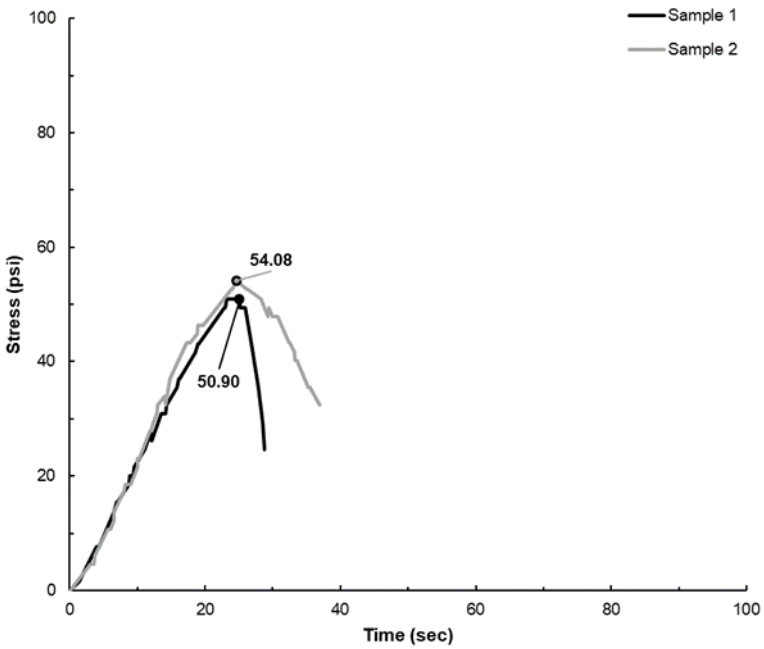

Figure 6.48. 24-hour samples with 25% cuttings addition UCS test results.

Test results for the cement with 32% dried water based cuttings are shown in Figure 6.49.

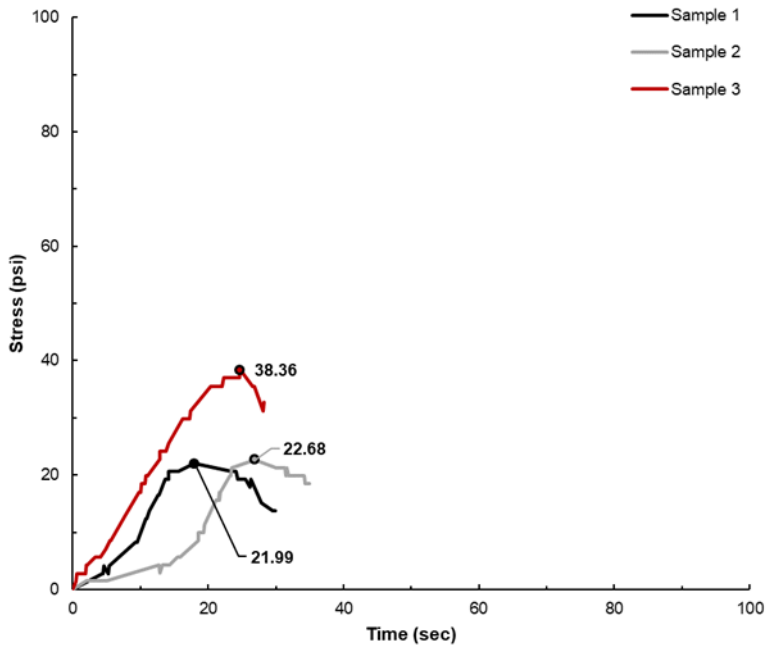

Figure 6.49. 24-hour samples with 32% water based cuttings addition UCS test results.

Test results for the cement with 32% dried oil based cuttings are shown in Figure 6.50.

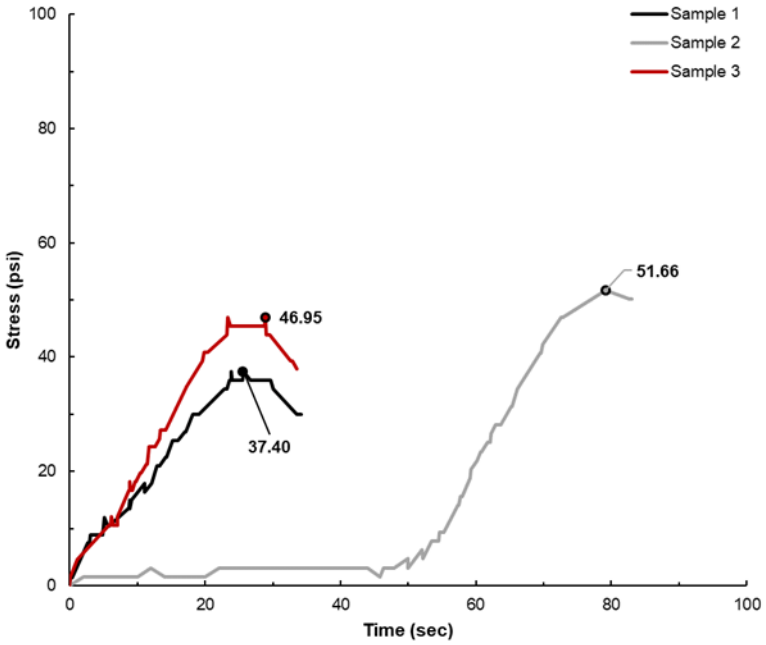

Figure 6.50. 24-hour samples with 32% oil based cuttings addition UCS test results.

Test results for the cement with 40% dried water based cuttings are shown in Figure 6.51.

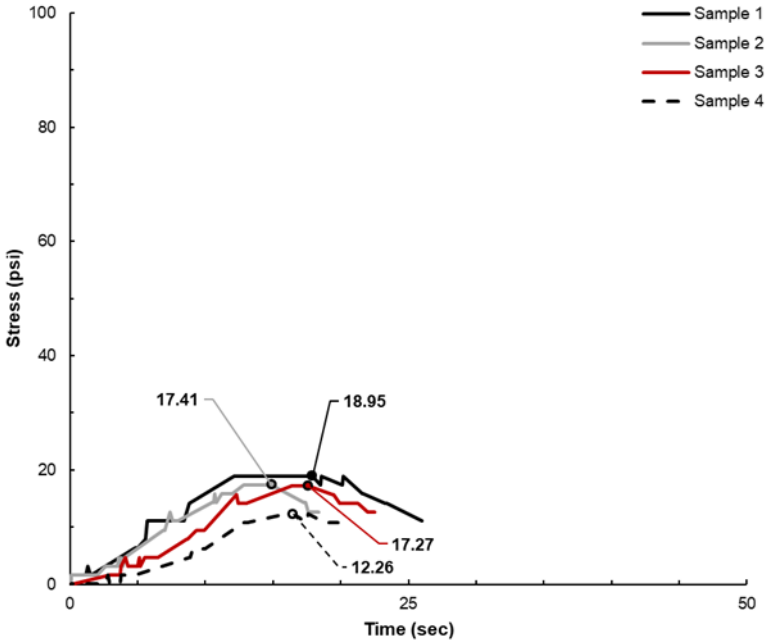

Figure 6.51. 24-hour samples with 40% cuttings addition UCS test results.

A full summary of the 24-hour *UCS*, including average *UCS* and standard deviation for each slurry type, is shown in Table 6.12.

Table 6.12. 24-hour UCS results.

Slurry	Sample Number	UCS (psi)	Average UCS (psi)	Std. Dev.
Base	1	393.1	334.3	70.5
	2	400.0		
	3	219.5		
	4	324.8		
15%	1	67.1	70.6	4.8
	2	74.0		
	3	64.9		
	4	76.5		
25%	1	50.9	52.5	1.6
	2	54.1		
32% Water	1	22.0	27.7	7.6
	2	22.7		
	3	38.4		
32% Oil	1	37.4	45.3	5.9
	2	51.7		
	3	47.0		
40%	1	19.0	16.5	2.5
	2	17.4		
	3	17.3		
	4	12.3		

6.3.4. Discussion

Particle size analysis shows that the dried water based cuttings post grinding have an average particle size of 33.5 microns with a minimum of 25.0 microns and a maximum particle size of 47.9. Agglomeration of particles is observed, but particle size analysis is done on individual grains. The agglomeration is most likely due to the fact that while the water based cuttings are dried, moisture is still present. EDS results show that the water based cuttings are highly carbon-based material with silicon, aluminum, calcium, and iron being the other predominant elements. The high silicon and aluminum content indicates that the Eagle Ford cuttings are indeed an alumino-siliceous material, better known as a pozzolan.

This is indicated by the moisture content that was determined over 7 days. Both the dried oil based and water based cuttings have a lower weight after being heated for 7 days. Any residual drilling fluid on the cuttings could impact the success of utilizing this material as a cement additive or replacement material. This is especially true of the oil based cuttings in that oil infiltration could hinder the hydration process of the cement and further impact placement and bonding within a wellbore.

For the base case, average *UCS* is 334.3 psi for four samples with a standard deviation of 70.5 psi. All but one of the samples exceeded the Texas Railroad Commission (TRC) requirements and are thus feasible for use in a wellbore. Sample 3 has the lowest *UCS* and did not meet the TRC requirements. This low *UCS* could be due to free water remaining in the sample as shown in the weight of the sample. While there are little to no flaws on the surface of the sample, there is a possibility that there was one or more surficial abnormalities that led to a lower *UCS*.

Average *UCS* for the Eagle Ford cement containing 15% cuttings addition is 70.6 psi and standard deviations for samples 1, 2, 3, and 4 is 4.8 psi. Sample 4 has the highest *UCS* of 76.5 psi and has the lowest weight of the tested 15% cuttings samples but also were not highly symmetrical prior to testing. Sample 3 has the lowest *UCS* of 64.9 psi and weighed the most of all the samples yet was relatively symmetric.

Due to flaws in two of the samples made with 25% cuttings, only two samples are able to be tested. *UCS* values are similar, with average *UCS* being 52.5 psi and standard deviations for both samples being 1.6 psi. The two samples are similar in weight and dimension, and shrinkage occurred during the curing period.

Three samples with 32% dried water based cuttings addition are tested. *UCS* values are somewhat similar, with average *UCS* being 27.7 psi and standard deviations being 7.6 psi. The samples are all fairly similar weights and dimensions yet sample 3 had a significantly higher *UCS* than the other two samples, between 41-43% higher. This could be due to the presence of less cuttings in this specific sample or better hydration of the particles.

The samples with 32% dried oil based cuttings show similar trends but have some variance in strength. Average *UCS* for the 32% oil based samples is 45.3 psi with a standard deviation of 5.9 psi. The samples containing 32% oil based cuttings are lighter than the samples made with 32% water based cuttings which could be because the density of the water based mud is higher than the density of the oil used in the drilling fluid. Sample 1 has the lowest *UCS* of 37.4 psi while sample 2 has the highest *UCS*, 51.7 psi. It is interesting to observe that the samples containing 32% oil based cuttings exhibit higher compressive strengths than the 32% water based cuttings. This could indicate that there is something in the oil that could actually benefit cement hydration.

Samples containing 40% cuttings have the lowest *UCS* values and the results were fairly consistent. Average *UCS* for the samples containing 40% cuttings is 16.5 psi with standard deviation being 2.5 psi for the samples. Due to the low strength of the samples, the time required to achieve *UCS* is reduced. The lowest *UCS*, 12.3 psi, is obtained from sample 4 while sample 1 has the max *UCS* of 19.0 psi. These samples are significantly lower than any of the other samples containing cuttings. The weight of the samples containing 40% water based cuttings are also notably lower than any other sample set. When de-molding the cement, the 40% water based cuttings addition samples are noticeably softer and more wet than the other samples, possibly indicating that the cuttings hindered hydration and potentially negatively interact with the additives used in the slurry.

To better understand how the addition as well as concentration of cuttings to cement has on 24-hour strength, normalized strength vs. cuttings concentration for all of the 24-hour cement slurries has been plotted in Fig. 6.52.

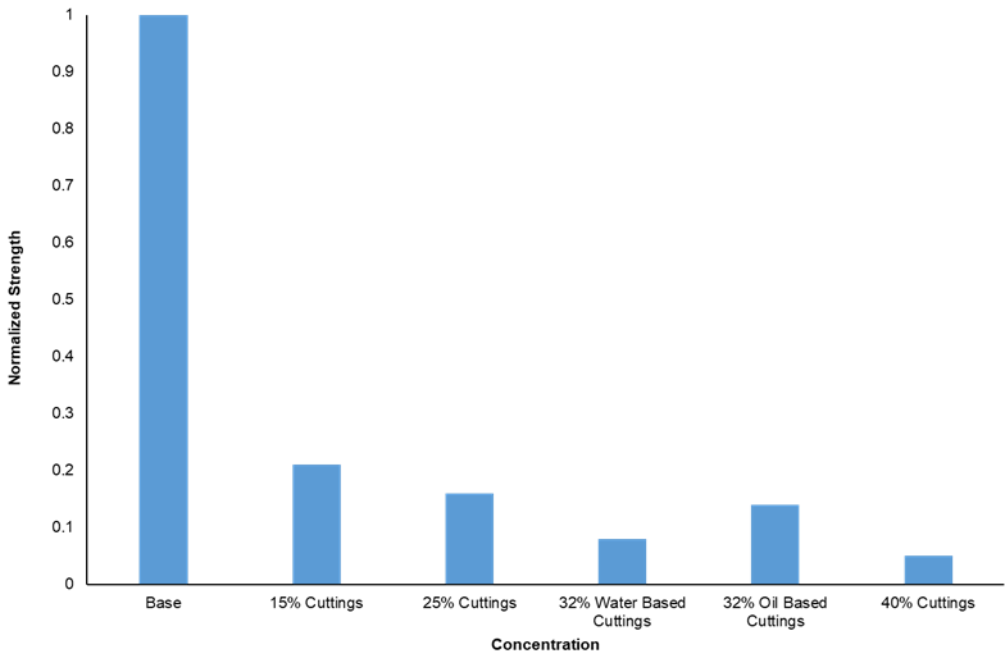

Figure 6.52. Normalized strength vs. cuttings concentration.

It is clear that the addition of cuttings to the cement slurry significantly decreases the 24-hour strength of the samples. With the addition of 15% cuttings, average *UCS* is 79% lower than the average base case *UCS*. Looking at the cement samples with water based cuttings addition, the *UCS* shows a somewhat exponential decline. Increasing the amount of water based cuttings reduces the strength by approximately 21%; from 15% to 25% cuttings addition, average *UCS* decreases by 26%, between 25% to 32% cuttings addition the *UCS* dropped by 47% and increasing cuttings content from 32% to 40% showed a 69% reduction in UCS.

An interesting observation is seen in regards to the addition of 32% dried oil based cuttings. After 24-hours, the samples containing oil based cuttings achiev a higher *UCS* than the 32%

water based cuttings samples. On average, the samples made with dried oil based cuttings have a *UCS* 17.7 psi greater than the water based counterparts. The *UCS* for the 32% oil based cuttings samples is slightly lower (14%) than the samples with 25% water based cuttings. This phenomena shows that the addition of oil based cuttings to cement does not significantly effect cement hydration.

Texas Railroad Commission requires that wellbore cement must achieve 250 psi compressive strength within 24-hours of being placed (16 Tex. Admin. Code §3.13 (2014)). From the 24-hour test results, it can be seen that using the provided cement composition and utilizing cuttings, whether water based or oil based, does not fulfill this requirement. The samples are not heated or pressurized when cured, and this could have a slight impact on the strength of the samples. Water-cement (w/c) ratio was constant for all samples and may have effected the compressive strength of the samples containing cuttings. When using pozzolanic material in cement with a high w/c ratio, early compressive strength is shown to be reduced; decreasing the w/c ratio may help to achieve a higher early compressive strength (Aïtcin, 2016).

Grinding of the cuttings may also help to achieve the necessary 24-hour strength as this would allow for additional surface area leading to faster hydration and enhanced hardening. To obtain the smaller sized particles, a Retsch EMAX High Energy Ball Mill with stainless steel grinding balls was utilized. Initially, water based cuttings are ground at 1,000 RPM for 10 minutes and resulted in the average particle size being 9.9 micron with a 11.9 micron standard deviation. A 15% water based cuttings slurry is made and 24-hour tests are run. Average *UCS* for the tests with the ground cuttings was 127.1 psi with a standard deviation of 24.5 psi, which is an 80% increase in compressive strength from the cuttings that were not ground. Additional cuttings are ground at 1,000 RPM for 30 minutes in an attempt to obtain even smaller particle sizes and

increase the compressive strength even further. Particle size analysis shows that after being ground for 30 minutes, the average particle size is 211.4 micron with a standard deviation of 238.0 micron. This increase in particle size may be due to the particles agglomerating and being larger. A 15% slurry using the cuttings ground for 30 minutes is made and 24-hour tests were run. Average *UCS* for the tests with the 30-minute ground cuttings is 105.1 psi with a standard deviation of 17.3 psi, which is approximately 49% higher than the compressive strength from the cuttings that are not ground but 17% lower than the 15% samples containing the cuttings ground for 10 minutes.

6.3.5. Conclusions

The utilization of dried water and oil based Eagle Ford drill cuttings as a wellbore cement additive has been studied to determine feasibility. It can be seen that:

- Cement slurries containing dried cuttings exhibited lower 24-hour *UCS* values than a conventional Eagle Ford cement slurry without cuttings.
- Although the cuttings used have been previously dried, residual moisture was still present and could have an impact on the mechanical properties.
- Particle size and particle size distribution is impacted by agglomeration. While the researchers attempted to minimize this effect, it is unknown whether this effect could play a role and impact the 24-hour *UCS* test results.
- When 32% of the dried cuttings are added to cement, the samples made with oil based cuttings considerably outperformed the samples comprised of water based cuttings. This is of interest because it is common knowledge that oil based mud contamination of

cement can significantly impact cement rheology, placement, and mechanical properties, yet the addition of the oil based cuttings do the opposite.

Chapter 7: Conclusions & Future Work

In this dissertation, wellbore cement has been investigated to improve well integrity models. To address how to appropriately model wellbore cement under downhole conditions, hydrostatic compression testing is performed to evaluate compressibility and poroelastic properties and CID testing is done to improve shear downhole behavior and failure criteria. Fracturing of the samples during CID testing provides valuable information regarding the coefficient of friction, cohesion, and deformation behavior under compressive shear stresses.

The utilization of cuttings as a wellbore cement additive was also investigated and could prove advantageous for a multitude of reasons, including minimizing the use of cement which in turn could aid in reducing the greenhouse gas emissions associated with cement manufacturing, lessen the cost of cuttings waste and corresponding costs, and potentially lead to better long-term wellbore integrity in that a geologic material that has been proven to trap hydrocarbons would be returned to the downhole environment. Investigating various particle size addition of this novel geologic additive allows for a preliminary understanding as to how it is able to bond within the cement.

7.1 Conclusions Drawn from This Research

In this work, the poroelastic constant, mechanical properties under downhole pressures, and shear behavior was investigated for class H wellbore cement containing a small amount of defoamer. Mechanical properties were further investigated for class H cement samples cured for either 7- or 28-days and containing a small amount of defoamer and varying quantities and

particles sizes of shale. The following information was obtained through the experimental testing described in this work.

1. The poroelastic constant, or Biot coefficient, of class H cement containing a small amount of defoamer was found to be between 0.80 and 0.82 for the three samples tested. While the poroelastic constant has not been greatly researched, specifically for wellbore cement, the findings are in good agreement with tests conducted on class G cement by Meng et al. (2020). It is common practice when calculating effective stress in the petroleum industry to assume that the Biot coefficient is 1, or an unconsolidated material. Knowing that this constant is not, in fact, 1 implies that a majority of the wellbore modeling done is inaccurate and incorrect assumptions have been made regarding cement sheath strength and integrity under realistic downhole conditions.
2. CID testing on wellbore cement can provide insight regarding the cement mechanical properties under real-world pressures. While CID testing is somewhat commonly performed on wellbore cement, the cement is often not cured for the early hydration period and only early-strength mechanical properties are able to be obtained. From this work, it can be seen that *CCS* for samples tested at low confining stress are similar but at high confining stress, are more variable. *YM* and *PR* are consistent at all confining stress but it should be noted that *YM* for the 30 MPa confining stress fluctuates. From the sheared samples, it was seen that the angle of friction, or the angle at which the sample breaks, are similar and are in agreement with previous literature on rocks.
3. Results of the cement samples containing various sizes and quantities of shale cured for 7-days show that the addition of shale could have a beneficial effect on cement mechanical properties. For the cement containing millimeter shale at 5%, 10%, and 15%

BWOC, *UCS, YM,* and *PR* results were lower than the base case, implying that the addition of millimeter shale may not be feasible as an additive. Cement samples containing 10% and 15% micron shale, however, have enhanced *UCS* but also a higher *YM* and *PR* indicating that cement ductility may be impacted. The 5% and 15% submicron shale addition to cement also have increased *UCS* and *YM* when compared to the base case but the *PR* was similar.

4. Samples cured for the cement early hydration period containing 5%, 10%, 15%, 25%, 50%, and 75% millimeter, micron, and submicron shale also provided insight into the feasibility of using shale as a cement additive or replacement material.
5. While the utilization of dried cuttings as a wellbore cement additive were not able to achieve the required 24-hour compressive strength designated by the Texas Railroad Commission, it is possible that adding cuttings to a different cement system could lead to increased 24-hour compressive strength.

7.2 Future Work

The results obtained in this work, while instrumental for a basic understanding of utilizing shale within cement, are preliminary and additional testing needs to be done to further validate the findings. Particle size can become problematic if the slurry is unable to be pumped in the field. To ensure that pumpability will not be a problem, rheology of the slurries containing shale should be done. Consistency, thickening time, and ultrasonic cement analysis should also be conducted to ensure that the cement is able to set when placed downhole under specific wellbore conditions as well as early mechanical properties. Other tests such as fluid loss, free fluid, and density can also be performed on the slurries with shale to further validate the behavior in the

field. Expansion and shrinkage tests may also be advantageous to see whether the shale aids or hinders these phenomena in cement.

Samples cured over the early hydration period should also be tested using a system that is able to record vertical and horizontal strain so that *PR* and *YM* are able to be obtained. While porosity and permeability measurements were performed on base samples, this testing should also be done on samples containing shale to see if there is any significant increase or decrease. Tensile and bond testing can also be performed to aid in understanding cement characteristics.

Microscopy should be further utilized for cement evaluation, not just for the purpose of this study but for any cement that may contain new additives or types of cement. Microscopic analysis provides an improved understanding as to how the cement and additives react and bond, micro porosity and permeability within the sample, and elemental composition of various particles or locations to help detect any potential abnormalities within the sample.

Hydrostatic compression and triaxial testing should be continued on cement systems that are currently or have the potential to be employed in the field. Knowing that additives can drastically alter the mechanical properties of cement, it would be worthwhile to determine whether they have any effect on the poroelastic properties or shear behavior and provide a more accurate failure envelope for real-world scenarios. Knowledge of this could enhance wellbore modeling and in turn, well integrity both short- and long-term. While this work focuses on utilizing shale cuttings as an additive, experimental testing utilizing actual field cuttings within cement should be performed to understand whether the results vary and, if so, how significantly they vary when compared to the shale results.

Appendix A. 90˚ Images of Samples Sheared During CID Testing

The following are images of the samples sheared during CID testing. From these images, the primary fracture was able to be identified and then used to determine the fracture angle. This can then be input into a failure envelope or modeling software to more accurately determine wellbore failure potential.

Figure A.1. Sample 1 sheared at 5 MPa.

Figure A.2. Sample 2 sheared at 5 MPa.

Figure A.3. Sample 3 sheared at 5 MPa.

Figure A.4. Sample 4 sheared at 15 MPa.

Figure A.5. Sample 5 sheared at 15 MPa.

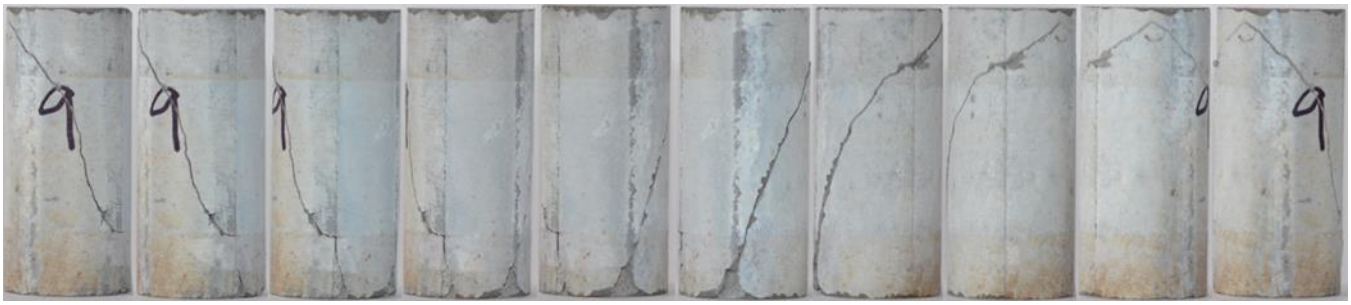

Figure A.6. Sample 6 sheared at 15 MPa.

Figure A.7. Sample 7 sheared at 30 MPa.

Figure A.8. Sample 8 sheared at 30 MPa.

Figure A.9. Sample 9 sheared at 30 MPa.

Figure A.10. Sample 10 sheared at 30 MPa.

Appendix B. Plasticity Modulus for Class H Cement

The plasticity modulus for the class H samples can be calculated for the samples that underwent CID testing. After plotting the vertical stress and axial strain, CCS is identified. The E50 value is then determined, and 25 points above and below this value are plotted. A trendline is then fit to the E50 curve and extrapolated forward in order to determine the 100% elastic scenario for the material. The axial strain between the tested sample and the 100% elastic scenario is determined and the percent difference can be found. The plasticity modulus for the 10 class H samples are shown below.

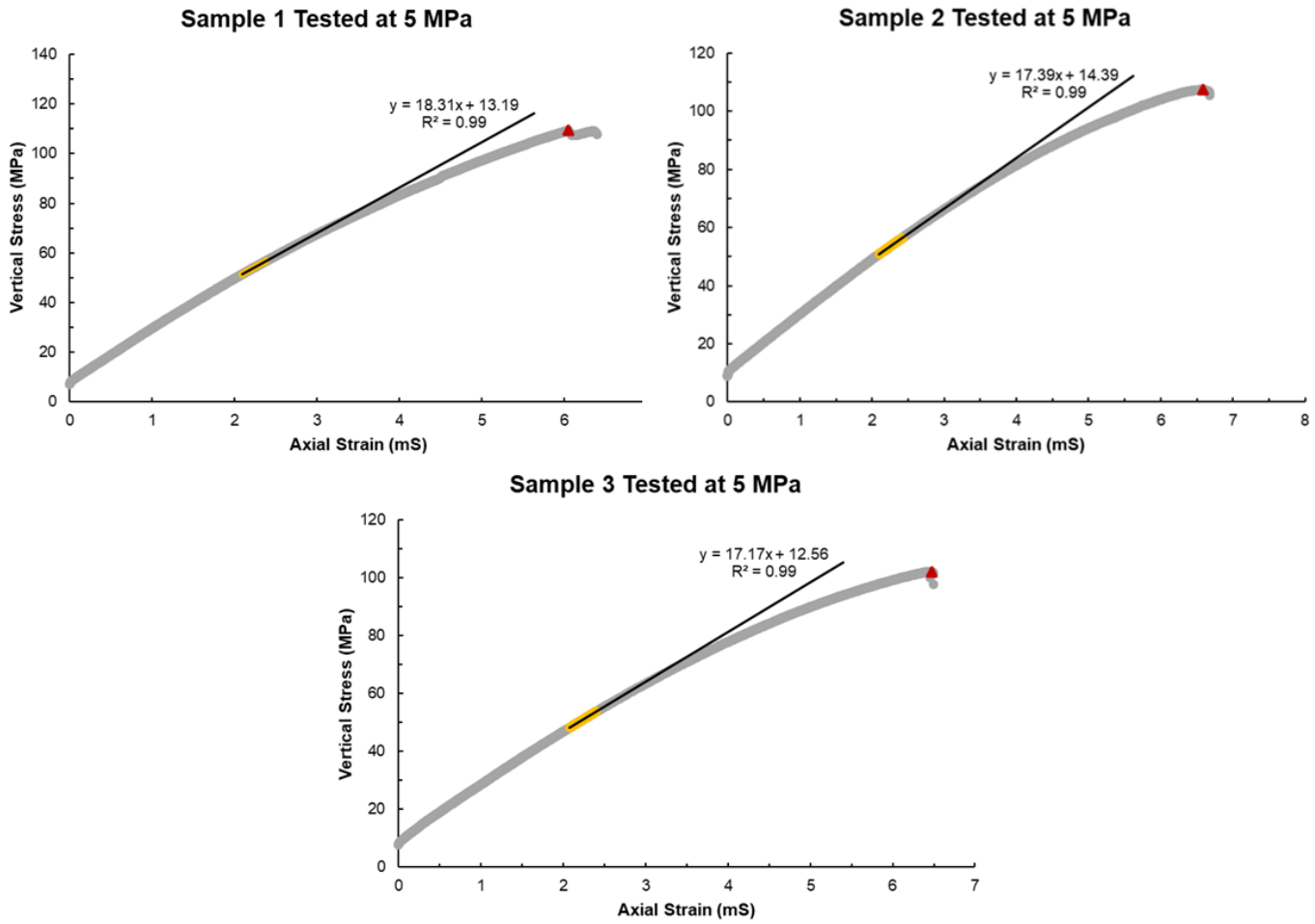

Figure B.11. Plasticity modulus for the samples tested at 5 MPa confining stress.

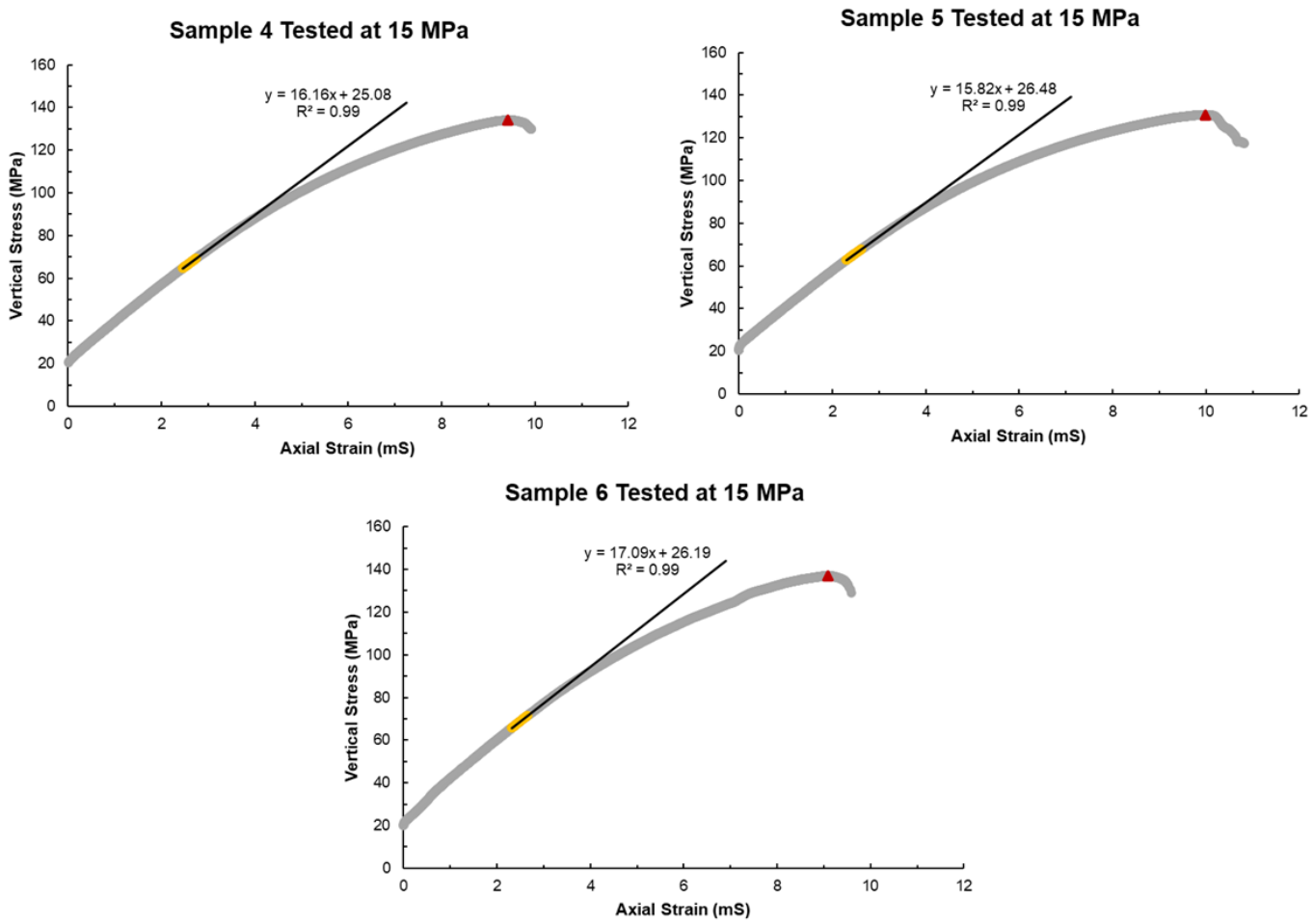

Figure B.12. Plasticity modulus for the samples tested at 15 MPa confining stress.

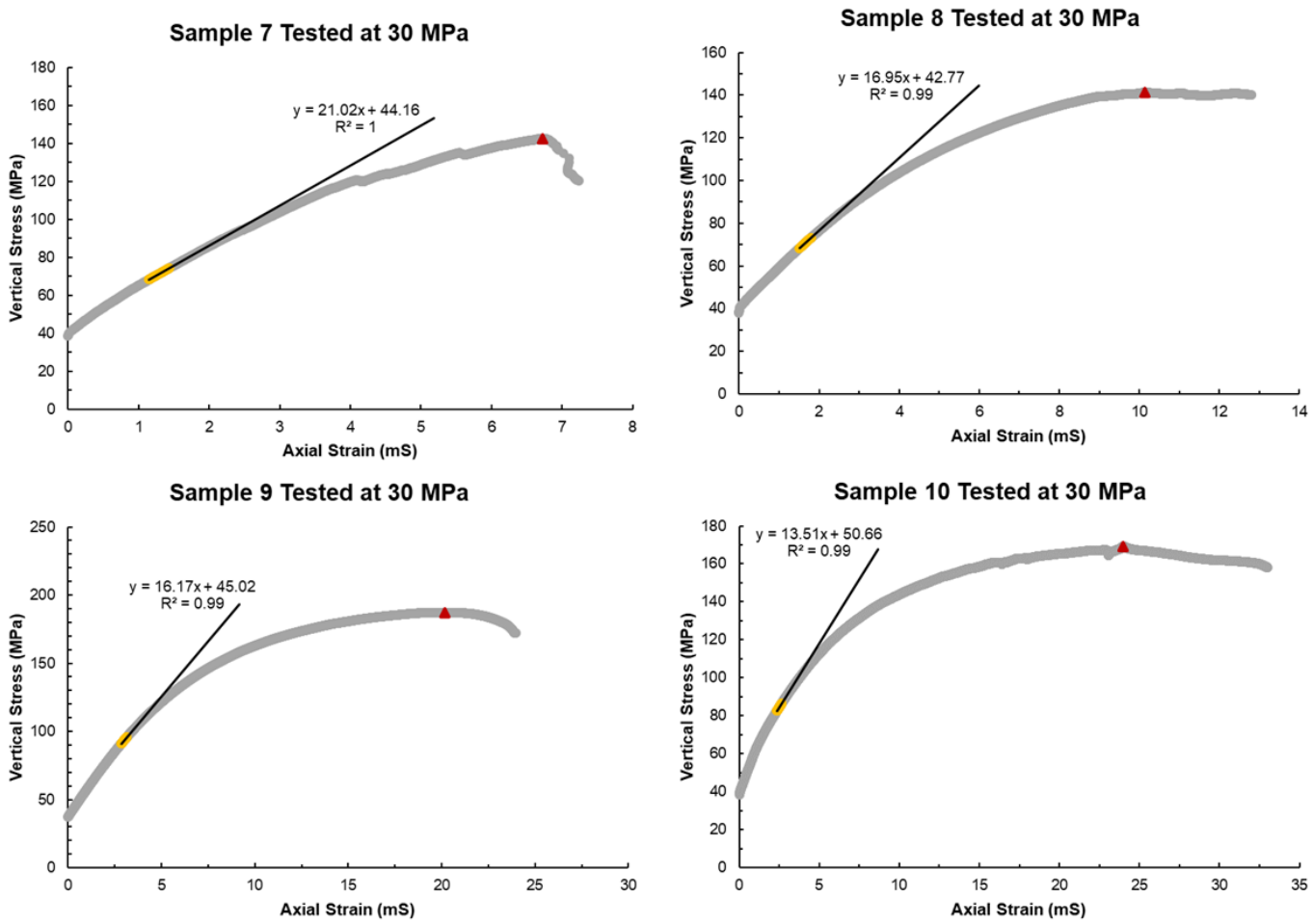

Figure B.13. Plasticity modulus for the samples tested at 30 MPa confining stress.

Appendix C. Stress-Strain Diagrams for Samples Cured Over 7-Days

In this section, *UCS* results for class H cement samples containing 5%, 10%, and 15% shale in millimeter, micron, and submicron sizes are shown. From these results, a comparison of *UCS*, *PR*, and *YM* values is able to be done and has been described in Chapter 6 of this work.

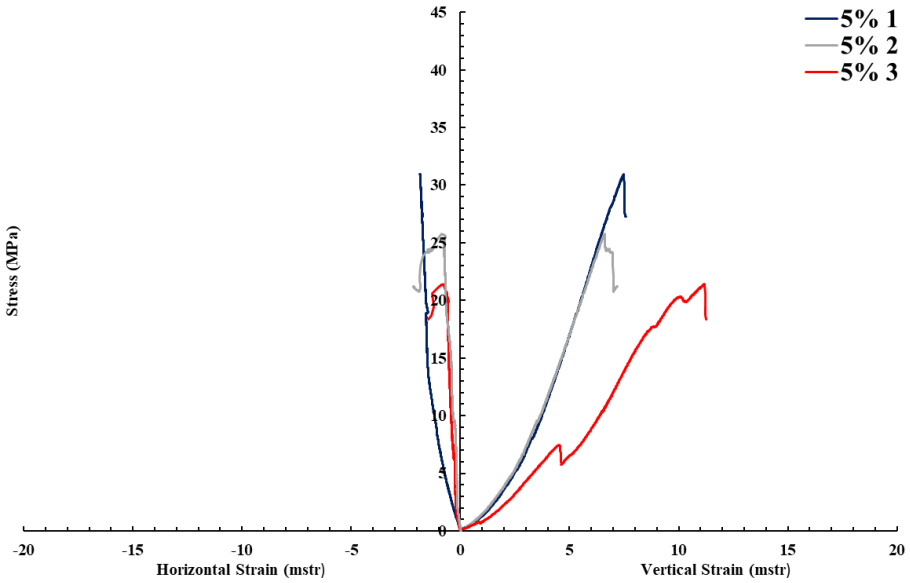

Figure C.1. 5% millimeter shale UCS test results.

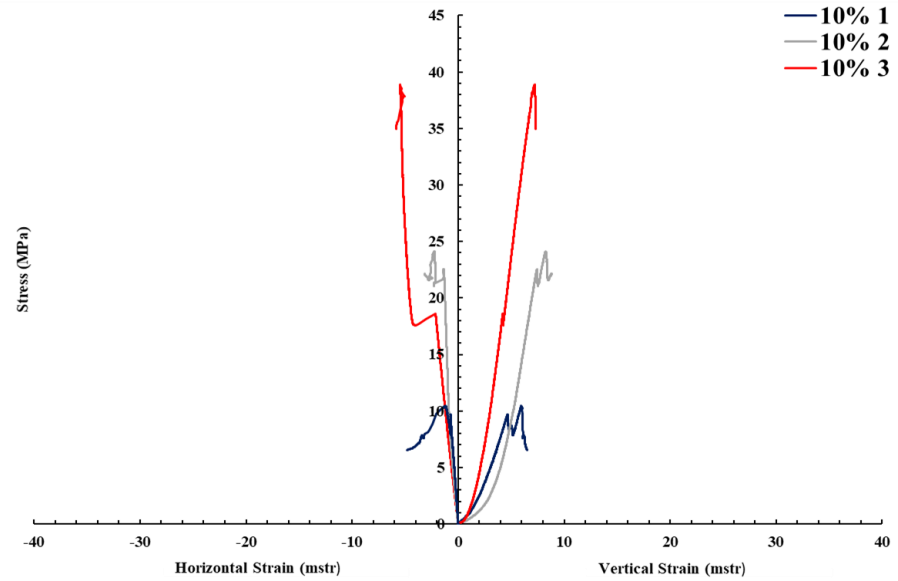

Figure C.2. 10% millimeter shale UCS test results.

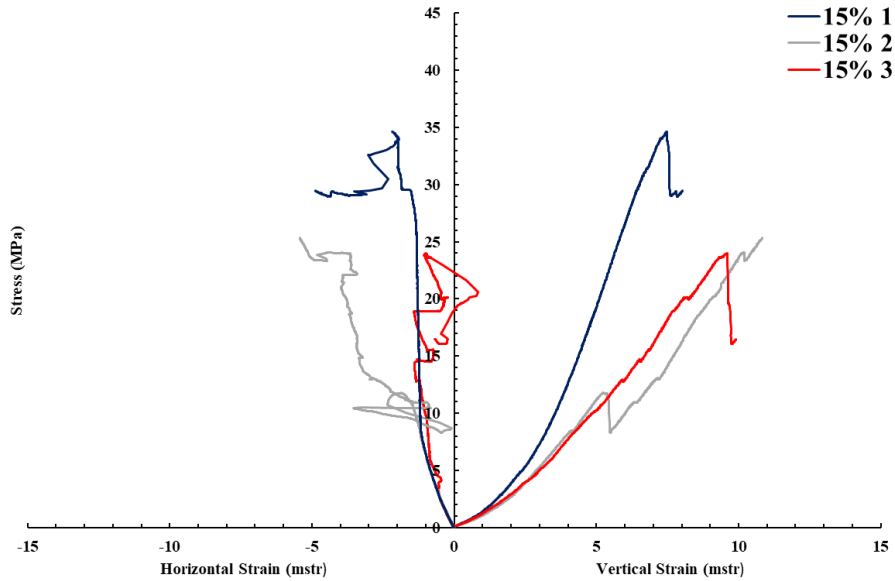

Figure C.3. 15% millimeter shale UCS test results.

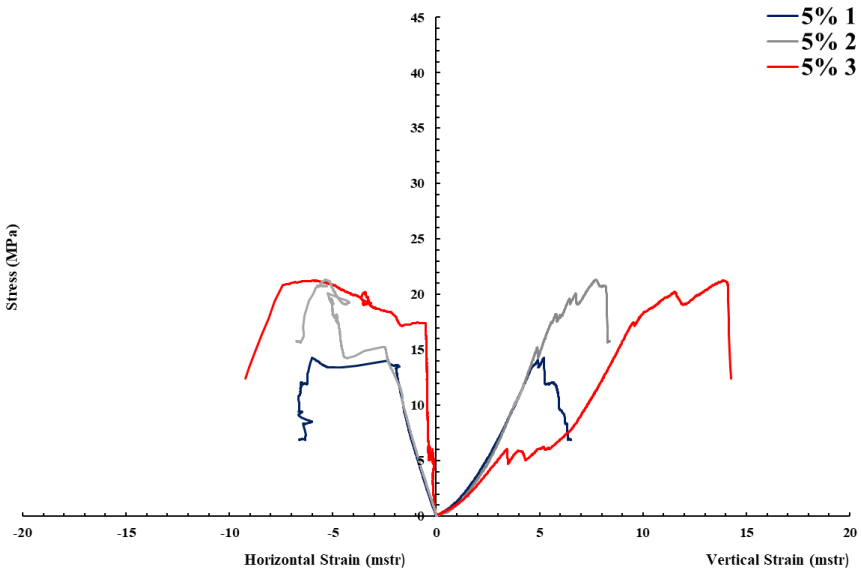

Figure C.4. 5% micron shale UCS test results.

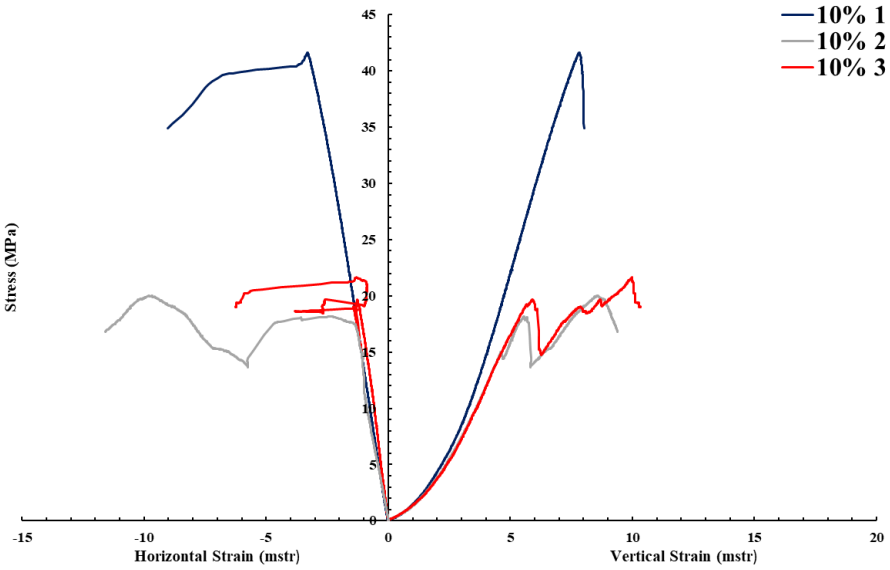

Figure C.5. 10% micron shale UCS test results.

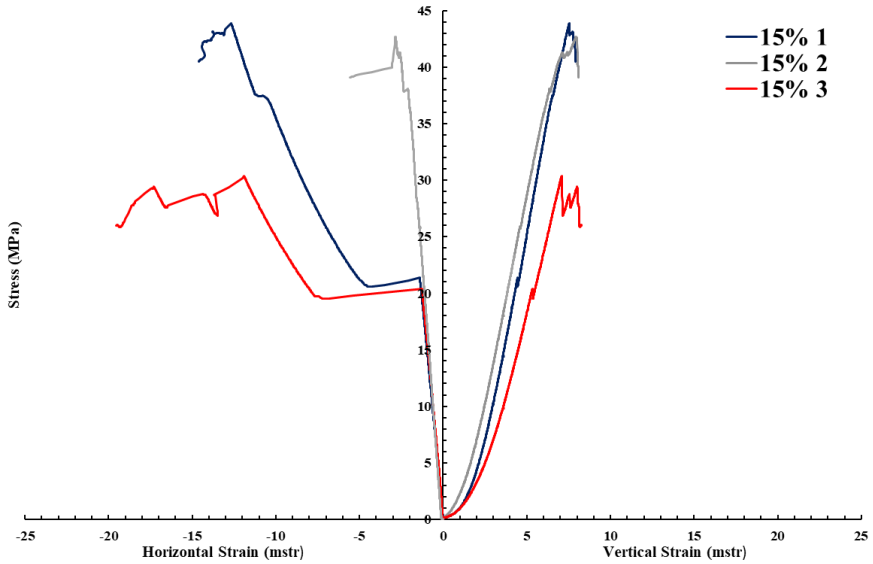

Figure C.6. 15% micron shale UCS test results.

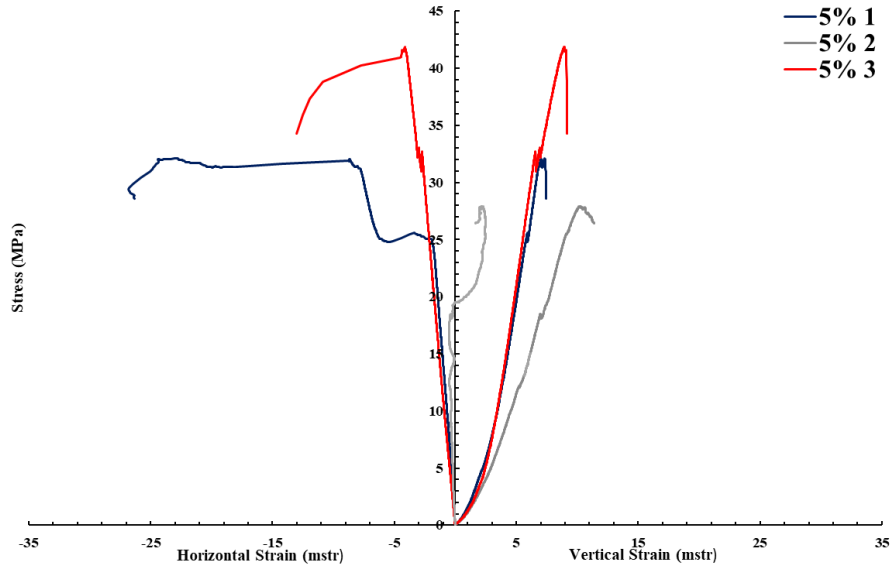

Figure C.7. 5% submicron shale UCS test results.

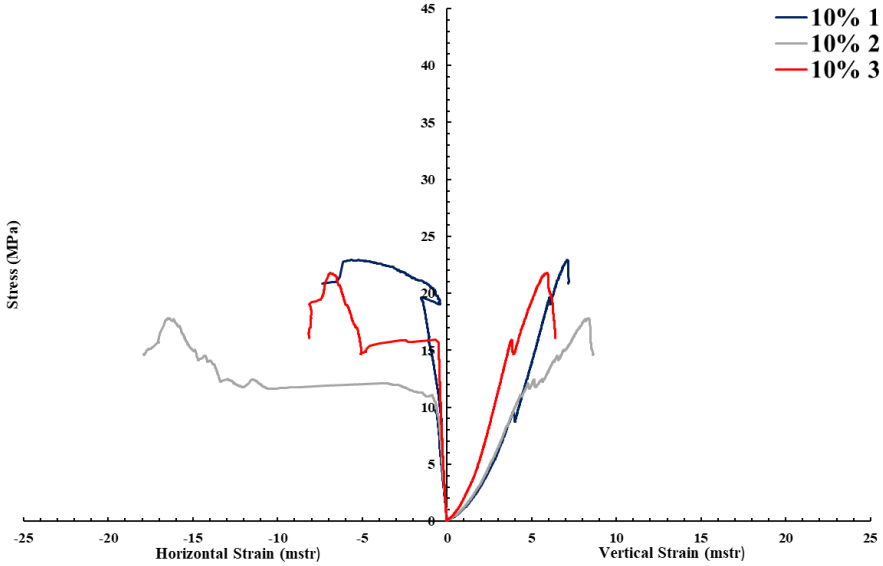

Figure C.8. 10% submicron shale UCS test results.

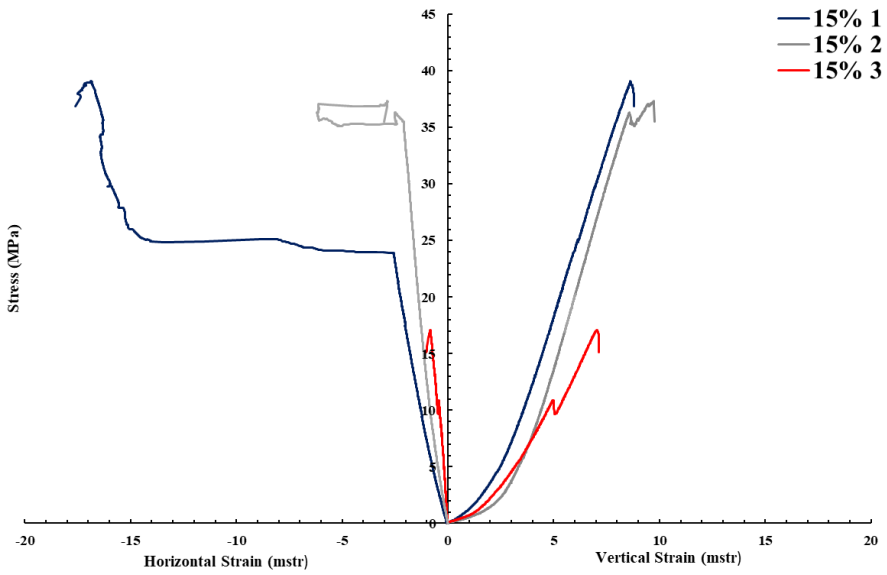

Figure C.9. 15% submicron shale UCS test results.

Appendix D. Samples Cured for 28-Days Post UCS Testing

In this section, images of the class H cement samples cured for 28-days and tested to determine the unconfined compressive strength are shown. It can be seen from the images of the millimeter shale samples that the shale particle distribution within the samples appear to be fairly homogenous.

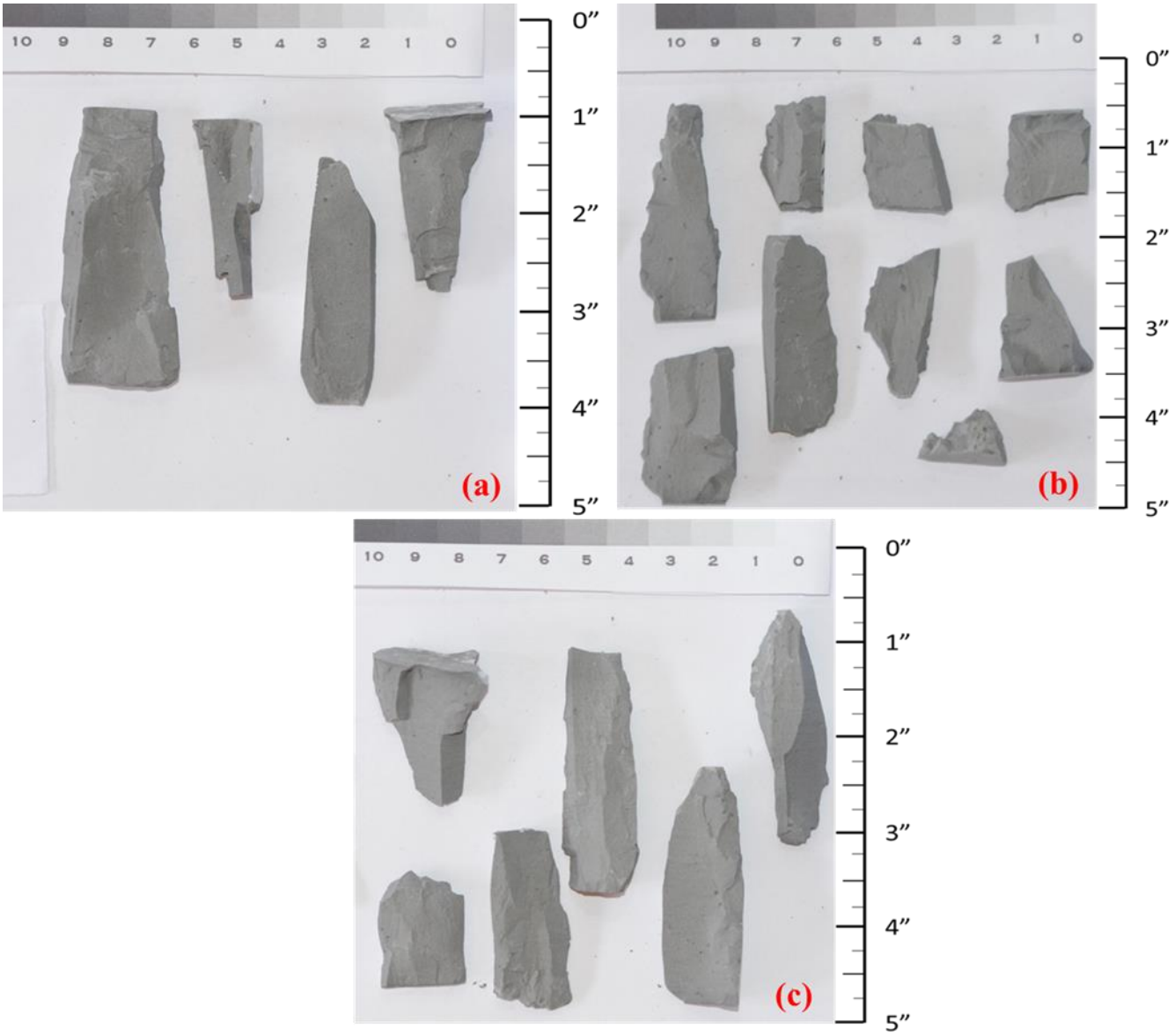

Figure D.1. Base case sample cured for 28-days (a) 1; (b) 2; (c) 3 after UCS testing.

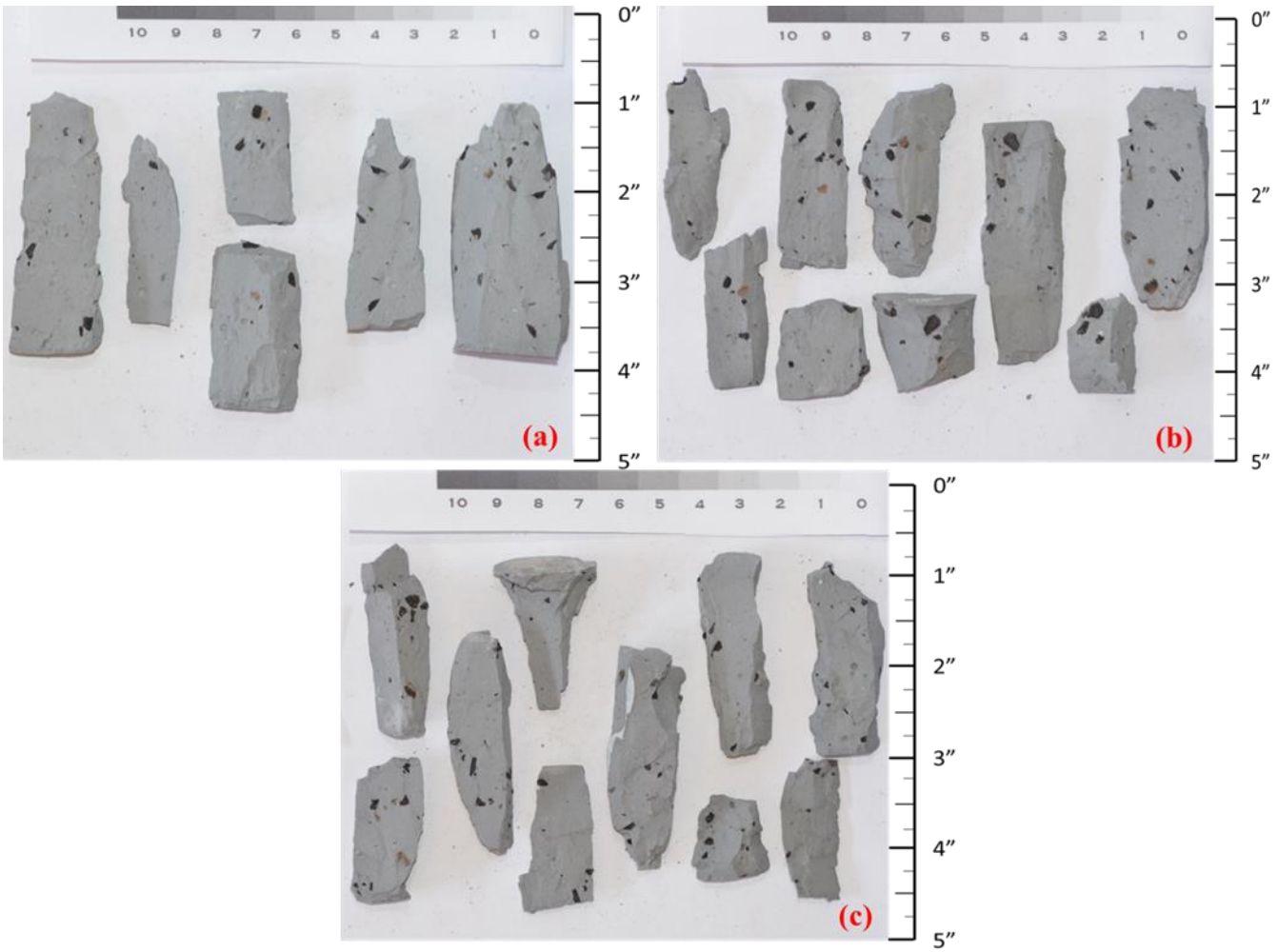

Figure D.2. 5% millimeter case sample cured for 28-days (a) 1; (b) 2; (c) 3 after UCS testing.

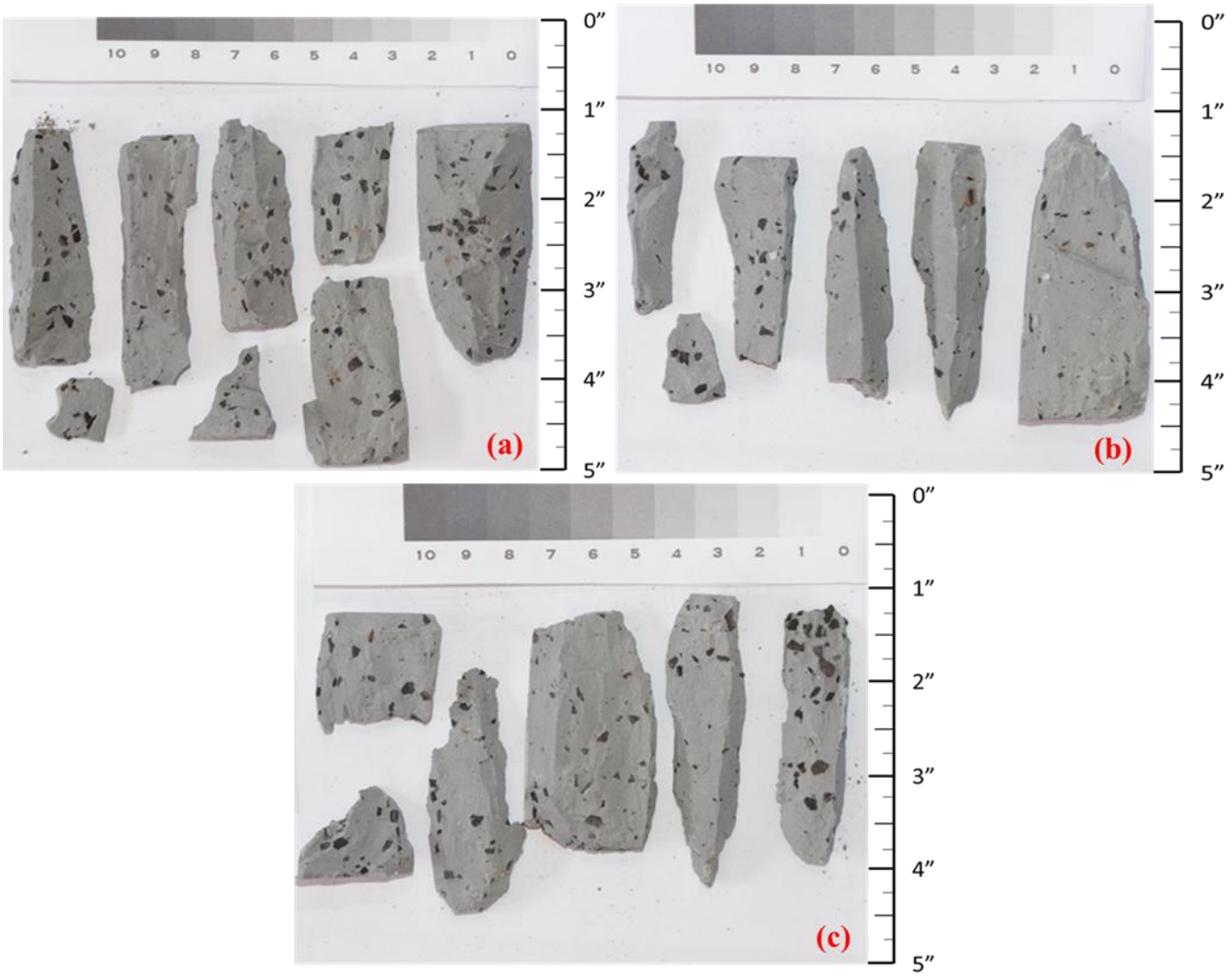

Figure D.3. 10% millimeter case sample cured for 28-days (a) 1; (b) 2; (c) 3 after UCS testing.

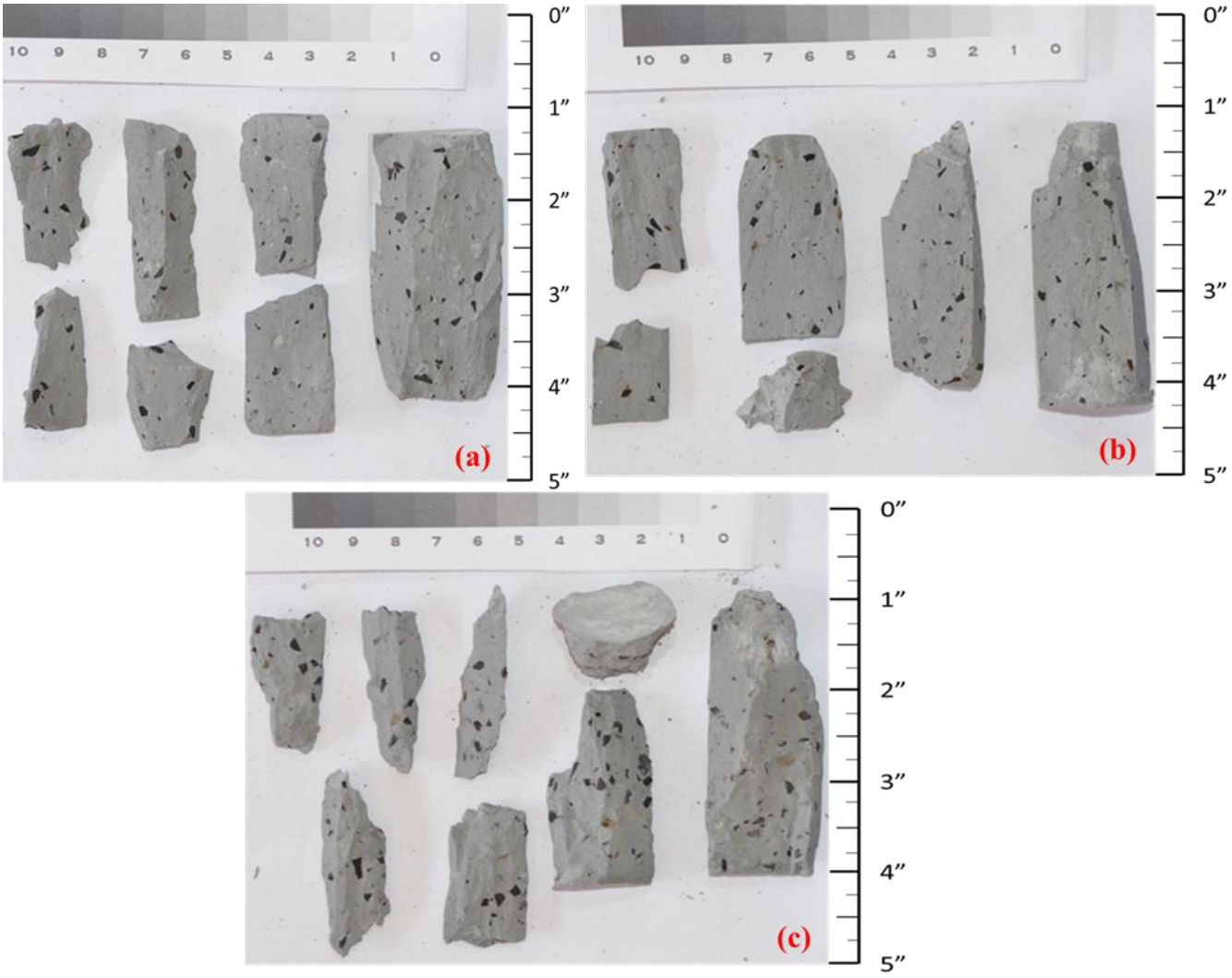

Figure D.4. 15% millimeter case sample cured for 28-days (a) 1; (b) 2; (c) 3 after UCS testing.

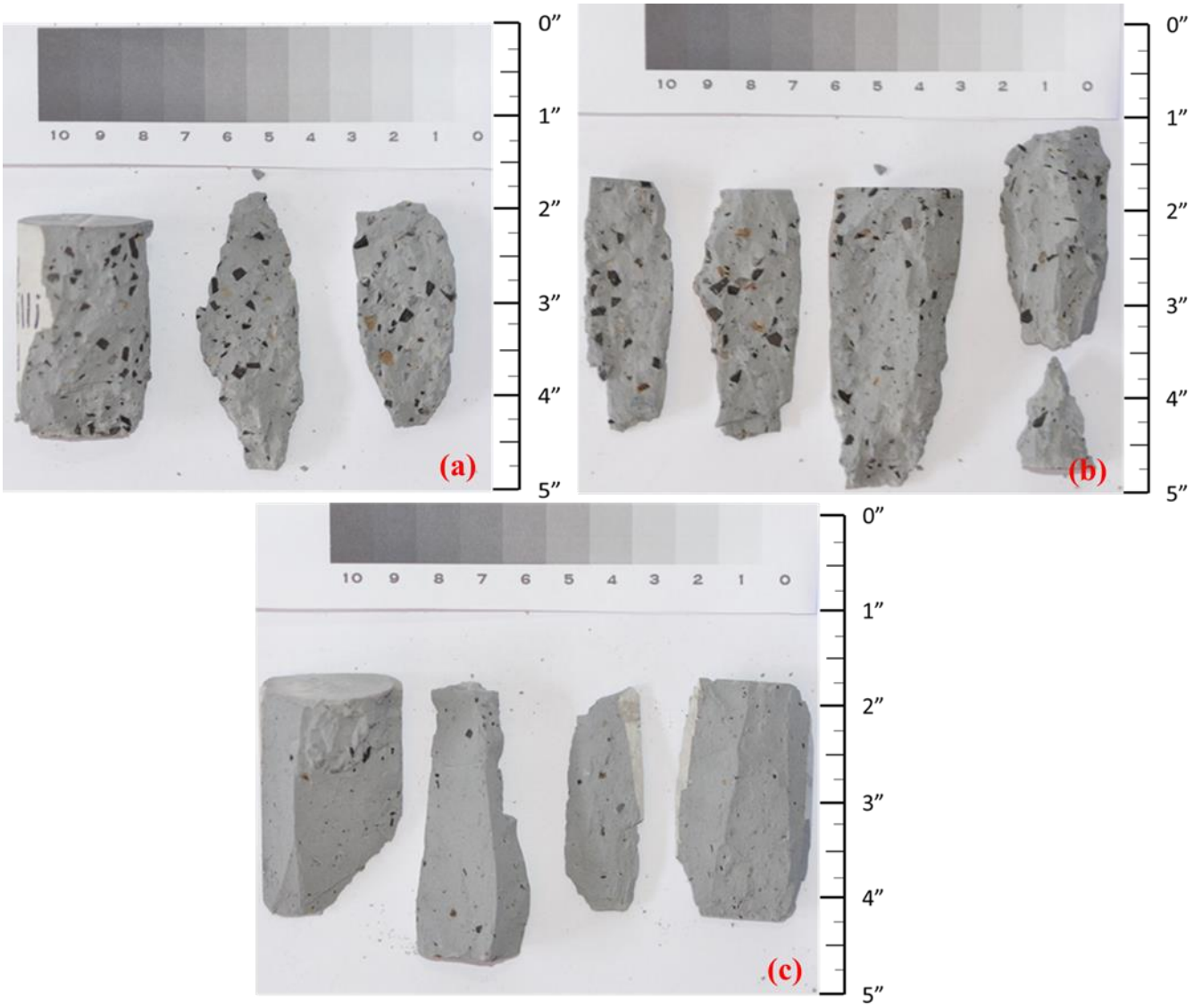

Figure D.5. 25% millimeter case sample cured for 28-days (a) 1; (b) 2; (c) 3 after UCS testing.

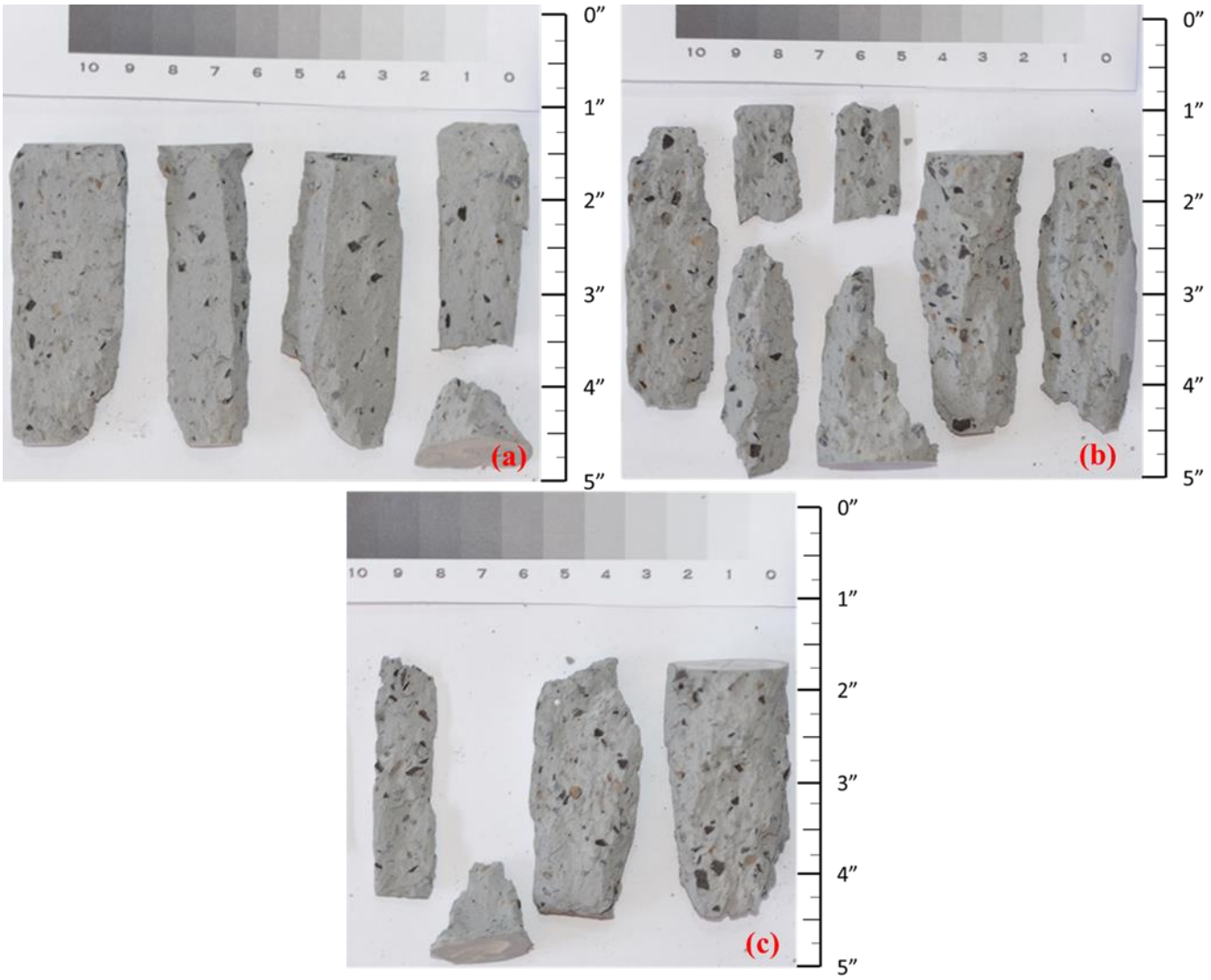

Figure D.6. 50% millimeter case sample cured for 28-days (a) 1; (b) 2; (c) 3 after UCS testing.

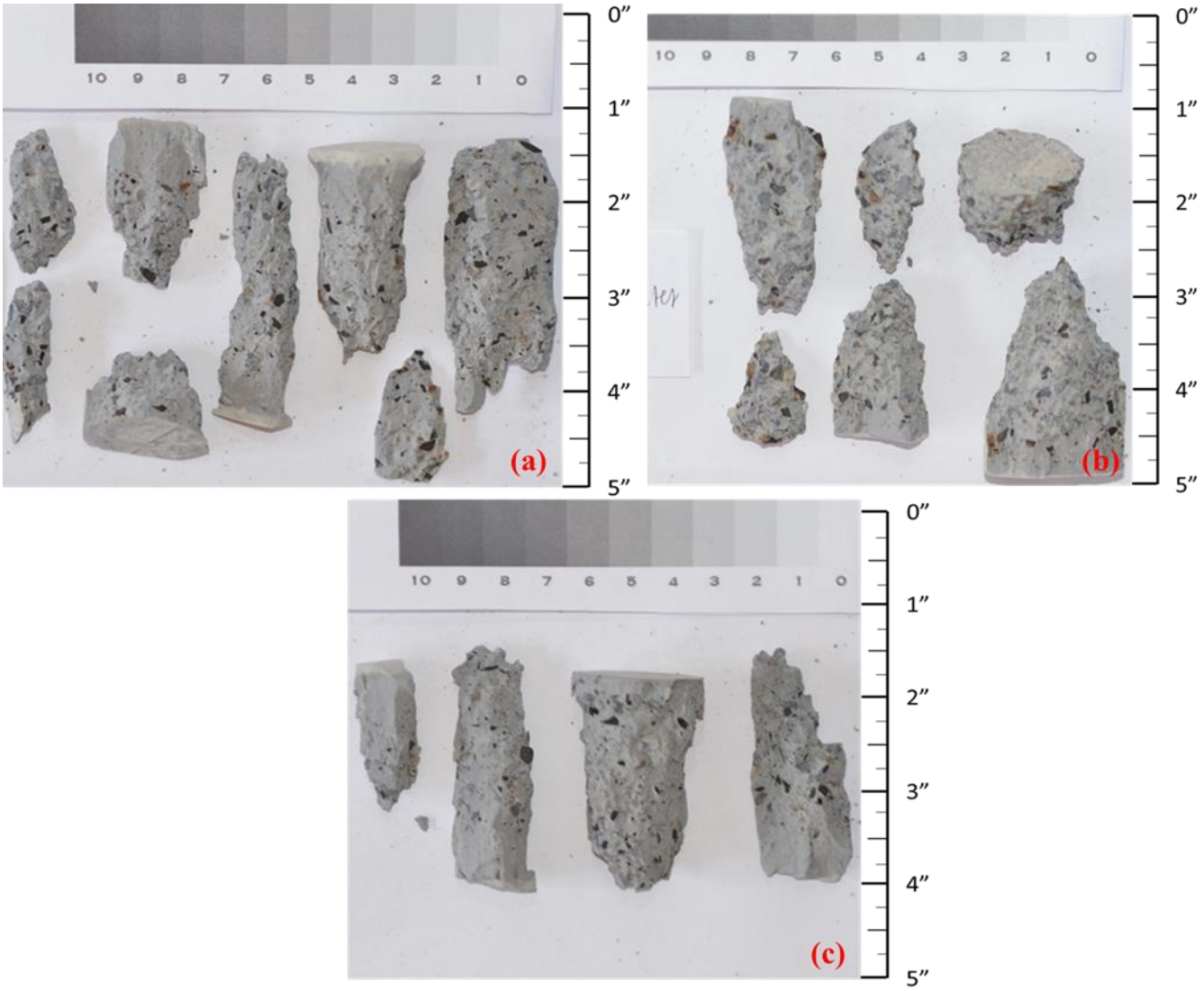

Figure D.7. 75% millimeter case sample cured for 28-days (a) 1; (b) 2; (c) 3 after UCS testing.

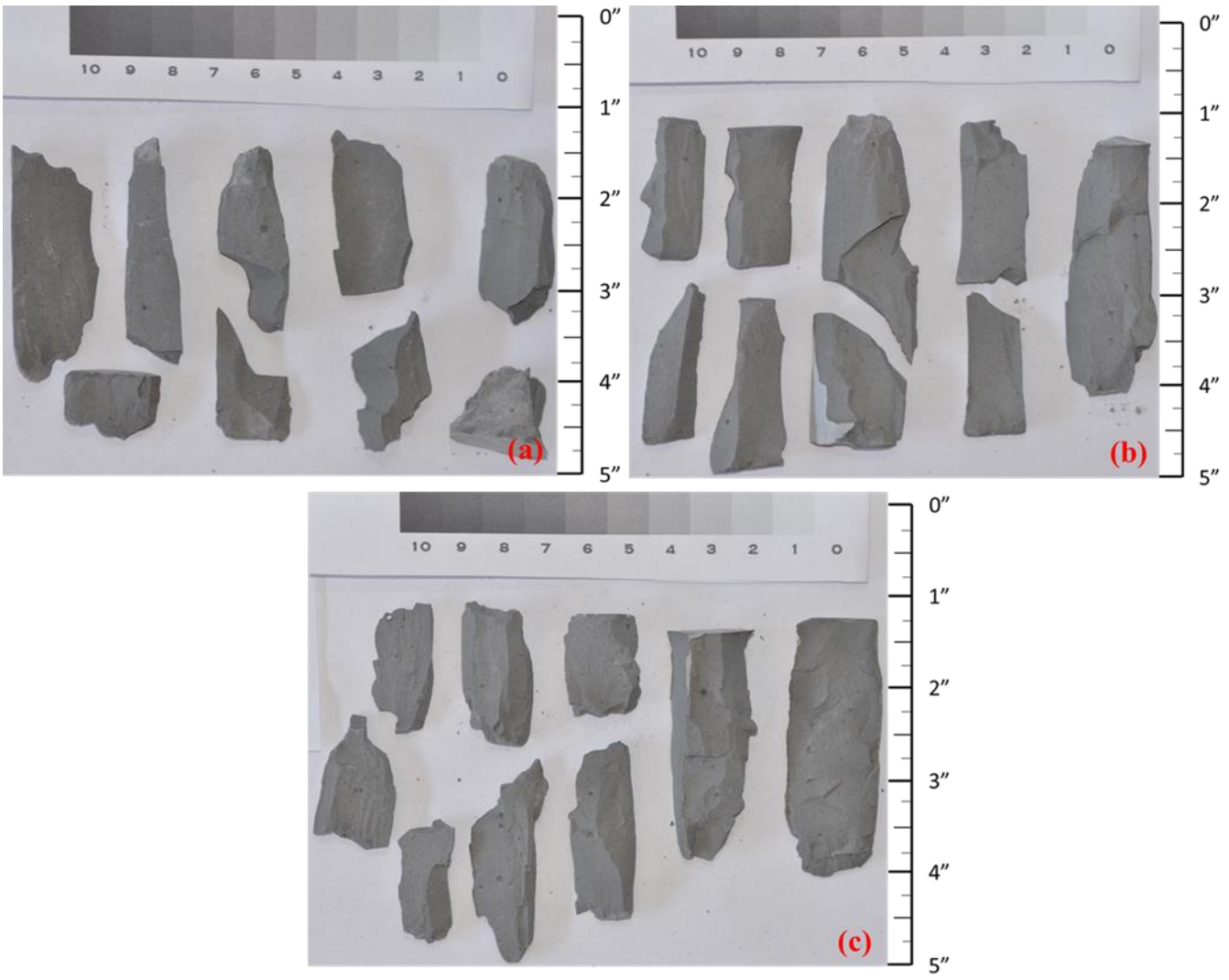

Figure D.8. 5% micron case sample cured for 28-days (a) 1; (b) 2; (c) 3 after UCS testing.

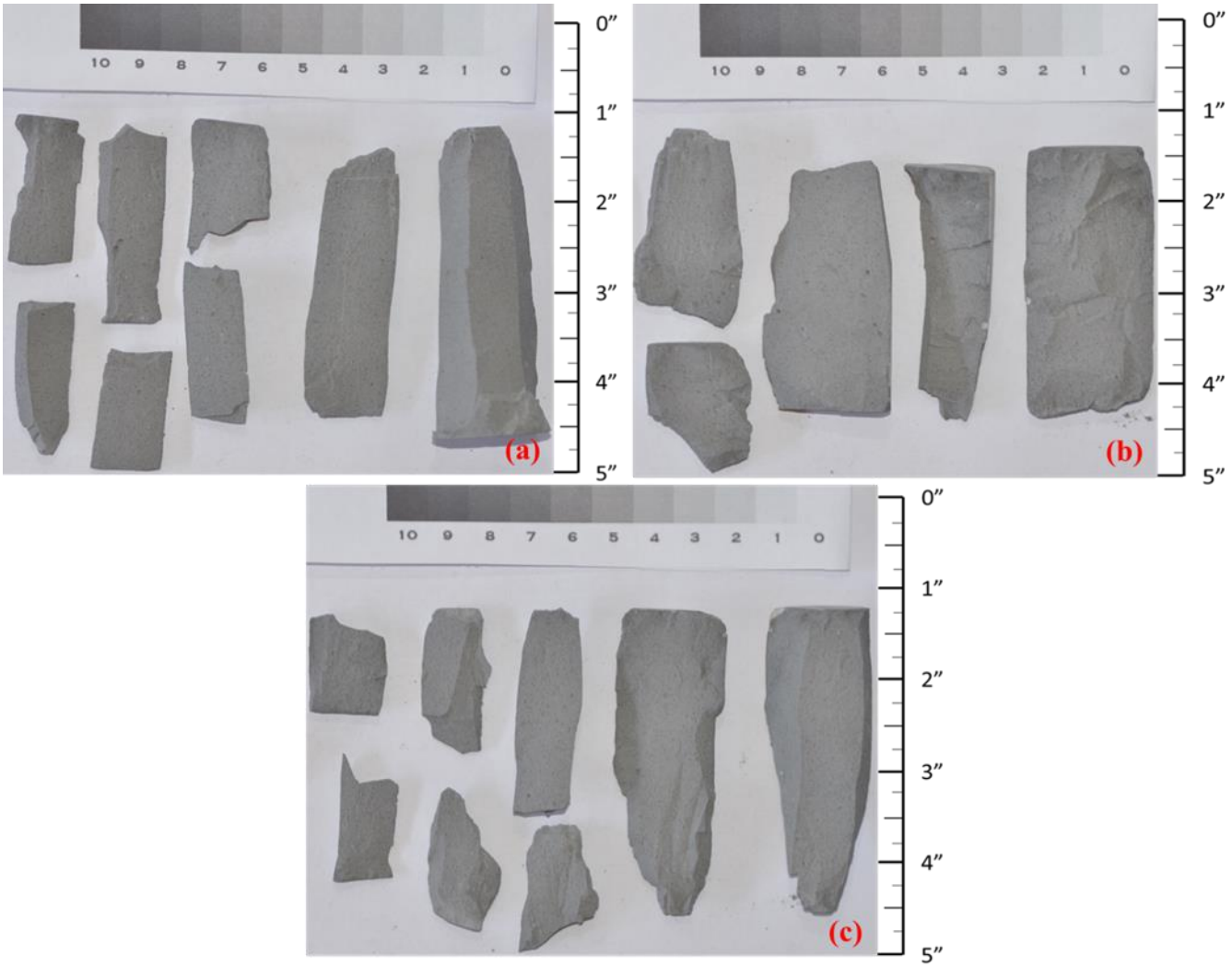

Figure D.9. 10% micron case sample cured for 28-days (a) 1; (b) 2; (c) 3 after UCS testing.

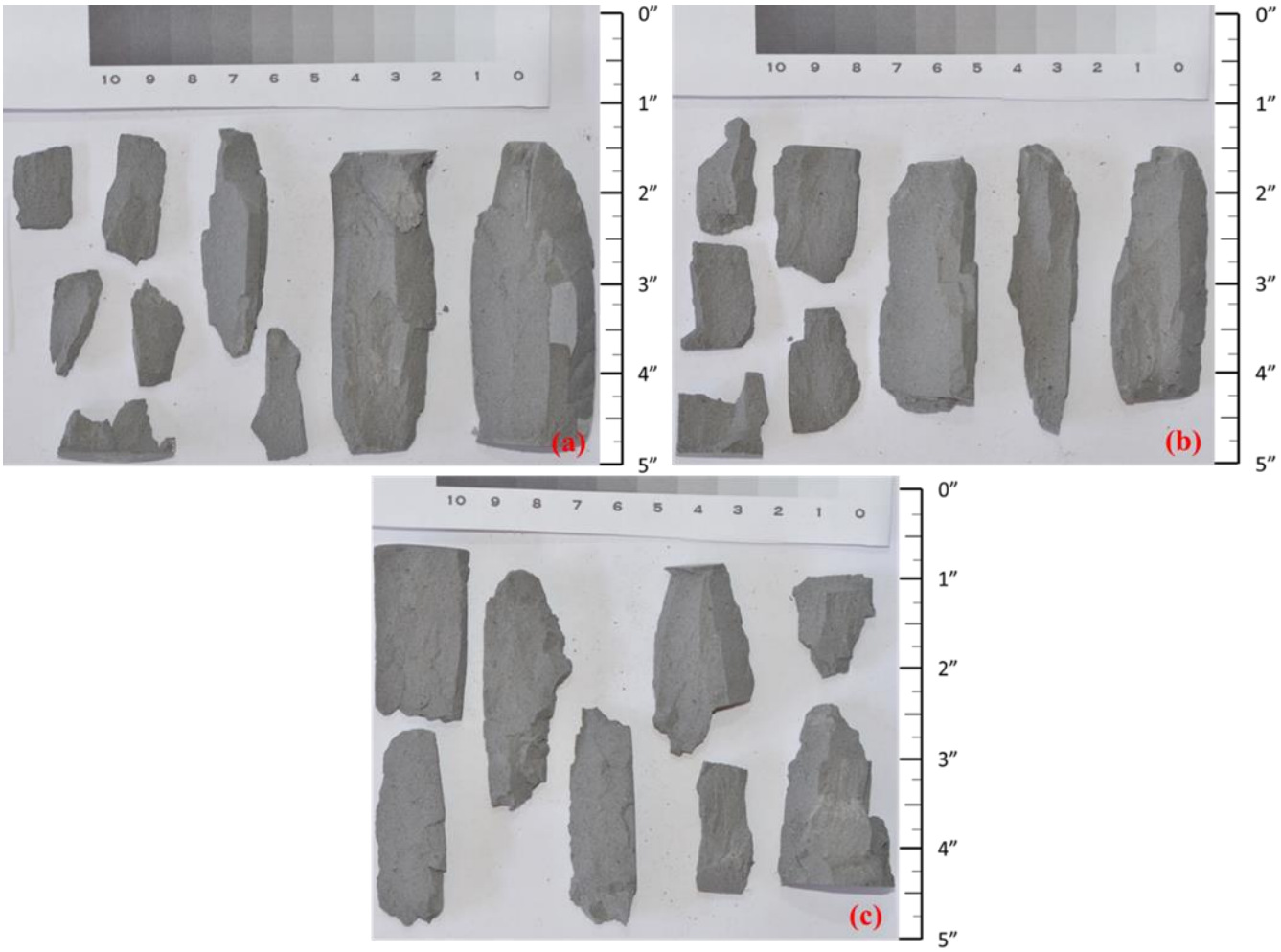

Figure D.10. 15% micron case sample cured for 28-days (a) 1; (b) 2; (c) 3 after UCS testing.

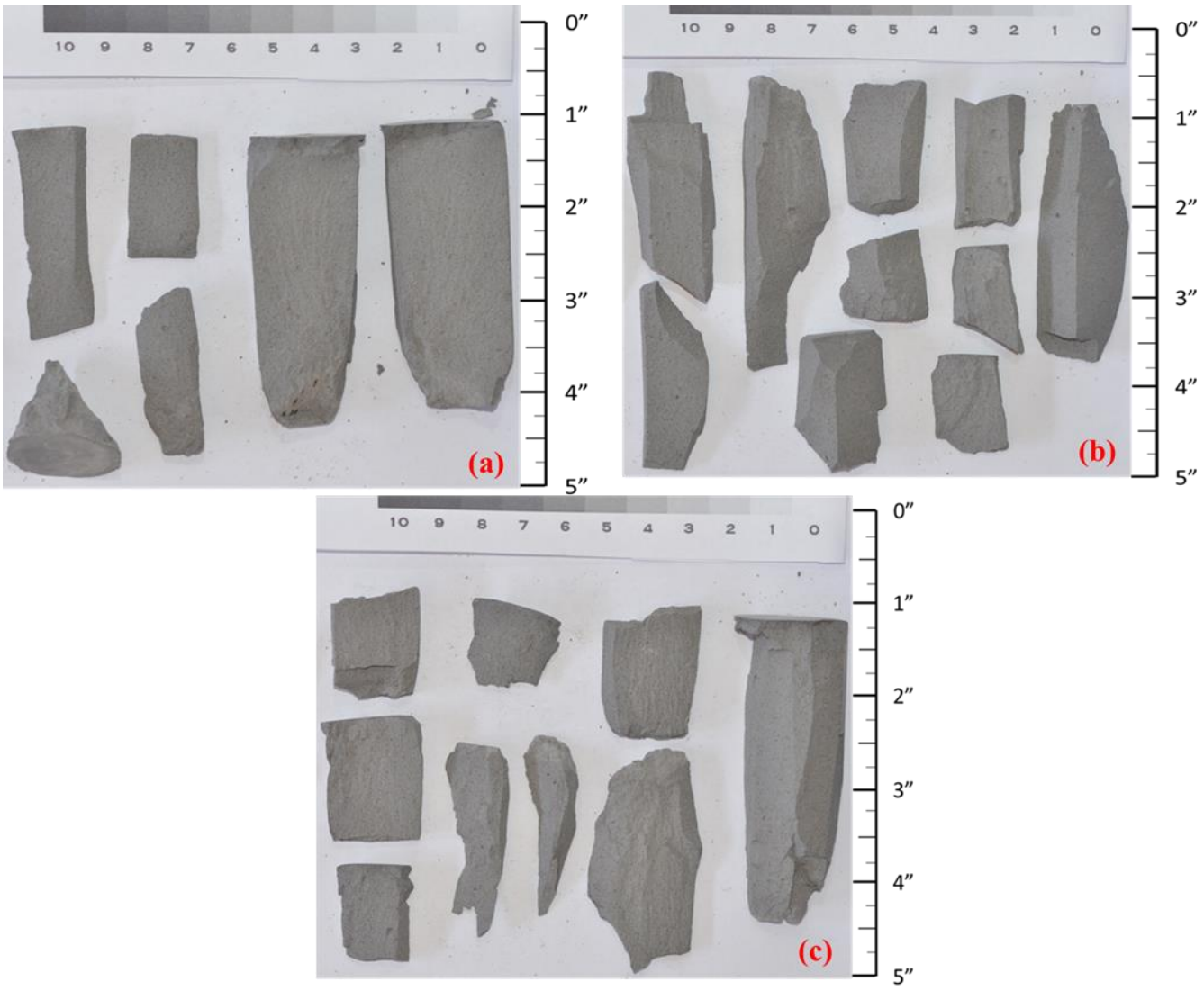

Figure D.11. 25% micron case sample cured for 28-days (a) 1; (b) 2; (c) 3 after UCS testing.

Figure D.12. 50% micron case sample cured for 28-days (a) 1; (b) 2; (c) 3 after UCS testing.

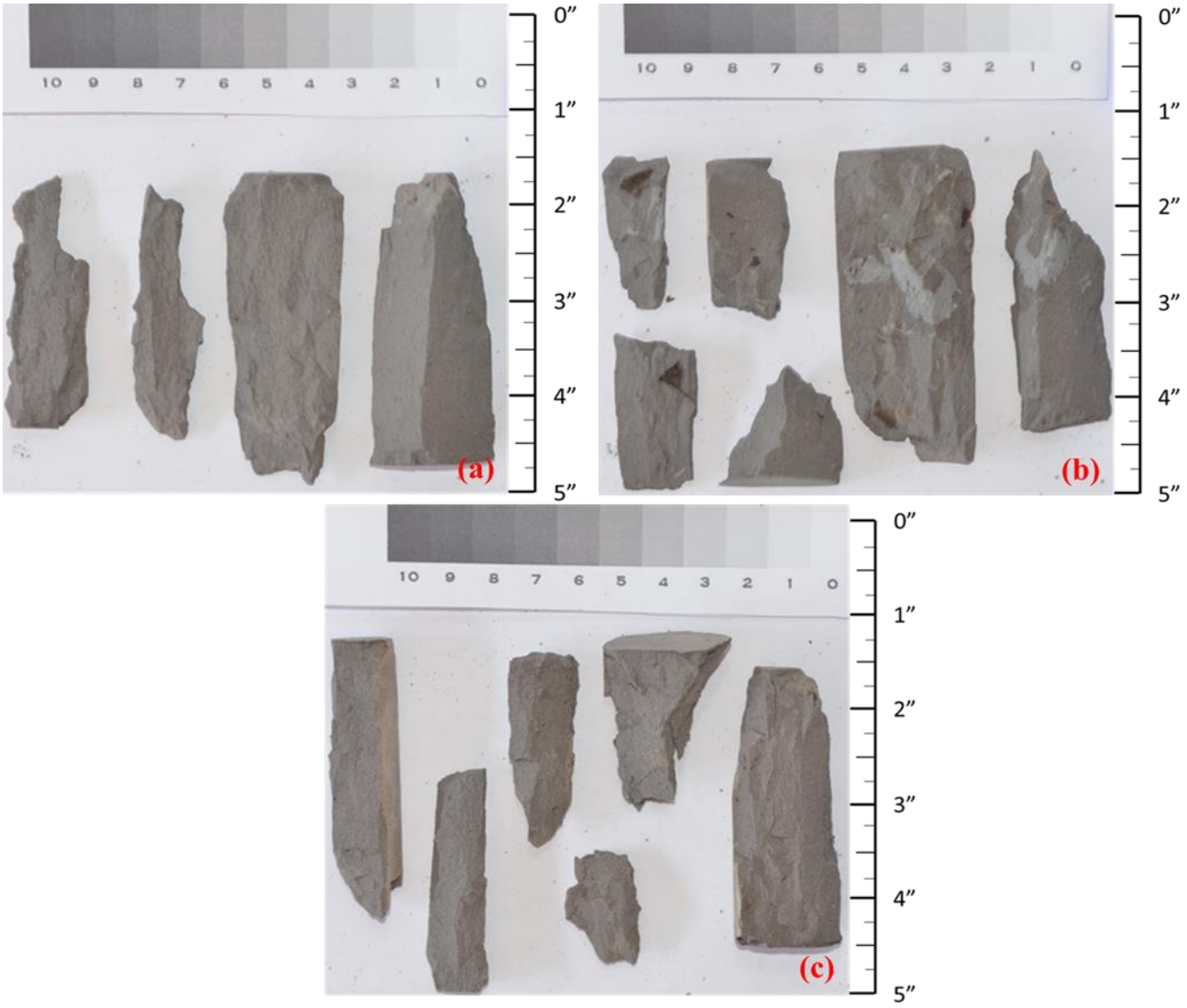

Figure D.13. 75% micron case sample cured for 28-days (a) 1; (b) 2; (c) 3 after UCS testing.

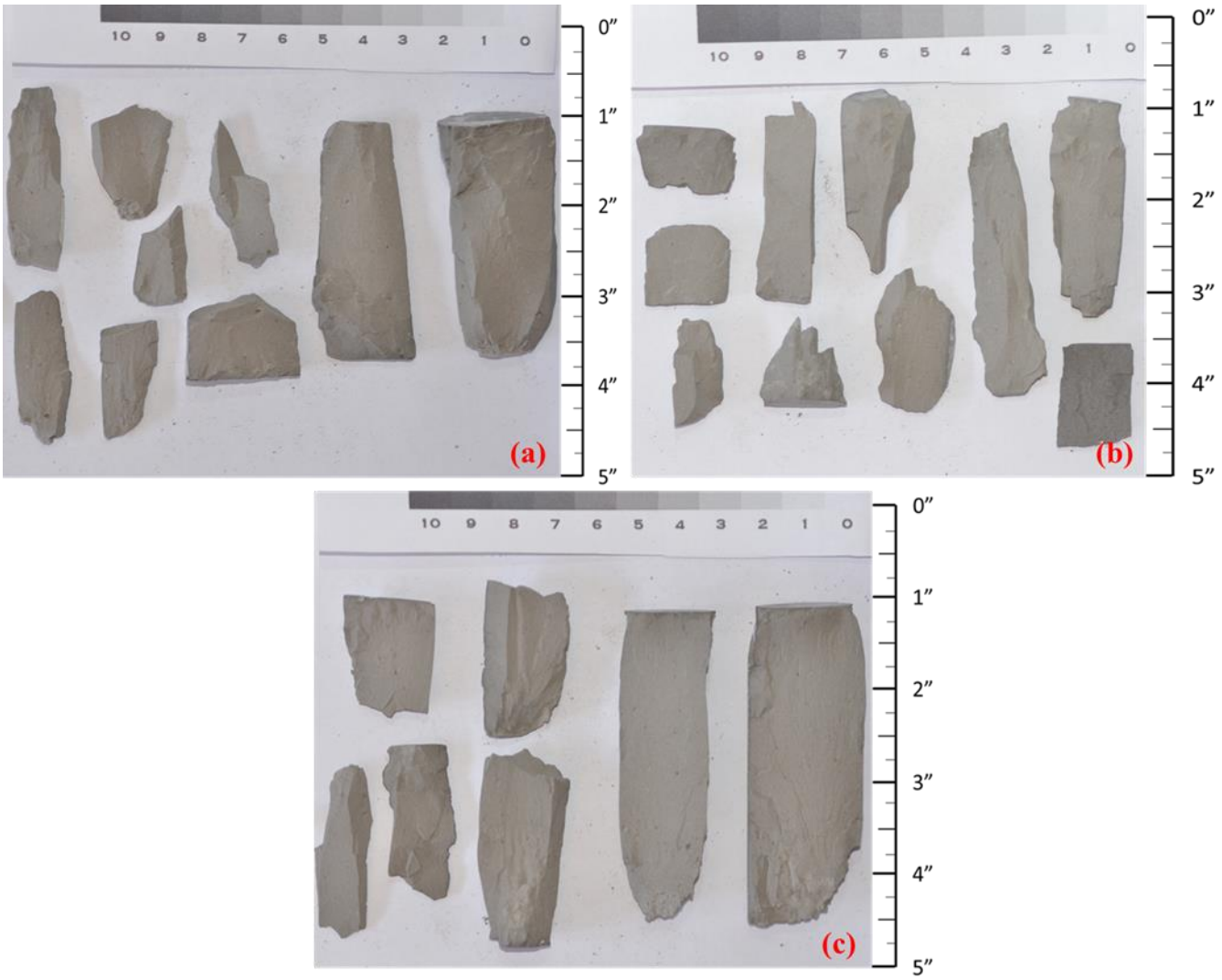

Figure D.14. 5% submicron case sample cured for 28-days (a) 1; (b) 2; (c) 3 after UCS testing.

Figure D.15. 10% submicron case sample cured for 28-days (a) 1; (b) 2; (c) 3 after UCS testing.

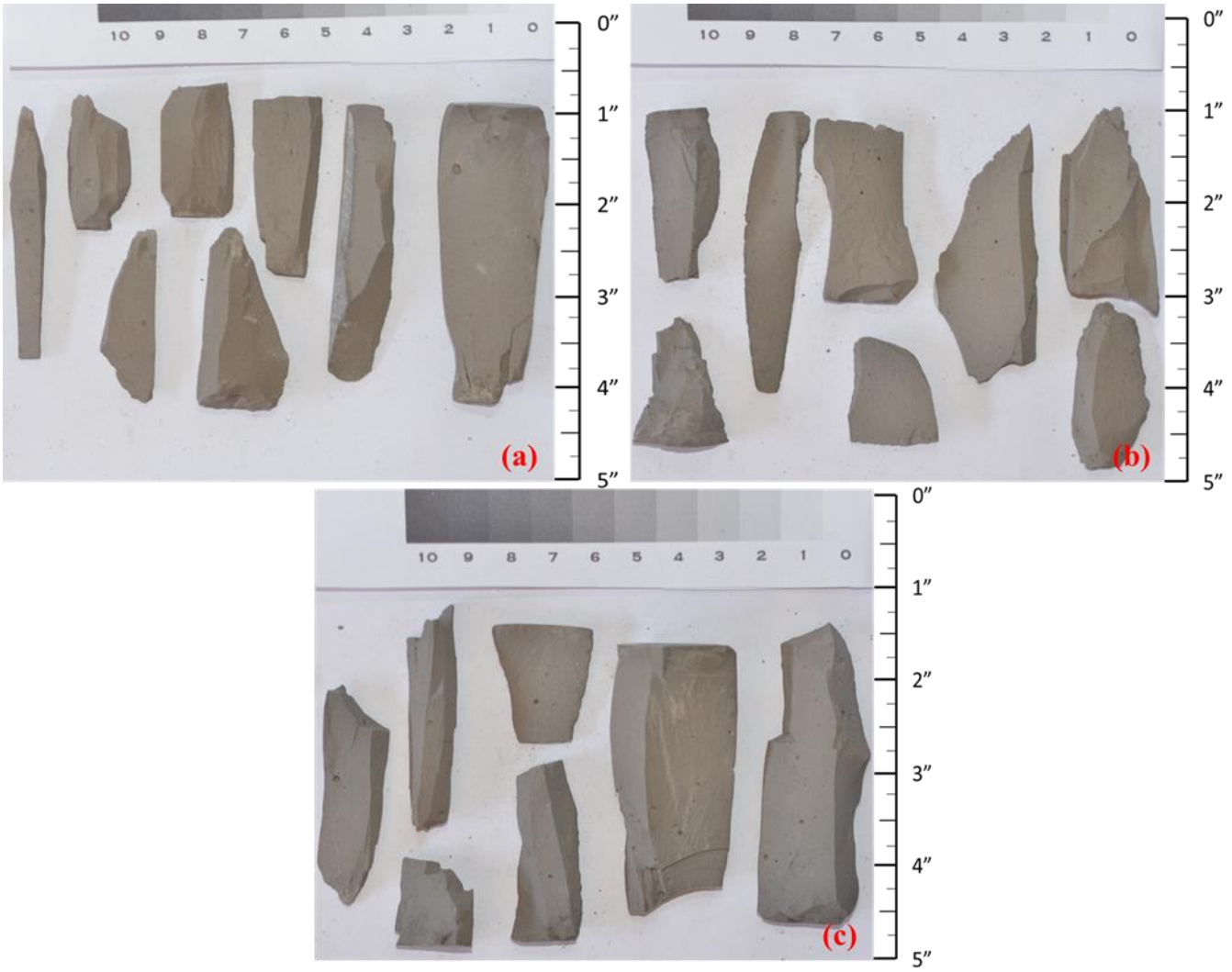

Figure D.16. 15% submicron case sample cured for 28-days (a) 1; (b) 2; (c) 3 after UCS testing.

Figure D.17. 25% submicron case sample cured for 28-days (a) 1; (b) 2; (c) 3 after UCS testing.

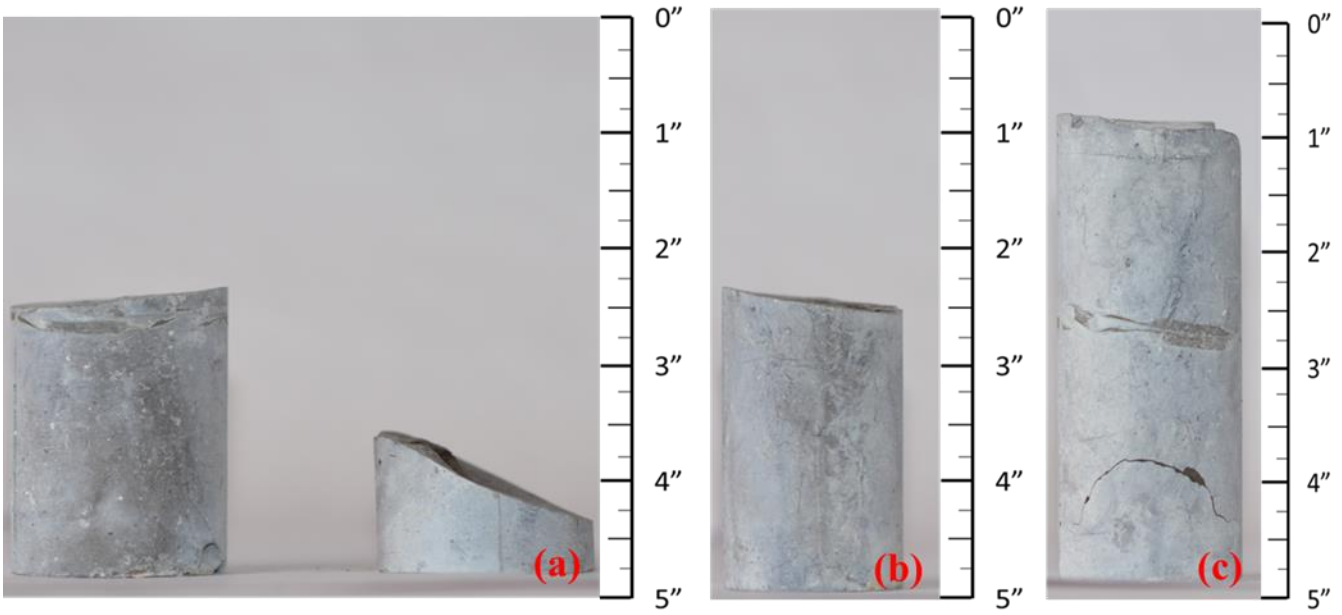

Figure D.18. 50% submicron case sample cured for 28-days (a) 1; (b) 2; (c) 3. Samples were broken during curing.

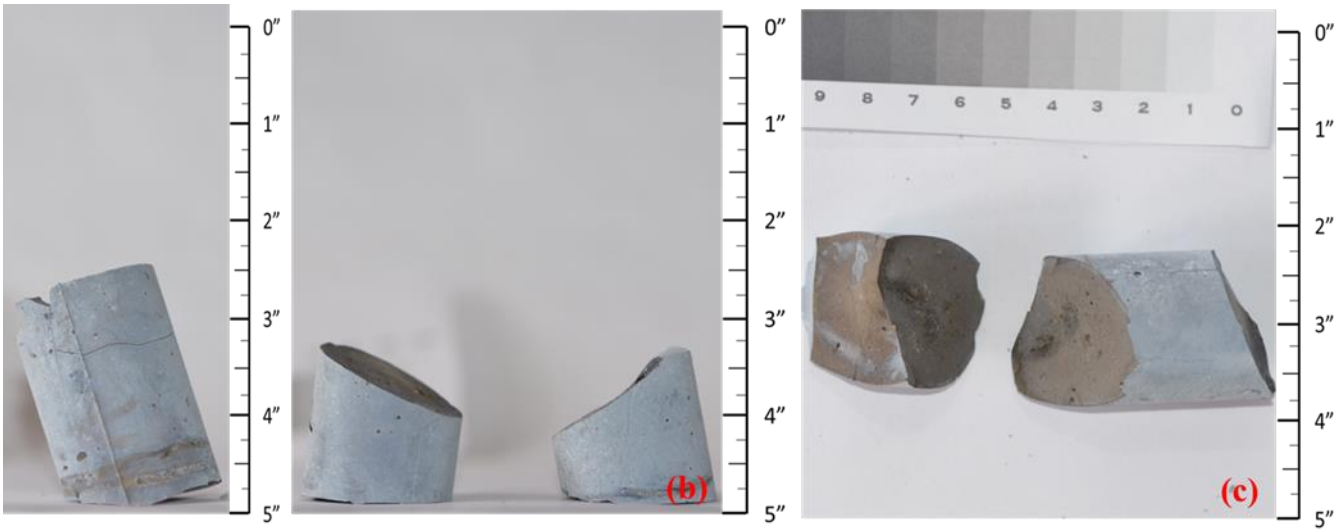

Figure D.19. 75% submicron case sample cured for 28-days (a) 1; (b) 2; (c) 3. Samples were broken during curing.

Appendix E: Wellbore Characteristics that Control Debonding Initiation and Microannuli Width in Finite Element Simulations

To understand how various parameters of a cement sheath and wellbore environment effect leakage potential, the following collaborative study (Wise et al., 2020) done as part of the thesis is included to show the importance and motivation of the first two chapters in this work. This article shows via a life of well advanced modeling that various factors can contribute to the magnitude and initiation of gaps at various downhole conditions, and cement stress at various pressures and temperatures can have a moderately high effect on the magnitude and initiation of gaps downhole. This stress can be more accurately predicted using the Biot coefficient, or the poroelastic constant. Due to the limited information on the Biot coefficient of cement used in wellbores, it can be implied that the current models being used are inaccurate to some degree.

Abstract

Environmental protection is an increasing concern for plugged and abandoned wells within the Gulf of Mexico. Leakage, however, has been shown to occur before the plug and abandonment (P&A) process takes place. The cement used when completing a well may develop leakage paths in the form of microannuli gaps between the casing and cement due to decreases in pressure and/or temperature. The goal of this paper is to use Finite Element Models (FEM) to determine the decrease in pressure or temperature required to initiate debonding of the cement sheath and the corresponding microannuli widths. Results of this paper show that there is a reduction threshold in which microannuli gaps start to initiate and increase in magnitude. A parametric analysis of the parameters within a wellbore has been performed and determined that the dimensions of the wellbore play a critical factor in microannuli gap width. With this knowledge, microannuli gap prediction graphs can be developed for different wellbore dimensions with

pressure and temperature variations to determine whether a wellbore is at risk for leakage prior to P&A.

1. Introduction

Wellbore leakage can occur throughout every stage of a wells life. The drilling process only accounts for a small portion of a wells life, thus wellbore leakage is more than likely to occur after drilling and completion once the casing and cement are present (Feng et al., 2017; Zhang and Bachu, 2010; Fourmaintraux et al., 2005). The presence of microannuli between the casing/cement and/or rock formation/cement interface has been shown to be a likely pathway for hydrocarbon migration within a wellbore (Wise et al., 2019; Vrålstad et al., 2018; Bois et al., 2011). Such migration can contaminate aquifers or potentially even reach the surface environment (Watson and Bachu, 2009). Before a well can be permanently plugged and abandoned (P&A'ed), it has to meet current standards designated by specific regulatory agencies for the region/country to prevent leakage. For instance, cement bond logs showing intact cement sheath is required before P&A procedures can take place according to NORSOK D-010 (2013). However, cement bond logs are not able to detect gas filled microannuli gaps or are able to quantify the gap sizes (De Andrade et al., 2019). To better understand how microannuli gaps form as well as what influences the size of such gaps, various modeling approaches have been evaluated as described in the review papers by Kiran et al. (2017), Bois et al. (2011), and Gray et al. (2009). A plethora of finite element models (FEM) have been established to analyze how cement sheath failure can occur and determine how such failure influences hydrocarbon leakage in a wellbore. Reported models have replicated of the life cycle of the well through staged steps (Gray et al., 2009; Nygaard et al., 2014), investigated varying rock/cement material properties (Wise et al., 2019), changing downhole temperature and pressure (Nygaard et al., 2014), and

pore pressure variations in the cement (Bois et al., 2011; Saint-Marc et al., 2008). Models have previously shown that gaps are created due to changes in internal casing pressure (Wise et al., 2019; Patel and Salehi, 2019; Nygaard et al., 2014; Bois et al., 2011) and changes in temperature within the wellbore (Zhang et al., 2017; Lavrov et al., 2015; Nygaard et al., 2014). The studies listed above determined that changes in pressure and temperature cause debonding, yet did not determine explicit values at which microannuli are initiated. The objective of this paper is to determine at which point changes in pressure or temperature cause microannuli gaps to initiate and to better understand how certain wellbore parameters can affect the initiation and gap magnitude. The quantification of the microannuli gap widths presented in this paper may be used as additional criterion to ensure the integrity of the cement sheath based off maximum changes in pressure and temperature before P&A procedures can take place.

2. Methodology

2.1. Study area

With more than 50,000 oil and gas wells, the High Island OPD, located in the Western Planning Area in the Gulf of Mexico, was selected to represent wells with a range of ages, statuses, and depths. The distribution of the True Vertical Depth (TVD) of the wells were analyzed and an average TVD was chosen. A well (API 427094116400) with a mean TVD was chosen to be the representative well in the model. The distribution of the wellbores in the High Island OPD is shown in Fig. 1 with a mean TVD of 2541 m (8336 ft).

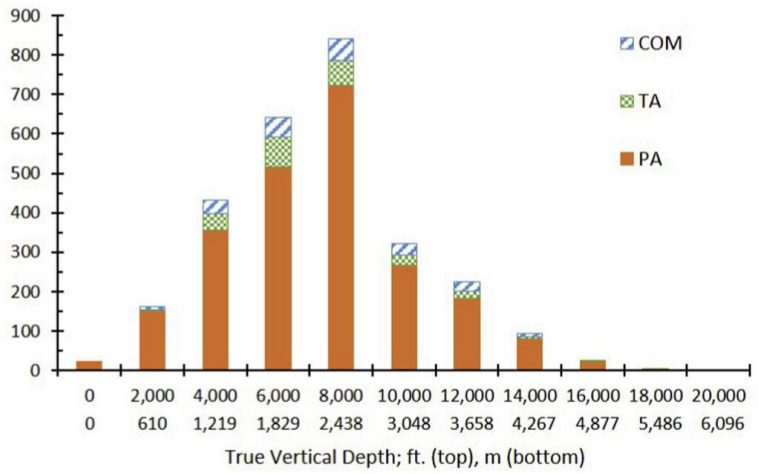

Figure E.1. True Vertical Depth (TVD) distribution of the number of wells in the High Island OPD with the distribution of their respective status codes of completed (COM), temporarily abandoned (TA), or permanently abandoned (PA) with an average being 2541 m (8336 ft). Raw data from BSEE (2018).

2.2. Long term modeling

The FEM replicates the well's lifecycle as described by Gray et al. (2009). This paper replicates the steps used by Wise et al. (2019) by including the initial conditions of the surrounding rock formation (in-situ stresses), drilling of the borehole (rock material removed and mud weight applied to the borehole), completion of the wellbore (cement displacing the mud column and hardening), and loading of the wellbore (drilling fluid column replaced with production pressure). One additional load step of thermal loading is included for the wellbore model presented in this paper. The thermal load is applied using a transient model with two days' worth of temperature change such that the temperature load would propagate completely throughout the cement sheath. The FEM was created and simulated using ANSYS™ 19.1 and is a static structural 3D thermo-poro-elastic model that uses a softening traction-separation law to model debonding of the casing/cement and cement/rock formation interfaces as described in Salehi and Nygaard (2015). The 3D model uses 25,552 CPT216 quadratic brick elements in which the element size in the interface zones is based on the Turon et al. (2006) approach which uses the element length determined by Hillerborg et al. (1976) and further divides the element length by

three to ensure the element size is fine enough to capture the delamination in the cohesive zones. Further refinement of the mesh was conducted using a mesh sensitivity analysis. The maximum gap width versus mesh density was analyzed to determine the optimal mesh density.

Fig. 2 shows a 2D (left) and 3D (right) cutaway of the model showing the three different materials within it (casing, cement, and rock formation). The 3D model dimensions are 1.5 m in the x and y (i.e. horizontal) directions and 0.05 m in the z (i.e. vertical) direction. A model with a vertical thickness of 0.05 m has 140,440 nodes with a computational run time of approximately 10 min. Thicker geometries of 0.5 m and 1.0 m would have 1,110,504 and 2,189,216 nodes, respectively with at least 12 h run times for a single simulation. The resulting gap width is the same magnitude between the 0.05 m and thicker models. Therefore, 0.5 m thickness was chosen.

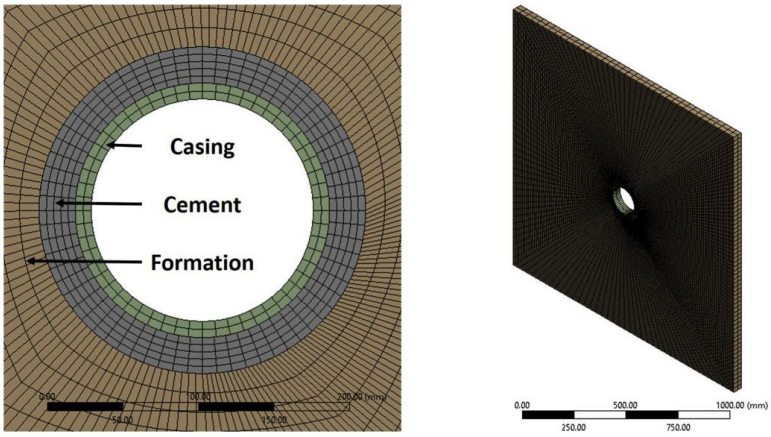

Figure E.2. 2D (left) and 3D (right) view of the gridded finite element model.

3D geometry is chosen such that plain-strain assumptions do not have to be made for the model. The scope of this paper is to model debonding initiation and gap width. Gap propagation is not considered in this model and therefore 3D vertical height does not affect the gap width. The model geometry is determined based on the Kirsch analytical solution that the ratio of the model size and the wellbore diameter is greater than three to represent a good approximation to the infinite case and to prevent unintentional boundary effects from the thermal distribution

throughout the model (Fjaer et al., 2008; Jaeger et al., 2007; Li and Nygaard, 2017). The model is constrained using frictionless supports on the top, bottom, and four edges to represent infinite supports. The dimensions of the borehole, casing thickness, and cement sheath thickness are based off the well selected in Section 2.1.

2.3.3 Mechanical properties

The input parameters for the base model are listed in Table 1 including the source(s) of the values. The simulation depth was chosen to be the depth of the deepest casing string prior to the production zones in the well. At this location, the cement sheath is assumed to be intact and not damaged from perforations. The TVD of the well would not be relevant for modeling cement sheath integrity due to the fact that it is below perforations and production zones and not acting as a primary barrier in preventing hydrocarbon migration or fresh water contamination.

Table E.1. Parameters for the base well (API # 427094116400) in the High Island OPD and the source of their values.

	Parameter	Value	
	TVD (m)	2623	1
	Simulation Depth (m)	1920	
Dimensions	Hole Size (cm)	31.12	1
	Casing OD (cm)	24.45	1
	Casing ID (cm)	21.68	1
	σ_H (MPa)	38.99	
In-Situ Stresses	σ_h (MPa)	36.98	1, 2, 3
	σ_v (MPa)	41.00	4
Casing	υ	0.30	5
	E (GPa)	200.00	5
	ρ (kg/m^3)	7938.00	1
	α (K^{-1})	1.14E-05	5
	κ (W/m•K)	43.00	5
	c (J/kg•K)	490.00	5
Cement	Pp (g/cc)	1.56	
	ρ_{slurry} (g/cc)	1.68	1
	σ_{cement}(MPa)	31.73	
	ν	0.18	6
	E (GPa)	6.38	6
	ρ_{dry} (kg/m^3)	1965.00	1
	α (K^{-1})	8.64E-06	6
	κ (W/m•K)	0.41	6
	c (J/kg•K)	490	6
Rock	Pp (g/cc)	1.56	1
	ν	0.34	7
	E (GPa)	3.9	7
	ρ (kg/m^3)	2600.00	7
	α (K^{-1})	1.00E-05	5
	κ (W/m•K)	2.40	5
	c (J/kg•K)	900.00	5

Casing/Cement	τ^0 (MPa)	0.50	8
	G_c (J/m^2)	100.00	8
Cement/Rock	τ^0 (MPa)	0.42	8
	G_c (J/m^2)	100.00	8
Loads	MW (g/cc)	30.49	1
	T_i (°C)	58.93	1

The model requires one of the principal in-situ stresses to align along the borehole direction for any given stress state. The in-situ stress gradients for the High Island OPD, reported to be a normal faulting regime, is based on correlations from Breckels and van Eekelen (1982), Wojtanowicz et al. (2000), Meng et al. (2018) as well as the drilling report for the well (OMB Control Number 1010-0141). The overburden stress gradient is based on data from Meng et al. (2018) for the Gulf of Mexico. The minimum horizontal stress is taken to be the average from the correlation from Breckels and van Eekelen (1982), measured leak off test (LOT) data from Wojtanowicz et al. (2000), and the fracture pressure gradient listed in the well drilling report. The maximum horizontal stress (σH) is taken to be the mean of the overburden (σv) and minimum horizontal stress (σh).

At the end of cement hydration, the pore pressure (Pp) of the cement is assumed to be equal to the pore pressure of the surrounding rock formation (Li and Nygaard, 2017; Zhang et al., 2017; Gray et al., 2009). The setting stress of the cement ($\sigma cement$) is assumed to be equal to the hydrostatic column of the cement slurry (Nygaard et al., 2014; Bois et al., 2012; Gray et al., 2009; Bosma et al., 1999). The mechanical and thermal properties of the cement was determined from a cement database created by the authors of this paper for Class H and G cement, which are most commonly used cements for wellbore completions. The summary of the database and the methodology used for determining the values can be found in Appendix B.

Log analysis of High Island OPD wells has been performed to determine representative rock mechanical values for this region since direct measurements are not known. The methodology

and correlations used can be found in Appendix A. It is important to mention that drilling induced fractures and natural fractured zones were excluded in this model. The rock formation mechanical properties are determined by log analysis of two Gulf of Mexico wells. The initial mechanical and thermal loads within the wellbore (*MW* and *Ti*, respectively) were determined from the drilling report (OMB Control Number 1010-0141).

A parametric analysis of parameters with uncertainties (in-situ stresses, cement mechanical and thermal properties, rock mechanical and thermal properties, and softening traction-separation law properties) as well as parameters that are easily changeable from an engineering perspective (wellbore dimensions) will be been simulated. The upper and lower bounds of the sensitivity analysis are shown in Table 2 and the methodology for obtaining the values are described Appendix A for the rock formation mechanical properties and Appendix B for the cement mechanical and thermal properties.

Table E.2. High and low values for the parametric study. These values apply for all three well depth parameters.

Parameter	Low	High
Dimensions	-40%	+40%
Isotropic Horizontal Stress Variation	$\sigma_v = \sigma_{v,base}$ $\sigma_H = \sigma_{h,base}$ $\sigma_h = \sigma_{h,base}$	$\sigma_v = \sigma_{v,base}$ $\sigma_H = \sigma_{v,base}$ $\sigma_h = \sigma_{v,base}$
Anisotropic Stress Variations	$\sigma_v = \sigma_{v,base}$ $\sigma_H = \sigma_{h,base}$ $\sigma_h = \sigma_{h,base}$	$\sigma_v = \sigma_{v,base}$ $\sigma_H = \sigma_{v,base}$ $\sigma_h = \sigma_{h,base}$
Vertical Stress Variations	$\sigma_v = -5\% \cdot \sigma_{v,base}$ $\sigma_H = \frac{\sigma_v + \sigma_h}{2}$ $\sigma_h = \sigma_{h,base}$	$\sigma_v = +5\% \cdot \sigma_{v,base}$ $\sigma_H = \frac{\sigma_v + \sigma_h}{2}$ $\sigma_h = \sigma_{h,base}$
Cement Stress (MPa)	*MW*	$P_{fracture}$
Cement Mechanical and Thermal Properties	25% Quartile	75% Quartile
Rock Mechanical Properties	Min from Log Data	Max from Log Data
Rock Thermal Properties	-40%	+40%
Traction Law Properties	-40%	+40%

The results are reported in terms of changes in pressure (ΔP) and temperature (ΔT) and are normalized with respect to initial conditions in Equations (1) and (2) respectively. As defined, a

positive Δ indicates a reduction in pressure or temperature, and a negative Δ indicates an increase in pressure or temperature.

$$\Delta P = 1 - \frac{Pressure\ Load}{MW} \cdot 100\% \quad (1)$$

$$\Delta T = 1 - \frac{Temperature\ Load}{T_i} \cdot 100\% \quad (2)$$

3. Results

The first section (3.1) describes the base model gap width with respect to ΔP and ΔT. Secondly, the parametric results are reported in Section 3.2. The results of analyzing concurrent changes in ΔP and ΔT with their respective gap widths are presented in Section 3.3. Lastly, the application of using this analysis as a criterion for P&A'ed wells is explained in Section 3.4.

3.1. Pressure and temperature curves

Fig. 3 shows the reduction (Δ) versus gap width for the casing/ cement interfaces and Fig. 4 shows the cement/rock interfaces results. The gaps primarily occur at the interface between the casing and cement sheath (Fig. 3). The cement/rock interface has gaps, yet they are on the nanometer scale whereas the gaps associated with the casing/cement interface are on the micron scale. Therefore, the gaps (or lack thereof) at the cement/rock interface are deemed negligible.

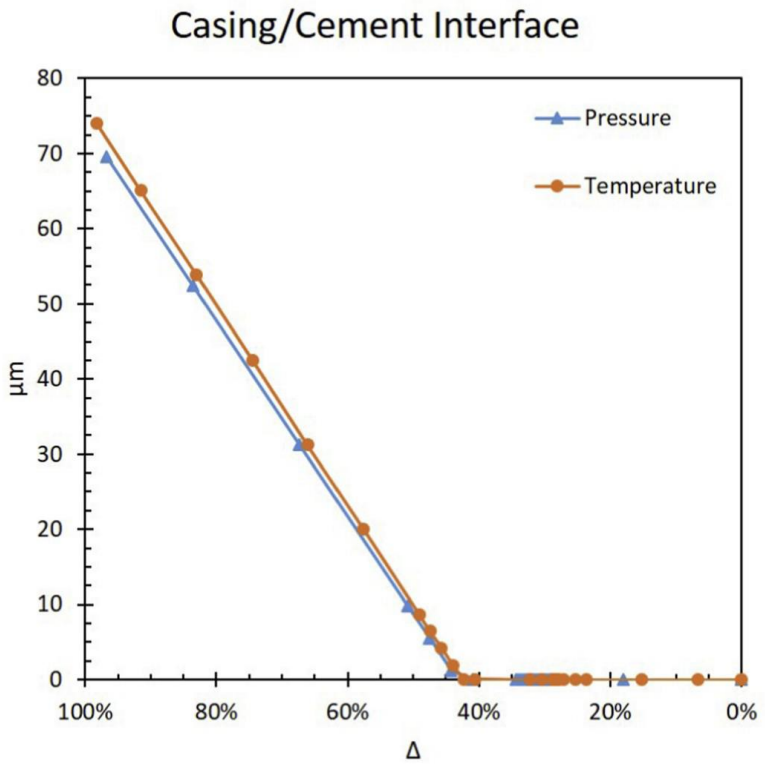

Figure E.3. Gap magnitude versus reduction in pressure (ΔP) and temperature (ΔT) at the casing/cement interface.

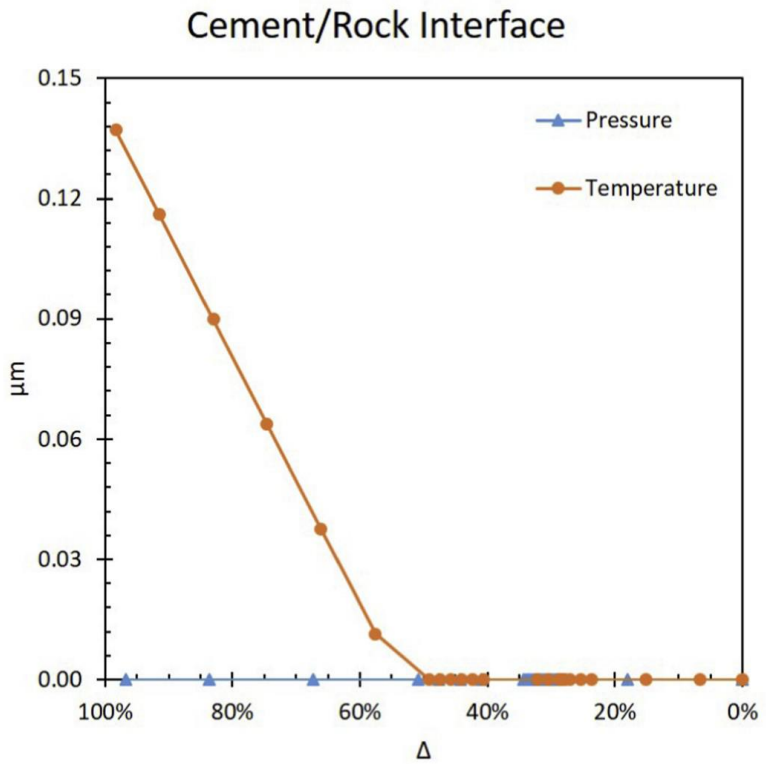

Figure E.4. ΔP and ΔT and the respective gap sizes at the cement/rock interface. Note that the max size of the gaps are two orders of magnitude smaller than the gaps at the casing/cement interface.

The gaps shown in Fig. 3 first occur (>1 nm) when pressure and temperature have a reduction of 29.5% and 28.4% respectively for this wellbore. Performing a linear fit to the significant gap portion of the data can be used to determine the ΔP and ΔT that causes significant gaps (>1 µm). This method determines that micron sized gaps initiate at 43.3% and 42.5% for ΔP and ΔT, respectively. The change from nanometer to micron gap sizes is a decrease in load of approximately 14% for both pressure and temperature. The non-linearity of gap size versus load reduction is due to the softening traction-separation law. The gaps are initiated at Δ Ό 29% but do not reach linearity until Δ Ό 43%. For the remainder of this work, the gap initiation threshold of micron sized gaps will be used, but it is important to note that nanometer sized gaps are occurring prior to this point. The maximum gaps for both ΔP = 0 and ΔT = 0 are 73.8 and 76.3 µm, respectively, as shown in Table 3. The slope of the temperature induced gaps is steeper than

the pressure induced gaps curve indicating that ΔT has a slightly greater impact on gap magnitude versus ΔP. The results of the gap initiation are in agreement with Nygaard et al. (2014) and Gray et al. (2009) in which debonding occurs at the casing/cement interface whereas Zhang et al. (2017) and Crain et al. (2018) observed debonding at the cement/rock interface.

Table E.3. Gap initiation reduction changes for ΔP and ΔT including nanometer (nm) gap and micrometer (μm) gap initiation Δ's.

	nm gaps	μm gaps	Max Gap (μm)
Δ P	29.5%	43.3%	73.8
Δ T	28.4%	42.5%	76.3

The results from Fig. 4 indicate that debonding occurs at the cement/ rock interface on the nanometer scale whereas Zhang et al. (2017) observed micron sized gaps. Debonding of the cement to the casing is most likely due to the vast difference between the material stiffness (Young's modulus, *E*). From Table 1, the stiffness of casing is an order of magnitude larger than the stiffness of the cement whereas the stiffness of the rock formation is the same order of magnitude as the cement. Therefore, it is to be expected that debonding occurs at the casing/cement interface. The results from this paper are in agreement with experimental results from Vrålstad et al. (2015) and later expanded by De Andrade et al. (2016). The experiments consisted of thermal cycle tests at on casing/cement/formation samples which were then scanned by CT. Their results show that cement sheath debonding occurs between the cement/casing interface when shale is the rock formation. Debonding between the cement/rock formation occurs when sandstone is the rock formation.

The magnitude of the microannuli gap at the casing/cement interface is in agreement with the reported value from Gray et al. (2009). Gray et al. (2009) reported a microannuli gap of 13.7 μm with a ΔP = 61%. From Fig. 3, ΔP = 61% results in a microannuli gap of 23.1 μm. The slight

discrepancy between the results can be attributed to the difference in wellbore dimensions (311.15 mm [12.25”] hole size with 244.48 mm [9.625”] casing thickness versus 241.30 mm [9.5”] hole size with 193.68 mm [7.625”] casing thickness), simulated depths (1920 m [6300 ft] versus 4572 m [15,000 ft]), and specific wellbore parameters.

3.2. Parameter sensitivity analysis

The change in pressure and temperature (ΔP and ΔT) have been shown to cause microannuli gaps, but there are numerous parameters within a wellbore that can affect the magnitude and initiation of such gaps. The parameters listed in Section 2 are tested with different ΔP’s and ΔT’s to determine which parameters are contributing factors to gap initiation and magnitude. The Δ’s are a reduction in both pressure and temperature of 29%, 44%, 50%, and 67% based off of the curves shown in Fig. 3. For a reduction of 29%, nanometer gaps were created from the base case curves and micron gaps were initiated at a 44% reduction. A reduction of 50% resulted in gaps of approximately 10 μm. A reduction of 67% resulted in gaps of approximately 30 μm. The results for all four percent reductions are shown in Fig. 5 for ΔP and Fig. 6 for ΔT for the maximum and minimum gap sizes. An individual analysis of each percent reduction for both ΔP and ΔT is discussed in the subsequent sections.

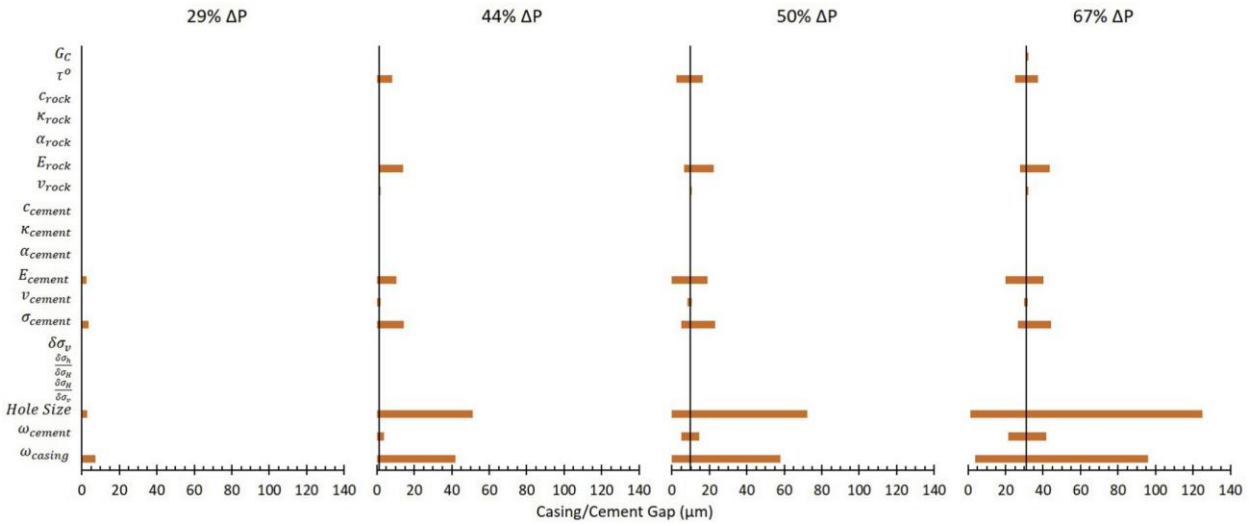

Figure E.5. Parametric analysis of the maximum and minimum variables tested for change in wellbore pressures (ΔP) of 29%, 44%, 50%, and 67%. Variances in the hole size and casing thickness have the largest change in resulting gap magnitudes.

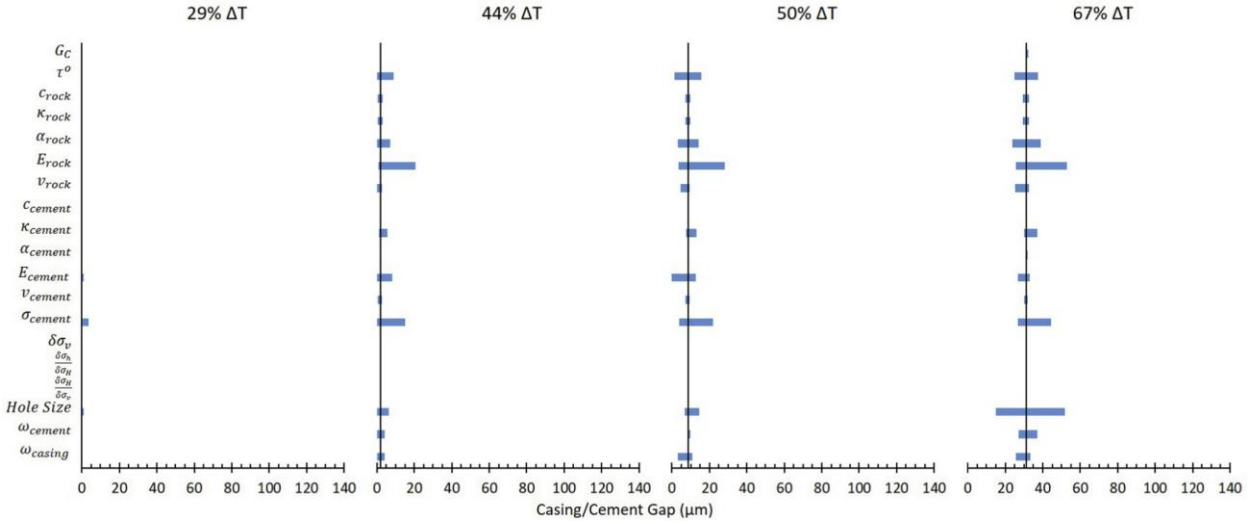

Figure E.6. Parametric analysis of the maximum and minimum variables tested for change in wellbore temperatures (ΔT) of 29%, 44%, 50%, and 67%. None of the wellbore parameters change gap magnitude as significantly as hole size and casing thickness do for change in pressures (ΔP).

3.2.1. 29% reduction

For a reduction of 29%, nanometer sized gaps occur in the base well, but variations of *Ecement*, *σcement*, *Hole Size*, and *ωcasing* cause micron sized gaps to occur. It should be noted that only *Ecement* and *σcement* cause gaps to occur with ΔT while all four cause gaps to occur with ΔT.

The gaps range from a size of 0 μm (no gap/nanometer size gap) to a maximum gap of 7.2 μm implying that these four parameters can cause the gap initiation to decrease from 43% to 29% (i.e. lower ΔP and ΔT). The variations of the four parameters are shown in Table 4 along with their respective gap sizes. An interesting observation is that the change in hole size effects the gaps created by pressure and temperature inversely. A larger hole size results in gaps with a 29% ΔP while a smaller hole size results is gaps with a 29% ΔT.

Table E.4. Gap magnitudes created by change in wellbore parameters for a 29% ΔP and ΔT. These parameters cause gaps to occur when the base case wellbore did not have gaps at 29% ΔP and ΔT.

Parameter	Δ P		Δ T	
	Parameter Change	Gap (μm)	Parameter Change	Gap (μm)
ω_{casing}	0.60	7.21		
σ_{cement}	1.21	3.71	1.21	3.50
$Hole\ Size$	1.40	2.73	0.60	0.90
E_{cement}	1.49	2.52	1.49	1.10

3.2.2. 44% reduction

The microannuli gaps for a 44% reduction in ΔP and ΔT range in size from 0 μm to 51.2 μm. For the base wellbore, ΔP resulted in a gap of 1.25 μm and variations of *τo*, *Erock*, *Ecement*, *vcement*, *σcement*, *Hole Size*, *ωcement*, and *ωcasing* caused changes in the base gap width. For the base wellbore, ΔT resulted in a gap of 1.95 μm and variations in *τo*, *crock*, *κrock*, *αrock*, *Erock*, *vrock*, *Ecement*, *vcement*, *σcement*, *Hole Size*, *ωcement*, and *ωcasing* all resulted in changes from the base gap. The reduction in temperature had variations in gap size due to more parameters than ΔP, but ΔP resulted in larger magnitude of gaps; primary due to *ωcasing* and *Hole Size*. Both of these parameters had gaps larger than 25 μm. One observation with the 44% reduction is that many of the wellbore parameters could be altered such that the base gaps for ΔP and ΔT (1.25 μm and 1.95 μm respectively) can be reduced down to no gap (0 μm). These parameters are listed in Table 5. Another observation is that the same trend occurs with the 44%

reduction as with the 29% reduction. The hole size variations have inverse effects on gap widths depending on ΔP or ΔT. A similar trend occurs for the casing thickness, except that thicker casings have smaller gaps for ΔP while thinner casings have smaller gaps for ΔT.

Table E.5. Parameters that caused the gap magnitudes to be eliminated (0 μm) with a 44% ΔP and ΔT.

Parameter	Δ P	Δ T
	Parameter Change	Parameter Change
$Hole\ Size$	0.60	1.20
ω_{casing}	1.40	0.60
σ_{cement}	0.93	0.93
E_{cement}	0.66	0.66
τ^0	1.40	1.40
ω_{cement}	1.20	0.80
υ_{cement}	1.33	
α_{rock}		0.60
υ_{rock}		0.74

3.2.3. 50% reduction

The microannuli gaps for a 50% reduction in ΔP and ΔT range from a size of 0 μm–72.2 μm. For the base case with a reduction of 50%, ΔP resulted in a gap of 9.79 μm and ΔT resulted in a gap of 8.72 μm. Every parameter that caused variations in the base gaps with ΔP and ΔT at 44% reduction caused variations in gap widths with 50% reduction. As with the 44% reduction, *ωcasing* and *Hole Size* created large variations in the gap widths for ΔP. The variations due to ΔT are not as significant. With a reduction of 50% in ΔP and/or ΔT, three of the parameters can be altered such that the base case gap can be reduced down to no gap (0 μm). The parameters that can be altered such that there is not a gap are *ωcasing*, *Hole Size*, and *Ecement*. All three parameters can eliminate the gap for ΔP, but only *Ecement* significantly reduced the gap for ΔT (0.1 μm).

3.2.4. 67% reduction

The microannuli gaps for a 67% reduction in ΔP and ΔT range in size from 1.3 μm to 125.2 μm. For the base case with a reduction of 67%, ΔP resulted in a gap of 31.13 μm and ΔT resulted in a

gap of 31.25 μm. Similar to the 50% and 44% reduction, *ωcasing* and *Hole Size* have the largest variation in gap width for ΔP. The largest gap variation for ΔT is the change in hole size with a range of 36.9 μm whereas the largest gap variation for ΔP is change in hole size with a range of 123.9 μm. The change in *Hole Size* did not have a major effect with respect to microannuli gap sizes with respect to ΔT with the 29%, 44%, and 50% reductions, but the *Hole Size* has a major effect with a 67% reduction most likely due to the softening traction-separation law. The 67% reduction in ΔT exceeded the threshold required to initiate significant microannuli gap growth with *Hole Size* variations whereas lesser temperature reductions did not. Based on the results from the 67% ΔP and ΔT reduction, changes in pressure with respect to wellbore parameters are more critical than changes in temperature.

The results of the parametric analysis are sorted based off their percent change of the maximum gap width (%MGW) from the base microannuli gap as shown in Table 6 in terms of 1st, 2nd, and 3rd Order Parameters. 3rd Order Parameters are defined as parameters with their %MGW less than 10%. 3rd Order Parameters have little to no effect on the development of the gap magnitude and therefore are not critical inputs into the well life cycle model. 2nd Order Parameters are defined as parameters with their %MGW larger than 10% but less than 100%. These parameters have some effect on the gap with magnitude, but are not critical. Finally, 1st Order Parameters are defined as parameters that have their %MGW larger than 100%. These input parameters (*Hole Size* and *ωcasing*) have the largest impact on the gap width development. It is important to note that only reductions in pressure (ΔP) have 1st Order Parameters. Reductions in temperature (ΔT) have 2nd and 3rd Order Parameters and therefore do not have a large impact on gap width development when compared to ΔP.

Table E.6. Wellbore parameters sorted based off their percent change of the maximum gap width (%MGW) from the base gap magnitude. 1st Order Parameters are critical in the development of the gap width magnitude at the casing/cement interface. 2nd Order Parameters have minor effect, and 3rd Order Parameters have little to no effect on the development of the gap widths.

	Δ P	%MGW	Δ T	%MGW
1st Order Parameters	$Hole\ Size$	302%		
	ω_{casing}	208%		
2nd Order Parameters	σ_{cement}	42%	E_{rock}	69%
	E_{rock}	40%	$Hole\ Size$	66%
	ω_{cement}	34%	σ_{cement}	42%
	E_{cement}	29%	α_{rock}	24%
	τ^0	20%	τ^0	20%
			ω_{casing}	19%
			κ_{casing}	18%
3rd Order Parameters	G_c	3%	ω_{casing}	7%
	υ_{rock}	3%	E_{cement}	6%
	υ_{cement}	2%	c_{rock}	5%
	α_{rock}	0%	κ_{rock}	5%
	$\delta\sigma_v$	0%	υ_{rock}	4%
	α_{cement}	0%	G_c	3%
	κ_{cement}	0%	υ_{cement}	2%
	c_{cement}	0%	α_{cement}	2%
	κ_{rock}	0%	c_{cement}	0%
	c_{rock}	0%	$\delta\sigma_v$	0%
	$\frac{\delta\sigma_H}{\delta\sigma_v}$	0%	$\frac{\delta\sigma_H}{\delta\sigma_v}$	0%
	$\frac{\delta\sigma_h}{\delta\sigma_H}$	0%	$\frac{\delta\sigma_h}{\delta\sigma_H}$	0%

3.3. Gap prediction

From the analyses from Sections 3.1 and 3.2, the microannuli gaps at the casing/cement interface are primarily a function of ΔP, ΔT, *ωcasing*, and *Hole Size*. For the purpose of determining if wells are intact and able to provide zonal isolation, the history of pressure and temperatures should be investigated. If the casing/cement interface experiences debonding at one point in the life cycle of a well, the bond is not going to "heal" and provide zonal isolation (Stormont et al., 2018). Figs. 7–10 depict the casing/cement interface gap when changing the pressure and temperature for the case study at four depths (6300 ft, 5233 ft, 4167 ft, and 3100 ft) along the primary cement barrier (i.e. intermediate casing string). The results of Figs. 7–10 show that when both pressure and temperature are reduced in the wellbore, the gap magnitude increases.

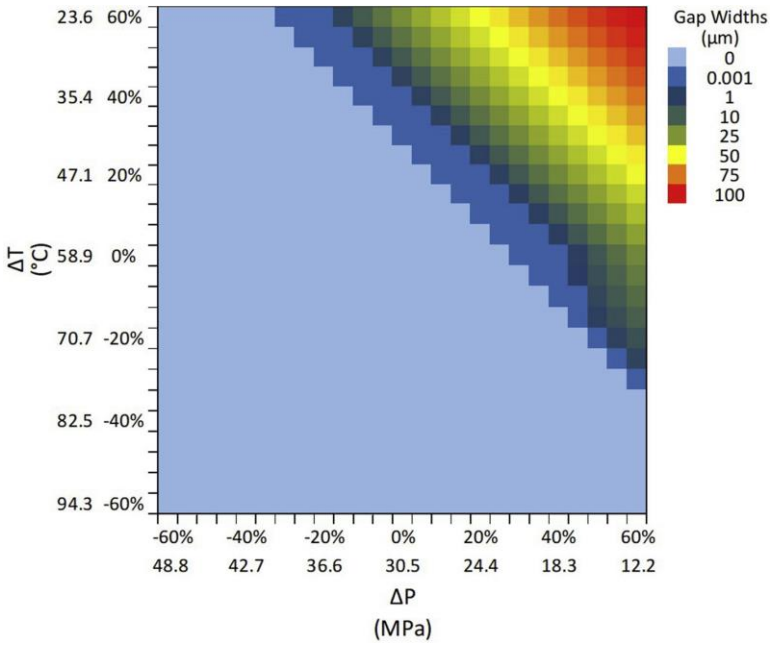

Figure E.7. Heat map showing the gap magnitudes resulting from a combination of ΔP and ΔT as explained from Equations (1) and (2). A positive Δ indicates a reduction while a negative Δ is an increase. Note in the legend that nanometer (nm) sized gaps are indicated (0.001 µm) along with micron (µm) sized gaps. The results of this heat map are indicative of a 12.2500 hole size with 9.62500 P-110EC casing at a depth of 6300 ft.

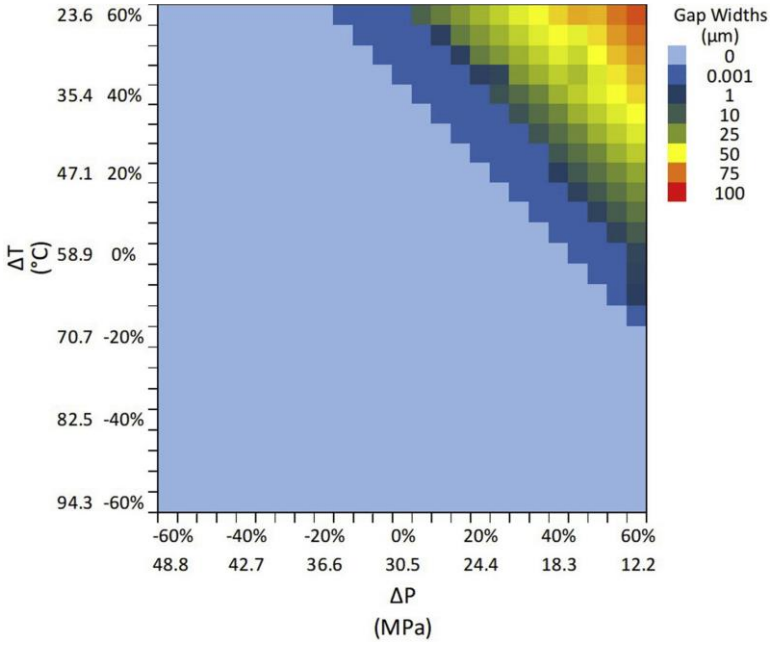

Figure E.8. Heat map showing the gap magnitudes resulting from a combination of ΔP and ΔT as explained from Equations (1) and (2). A positive Δ indicates a reduction while a negative Δ is an increase. Note in the legend that nanometer (nm) sized gaps are indicated (0.001 µm) along with micron (µm) sized gaps. The results of this heat map are indicative of a 12.2500 hole size with 9.62500 P-110EC casing at a depth of 5233 ft.

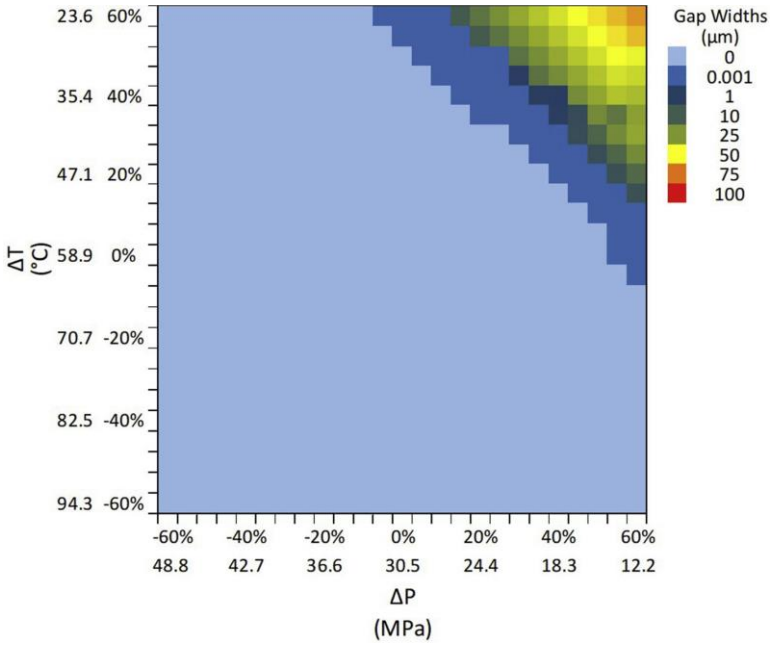

Figure E.9. Heat map showing the gap magnitudes resulting from a combination of ΔP and ΔT as explained from Equations (1) and (2). A positive Δ indicates a reduction while a negative Δ is an increase. Note in the legend that nanometer (nm) sized gaps are indicated (0.001 μm) along with micron (μm) sized gaps. The results of this heat map are indicative of a 12.2500 hole size with 9.62500 P-110EC casing at a depth of 4167 ft.

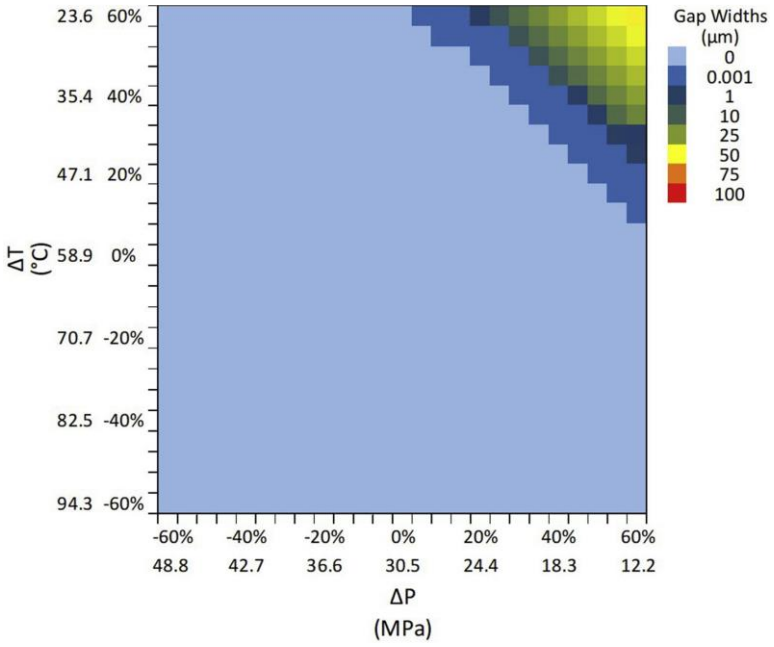

Figure E.10. Heat map showing the gap magnitudes resulting from a combination of ΔP and ΔT as explained from Equations (1) and (2). A positive Δ indicates a reduction while a negative Δ is an increase. Note in the legend that nanometer (nm) sized gaps

are indicated (0.001 μm) along with micron (μm) sized gaps. The results of this heat map are indicative of a 12.2500 hole size with 9.62500 P-110EC casing at a depth of 3100 ft.

The maximum gap magnitude caused by only a reduction of pressure or only a reduction of temperature is 73.8 μm and 76.3 μm, respectively as shown previously in Table 3. However, Fig. 7 shows that a reduction of pressure can be offset by an increase in temperature and vice versa. A pressure reduction of 60% (ΔP = 60%) and an increase in temperature of 60% (ΔT= -60%) results in zero gap width whereas a reduction of only pressure or temperature of 60% results in gaps as shown in Fig. 3. It should be noted that the pressure and temperature curves are not symmetric in Fig. 7 as shown by the micron sized gaps occurring due to pressure reduction of 60% (ΔP = 60%) and a temperature increase of 25% (ΔT = -25%) while a temperature reduction of 60% (ΔT = 60%) and a pressure increase of 15% (ΔP = 15%) develops micron sized gaps. This phenomenon is explained by the individual pressure and temperature curves in Fig. 3. The individual curves do not overlap exactly and therefore this asymmetry is shown in Fig. 7. It is important to note that the apparent symmetry shown for other combinations of ΔP and ΔT is due to the legend scale resolution.

3.4. P&A implications

The results of this paper indicate that careful consideration should be considered when planning and operating a wellbore. For example, if a wellbore is designed to have a certain drilling fluid density (mud weight) when drilled and the production engineers anticipate that the production pressure will be significantly lower than the planned mud weight, changes should be made to the drilling plan to decrease the mud weight such that a significant drop in wellbore pressure will not occur. The same type of planning can be used for maintaining wellbore temperature. For example, if a wellbore has a temperature gradient that is significantly higher than the injection temperature of supercritical CO_2, then the proposed wellbore should not be used as an injection

well knowing there would be a high probability of temperature induced microannuli creation. The curves produced in Fig. 3 could be useful in planning and operating a wellbore such that they can be used to predict the potential for microannuli gaps to occur. These curves may also be used as a post analysis tool to determine if existing wells are experiencing debonding of the cement sheath to the casing based off their historical pressure and temperatures. The heat map analysis can be developed further with additional combinations of wellbore dimensions such that regulatory agencies/ companies can use this method to determine if P&A candidate wells need remediation work to fix cement sheath leakage prior to abandonment. Completion and production reports can be investigated to determine the historical pressures and temperatures of a well. The pressures and temperatures can then be analyzed with the wellbore dimensions to determine if the well is at risk for microannuli gaps in the cement sheath.

4. Conclusions

A staged 3D finite element model with dimensions from a wellbore in the High Island OPD in the Gulf of Mexico was developed to assess the integrity of the cement sheath in regards to the potential of P&A of the wellbore with the casing (and cement sheath) left in the borehole. Microannuli gaps caused by debonding of the casing and cement sheath have previously been shown to be the primary leakage pathway in vertical wellbores due to changes in internal casing pressure (ΔP) and thermal changes (ΔT). The results of this paper show that ΔP and ΔT have a reduction threshold in which microannuli gaps start to initiate and increase in magnitude. A parametric analysis was performed to determine the contributing factors within a wellbore that enable or hinder microannuli growth and showed that hole size and casing thickness were the main factors in growth or prevention of microannuli development. With this knowledge, a gap magnitude prediction graph in the form of a heat map was developed for the depth of the well

(specific hole size) with the casing grade (casing thickness) to understand which combinations of ΔP and ΔT result in microannuli gap widths between the casing and cement sheath. A main output of this development is that microannuli gap magnitudes can be quantified. Another output is that the method presented in this paper can be used as a tool to determine if the cement sheath of a wellbore is intact and if the P&A process can continue or if remediation work is required. This analysis can also be used as a planning tool to prevent microannuli gaps from developing in a well's life cycle.

References

1. Ahdaya, M.S., Imqam, A., Jani, P., Fakher, S. & ElGawady, M. 2019. New Formulation of Fly Ash Class C Based Geopolymer for Oil Well Cementing. Presented at the International Petroleum Technology Conference, Beijing, China, 26-28 March. IPTC-19393-MS.
2. Ahmed, A., Elkatatny, S., Adjei, S. & Al-Majed, A. 2020. Influence of Weighting Materials on the Properties of Oil-Well Cement, in *ACS Omega* **5**(2020): 27618-27625. https://dx.doi.org/10.1021/acsomega.0c04186.
3. Aïtcin, P-C. 2016. Supplementary cementitious materials and blended cements. Science and Technology of Concrete Admixtures, 1st ed., Woodhead Publishing, Waltham, MA. http://dx.doi.org/10.1016/B978-0-08-100693-1.00004-7.
4. Alam, M.M., Christensen, H.F. & Fabricius, I.L. Effective Stress Coefficient and Biot's Coefficient of Chalk from the Valhall Field, North Sea. Presented at EUROPEC/EAGE Conference and Exhibition, Amsterdam, The Netherlands, 8-11 June.SPE-121795-MS https://doi.org/10.2118/121795-MS.
5. Alkhamis, M. & Imqam, A. 2018. New Cement Formulations Utilizing Graphene Nano Platelets to Improve Cement Properties and Long-term Reliability in Oil Wells. Presented at the SPE Kingdom of Saudi Arabia Annual Technical Symposium and Exhibition, Dammam, Saudi Arabia, 23-26 April. SPE-192342-MS.
6. Andreassen, K.A. 2017. Induration and Biot's Coefficient of Palaeogene Limestone, in: Poromechanics VI: Proceedings of the Sixth Biot Conference on Poromechanics.
7. Anya, A. 2018. Lightweight and Ultra-Lightweight Cements for Well Cementing-A Review. Presented at the SPE Western Regional Meeting, Garden Grove, CA, 22-27 April. SPE-190079-MS. https://doi-org.ezproxy.lib.ou.edu/10.2118/190079-MS.
8. API RP 10B-2, Recommended Practice for Testing Well Cements, second edition. 2013. Washington, DC: API.
9. API Spec 10A, Specification for Cements and Materials for Well Cementing. 23rd ed. 2002. Washington, DC: API.
10. API Standard 65-2, Isolating Potential Flow Zones During Well Construction. 2nd ed. 2010. Washington, DC: API.
11. Ashraf, S., Haidzar, R., Husin, M. & Hafiz, F.U.M. 2021. Effects of Well Cement Additive Particle Size and Density Towards Overall Blend Characterization. Presented at the IADC/SPE Asia Pacific Drilling Technology Conference, 8-9 June. IADC/SPE-201049-MS.
12. ASTM C150/C150M-21, Standard Specification for Portland Cement. 2021. West Conshohocken, Pennsylvania: ASTM International.
13. Bachu, S. & Bennion, D.B. 2009. Experimental assessment of brine and/or CO2 leakage through well cements at reservoir conditions, in *Int. J. Greenh. Gas Contr*. **3**(2009) 494-501. https://doi.org/10.1016/j.ijggc.2008.11.002.
14. Bakhorji, A. & Schmitt, D.R. 2010. Laboratory measurements of static and dynamic bulk moduli in carbonate, in: 44th US Rock Mechanics Symposium and 5th U.S.-Canada Rock Mechanics Symposium, Salt Lake City, Utah, 27-30 June. ARMA-10-465.

15. Barcelo, L. & Kline, J. 2012. The Cement Industry Roadmap to Reduce Carbon Emissions. Presented at the Carbon Management Technology Conference, Orlando, Florida, 7-9 February. CMTC-152259-MS.
16. Barry, J.A., Esafyana, E., El Sayed, K.L. & El-Husseiny, M.A. 2022. Novel Applications of Pozzolans to Treat Wellbore prior to Cement, Casing and While Drilling to Prevent Overburden Stress Fractures. Presented at the IADC/SPE International Drilling Conference and Exhibition, Galveston, Texas, 8-10 March. IADC/SPE-208757-MS.
17. Bear, J. 1972. Dyanmics of Fluids in Porous Media, Dover Publications, Inc., New York, 1972.
18. Behl, M. & Lendlein, A. 2007. Shape-memory polymers, in *Materialstoday* **10**(4): 20-28. https://doi.org/10.1016/S1369-7021(07)70047-0.
19. Bell, D.R. & Nelson, E.B. 1990. Laboratory Testing, Evaluation, and Analysis of Well Cements. In Well Cementing, ed. E.B. Nelson, App. B 1-16. Houston: Schlumberger Education Services.
20. Bensted, J. 2002. Developments with oilwell cements. In Structure and Performance of Cements, ed. J. Bensted & P. Barnes, 237-252.
21. Beltrán-Jiménez, K., Gardner, D., Kragset, S., Gebremariam, K.F., Reales, O.A.M., Minde, M.W., de Souza, M.I.L., Aasen, J.A., Skadsm, H.J. & Delabroy, L. 2022. Cement properties characterization from a section retrieved from an oil production well after 33 years of downhole exposure, in *J. Pet. Sci. Eng.* **208**(2022): 109334.
22. Benelkadi, S., Bianco, E.V., Burton, P. & Motta, M.D. 2019. Subsurface Drilling Waste Injection: Challenges, Recent Advances and Case Studies. Presented at the Offshore Technology Conference Brasil, Rio de Janeiro, Brazil, 29-31 October. OTC-29920-MS.
23. Bhaidasna, K. & Leblanc, C. 2009. Next Generation Cement Analyzers. Presented at the 2009 SPE Production and Operations Symposium, Oklahoma City, Oklahoma, 4-8 April. SPE-120640-MS. https://doi.org/10.2118/120640-MS.
24. Bílek, V., Soucek, K., Khestl, F., Bujdos, D. & Seitl, S. 2023. Mechanical and Fracture Parameters of Concretes with Different Water to Cement Ratio in Two Different Conditions of Curing. In *Procedia Structural Integrity* **43**(2023): 107-112.
25. Biot, M.A. 1957. The Elastic Coefficients of the Theory of Consolidation, in *J. Appl. Mech.* **24**(1957): 594-601. https://doi.org/10.1115/1.4011606.
26. Biot, M.A. & Willis, D.G. 1957. The elastic coefficients of the theory of consolidation, in *J. Appl. Mech* **24**(4): 594-601. https://doi.org/10.1115/1.4011606.
27. Bodaghabadi, S. & Moosavi, S.J. 2008. A simple practical method to determine the Biot coefficient for hydromechanical analyses. Presented at the 5th Asian Rock Mechanics Symposium (ARMS5), Tehran, Iran, 24-26 November. ISRM-ARMS5-2008-020.
28. Bois, A-P., Garnier, A., Rodot, F., Saint-Marc, J. & Aimard, N. 2011. How to Prevent Loss of Zonal Isolation Through a Comprehensive Analysis of Microannulus Formation, in *SPE Drill & Compl.* **26**(01): 13-31. https://doi-org.ezproxy.lib.ou.edu/10.2118/124719-PA.
29. Bois, A-P., Vu, M.H., Galdiolo, G. & Badalamenti, A. 2017. Use of Advanced Migration Model to Optimize Zonal Isolation. Presented at the 2017 AADE National Technical Conference and Exhibition, Houston, Texas 11-12 April. AADE-17-NTCE-104.

30. Bosma, M., Ravi, K., van Driel, W. & Schreppers, G.J. 1999. Design Approach to Sealant Selection for the Life of the Well. Presented at the 1999 SPE Annual Technical Conference and Exhibition, Houston, Texas, 3-6 October. https://doi.org/10.2118/56536-MS.
31. Boul, P.J., Ellis, M. & Thaemlitz, C.J. 2016. Retarder Interactions in Oil Well Cements. Presented at the 2016 AADE Fluids Technical Conference and Exhibition, Houston, Texas, 12-13 April. AADE-16-FTCE-12.
32. Brandão, N.B., Roehl, D., de Andrade Silva, F. & e Silva, R.R. 2017. The impact of cement slurry aging creep on the construction process of oil wells, in *J. Pet. Sci. Eng.* **157**(2017): 422-429. http://dx.doi.org/10.1016/j.petrol.2017.07.051.
33. Brandl, A., Bray, W.S. & Doherty, D.R. 2010. Technically and Economically Improved Cementing System with Sustainable Components. Presented at the IADC/SPE Asia Pacific Drilling Technology Conference and Exhibition, Ho Chi Minh, Vietnam, 1-3 November. IADC/SPE-136276-MS.
34. Breckels, I.M., van Eekelen, H.A.M., 1982. Relationship between horizontal stress and depth in sedimentary basins, in *J. Petrol. Technol.* **34**(9): 2–191. https://doi.org/10.2118/10336-PA. SPE-10336-PA.
35. Bullard, J.W., Jennings, H.M., Livingston, R.A., Nonat, A., Scherer, G.W., Schweitzer, J.S., Schrivener, K.L. & Thomas, J.J. 2010. Mechanisms of cement hydration, in *Cement Concr. Res*. **41**(2011): 1208-1223. 10.1016/j.cemconres.2010.09.011.
36. Cadix, A., Wilson, J., Bzducha, W., Gomez, J.-R., Feuillette, A., Guichon, H., Thant, K. & Nelson, T. 2016. High Temperature Cementing: Fluid Loss Control Polymers Performance and Limitations. Presented at the Abu Dhabi International Petroleum Exhibition & Conference, Abu Dhabi, UAE, 7-10 November. SPE-183129-MS. https://doi.org/10.2118/183129-MS.
37. Cardott, B.J. 2012. Thermal maturity of Woodford shale gas and oil plays, Oklahoma, USA, in *International Journal of Coal Geology* **103**(1 December 2012): 109-119. https://doi.org/10.1016/j.coal.2012.06.004.
38. Carrascal-Delgado, F., Abedi, S. & Zhu, D. 2022. Feasibility of Using Drill Cuttings as Proppants in Unconventional Reservoirs. Presented at the SPE Hydraulic Fracturing Technology Conference and Exhibition, The Woodlands, Texas, 1-3 February. SPE-209173-MS.
39. Cedola, A.E., Nygaard, R. & Hareland, G. 2020. Cuttings Disposal in Cement: Investigation of the Effect on Mechanical Properties. Presented at the 54th US Rock Mechanics/Geomechanics Symposium, Golden, CO, 28 June-1 July. ARMA-20-1677.
40. Chandra, S. & Flodin, P. 1987. Interactions of Polymers and Organic Admixtures on Portland Cement Hydration. In *Cem. Concr. Res.* **17**(6): 875-890.
41. Chang, C., Zoback, M.D. & Khaksar, A. 2006. Empirical relations between rock strength and physical properties in sedimentary rocks, in *J. Pet. Sci. Eng.* **51**(2006): 223-237. https://doi.org/10.1016/j.petrol.2006.01.003.
42. Chen, Y., Ding, Y., Liang, C., Bai, Y., Zhu, D. & Zou, C. 2021. An Analytical Model for Fracture Initiation of Radial Drilling-Fracturing in Shale Formations. In *Lithosphere* **2021**. https://doi.org/10.2113/2021/3387123.

43. Clements, K., Veil, J.A. & Leuterman, A.J.J. 2010. Global Practices and Regulations for Land Application and Disposal of Drill Cuttings and Fludis. Presented at the SPE International :Conference on Health, Safety and Environment in Oil and Gas Exploration and Production, Rio de Janeiro, Brazil, 12-14 April. SPE-126565-MS.
44. Contreras, E.Q. & Santra, A. 2021. Wellbore Integrity and CO2 Sequestration Using Polyaramide Vesicles. Presented at the SPE International Conference on Oilfield Cement Chemistry, The Woodlands, Texas, 6-7 December. SPE-204385-MS.
45. Cosenza, P., Ghoreychi, M., de Marsily, G., Vasseur, G. & Violette, S. 2002. Theoretical prediction of poroelastic properties of argillaceous rocks from in situ specific storage coefficient, in *Water Resources Research* **1207**(2002) 25-1-25-12. https://doi.org/10.1029/2001WR001201.
46. Coussy, O. 1989. A general theory of thermoporoelastoplasticity for saturated porous media, in *Transp. Porous Media* **4**(1989): 281-293. https://doi.org/10.1007/BF00138040.
47. Crain, D., Zhang, W. & Eckert, A. 2018. Numerical simulation of micro-annuli attributes imposed by stress regime and elastic contrast. Presented at the 52nd US Rock Mechanics/Geomechanics Symposium, Seattle, Washington, 17-20 June. ARMA-2018-1026.
48. Cvetic, P., Wright, R., Spaulding, R., Moore, J., Crandall, D., DiCarmine, P., Babakhani, A. & Ohodnicki, P. 2020. Cement properties with embedded sensors for wellbore integrity monitoring, in *Smart Structures and NDE for Industry 4.0, Smart Cities, and Energy Systems* (2020). 10.1117/12.2557318.
49. Dadstean, S. & Bai, J. 2017. Mechanical and microstructural properties of self-compacting concrete blended with metakaolin, ground granulated blast-furnace slag and fly ash, in *Construction and Building Materials* **146**(2017): 658-667. http://dx.doi.org/10.1016/j.conbuildmat.2017.04.158.
50. Dao, B. & Vijn, P. 2002. Environmentally Acceptable Cement Fluid Loss Additive. Presented at the SPE International Conference on Health, Safety and Environment in Oil and Gas Exploration and Production, Kuala Lumpur, Malaysia, 20-22 March. SPE-74088-MS.
51. Dassanayake, A.B.N. & Fujii, Y. 2014. Biot's effective stress coefficient of rocks for peak and residual strengths by modified failure envelope method, Rock Mech Rock Eng. Taylor & Francis Group, London, 2014.
52. De Andrade, J., Fagerås, S., Sangesland, S., 2019. A novel mechanical tool for annular cement verification. Presented at SPE/IADC International Drilling Conference and Exhibition. Society of Petroleum Engineers, The Hague, The Netherlands, 5-7 March. https://doi.org/10.2118/194135-MS. SPE-194135-MS.
53. De Castro Dantas, T.N., da Silva, D.N.N., Neto, A.A.D., de Oliverira Cabral, T.J. & dos Anjos, A.S.D. 2019. Treatment of drill cuttings using microemulsion, in *Journal of Petroleum Exploration and Production Technology* **10**(2020): 1243-1251. https://doi.org/10.1007/s13202-019-00813-3.
54. Deshpande, A., Jones, P., Jadhav, R., Pangu, G. & Mishra, V. 2019. Comparative Study of the Mechanical Properties of Reduced Density Cements. Presented at the SPE Middle

East Oil and Gas Show and Conference held in Manama, Bahrain, 18-21 March 2019. SPE-194918-MS.
55. Deshpande, A. & Patil, R. 2017. Applications of Nanotechnology in Oilwell Cementing. Presented at the SPE Middle East Oil & Gas Show and Conference, Manama, Kingdom of Bahrain, 6-9 March. SPE-183727-MS. https://doi.org/10.2118/183727-MS.
56. Detournay, E. & Cheng, A.H.D. 1993. Fundamentals of Poroelasticity, in: C. Fairhusrst (Ed.), Analysis and Design Methods. https://doi.org/10.1016/B978-0-08-040615-2.50011-3.
57. Doan, A., Brandl, A., Vorderbruggen, M. & Leonard, D.D. 2015. Innovative Well Cementing Applications by Using Large Particle Sizes of Cement Additives. Presented at the SPE/IATMI Asia Pacific Oil & Gas Conference and Exhibition, Nusa Dua, Indonesia, 20-22 October. SPE-176102-MS.
58. Dorn, T., Blask, O. & Stephan, D. 2022. Acceleration of cement hydration-A review of the working mechanisms, effects on setting time, and compressive strength development of accelerating admixtures. In *Constr. Build. Matr.* **323**(2022): 126554.
59. Dung, T.T., Sondergeld, C.H. & Roegiers, J-C. 2017. Different forms of Gassmann Equation and Implications for the Estimation of Rock Properties, in *PetroVietnam* **10**(2017): 23-29.
60. Dzialowski, A., Hale, A. & Mahajan, S. 1993. Lubricity and Wear of Shale: Effect of Drilling Fluids and Mechanical Parameters. Presented at the 1993 SPE/IADC Drilling Conference, Amsterdam, The Netherlands, 23-25 February. SPE/IADC-25730-MS.
61. Egerton, R.F. & Zhu, Y. 2022. Spatial resolution in secondary-electron microscopy. In *Microscopy* **72**(2): 66-77.
62. Fabre, D. & Gustkiewicz, J. 1997. Poroelastic Properties of Limestones and Sandstones under Hydrostatic Conditions, in *Int. J. Rock Mech. Sin. Sci*. **34**(1997) 127-134.
63. Fallahzadeh, S.H. & Rasouli, V. 2012. The impact of cement sheath mechanical properties on near wellbore hydraulic fracture initiation. Presented at the ISRM International Symposium-EUROCK 2012, Stockholm, Sweden, 28 May. ISRM-EUROCK-2012-100.
64. Feng, Y., Li, X., Gray, K.E., 2017. Development of a 3D numerical model for quantifying fluid-driven interface debonding or an injector well, in *Int. J. Greenh. Gas Contr*. **62**: 76-90. https://doi.org/10.1016/j.ijggc.2017.04.008.
65. Fjaer, E., Holt, R.M., Horsrud, P., Raaen, A.M. & Risnes, R. 2008. Petroleum Related Rock Mechanics, vol. 53. Elsevier.
66. Fleckenstein, W.W., Eustes III, A.W. & Miller, M.G. 2001. Burst-Induced Stresses in Cemented Wellbores, in *SPE Drill & Compl.* **16**(02): 74-82. https://doi.org/10.2118/72059-PA.
67. Flores, J.C., Patterson, D.J., Wakefield, J., Chace, D., & Malbrel, C. 2019. Acoustic and Nuclear Wireline Logging Validation of Shape Memory Polymer Screen Expansion. Presented at the SPE Annual Technical Conference and Exhbition, Calgary, Canada, 30 September-2 October. SPE-196047-MS. https://doi-org.ezproxy.lib.ou.edu/10.2118/196047-MS.

68. Ford, E., Moeinikia, F., Majoumerd, M.M., Lohne, H.P. & Arild, Ø. 2018. Consequence Quantification of Barrier System Failures in Permanently Plugged and Abandoned Wells. Presented at the SPE Norway One Day Seminar, Bergen, Norway, 18 April. SPE-191298-MS. https://doi.org/10.2118/191298-MS.
69. Forni, P., Magistri, M., Lo Presti, A. & Salvioni, D. 2015. Investigation of Fly Ash Activation with Chemical Additives: Interactions with Portland Cement Hydration. In Abstracts of the Thirty-Seventh International Conference on Cement Microscopy Seattle, Washington, 3-7 May.
70. Foroutan, M., Hassan, M.M., Desrosiers, N. & Rupnow, T. 2017. Evaluation of the reuse and recycling of drill cuttings in concrete applications. In *Constr. Build. Mater.* **164**(2018): 400-409. https://doi.org/10.1016/j.conbuildmat.2017.12.180.
71. Foster, A., Pollema, A., Petitt, I., Heathman, J., Johnson, C. & Schlepers, R. 2012. Contemporary Approach Coupled with Traditional Techniques Tackles Extreme Wellbore Environment in Schoonebeek Heavy Oil Field, in *SPE Drill & Compl.* **27**(04): 516-530. SPE-150022-PA. https://doi.org/10.2118/150022-PA.
72. Fourmaintraux, D.M., Bois, A.P., Fraboulet, B., 2005. Efficient wellbore cement sheath design using the SRC (System Response Curve) method. Presented at SPE Europe/EAGE Annual Conference. 13-16 June, Madrid, Spain. SPE-94176-MS. https://doi.org/10.2118/94176-MS.
73. Franquet, J.A. & Abass, H.H. 1999. Experimental evaluation of Biot's poroelastic parameter-Three different methods. Presented at the Vail Rocks 1999, The 37th U.S. Symposium on Rock Mechanics (USRMS), Vail, CO, 7 June. ARMA-99-0349.
74. Franus, W., Panek, R. & Wdowin, M. 2015. "SEM Investigation of Microstructures in Hydration Products of Portland Cement", 2nd International Multidisciplinary Microscopy and Microanalysis Congress, 10.1007/978-3-319-16919-4_14.
75. Gahlawat, R., Jandhyala, S.R.K., Mishra, V. & Patil, S. 2016. Rheology Modification for Safe Cementing of Low-ECD Zones. Presented at the IADC/SPE Asia Pacific Drilling Technology Conference, Singapore, 22-24 August. SPE-180523-MS. https://doi.org/10.2118/180523-MS.
76. Garnier, A., Fraboulet, B., Saint-Marc-J. & Bois, A.-P. 2007. Characterization of Cement Systems to Ensure Cement Sheath Integrity. Presented at the 2007 Offshore Technology Conference, Houston, Texas, 30 April-3 May. OTC-18754-MS. https://doi.org/10.4043/18754-MS.
77. Geertsma, J. 1957. The Effect of Fluid Pressure Decline on Volumetric Changes of Porous Rocks. Presented at the Petroleum Branch Fall Meeting, Los Angeles, CA, 14-17 October. SPE-728-G. https://doi.org/10.2118/728-G.
78. Ghabezloo, S., Sulem, J., Gúedon, S., Martineau, F. & Saint-Marc, J. 2008. Poromechanical behaviour of hardened cement paste under isotropic loading, in *Cement Concr. Res*. **38**(12): 1424-1437. https://doi.org/10.1016/j.cemconres.2008.06.007.
79. Gibson, L.T. 2005. Archeaometry and Antique Analysis Metallic and Ceramic Objects. *Encyclopedia of Analytical Science*, 2nd ed. Glasgow, United Kingdom.

80. Gong, F., Luo, S., Lin, G. & Li, X. 2020. Evaluation of Shear Strength Parameters of Rocks by Preset Angle Shear, Direct Shear and Triaxial Compression Tests, in *Rock Mech. Rock Eng.* **53**(2020): 2505-2519. https://doi.org/10.1007/s00603-020-02050-1.
81. Gray, K.E., Podnos, E. & Becker, E. 2009. Finite-Element Studies of Near-Wellbore Region During Cementing Operations: Part I, in *SPE Drill & Compl.* **24**(01) 127-136. https://doi.org/10.2118/106998-PA.
82. Guo, J., Zheng, Y., Li, W., Li, B., Yuan, B. & Xu, B. 2019. Design and application of well cementing technology based on the precise managed pressure balancing method in narrow pressure window hole sections, in *Natural Gas Industry B* **7**(3): 285-291. https://doi.org/10.1016/j.ngib.2019.11.004.
83. Gutierrez, M.S. & Lewis, R.W. 2002. Coupling of Fluid Flow and Deformation in Underground Formations, in *J. Eng. Mech.* **128**(07): 779-787. 10.1061/~ASCE!0733-9399~2002!128:7~779!.
84. Hart, D.J. & Wang, H.F. 1995. Laboratory measurements of a complete set of poroelastic moduli for Berea sandstone and Indiana limestone, in *J. Geophys. Res.* **100**(1995): 17741-17751.
85. He, J. & Ling, K. 2014. A New Method to Determine Biot Coefficients of Bakken Samples, in: 48th US Rock Mechanics/Geomechanics Symposium, 1-4 June (2014), Minneapolis, MN. ARMA-14-7022.
86. He, J., Rui, Z. & Ling, K. 2016. A new method to determine Biot's coefficients of Bakken samples. In Journal of Natural Gas Science and Engineering 35(2016): 259-264. http://dx.doi.org/10.1016/j.jngse.2016.08.061.
87. Heinold, T., Dillenbeck, R.L. & Rogers, M.J. 2002. The Effect of Key Cement Additives on the Mechanical Properties of Normal Density Oil and Gas Well Systems. Presented at the SPE Asia Pacific Oil and Gas Conference and Exhibition, Melbourne, Australia, 8-10 October. SPE-77867-MS.
88. Hellmann, J.R., Scheetz, B.E., Luscher, W.G., Hartwich, D.G. & Koseski, R.P. 2014. Proppants for shale gas and oil recovery, in *American Ceramic Society Bulletin* **93**(1): 28-35.
89. Henry, L-A., Harries, D., Kingston, P. & Roberts, J.M. 2017. Historic scale and persistence of drill cuttings impacts on North Sea benthos, in *Marine Environmental Research* **129**(2017): 219-228. https://doi.org/10.1016/j.marenvres.2017.05.008.
90. Hillerborg, A., Modéer, M. & Petersson, P.E. 1976. Analysis of crack formation and crackgrowth in concrete by means of fracture mechanics and finite elements, in *Cement Concr. Res*. **6**(6): 773–781. https://doi.org/10.1016/0008-8846(76)90007-7.
91. Hossain, K.M.A. 2004. Volcanic ash and pumice as cement additives: pozzolanic, alkali-silica reaction and autoclave expansion characteristics, in *Cement Concr. Res.* **35**(2005): 1141-1144. 10.1016/j.cemconres.2004.09.025.
92. Huang, Z., Xu, Z., Quan, Y., Jia, H., Li, J., Li, Q., Chen, Z. & Pu, K. 2018. A review of treatment methods for oil-based drill cuttings, in *IOP Conf. Series: Earth and Environmental Science* **170**(2018). 10.1088/1755-1315/170/2/022074.
93. Huang, L., Yu, M., Miska, S., Takach, N. & Bloys, J.B. 2011. Modeling Chemically Induced Pore Pressure Alterations in Near Wellbore Region of Shale Formations.

Presented at the SPE Eastern Regional Meeting, Columbus, Ohio, 17-19 August. SPE-149415-MS.
94. Innes, G. & Morris, A. 2020. Reducing Carbon Footprint Through Wellsite Processing. Presented at the Abu Dhabi International Petroleum Exhibition & Conference, Abu Dhabi, UAE, 9-12 November. SPE-202639-MS.
95. Innes, G., Nesse, S. & Eia, J.T. 2021. A Comparative Emissions Assessment-Drill Cuttings Treatment Alternatives. Presented at the Abu Dhabi International Petroleum Exhibition & Conference, Abu Dhabi, UAE, 15-18 November. SPE-207519-MS.
96. ISO Standard 10426-2:2003. Petroleum and natural gas industries-Cement and materials for well cementing-Part 2: Testing of well cements. 1st ed. Geneva, Switzerland: ISO.
97. Jaeger, J.C., Cook, N.G.W. & Zimmerman, R.W. 2007. Fundamentals of Rock Mechanics, fourth ed. Blackwell Pub, Malden, MA.
98. Jafariesfad, N., Sangesland, S., Gawel, K. & Toræter, M. 2020. New Materials and Technologies for Life-Lasting Cement Sheath: A Review of Recent Advances, in *SPE Drilling & Completion* **35**(02): 262-278. https://doi.org/10.2118/199885-PA.
99. Jaidka, S., Sharma, R., Kaur, S. & Singh, D.P. 2022. Scanning Electron Microscopy (SEM): Learning to Generate and Interpret the Topographical Aspects of Materials. *Microscopic Techniques for the Non-Expert,* chp. 7: 165-185.
100. James, S. & Boukhelifa, L. 2008. Zonal Isolation Modeling and Measurements-Past Myths and Today's Realities, in *SPE Drill & Compl.* **23**(01): 68-75. SPE-101310-PA. https://doi-org.ezproxy.lib.ou.edu/10.2118/101310-PA.
101. Johnson, K.S. & Cardott, B.J. 1992. Geologic Framework and Hydrocarbon Source Rocks of Oklahoma, in Oklahoma Geological Survey Circular **93**.
102. Kalyanraman, R.S., Chen, X., Wu, P.-Y., Constable, K., Govil, A. & Abubakar, A. 2021. Autonomous Interpretation Methods of Ultrasonic Data Through Machine Learning Facilitates Novel and Reliable Casing Annulus Characterization. Presented at the SPE/IADC International Drilling Conference and Exhibition, Virtual, 8-12 March. SPE/IADC-204078-MS. https://doi.org/10.2118/204078-MS.
103. Kang, M. Dong, Y., Liu, Y., Williams, J.P., Douglas, P.M.J. & McKenzie, J.M. 2019. Potential increase in oil and gas well leakage due to earthquakes, in *Environ. Res. Commun.* **1**(12): 121004. 10.1088/2515-7620/ab576e.
104. Karakosta, E., Lagkaditi, L., ElHardalo, S., Biotaki, A., Kelessidis, V.C., Fardis, M. & Papavassiliou, G. 2015. Pore structure evolution and strength development of G-type elastic oil well cement. A combined 1H NMR and ultrasonic study, in *Cement Concr. Res.* **72**(2015): 90-97. https://doi.org/10.1016/j.cemconres.2015.02.018.
105. Kasani, H.A. & Selvadurai, A.P.S. 2022. A Review of Techniques for Measuring the Biot Coefficient and Other Effective Stress Parameters for Fluid-Saturated Rocks. In *Applied Mechanics Review* **75**(March 2023): 020801.
106. Kell, S. 2011. State Oil and Gas Agency Groundwater Investigations and Their Role in Advancing Regulatory Reforms A Two-State Review: Ohio and Texas, Ground Water Protection Council.

107. Khalifeh, M. & Saasen, A. 2020. Types of Permanent Plugging Materials. In Introduction to Permanent Plug and Abandonment of Wells, Chap. 4, 97-136. Springer, Cham. https://doi.org/10.1007/978-3-030-39970-2.
108. Khalil, M., Amanda, A., Yunarti, R.T., Jan, B.M. & Irawan, S. 2020. Synthesis and application of mesoporous silica nanoparticles as gas migration control additive in oil and gas cement, in *J. Pet. Sci. Eng.* **195**(December 2020): 107660. https://doi.org/10.1016/j.petrol.2020.107660.
109. Khodadadi, M., Moradi, L., Dabir, B., Nejad, F.M. & Khodaii, A. 2020. Reuse of drill cuttings in hot mix asphalt mixture: A study on the environmental and structure performance. In *Constr. Build. Mater.* **256**(2020): 119453. https://doi.org/10.1016/j.conbuildmat.2020.119453.
110. Kim, K. & Makhnenko, R.Y. 2020. Coupling Between Poromechanical Behavior and Fluid Flow in Tight Rock. In *Transport in Porous Media* **135**(2020): 487-512.
111. Kim, J., Moridis, G.J., Martinez, E.R. 2016. Investigation of possible wellbore cement failures during hydraulic fracturing operations, in *J. Pet. Sci. Eng.* **139**(2016): 254-263. https://doi.org/10.1016/j.petrol.2016.01.035.
112. Kimanzi, R., Wu, Y., Salehi, S., Mokhtari, M. & Khalifeh, M. 2020. Experimental Evaluation of Geopolymer, Nano-Modified, and Neat Class H Cement by Using Diametrically Compressive Tests, in *Journal of Energy Resources Technology* **142**(September 2020): 092101-1-092101-7.
113. Kiran, R., Teodoriu, C., Dadmohammadi, Y., Nygaard, R., Wood, D., Mokhtari, M. & Salehi, S. 2017. Identification and evaluation of well integrity and causes of failure of well integrity barriers (A review), in *J. Nat. Gas Sci. Eng.* **45**: 511–526. https://doi.org/10.1016/j.jngse.2017.05.009.
114. Kulakofsky, D., Avalos, A. & Hernandez, R. 2006. Superior Zonal Isolation Provided by Ultralightweight Cementing Technology Increases Profitability of Wells in Difficult-to-Cement Areas. Presented at the First International Oil Conference and Exhibition in Mexico, Cancun, Mexico, 31 August-2 September. SPE-104066-MS.
115. Kurdowski, W. 2014. Portland Cement Clinker Burning. In Cement and Concrete Chemistry, Chap. 2.1, 21-32. 10.1007/978-94-007-7945-7_2.
116. Kuuskraa, V.A. 2019. Eagle Ford Shale Basin Study. DOE Report DE-FE0025912.
117. Lackey, G., Rajaram, H., Bolander, J., Sherwood, O.A., Ryan, J.A., Shih, C.Y., Bromhal, G.S. & Dilmore, R.M. 2021. Public data from three US states provides new insights into well integrity, in *PNAS* **118**(14): e2013894118. https://doi.org/10.1073/pnas.2013894118.
118. Laik, S. 2018. Offshore Petroleum Drilling and Production. Taylor & Francis Group.
119. Lapeyre, J., Ma, H. & Kumar, A. 2019. Effect of particle size distribution of metakaolin on hydration kinetics of tricalcium silicate, in *Journal of the American Ceramic Society* **102**(10): 5976-5988. https://doi.org/10.1111/jace.16467.
120. Lau, H.C., Yu, M. & Nguyen, Q.P. 2016. Nanotechnology for Oilfield Applications: Challenges and Impact. Presented at the Abu Dhabi International Petroleum Exhibition and Conference, Abu Dhabi, UAE, 7-10 November. SPE-183301-MS.

121. Lavrov, A., Todorovic, J. & Torsæter, M., 2015. Numerical study of tensile thermal stresses in a casing-cement-rock system with heterogeneities. Presented at the 49th US Rock Mechanics/Geomechanics Symposium, 28 June-1 July, San Francisco, California, USA. ARMA-2015-110.
122. Lavrov, J. Todorovic, M. Torsæter. 2016. Impact of voids on mechanical stability of well cement, in *Energy Procedia* **86**(2016): 401-410. https://doi.org/10.1016/j.egypro.2016.01.041.
123. Lavrov, A. & Torsæter, M. 2016. Physics and Mechanics of Primary Well Cementing, Springer Nature, Switzerland.
124. Leonard, S.A. & Stegemann, J.A. 2010. Stabilization/solidification of petroleum drill cuttings: Leaching studies, in *Journal of Hazardous Materials* **174**(2010): 484-491. 10.1016/j.jhazmat.2009.09.078.
125. Li, X., Bizzozero, J. & Hesse, C. 2022. Impact of C-S-H seeding on hydration and strength of slag blended cement, in *Cement Concr. Res.* **161**(2022): 106935. https://doi.org/10.1016/j.cemconres.2022.106935.
126. Li, J., Duan, Q., Zhang, E. & Wang, J. 2018. Applications of Shape Memory Polymers in Kinetic Buildings, in *Advances in Materials Science and Engineering* **2018**. https://doi.org/10.1155/2018/7453698.
127. Li, L., Go Boncan, V.C., Brandl, A. & Jordan, A.K. 2015. Fundamental Investigation of Mechanical Properties of Additives and Class H Cement Under Downhole Conditions. Presented at the SPE/IATMI Asia Pacific Oil & Gas Conference and Exhibition, Nusa Dua, Indonesia, 20-22 October. SPE-176175-MS.
128. Li, W., Li, X., Chen, S.J., Liu, Y.M., Duan, W.H. & Shah, S.P. 2017. Effects of graphene oxide on early-age hydration and electrical resistivity of Portland cement paste. In *Constr. Build. Matr.* **136**(2017): 506-514.
129. Li, Y. & Nygaard, R. 2017. A numerical study on the feasibility of evaluating CO2 injection wellbore integrity through casing deformation monitoring, in *Greenh. Gases Sci. Technol.* **8**(2018): 51–62. https://doi.org/10.1002/ghg.1733.
130. Li, J., Zhang, C., Wu, Z., Zhang, G., Gao, Q., Liu, K. & Cheng, X. 2021. Can low hydration heat cement prevent the decomposition of natural gas hydrate under high pressure and low temperature?, in *Journal of Natural Gas Science and Engineering* **97**(2022): 104347. https://doi.org/10.1016/j.jngse.2021.104347.
131. Ling, K., He, J., Pei, P., Wang, S. & Ni, X. 2016. Comparisons of Biot's Coefficients of Bakken Core Samples Measured by Three Methods. Presented at the 50th US Rock Mechanics/Geomechanics Symposium, 26-29 June (2016), Houston, TX, ARMA-2016-030.
132. Liteanu, E., Spiers, C.J. & Peach, C.J. 2009. Failure behaviour wellbore cement in the presence of water and supercritical CO2, in *Energy Procedia* **1**(2009): 3553-3560. https://doi.org/10.1016/j.egypro.2009.02.149.
133. Liu, K., Cheng, X., Zhang, C., Gao, X., Zhuang, J. & Guo, X. 2019. Evolution of pore structure of oil well cement slurry in suspension-solid transition stage, in *Construction and Building Materials* **214**(2019): 382-398. https://doi.org/10.1016/j.conbuildmat.2019.04.075.

134. Liu, K., Gao, D., Zeng, J. & Wang, Z. 2018. Study on Cement Sheath Integrity in Horizontal Wells during Hydraulic Fracturing Process. Presented at the 52nd US Rock Mechanics/Geomechanics Symposium, Seattle, Washington, 17-20 June. ARMA-18-1267.
135. Locher, F.W. 2006. Cement Principles of Production and Use. Düsseldorf, Germany: Verlag Bau+Technik.
136. Lyon, D.Y., Smit, M., Lee, B. & Conley, B. 2019. Modeled Environmental Risk of Offshore Drill Cuttings Discharges with Different Drilling Base Fluids. Presented at the Offshore Technology Conference Brasil, Rio de Janiero, Brazil, 29-31 October. OTC-29835-MS.
137. Ma, S. & Gutierrez, M. 2021. Coupled Damage-Plasticity Modelling of Saturated Shale under Undrained Condition, in *Journal of the Korean Society of Civil Engineers* **25**(2021): 316-325.
138. Ma, S. & Gutierrez, M. 2021. Determination of the poroelasticity of shale, in *Acta Geotechnica* **16**(2021) 581-594. https://doi.org/10.1007/s11440-020-01062-z.
139. Mahji, R.K. & Nayak, A.N. 2019. Bond, durability and microstructural characteristics of ground granulated blast furnace slag based recycled aggregate concrete, in *Construction and Building Materials* **212**(2019): 578-595. https://doi.org/10.1016/j.conbuildmat.2019.04.017.
140. Mainali, P., Crosby, Z., Dix, M., Yemidale, G., Heard, S., Austin, J. & Tilford, M. 2017. Advanced Well-Site Geochemistry While Drilling: Improved Wellbore Positioning and Formation Evaluation of Unconventional Reservoirs. Presented at the AAPG 2016 International Convention and Exhibition, Cancun, Mexico, 6-9 September.
141. Mangadlao, J.D., Cao, P. & Advincula, R.C. 2015. Smart cements and cement additives for oil and gas operations, in *Journal of Petroleum Science and Engineering* **129**(2015): 63-76. http://dx.doi.org/10.1016/j.petrol.2015.02.009.
142. Mansour, A.K., Taleghani, A.D. & Li, G. 2017. Smart Lost Circulation Materials for Wellbore Strengthening. Presented at the 51st US Rock Mechanics/Geomechanics Symposium, San Francisco, CA, 25-28 June. ARMA-17-0492.
143. Mechtcherine, V. & Müller, H.S. 2001. Fractological investigations on the fracture in concrete. Presented at the Fourth International Conference on Fracture Mechanics of Concrete and Concrete Structures, Cachan, France, 28 May-1 June.
144. Meng, M., Frash, L.P., Carey, J.W., Li, W. Welch, N. 2020. Rapid Measurements of Biot effective stress coefficient for Class-G Oil Well Cements. Presented at the 54th U.S. Rock Mechanics/Geomechanics Symposium, 28 June-1 July (2020), Golden, Colorado, USA. ARMA-2020-1745.
145. Meng, M., Frash, L.P., Carey, J.W., Li, W., Welch, N.J. & Zhang, W. 2021. Cement stress and microstructure evolution during curing in semi-rigid high-pressure environments, in *Cement Concr. Res.* **149**(2021): 106555. https://doi.org/10.1016/j.cemconres.2021.106555.
146. Meng, J., Pashin, J.C., Nygaard, R. & Chandra, A. 2018. Analysis of the stress field in the DeSoto canyon Salt Basin for ensuring safe offshore carbon storage, in *Int. J. Greenh. Gas Contr.* **79**: 279–288. https://doi.org/10.1016/j.ijggc.2018.11.006.

147. Meredith, P., Donald, A.M. & Luke, K. 1995. Pre-Induction and induction hydration of tricalcium silicate: an environmental scanning electron microscope study, in *Journal of Materials Science* **30**(1995): 1921-1930. https://doi.org/10.1007/BF00353014.
148. Mesri, G., Adachi, K. & Ullrich, C.R. 1976. Pore-pressure response in rock to undrained change in all-round stress, in *Geotechnique* **26**(1976): 317-330. https://doi.org/10.1680/geot.1976.26.2.317.
149. Michaux, M., Nelson, E.B. & Vidick, B. 1990. Chemistry and Characterization of Portland Cement. In Well Cementing, ed. E.B. Nelson, Chap. 2, 1-17. Houston: Schlumberger Education Services.
150. Milman, Y.V., Galanov, B.A. & Chugunova, S.I. 1993. Plasticity characteristic obtained through hardness measurement, in *Acta Metallurgica et Materialia* **41**(1993): 2523-2532. https://doi.org/10.1016/0956-7151(93)90122-9.
151. Mohamed, A., Giovannetti, B. Salehi, S. & Muhammed, F. 2022. A Novel Cement Additive to Prevent Gas Migration in Producing and Abandoned Oil and Gas Wells. Presented at the ADIPEC, Abu Dhabi, UAE, 31 October-3 November. SPE-211513-MS.
152. Nelson, E.B. & Guillot, 2006. Well Cementing. 2nd ed. Schlumberger, Texas.
153. Nygaard, R., Salehi, S. & Lavoie, R. 2011. Effect of Dynamic Loading on Wellbore Leakage for the Wabamun Area CO2 Sequestration Project. Presented at the Canadian Unconventional Resources Conference, Calgary, Alberta, Canada, 15-17 November. CSUG/SPE-146640-MS. https://doi.org/10.2118/146640-MS.
154. Orlander, T., Adamopoulou, E., Jerver Asmussen, J., Marczyski, A.A., Milsch, H., Pasquinelli, L. & Fabricius, I.L. 2018. Thermal conductivity of sandstones from Biot's coefficient, in *Geophysics* **83**(2018) D173-D185. https://doi.org/10.1190/geo2017-0551.1.
155. Pang, X., Hundt, G., Lewis, S., Vargo, R. & Tan, B. 2018. Storable Liquid-Bead System as Lightweight Additives for Oilwell Cementing. Presented at the Offshore Technology Conference Asia, Kuala Lumpur, Malaysia, 20-23 March. OTC-28273-MS. https://doi.org/10.4043/28273-MS.
156. Pariseau, W.G. 1988. On the Concept of Rock Mass Plasticity. Presented at the 29th U.S. Symposium on Rock Mechanics, Minneapolis, Minnesota, June 1988. ARMA-88-0291.
157. Patel, H., Johnson, K. & Martinez, R. 2021. Triazine Polymers for Improving Elastic Properties in Oil Well Cements. Presented at the SPE International Conference on Oilfield Chemistry, The Woodlands, Texas, 6-7 December. SPE-204333-MS.
158. Patel, H. & Salehi, S. 2019. Development of an advanced finite element model and parametric study to evaluate cement sheath barrier, in *J. Energy Resour. Technol*. **141**(9): 092902 https://doi.org/10.1115/1.4043137.
159. Pérez, H.G., Ali, S.S., Jin, G. & Al Dhamen, A.A. 2015. Mapping Geomechanical State of Unconventional Shale-A More Robust, Faster Lab Characterization Method. Presented at the Abu Dhabi International Petroleum Exhibition and Conference, Abu Dhabi, UAE, 9-12 November. SPE-177631-MS.
160. Pernites, R., Brady, J., Padilla, F., Clark, J., Ramos, G., Callahan, J., Garzon, R., Sama, R., Embrey, M., Fu, D., Johnson, D. & Richey, N. 2019. Laboratory Development to Successful Field Application of Unconventional Non-Beaded Micromaterial for Making

Lower Permeability Lighter and Stronger Cements. Presented at the SPE Annual Technical Conference and Exhibition, Calgary, Alberta, Canada, 30 September-2 October. SPE-196059-MS.
161. Pernites, R., Clark, J., Padilla, F. & Jordan, A. 2018. New Advanced High-Performance Ultrafine Micromaterials for Providing Superior Properties to Cement Slurry and Set Cement in Horizontal Wells. Presented at the 2018 SPE Annual Technical Conference and Exhibition, Dallas, Texas, 24-26 September. SPE-191451-MS.
162. Petri, I.,Silva Mota, A.C., Martins, A.L., Marques, C.H., Pereira, M.S. & Ataíde, C.H. 2019. Microwave Drying of Reservoir Drilled Cuttings. Presented at the Offshore Technology Conference Brasil, Rio de Janeiro, Brazil, 29-31 October. OTC-29964-MS.
163. Petty, S., Gastineau, J., Bour, D.L. & Ravi, K. 2003. Life Cycle Modeling of Wellbore Cement Systems Used for Enhanced Geothermal System Development, in *Proceedings of the Twenty-Eighth Workshop on Geothermal Reservoir Engineering*, Stanford, CA, 27-29 January.
164. Preece, S.J., Billingham, J. & King, A.C. 2000. On the initial stages of cement hydration, in *Journal of Engineering Mathematics* **40**(2001): 43-58. https://doi.org/10.1023/A:1017533810329.
165. Prevost, J.H. 1980. Mechanics of continuous porous media, in *Int. J. Eng. Sci.* **18**(6) 787-800. https://doi.org/10.1016/0020-7225(80)90026-9.
166. Prevost, J.H. 1982. Nonlinear Transient Phenomena in Saturated Porous Media, in *Comput Methods Appl Mech. Eng*. **20**(1982) 3-18. https://doi.org/10.1016/0045-7825(82)90052-4.
167. Qi, C., Manzano, H., Spagnoli, D., Chen, Q. & Fourie, A. 2021. Initial hydration process of calcium silicates in Portland cement: A comprehensive comparison from molecular dynamics simulations. In *Cem. Concr. Res.* **149**(2021): 106576.
168. Quennoz, A. & Scrivener, K.L. 2012. Hydration of C3A-gypsum systems, in *Cement Concr. Res.* **42**(2012): 1032-1041. http://dx.doi.org/10.1016/j.cemconres.2012.04.005.
169. Rae, P. 1990. Cement Job Design. In Well Cementing, ed. E.B. Nelson, Chap. 11, 1-17. Houston: Schlumberger Education Services.
170. Ramezanianpour, A.A. & Jovein, H.B. 2012. Influence of metakaolin as supplementary cementing material on strength and durability of concretes, in *Constr. Build. Mater.* **2012**(30): 470-479. doi:10.1016/j.conbuildmat.2011.12.050.
171. Ravi, K., Bosma, M. & Gastebled, O. 2002. Improve the Economics of Oil and Gas Wells by Reducing the Risk of Cement Failure. Presented at the IADC/SPE Drilling Conference, Dallas, Texas. 26-28 February. https://doi.org/10.2118/74497-MS.
172. Reddoch, J. 2000. Cuttings re-injection can solve disposal problems. In Drilling Contractor: 28-29.
173. Regel, J.B., Orozova-Bekkevold, I., Andreassen, K.A., Hoegh van Gilse, N.C. & Fabricius, I.L. 2016. Effective stresses and shear failure pressure from in situ Biot's coefficient, Hejre Field, North Sea, in *Geophysical Prospecting* **2017**(65): 808-822. 10.1111/1365-2478.12442.

174. Rice, J.R. & Cleary, M.P. Some Basic Stress Diffusion Solutions for Fluid-Saturated Elastic Porous Media with Compressible Constituents, in *Reviews of Geophysics and Space Physics* **14**(1976) 227-241. https://doi.org/10.1029/RG014i002p00227.
175. Romanowski, N., Ichim, A. & Teodoriu, C. 2018. Investigations on Oilwell Cement Strength Response to Ultrasonic Measurements in the Presence of Additives, in *Journal of Energy Resources Technology* **140**(July 2018): 072904-1-072904-7. 10.1115/1.4039316.
176. Roy, D.M., Scheetz, B.E., Pommersheim, J. & Licasttro, P.H. 1993. Development of Transient Permeability Theory and Apparatus for Measurements of Cementitious Materials, Strategic Highway Research Program (1993). SHRP-C-627.
177. Saint-Marc, J., Garnier, A. & Bois, A-P. 2008. Initial State of Stress: The Key to Achieving Long-Term Cement-Sheath Integrity. Presented at the 2008 SPE Annual Technical Conference and Exhibition, Denver, Colorado, 21-24 September. SPE-116651-MS.
178. Saleh, F.K. & Teodoriu, C. 2016. The mechanism of mixing and mixing energy for oil and gas wells cement slurries: A literature review and benchmarking of the findings, in *Journal of Natural Gas Science and Engineering* **38**(2017): 388-401. http://dx.doi.org/10.1016/j.jngse.2016.12.017.
179. Salehi, S., Khattak, M.J., Ali, N. & Rizvi, H.R. 2016. Development of Geopolymer-based Cement Slurries with Enhanced Thickening Time, Compressive, and Shear Bond Strength and Durability. Presented at the IADC/SPE Drilling Conference and Exhibition, Fort Worth, TX, 1-3 March. IADC/SPE-178793-MS.
180. Salehi, S. & Nygaard, R. 2015. Full fluid–solid cohesive finite-element model to simulate near wellbore fractures, in *J. Energy Resour. Technol.* **137**(1): 012903 https://doi.org/10.1115/1.4028251.
181. Salemi, H., Iglauer, S., Rezagholilou, A. & Sarmadivaleh, M. 2018. Laboratory measurements of Biot's coefficient and pore pressure influence on poroelastic rock behaviour, in *APPEA Journal* **58**(01):182-189. https://doi.org/10.1071/AJ17069.
182. Salmina, T., Shabzova, S., Koval, M. & Bogatkin, S. 2019. The Opportunity of Drilled Solids Use in Lost Circulation Control. Presented at the SPE Russian Petroleum Technology Conference, Moscow, Russia, 22-24 October. SPE-197003-MS.
183. Sarmah, P., Al Tawat-N., Yadav, P. & Agrawal, G. 2016. High Compressive Strength, Ultra-Lightweight and Lightweight Cement-Formulated with Raw Material Locally Available in Saudi Arabia. Presented at the SPE Kingdom of Saudi Arabia Annual Technical Symposium and Exhibition, Dammam, Saudi Arabia, 25-28 April. SPE-182736-MS. https://doi.org/10.2118/182736-MS.
184. Schwartz, A.E. 1964. Failure of Rock in the Triaxial Shear Test. Presented at the 6th U.S. Symposium on Rock Mechanics, Rolla, Missouri, October. ARMA-64-109.
185. Scott, P. & Candler, J. 2010. Size Degradation of Shale Drill Cuttings in Deepwater Discharge Conditions from Synthetic-Based Drilling Fluids. Presented at the SPE International Conference on Health, Safety and Environment in Oil and Gas Exploration and Production, Rio de Janeiro, Brazil, 12-14 April. SPE-126253-MS.

186. Sellassie, E.G. 2011. Estimation of Drilling Wastes-An Environmental Concern While Drilling Oil and Gas Wells. MS Thesis, African University of Science and Technology, Abuja, Nigeria.
187. Selvadurai, A.P.S. 2019. The Biot coefficient for a low permeability heterogeneous limestone. In *Continuum Mech. Thermodyn.* **31**(2019) 939-953. https://doi.org/10.1007/s00161-018-0653-7.
188. Shadravan, A., Kias, E., Lew, R. & Maharidge, R. 2015. Utilizing the Evolving Cement Mechanical Properties Under Fatigue to Predict Cement Sheath Integrity. Presented at the SPE Kuwait Oil and Gas Show and Conference, Mishref, Kuwait, 11-14 October. SPE-175231-MS.
189. Sigal, R.F. 2002. The Pressure Dependence of Permeability, in *Petrophysics* **43**(2002) 92-102. SPWLA-2002-v43n2a3.
190. Sintef. 2007. Environmentally Sound Management of Hazardous and Industrial Wastes in Cement Kilns-Waste as Alternative Raw Materials. Open Report, No. SBF IN A07322, Trondheim, Norway (December, 2007).
191. Skempton, A.W. 1961. Effective stress in soils, concrete and rock, in Pore Pressure & Suction in Soils Conference, Butterworth & Company Ltd., London, 1961.
192. Skempton, A.W. 1960. The Pore-Pressure Coefficient in Saturated Soils, in *Géotechnique* **10**(04). https://doi.org/10.1680/geot.1960.10.4.186.
193. Smith, D.K. 1987. Cementing, Vol. 4. Richardson, Texas: Monograph Series, Society of Petroleum Engineers.
194. Somee, M.R., Shavandi, M., Dastgheib, S.M.M. & Amoozegar, M.A. 2018. Bioremediation of oil-based drill cuttings by a halophilic consortium isolated from oil-contaminated saline soil, in *3 Biotech* **8**(5): 229. https://doi.org/10.1007%2Fs13205-018-1261-8.
195. Soroka, I. Portland Cement Paste and Concrete, first ed., The Macmillian Press LTD., London and Basingstroke, 1979.
196. Speight, J.G. 2017. Gas and Oil Resources in Tight Formations. In Deep Shale Oil and Gas, Gulf Professional Publishing, Cambridge, MA. https://doi.org/10.1016/B978-0-12-803097-4.00003-6.
197. Stanciu, C., Fernandez, J.M. & Lambert, B. 2016. The Influence of HLB in Surfactants for Drill Cuttings Cleaning. Presented at the SPE Annual Technical Conference and Exhibition, Dubai, UAE, 26-28 September. SPE-181310-MS.
198. Sullivan, R., Anderson, R., Biesiadecki, J., Bond, T. & Stewart, H. 2011. Cohesions, friction angles, and other physical properties of Martian regolith from Mars Exploration Rover wheel trenches and wheel scuffs, in *J. Geophys. Res.* (2011) E02006. https://doi.org/10.1029/2010JE003625.
199. Sun, M., Deng, J., Feng, Y. & Gui, Y. 2022. Optimization of Reinjection fluids of Oil-based Drilling Cuttings. Presented at the 56th US Rock Mechanics/Geomechanics Symposium, Santa Fe, New Mexico, 26-29 June. ARMA-22-0079-MS.
200. Sweatman, R.E., Nahm, J.J., Loeb, D.A. & Porter, D.S. 1995. First High-Temperature Applications of Anti-Gas Migration Slag Cement and Settable Oil-Mud Removal Spacers

in Deep South Texas Gas Wells. Presented at the SPE Annual Technical Conference & Exhibition, Dallas, Texas, 22-25 October. SPE-30512-MS.
201. Tabatabaei, M., Santos, L., Al Hassan, A.A. & Taleghani, A.D. 2022. Limiting Deteriorative Impacts of Oil-Based Mud Residuals on Cement Bonding. Presented at the SPE Annual Technical Conference and Exhibition, Houston, Texas, 3-5 October. SPE-210155-MS.
202. Tabatabaei, M., Taleghani, A.D. & Alem, N. 2019. Economic Nano-Additive to Improve Cement Sealing Capability. Presented at the SPE Western Regional Meeting, San Jose, CA, 23-26 April. SPE-195259-MS.
203. Taghiyev, F., Hodne, H. & Saasen, A. 2015. Using Drill Cuttings Waste as Resource for Spud Mud. Presented at the SPE/IADC Drilling Conference and Exhibition, London, United Kingdom, 17-19 March. SPE/IADC-173033-MS.
204. Takla, I., Burlion, N., Shao, J-F., Saint-Marc, J. & Garnier, A. 2011. Effects of the Storage of CO2 on Multiaxial Mechanical and Hydraulic Behaviors of Oil-Well Cement, in *J. Mater. Civ. Eng.* **23**(6) (2011) 741-746. 10.1061/(ASCE)MT.1943-5533.0000174.
205. Taleghani, A.D., Li, G. & Moayeri, M. 2017. Smart Expandable Cement Additive to Achieve Better Wellbore Integrity, in *Journal of Energy Resources Technology* **139**(November 2017): 062903-062911. https://doi.org/10.1115/1.4036963.
206. Tan, B., Lang, M. & Harshad, D. 2012. High-Strength, Low-Density Cement Pumped On-the-Fly using Volumetric Mixing Achieves Cement to Surface in Heavy Loss Coal Seam Gas Field. Presented at the SPE Asia Pacific Oil and Gas Conference and Exhibition, Perth, Australia, 22-24 October. SPE-158092-MS. https://doi-org.ezproxy.lib.ou.edu/10.2118/158092-MS.
207. Tare, U.A., Growcock, F.B., Takach, N.E., Miska, S.Z. & Davis, N. 1998. Investigation of Blast Furnace Slag Addition to Water-Based Drilling Fluids for Reduction of Drilling Fluid Invasion into Permeable Formations. Presented at the 1998 IADC/SPE Asia Pacific Drilling Conference, Jakarta, Indonesia, 7-9 September. IADC/SPE-47800-MS.
208. Teodoriu, C. & Asamba, P. 2015. Experimental study of salt content effect on class G cement properties with application to well integrity, in *Journal of Natural Gas Science and Engineering* **24**(2015): 324-329. http://dx.doi.org/10.1016/j.jngse.2015.03.039.
209. Terzaghi, K. Die berechnung der durchlassigkeitzifer des tones aus dem verlauf der hydrodynamischen spannungserscheinungen, Mathematish-naturwissenschaftliche, Klasse. Akademie der Wissenschaften, Vienna, 125-138.
210. Terzaghi, K. 1925. Principles of Soil Mechanics: I-Phenomena of Cohesion of Clays, in *Engineering News-Record* **95**(19): 742-746.
211. Thakkar, A., Raval, A., Chandra, S., Shah, M. & Sircar, A. 2019. A comprehensive review of the application of nano-silica in oil well cementing, in *Petroleum* **6**(02):123-129. https://doi.org/10.1016/j.petlm.2019.06.005.
212. Thiercelin, M.J., Dargaud, B., Baret, J.F. & Rodriquez, W.J. 1998. Cement Design Based on Cement Mechanical Response, in *SPE Drill & Compl* **13**(04): 266-273. SPE-52890-PA. https://doi.org/10.2118/52890-PA.

213. Turon, A., Dávila, C.G., Camanho, P.P. & Costa, J. 2006. An engineering solution for mesh size effects in the simulation of delamination using cohesive zone models, in *Eng. Fract. Mech.* **74**(2007): 1665–1682. https://doi.org/10.1016/j.engfracmech.2006.08.025.
214. Uesugi, M. & Kishida, H. 1986. Influential Factors of Friction Between Steel and Dry Sands. In *Soils and Foundations* **26**(2): 33-46.
215. USGS, Mineral Commodity Summaries 2022-Cement. https://pubs.usgs.gov/periodicals/mcs2022/mcs2022-cement.pdf.
216. Verba, C., Montross, S., Spaudling, R., Dalton, L. et al. 2017. Foamed Cement Interactions with CO2. NETL-TRS-2-2017.
217. Vermeer, P.A. Non-Associated Plasticity for Soils, Concrete and Rock, in: H.J. Herrmann, J-P. Hovi, S. Luding (Eds.), Physics of Dry Granular Media, Springer Science+Business Media, Dordrecht, 1998, pp. 163-195.
218. Verrujit, A. 1969. Elastic Storage of Aquifers, in: R.J.M. De Wiest (ed), Flow through Porous Media, Academic Press, New York, 1969, 331-376.
219. Virgilio, L.L., Boncan, C.G., Brandl, A. & Jordan, A.K. 2015. Fundamental Investigation of Mechanical Properties of Additives and Class H Cement Under Downhole Conditions. Presented at the SPE/IATMI Asia Pacific Oil & Gas Conference and Exhibition, Nusa Dua, Indonesia, 20-22 October. SPE-176175-MS. https://doi.org/10.2118/176175-MS.
220. Vrålstad, T., Saasen, A., Fjær, E., et al., 2018. Plug & abandonment of offshore wells:mensuring long-term well integrity and cost-efficiency, in *J. Petrol. Sci. Eng.* **173**: 478–491. https://doi.org/10.1016/j.petrol.2018.10.049.
221. Wang, R., Ong, D.E.L., Peerun, M.I. & Jeng, D-S. 2022. Influence of Surface Roughness and Particle Characteristics on Soil-Structure Interactions: A State-of-the-Art Review. In *Geosciences* **12**(4): 145.
222. Wang, S., Jian, L., Shu, Z. Wang, J., Hua, X. & Chen, L. 2019. Preparation, properties and hydration process of low temperature nano-composite cement slurry, in *Constr. Build. Mater.* **205**(2019): 434-442. https://doi.org/10.1016/j.conbuildmat.2019.02.049.
223. Watson, T. & Bachu, S. Evaluation of the Potential for Gas and CO2 Leakage Along Wellbores, in *SPE Drill. Complet*. **24**(01): 115-126. https://doi.org/10.2118/106817-PA.
224. Wawrzyniak-Guz, K. 2019. Rock physics modelling for determination of effective elastic properties of the lower Paleozoic shale formation, North Poland. In *Acta Geophysica* **67**(2019): 1967-1989.
225. Weideman, B. & Nygaard, R. 2014. How Cement Operations affect your Cement Sheath Short and Long Term Integrity. Presented at the 2014 AADE Fluids Technical Conference and Exhibition, Houston, Texas, 15-16 April. AADE-14-FTCE-20.
226. Welch, N.J., Frash, L.P. & Carey, J.W. 2019. Effective cement stress in well completions: An important unknown. Presented at the 53rd US Rock Mechanics/Geomechanics Symposium, New York, NY, 23-26 June. ARMA-19-1769.
227. Wild, S., Khatib, J.M. & Jones, A. 1996. Relative Strength, Pozzolanic Activity and Cement Hydration In Superplasticised Metakaolin Concrete, in *Cement Concr. Res.* **26**(10): 1537-1544.

228. Wise, J. 2021. Numerical Simulations of Wellbore Cement Sheath Microannuli Leakage in Gulf of Mexico Wells, University of Oklahoma, Oklahoma.
229. Wise, J., Cedola, A., Nygaard, R., Hareland, G., Arlid, Ø., Lohne, H.P. & Ford, E.P. 2020. Wellbore characteristics that control debonding initiation and microannuli width in finite element simulations, in *J. Pet. Sci. Eng.* **191**(2020). https://doi.org/10.1016/j.petrol.2020.107157.
230. Wise, J., Karami, H., Corina, A.N., van der Tuuk Opedal, N., Vrålstad, T., Sangesland, S. & Nygaard, R. Prediction of Methane Leakage Through Primary Cement Barrier in the High Island OPD, Gulf of Mexico, in *J. Nat. Gas Sci. Eng.* **101**(May 2022) 104511 https://doi.org/10.1016/j.jngse.2022.104511.
231. Wise, J., Nygaard, R., Hareland, G., 2019. Numerical analysis of wellbore integrity and cement sheath debonding for wells in the eugene Island OPD, Gulf of Mexico. Presented at the 53rd US Rock Mechanics/Geomechanics Symposium, New York City, New York, 23-26 June. ARMA-2019-0439.
232. Wisen, J., Chesnaux, R., Werring, J., Wendling, G., Baudron, P. & Barbecot, F. 2019. A portrait of wellbore leakage in northeastern British Columbia, Canada, in *PNAS* **117**(02): 913-922. http://www.pnas.org/cgi/doi/10.1073/pnas.1817929116.
233. Wojtanowicz, A.K., Bourgoyne, A.T., Zhou, D. & Bender, K. 2000. Strength and Fracture Gradients for Shallow Marine Sediments. US Department of Interior Mineral Management Service Final Report.
234. Wolterbeek, T.K.T., Cornelissen, E.K., Nolan, S., Todea, F., Stam, W., Roggeband, S.M., Dam, L., van Riet, F., Ruckert, F. & Keultjes, W.J.G. 2021. Restoration of annular zonal isolation using localized casing expansion (LCE) technology: A proof of concept based on laboratory studies and field trial results, in *J.Pet. Sci. Eng.* **197**(2021): 108103. https://doi.org/10.1016/j.petrol.2020.108103.
235. Wu, J., Pan, J., Wang, H., Wang, L., Lan, X., Yang, L. & Liu, W. 2019. The Application of Cyclone Desorption Technology for OBM Drill Cuttings Disposal. Presented at the International Petroleum Technology Conference, Beijing, China, 26-28 March. IPTC-19223-MS.
236. Wu, J., Pan, J., Wang, H., Wang, L., Liu, W. & Zhang, L. 2021. Cyclone Oil Desorption Technology for the Disposal of Oil-Based Mud Cuttings, in *SPE Journal* **26**(06): 3561-3574. SPE-205375-PA. https://doi.org/10.2118/205375-PA.
237. Wyllie, D.C. & Norrish, N.I. Chapter 14-Rock Strength Properties and their Measurements, in: Landslides: Investigation and Mitigation, National Academy Press, Washington, 1996, pp. 372-390. http://onlinepubs.trb.org/Onlinepubs/sr/sr247/sr247-014.pdf.
238. Xiaoyu, G., Yingfang, F. & Haiyang, L. 2018. The compressive behavior of cement mortar with the addition of nano metakaolin, in *Nanomaterials and Nanotechnology* **8**. https://doi.org/10.1177/1847980418755599.
239. Yang, Y. & Deng, Y. 2018. Mechanical properties of hybrid short fibers reinforced oil well cement by polyester fiber and calcium carbonate whisker, in *Constr. Build. Mater.* **182**(2018): 258-272. https://doi.org/10.1016/j.conbuildmat.2018.06.110.

240. Zhang, M., Bachu, S., 2010. Review of integrity of existing wells in relation to CO2 geological storage: what do we know? in *Int. J. Greenh. Gas Contr.* **5**(4): 826–840. https://doi.org/10.1016/j.ijggc.2010.11.006.
241. Zhang, C., Brom, R., Getliff, J. & Smith, J.P. 2016. Improving Environmental Performance by Sharing Information on Offshore Drilling Discharge Environmental Science and Drill Cuttings Treatment Technology. Presented at the SPE International Conference and Exhibition on Health, Safety, Security, Environment and Social Responsibility, Stavanger, Norway, 11-13 April. SPE-179271-MS.
242. Zhang, H. & Li, C.C. Effects of Confining Stress on the Post-Peak Behaviour and Fracture Angle of Fauske Marble and Iddefjord Granite, in *Rock Mech. Rock Eng.* **52** (2019) 1377-1385. https://doi.org/10.1007/s00603-018-1695-7.
243. Zhang, W., Eckert, A., Liu, X., 2017. Numerical simulation of micro-annuli generation by thermal cycling. Presented at the 51st US Rock Mechanics/Geomechanics Symposium, 25-28 June, San Francisco, California. ARMA-2017-0354.
244. Zhao, C., Li, J., Liu, G. & Zhang, X. 2019. Analysis of the influence of cement sheath failure on sustained casing pressure in shale gas wells, in *Journal of Natural Gas Science and Engineering* **66**(June 2019): 244-254. https://doi.org/10.1016/j.jngse.2019.04.003.
245. Zhou, X., Ghassemi, A., Riley, S. & Roberts, J. 2017. Biot's Effective Stress Coefficient of Mudstone Source Rocks. Presented at the 51st US Rock Mechanics/Geomechanics Symposium, San Francisco, California, 25-28 June. ARMA-17-235.
246. Ziashahabi, P., Ravi, K. & Prohaska, M. 2019. Polymer-Based Sealing Materials as Cement Additives to Restore Wellbore Isolation. Presented at the SPE Gas & Oil Technology Showcase and Conference, Dubai, UAE, 21-23 October. SPE-198584-MS.
247. Zielonka, M.G., Searles, K.H., Ning, J. & Buechler, S.R. 2014. Development and Validation of Fully-Coupled Hydraulic Fracturing Simulation Capabilities, in *Proceedings of the SIMULIA Community Conference*.
248. Zienkiewicz, O.C. 1987. The coupled problems of soil-pore fluid-external fluid interaction: basis for a general geomechanics code, in proceedings of the 5th International Conference on Numerical Methods in Geomechanics, Nagoya, Japan, 1-5 April, 1731–1740.
249. Zimmerman, R.W. 2000. Coupling in poroelasticity and thermoelasticity, in *Int. J. Rock Mech. Min.* **37**(2000): 79-87. https://doi.org/10.1016/S1365-1609(99)00094-5.